Quantitative soft-tissue imaging by spectral CT with Medipix3

J Paul Ronaldson

A thesis submitted for the degree of Doctor of Philosophy
at the University of Otago, Christchurch, New Zealand

November 1, 2012

Contents

List of Figures

List of Tables

Abstract

This thesis investigates the potential for quantifying soft tissues in preclinical studies by spectral computed tomography (CT) using the Medipix3 spectroscopic photon counting detector. Currently available methods for characterizing the composition of excised specimens and small animal models are insensitive, expensive or destructive. Quantitative imaging by spectral CT would provide a convenient alternative technique for preclinical studies of human diseases such as atherosclerosis and the metabolic syndrome. The work is presented as a series of interrelated studies describing the technical evaluation of the Medipix All Resolution System (MARS) spectral CT system, and the subsequent development and validation of a quantitative spectral analysis method.

The MARS-CT system and components were characterized in three stages. Firstly, the performance of a prototype MARS x-ray camera incorporating a single Medipix3 was assessed. High quality images were obtained in single pixel mode, but, in charge summing mode image quality was severely degraded by electronic instabilities and biases. Secondly, methods for calibrating the global DACs and equalizing the pixel thresholds of a quad Medipix3 array were developed and tested. These methods enabled the Medipix3 array to operate as a homogeneous large area imaging device. Thirdly, a MARS-CT system, incorporating a MARS camera with Medipix3 and silicon sensor layer, was evaluated and found to give acceptable performance for preclinical imaging of soft tissues.

A reconstruction domain material decomposition method for quantifying soft tissue components was developed and validated. Calcium, fat and water components were successfully quantified in mouse and atheroma equivalent phantoms. The material decomposition method was then validated in a preclinical study of excised mice livers. The fat mass fractions of twelve wild type and twelve transgenic mice were quantified by spectral CT and the results compared with those of biochemical analysis.

In conclusion, this thesis has developed and validated a new reconstruction image domain analysis method and has shown that quantitative soft tissue imaging of excised specimens and small animal models by spectral CT is feasible. It is a strength of the analysis method that the responses of arbitrary detector types are easily accommodated. The method is thus applicable to other areas such as functional imaging with high-Z nanoparticles.

Acknowledgements

Firstly, I thank Dr Anthony Butler and Professor Phil Butler who have supervised my thesis work, and for their help, I am most grateful. Aspects of this research are located somewhere close to the boundaries between physics, radiology and biology, and progress would have been impossible without significant advice and contributions from Dr Nigel Anderson, Dr Nicola Scott and Associate Professor Steven Gieseg in their capacities as clinical advisors.

I gratefully acknowledge the technical support of all those, past and present, in the MARS team who have developed the electromechanical systems, imaging electronics, software libraries and experimental protocols that are necessary for the progress of all involved with this project. Special thanks are due to Rafidah Zainon for collaborating on many aspects of the experimental work and for proofreading parts of this thesis.

This study was completed at a difficult time for many in Christchurch; for their help with temporary research accommodation and access to technical resources and materials, I thank the Canterbury District Health Board and the Medical Physics and Bioengineering Department in particular.

Finally, I thank my family for their support, and especially my wife Anna for her help and patience throughout this study.

This research was supported by a grant administered by MARS Bioimaging Ltd.

Academic contributions

During the course of this thesis the candidate has personally prepared one published journal article [3], one conference paper [4] and a further journal article [6] for submission. Work from this thesis has contributed to a number of other journal and conference publications for which the candidate is a co-author.

[1] Bones, P. J., Butler, A. P. H., **Ronaldson, J. P.**, and Opie, A. M. T. (2010). Development of a CT scanner based on the Medipix family of detectors. In *Developments in X-Ray Tomography VII, Proceedings of SPIE, 7804, 780410(1-10).*

[2] Hurrell, M. A., Butler, A. P. H., Cook, N. J., Butler, P. H., **Ronaldson, J. P.**, and Zainon, R. (2012). Spectral Hounsfield units: a new radiological concept. *European Radiology*, 22(5):1008–1013.

[3] **Ronaldson, J. P**., Walsh, M., Nik, S. J., Donaldson, J., Doesburg, R. M. N., van Leeuwen, D., Ballabriga, R., Clyne, M. N., Butler, A. P. H., and Butler, P. H. (2011a). Characterization of Medipix3 with the MARS readout and software. *Journal of Instrumentation*, 6(01):C01056.

[4] **Ronaldson, J. P.**, Zainon, R., Anderson, N., Butler, A., and Butler, P. (2011b). Performance of MARS-CT using Medipix3 for spectral imaging of soft-tissue. In *Proceedings of Nuclear Science and Medical Imaging Conference, 2011.* IEEE.

[5] **Ronaldson, J. P.**, Zainon, R., Sedayo, A., Scott, N., Butler, A., Butler, P., and Anderson, N. (2011c). Towards quantifying the composition of soft-tissues by spectral CT imaging with Medipix3. In *Proceedings of RSNA 2011 Scientific Assembly and Annual Meeting.*

[6] **Ronaldson, J. P.**, Zainon, R., Scott, N., Gieseg, S., Butler, A., and Butler, P. (2012). Towards quantifying the composition of soft-tissues by spectral CT imaging with Medipix3. Unpublished manuscript.

[7] Walsh, M. F., Opie, A. M. T., **Ronaldson, J. P.**, Doesburg, R. M. N., Nik, S. J., Mohr, J. L., Ballabriga, R., Butler, A. P. H., and Butler, P. H.

(2011). First CT using Medipix3 and the MARS-CT-3 spectral scanner. *Journal of Instrumentation*, 6(01):C01095.

[8] Zainon, R., **Ronaldson, J. P.**, Butler, A., and Butler, P. (2011). Establishing a linear basis for quantifying material composition using spectral computed tomography. In *Proceedings of 2011 International Conference on Biomedical Engineering and Biotechnology (BEB2011)*. IEEE.

[9] Zainon, R., **Ronaldson, J. P.**, Janmale, T., Scott, N. J., Buckenham, T., Butler, A., Butler, P., Doesburg, R., Gieseg, S. P., Roake, J., and Anderson, N. (2012). Spectral CT of carotid atherosclerotic plaque: comparison with histology. *European Radiology*. Published online before print July 4, 2012. PubMed PMID:22760344. doi:10.1007/s00330-012-2538-7.

Glossary

ASIC	Application Specific Integrated Circuit.
CCD	Charge Coupled Device.
CERN	European Organization for Nuclear Research.
CMOS	Complementary Metal Oxide Semiconductor.
CRP	C-reactive protein. A protein in the blood, the concentration of which increases in response to inflammation.
CSM	Charge Summing Mode. A special Medipix3 operating mode designed to eliminate charge sharing.
CT	Computed Tomography.
CVD	Cardiovascular Disease.
DAC	Digital to Analogue Converter.
dKO	Double Knock Out. The phenotype of a species with two inoperative genes.
FBP	Filtered Backprojection.
FDK	Feldkamp-Davis-Kress. A cone beam reconstruction algorithm.
FOV	Field of View.
GOS	Gadolinium oxysulphide, a ceramic scintillator.
HDL	High Density Lipoprotein.
HSV	Hue, Saturation and Value.
HU	Hounsfield Unit.
ICUS	Intracoronary Ultrasound.
IQR	Inter Quartile Range.
kVp	Peak kilovoltage applied to an x-ray tube.
$LD_{50}(30)$	Dose expected to be lethal to 50% of the population within 30 days.
LDL	Low Density Lipoprotein. The form of lipoprotein in which cholesterol is transported in the blood.

LSB	Least Significant Bit.
MARS	Medipix All Resolution System.
MDCT	Multi Detector Computed Tomography.
MetS	Metabolic Syndrome.
MRI	Magnetic Resonance Imaging.
MRS	Magnetic Resonance Spectroscopy.
MSB	Most Significant Bit.
MTF	Modulation Transfer Function. The discrete fourier transform of the line spread function.
NAFLD	Non Alcoholic Fatty Liver Disease.
NPS	Noise Power Spectrum. A description of the spatial frequency content of image noise.
OLP	Ordinary Least Products.
OLS	Ordinary Least Squares.
PCA	Principal Component Analysis.
PP	Polypropylene.
PVC	Polyvinylchloride.
ROI	Region of Interest.
SDD	Source to Detector Distance.
SOD	Source to Object Distance.
SPM	Single Pixel Mode. The basic Medipix3 operating mode without charge summing.
THA	Threshold adjustment bits associated with counter 0.
THB	Threshold adjustment bits associated with counter 1.
WHO	World Health Organization.
WT	Wild Type. The phenotype of the natural form of a species.

Chapter 1

Introduction

This chapter describes the aim and scope of the thesis and introduces the research topic: spectral computed tomography (CT) for enhanced imaging of soft tissues in preclinical health research. The distinctions between standard CT and the various forms of spectral CT are explained. A description of the current limitations and potential advantages of spectral over other forms of computed tomography is followed by a discussion of some relevant preclinical applications. The chapter concludes with an outline of the rest of the thesis.

1.1 Aim

The aim of this thesis is to investigate the potential for enhancing soft tissue imaging through the application of spectral CT using the Medipix3 photon counting detector. The significance of this work is its relevance to small animal and specimen imaging for preclinical health research. Currently available methods for characterizing the composition of excised specimens and animal models of human diseases are typically insensitive, expensive or destructive. Improved tomographic imaging techniques will provide alternative and more convenient methods for preclinical studies of human diseases such as atherosclerosis and the metabolic syndrome. It is anticipated that a better understanding of the pathology of these common diseases, as well as improved methods for monitoring the effectiveness of treatments, will have widespread clinical benefits.

1.2 Background

The MARS research group is a collaboration of scientists, and engineers associated with the Universities of Otago and Canterbury, Christchurch, New Zealand. The group is exploring many mathematical, technological, clinical and pre-clinical avenues of research. A current goal of the team is to work with local industry to develop a commercial spectral CT scanner based on the Medipix family of detectors.

1.2.1 Spectral CT

X-rays can be used to form radiographic images of the interior of heterogeneous objects. As a beam of x-rays passes through an object, it is attenuated according to local variations in material density and composition. Viewing an object with x-rays projected in a single direction produces a 2D representation of its internal composition and density. Viewing an object with x-rays projected from many angles allows a cross-sectional representation of the interior of the object to be reconstructed. Computed tomography (CT) is regarded as perhaps the greatest invention in diagnostic radiology [Hounsfield, 1973].

The attenuation of the x-ray beam also depends on the energy distribution of the beam itself. Most image reconstruction techniques assume that the x-ray beam is monoenergetic. Consequently, polychromatic artefacts can appear in the reconstructed images. Furthermore, attenuation varies with energy in a manner characteristic of the elemental composition of the material and thus the x-ray energy spectrum becomes distinctively 'coloured' during its passage through the object. However, detectors used in traditional CT record only the intensity of the x-ray beam and not its energy distribution. Information about the composition is thus discarded reducing our ability to distinguish one material type from another.

Spectral CT aims to improve the ability to distinguish material types by measuring x-ray attenuation as a function of energy. Consequently it can also be used to eliminate polychromatic image artefacts. To implement spectral CT we could choose to vary the spectrum emitted from the x-ray source, for example, by making sequential measurements at different beam energies or by including two independent detector–source arrangements within the system. These methods are known as dual energy CT. An alternative approach is to introduce energy resolving detectors. In this thesis we will refer to this as simply *spectral CT* and make the distinction from other methods clear from the context where necessary [1].

Dual energy CT allows the continued use of traditional x-ray detectors, and, because of the stringent demands placed on detector performance, it is the method that has been implemented in human scale clinical CT. On the other hand, spectral CT with spectroscopic photon counting detectors avoids the complexities and space constraints associated with fast switching and multiple imaging systems, but requires the use of sophisticated detectors, such as Medipix3, that are available for research but have not yet been developed for clinical use. Medipix3 provides the additional benefit of simultaneous acquisition in multiple energy bins.

The latest developments in detector technology include segmented spectroscopic x-ray detectors that can sense both the intensity and energy distribution of an x-ray beam. Although limitations in sensor size and count rate performance currently preclude the use of these detectors in mainstream clinical CT, their use in preclinical health research applications is quite feasible and some potential benefits have already been demonstrated. Small animal

---

[1] Computed tomography implemented using energy resolving detectors is known variously as spectroscopic, multi-energy, multi-colour, photon counting, spectral, and multi-spectral CT.

and specimen imaging systems are used in preclinical health research to study the progression of disease and the composition of excised tissues. As part of a micro CT system, spectroscopic photon counting detectors can be used to form CT images from selected portions of the x-ray spectrum.

The Medipix family of x-ray imaging detectors are spectroscopic photon counting detectors developed by an international collaboration led by designers at CERN [Campbell et al., 1998, Llopart et al., 2002, Ballabriga et al., 2006]. The collaboration aims to apply detector technology to medical imaging. Earlier models suffered from the charge-sharing effect that is a common problem with fine-pitch detectors. The charge created in the detector by the x-ray interaction must be collected to form the imaging signal. However, in fine-pitch detectors the charge spreads into neighbouring pixels during the collection process, and both spatial and energy resolution are compromised. Medipix3 is the latest and most advanced in this series of photon counting detectors. Medipix3 was developed to enhance count rate performance and to overcome the problems of charge sharing. Initial testing results [Tlustos, 2010] were positive and showed that the low energy tail was significantly reduced. Small animal imaging with materials analysis using either a statistical or physical model was suggested as a suitable application for this technology.

1.2.2 Preclinical research

Compared with standard clinical CT, preclinical micro CT of small animals and specimens is less demanding of detector size and performance and is therefore well placed to benefit from the development of spectroscopic photon counting detectors. Already, researchers have used this technology to reduce artefacts, distinguish contrast agents, and determine material composition [Schlomka et al., 2008, Butler et al., 2008a, Butler et al., 2008b, Shikhaliev and Fritz, 2011].

The MARS research group has identified some key preclinical research areas for immediate investigation, including studies of nanoparticle contrast agents, ex vivo atherosclerosis, and fatty liver disease as a marker of the metabolic syndrome. These research areas may each benefit in different ways from technical improvements offered by spectral CT.

Firstly, high-Z nanoparticle contrast agents such as gold [Hainfeld et al., 2006] are now available that are more opaque and less toxic than traditional contrast agents such as iodine. High-Z nanoparticles can be used to facilitate in vivo functional imaging. For example, gold nano-particles can be designed to selectively target tumour antigens. The presence of gold can be uniquely and sensitively detected by the effect of its K absorption edge on pairs of spectral images acquired at energies above and below the edge. The K-edge of gold (at 81 keV) is within the range of some spectroscopic sensor materials and thus K-edge imaging with spectral CT may be particularly effective for in vivo functional studies.

Secondly, preclinical studies of human atherosclerosis may benefit from improved characterization of sample composition and morphology using spectral CT. Atherosclerosis is hardening of the arteries characterized by deposits of calcified plaques on the artery wall. Most plaques are stable, but some are prone to rupture and can cause cardiovascular events and strokes [Davies and Woolf, 1993]. It has been proposed that aspects of the morphology and composition of the plaques can serve as markers for cases at risk of rupture. Spectral CT could thus prove to be an important tool for the study and diagnosis of atherosclerosis.

Finally, small animal model studies of human diseases such as the metabolic syndrome will benefit from improved non-invasive quantitative analysis by spectral CT. The metabolic syndrome is a common condition affecting $\sim$40% of adults in the western world [Reilly and Rader, 2003, Cameron et al., 2004]. The extreme clinical outcomes of the metabolic syndrome are increased risk of cardiovascular disease and type 2 diabetes. There are a number of recognized risk factors for the disease including: abdominal obesity, elevated triglyceride levels, reduced levels of high density lipids, increased blood pressure, and insulin resistance. An additional marker that has been proposed is the fat content of the liver. Standard non-invasive imaging methods are typically insensitive or expensive and not widely available. Spectral CT may provide a convenient option for studying the progression of the disease in small animal studies.

These preclinical research areas will each benefit from improvements due to the development of spectral CT. In particular, research into atherosclerosis and the small animal imaging studies of human diseases such as the metabolic syndrome require improved *soft tissue* imaging methods to enable biological tissues to be distinguished without the use of traditional contrast agents. For the purposes of this work we will define soft tissues as all biological tissue that is not bone. Thus soft tissues will tend to be of moderate density and comprise elements of low atomic number such as hydrogen, carbon, nitrogen and oxygen. We may also expect to find calcium ($Z = 20$) within soft tissues since it is a major component of calcifications found in many tissues. Other elements will be present in lesser quantities and may usually be ignored. Iron is a notable exception; it is a component of blood that is of particular interest to atherosclerosis researchers as it may be a marker for vulnerable plaques.

The scope above precludes the use of K-edge imaging for material discrimination as none of the soft tissue components has a K-edge at an energy suitable for x-ray imaging. Thus, a key question is whether soft tissue components are sufficiently distinctive for useful measurement by spectral CT.

1.3 Thesis outline

This thesis will show, by simulation and experiment, that soft tissue components can be individually distinguished and quantified by spectral CT. The early chapters of this thesis review relevant existing work and provide an introduction to the physics and technology of spectral CT. The middle chapters describe the bulk of the candidate's developmental and investigative work culminating in a method for material discrimination and a novel implementation for assessing the effectiveness of quantitative spectral CT. An example quantitative application is then presented before the work is discussed and summarized in the final chapter.

Chapter 2 reviews the development of spectral CT and some preclinical applications that may benefit from this technology. After a historical review of the development of clinical CT, micro CT using spectroscopic photon counting detectors is discussed. Preclinical small animal and specimen imaging research applications are then reviewed to identify the gaps within the body of existing work that are relevant to this thesis.

Chapter 3 describes the physical processes of x-ray imaging. Atomic level descriptions of relevant radiation interaction mechanisms are given. The use of attenuation coefficients for calculating the effect of bulk elemental and compound materials on a narrow beam of x-ray photons is introduced. The physical principles of x-ray detectors are then described and the properties of various scintillator and semiconductor materials are compared. Finally, the Medipix3 detector used within this work is described.

In *Chapter 4* the basic theory for obtaining cross sectional reconstructions from many parallel projections is given and extended to the cone beam geometry used for this work. Some practical aspects of standard clinical tomography including common imaging artefacts are then discussed. Finally, spectral CT is introduced and its performance simulated and analysed using a numerical model developed for this work.

Chapter 5 evaluates the Medipix3 with silicon sensor layer using the MARS x-ray camera system. A preliminary method for pixel threshold equalization based on a procedure provided by the chip designers is tested. Electronic stability, image quality and spectroscopic performance of the detector are evaluated. Some limitations in performance, such as poor image quality in charge summing mode and a sensitivity to variations in temperature, are noted.

In *Chapter 6* a temperature stabilized Medipix3 chip array is configured and operated as a single large-area detector unit. The necessary protocols for calibrating the Medipix3 DACs are given. An improved method for threshold equalization developed for this work is presented. Finally, an energy calibration and inter-chip equalization protocol is described and evaluated.

Chapter 7 compares the performance of the MARS-CT system incorporating Medipix3 with the anticipated requirements for soft-tissue imaging research. Methods for determining spatial resolution, response uniformity, pixel noise, CT number linearity and the spectroscopic energy calibration are given followed by the results for the MARS-CT system. It is found that the system is suitable for preclinical imaging, although some lack of spatial resolution is noted.

Chapter 8 presents the theory of a constrained least squares method for material decomposition and quantification. The method is experimentally validated using clinically relevant phantoms and biological specimens. A novel (in this area) method of assessing the performance of spectral CT is presented and the performance of the MARS-CT system assessed against target concentrations of key soft tissue components. The ability to distinguish and quantify key materials such as calcium and fat is confirmed, however, the system is unable to quantify iron (in the presence of calcium) at the required levels.

Chapter 9 presents a preclinical biological imaging application of the quantitative method developed in the previous chapter. A quantitative study of the fat content of excised mice livers comparing spectral CT results against those of a standard biochemical analysis is described and discussed.

Chapter 10 examines the overall thesis objective in the context of the results obtained during this work. This chapter confirms that the spectral CT technique does indeed enhance soft tissue imaging performance. Although, not all of the target requirements for preclinical soft tissue imaging are met by the

MARS-CT used for this work; the reasons for this are discussed and potential improvements in technique are proposed. The limitations of this study are considered before recommendations for possible future work are given.

Chapter 2

Literature review

This chapter reviews the development of spectral CT and some preclinical applications that may benefit from this technology. After a review of the development of clinical CT and dual energy CT, the chapter assesses micro CT using spectroscopic photon counting detectors. Finally, gaps that exist in preclinical small animal and specimen imaging are identified and related to this thesis.

2.1 Computed tomography

Wilhelm Conrad Röentgen discovered x-rays in 1895. He was awarded the 1901 Nobel Prize in Physics for his discovery of the unknown radiation that could pass through matter. X-ray radiography utilizes the differential absorption of these x-rays during their passage through matter to create 2D images of the internal structure. Formed using a static source and photographic film, radiographic images suffer from the superposition of the intervening structures. Although the mathematical foundations for modern computed tomography (CT) were laid in 1917 by Johann Radon with the development of mathematics for reconstructing cross sections from multiple projections [Radon, 1986], the engineering necessary for a practical implementation came much later.

2.1.1 Clinical CT

In 1972 Sir Godfrey Hounsfield developed the first practical computed tomography (CT) scanner [Hounsfield, 1973]. The invention marked a paradigm shift in diagnostic radiology and earned Hounsfield the 1979 Nobel Prize for Medicine which he shared with Allan Cormack for his earlier theoretical work on line integrals and their radiological applications [Cormack, 1963, Cormack, 1964]. Hounsfield's CT system was a head scanner comprising a single scintillating detector and source arranged on a translating bed that could rotate around the object. Although the use of the Fourier transform for x-ray tomography had already been demonstrated [Bates and Peters, 1971], Hounsfield's system used an algebraic reconstruction technique to produce a cross sectional map of attenuation coefficient. To emphasize the subtle differences in attenuation, the system displayed its results on a scale normalized to water (the Hounsfield scale). Compared with traditional radiographic images of the time, the new CT systems offered greatly improved contrast due to their ability to measure the attenuation within individual voxels rather than superpositions of attenuation values along ray paths. Hounsfield suggested that the machine should be able to differentiate soft tissues of similar densities and even described how material types could be determined by comparing tomographic slices taken at different x-ray beam energies. Despite its immediate impact, there were of course many areas for improvement in both technique and technology and a period of rapid innovation followed.

In 1974 Ledley [Ledley et al., 1974] developed a first generation whole body scanner and implemented convolution algorithms for reconstruction. The second generation of scanners included multiple detectors placed opposite a single source in a partial fan beam geometry to improve the overall acquisition time. The third generation of scanners introduced in 1976 were much faster and provided full coverage of the object without the need for the translation mechanism. High pressure xenon detectors were favoured at this time because of the ease with which homogeneous 1D detector arrays could be constructed. Developments aimed at improving scan speeds continued, and, for a while, fourth generation systems using a fixed ring of detectors provided the ultimate in fast imaging. However, slip-ring technology, multi-slice detector systems and spiral scanning protocols were introduced [Kalender, 1994] and the third generation was adopted as the standard configuration. Solid state ceramic scintillator detectors made from gadolinium oxysulphide (Gd_2O_2S also known as GOS) were used to form the 2D arrays used in multi-slice systems. Multi-detector spiral CT (MDCT) with a sub-second scan time per revolution is now the norm in clinical CT.

Clinical computed tomography is now very mature and meets almost all routine clinical requirements [Kalender, 2005]. As the significance of incremental engineering developments reduces, the impact of research into new measurement principles such as spectral CT and quantitative volumetric imaging may figure more prominently [Wang et al., 2008].

2.1.2 Spectral CT

The development of clinical CT has been primarily focussed on reducing scan times. The development of commercial spectral CT systems capable of material identification came about indirectly. Initial experiments envisaged a single tube switched to multiple voltages for successive scans. Alvarez and Macovski analysed the problem in the projection image domain, decomposing the observed projections at multiple tube voltages into Compton and photoelectric components. Brooks [Brooks, 1977] successfully demonstrated the dual energy spectral CT method in the reconstruction image domain. Brooks studied the relationship between the CT number of a material and the x-ray spectrum of the interrogating flux. His dual energy method decomposed the pair of measured CT numbers into photoelectric and Compton components characteristic of each material. Both of these early methods assumed an absence of K-edges within the energy region of interest which is not always the case. However, the main obstacles to the implementation of dual energy CT at this time were practical ones.

The main practical problems associated with early dual energy CT systems using sequential acquisitions at multiple tube voltages [Rutherford et al., 1976] were the lengthy acquisition times and issues of stability and registration. Prototype systems using fast kVp switching during each scan revolution were tried [Kalender et al., 1986]. However, these systems were more complex than standard systems and dual energy CT was not initially adopted for mainstream applications; it was the later development of fast cardiac imaging methods that enabled the introduction of the first commercial dual energy systems [Flohr et al., 2006, Petersilka et al., 2008]. These systems included multiple x-ray sources primarily for fast cardiac imaging and secondarily for dual energy spectral CT scanning. Materials analysis methods have subsequently been developed for dual energy CT that use intrinsic differences in the energy-dependent absorption coefficients to differentiate bone, soft tissue and collagen as well as artificial contrast agents such as iodine [Johnson et al., 2007].

The currently accepted practice is to simultaneously acquire data from two detector–x-ray tube combinations arranged at 90-degrees with one tube voltage at 140 kVp and the other at 80 kVp. The extended x-ray continua emitted from these devices have average x-ray energies of typically 76 keV and 56 keV respectively. Spectral overlap reduces the contrast of the method. The contrast can be enhanced by filtering the high energy beam with some absorbing material to remove the low energy component [Johnson et al., 2007]. Dual-energy spectral CT has only two measurement dimensions and simple empirical models can be used for materials analysis. The *three materials discrimination* method [Petersilka et al., 2008] regards the two CT values as a single vector in 2D space and compares this with known vectors for up to three reference materials. Material compositions are assigned to individual voxels according to the similarity of the measured spectral CT vector with those of the reference materials. This empirical model is easily understood and implemented but not easily generalized to higher dimensions.

Whereas dual energy spectral CT varies the interrogating spectrum (entrance flux) to gain spectroscopic information, other forms of spectral CT obtain spectroscopic information by sampling the exit flux at different energies [Kappler et al., 2009]. This has been implemented in two forms: with dual layer detectors [Barnes et al., 1985] and energy selective photon counting detectors. The dual layer approach produces spectral data limited to two dimensions and is primarily used as a research tool [Carmi et al., 2005, Goshen et al., 2008]. More recently, sophisticated photon counting detectors capable of full spectroscopic imaging have been developed [Campbell et al., 1998, Llopart et al., 2002, Ballabriga et al., 2006, Delpierre et al., 2007, Henrich et al., 2009]. Rather than the two spectral components measured by the dual energy and dual layer systems previously mentioned, spectroscopic photon counting detectors are capable of imaging over an arbitrary number of energy ranges. However, limitations in material technology and count rate capabilities have so far restricted spectral CT with spectroscopic photon counting detectors to research applications such as small animal and specimen micro CT imaging.

2.1.3 Micro CT

In contrast to clinical CT, the development of small animal and specimen imaging systems has been driven, predominantly, by the desire for improved contrast to noise ratio and spatial resolution rather than scanning speed [Ritman, 2007]. This has led to the widespread use of micro focus x-ray tubes and alternative high resolution detector technology such as flat panel detectors with amorphous silicon and CCD camera readout systems together with the adoption of cone beam geometry [Paulus et al., 2000, Kim et al., 2005, Ross et al., 2006, Zhu et al., 2009, Wang et al., 2011b].

Small animals and specimens are less attenuating than human subjects, and the source and detector characteristics must be adjusted to obtain maximum tissue contrast. The optimum average beam energy to obtain best contrast with mouse-sized subjects is around ~25 keV [Paulus et al., 2000]. At this energy silicon-based detectors perform comparatively well [Yaffe and Rowlands, 1997].

For small animal imaging, a voxel size of $\sim(100\ \mu\text{m})^3$ is required for scale equivalence to human CT. To achieve an acceptable contrast to noise ratio at this higher spatial resolution, the radiation dose must be greatly increased. The relationship between dose and linear resolution is $\textit{dose rate} \propto \textit{resolution}^{-4}$ [Badea et al., 2008]. For in vitro specimen imaging, radiation dose is not a concern and good image quality at voxel sizes of $(< 50\ \mu\text{m})^3$ is readily achievable. The dose rate–resolution relation is an issue for live animal imaging but can be managed [Ford et al., 2003, Ritman, 2007]. For example, the lethal dose $(LD_{50}(30))$ for a mouse is around 7 Gy [Sato et al., 1981], and it is observed that rodents are able to recover quickly (in a few hours) from sub-lethal doses [Ford et al., 2003]. Thus, in terms of the effect of an overall dose administered during longitudinal studies, mice can be imaged repeatedly with sub-lethal doses without terminal effects. Nevertheless, radiation dose limits the spatial and contrast resolution achievable with standard systems and improvements in technology and technique are necessary to enhance image quality beyond the current limits.

Spectral CT has the potential to enhance the quality of CT images without a prohibitive dose penalty [McCollough et al., 2012]. The different modes of spectral CT in common use are based upon controlling either the x-ray source spectrum or x-ray detector response characteristics to sample the attenuation coefficient of the object across different energy ranges. Thus dual x-ray sources or voltage switching with a single tube are both potentially viable methods. However, these implementations are limited by constraints of size and mechanical complexity. Dual layer detectors have also been used for spectral CT however these provide limited information in the form of just two spectroscopic signals. Thus it is the development of sophisticated spectroscopic photon counting detectors with adjustable energy thresholds which are the current focus of much research.

2.2 Spectroscopic photon counting detectors

Clinical imaging systems generally use arrays of discrete inorganic scintillator (GOS) detectors operated in energy integrating mode [van Eijk, 2003]. These are selected to have a fast response time and high absorption at clinical energies (∼10–150 kVp). Where the requirements for throughput and quantum efficiency at high energy are relaxed, other detector materials and modes of operation may be considered. Compared with whole body CT, other clinical applications such as mammography and research applications such as small animal imaging have reduced count rate requirements and use lower accelerating voltages (∼25–50 kVp) to obtain good soft tissue contrast [Gong et al., 2004, Lemacks et al., 2002, Paulus et al., 2000]. Consequently, detector types such as amorphous silicon panels and low Z semiconductors may be used together with pulse mode counting devices [Yaffe, 2001, Yaffe and Rowlands, 1997, Goertzen et al., 2004].

Where the count rate is low enough to permit its use, pulse mode counting allows for more flexible event processing than integrating mode. Traditional energy integrating detectors produce a scalar signal that is proportional to the rate of energy deposited (or charge created). In contrast, spectroscopic pulse mode photon counting detectors process each event individually, recording the distribution of energies within timed intervals. The distribution of events can thus be arbitrarily weighted to maximize contrast [Lehmann et al., 1981, Anton et al., 2007, Carramate et al., 2011] or used to form spectroscopic images for further analysis [Manuilskiy et al., 2004, Giersch, 2005, Jakůbek, 2009].

To preserve spatial resolution, direct conversion thin semiconductor detectors are segmented with the readout electronics attached directly to each sensor segment. They may be arranged as 1D strips or 2D pixel arrays. Strip detectors may integrate only the analogue electronics directly within the readout circuitry whereas hybrid pixel detectors include both the analogue and digital processing in the readout ASIC (Application Specific Integrated Circuit). Examples of 2D pixel detectors include XPAD [Delpierre et al., 2007] and PILATUS [Henrich et al., 2009] both of which were developed for x-ray crystallography and have pixel pitches in the range ∼130–200 μm. In comparison, the Medipix family of 2D photon counting pixelated detectors [Campbell et al., 1998, Llopart et al., 2002, Ballabriga et al., 2006] are hybrid detectors with a fine pixel pitch of 55–110 μm.

2.2.1 Medipix

The Medipix family of x-ray imaging detectors are developed by an international collaboration led by designers at CERN [Campbell et al., 1998, Llopart et al., 2002, Ballabriga et al., 2006]. The collaboration aims to apply detector technology, developed in support of high energy physics, to medical imaging. Medipix3 is the latest and most advanced in this series of photon counting detectors and has been made available for testing and evaluation.

Medipix detectors have been proposed for use as medical imaging devices, however the early detector models exhibited a number of problems. Good spatial resolution, high signal to noise ratio, high sensitivity and high count rate capability with a large dynamic range are among the major requirements for medical use. Medipix1 was a relatively low resolution device with a pixel pitch of 170 μm and it supported only silicon sensor layers. It was used to demonstrate the photon counting principle. Medipix1 was superseded by Medipix2 with a pixel pitch of 55 μm and its ability to collect both holes and electrons that allowed the use of alternative sensor layers. Pfeiffer [Pfeiffer, 2004] showed that Medipix2 had the required spatial resolution and high contrast object definition, but noted that the 300 μm silicon layer has poor absorption efficiency. In addition, with its fine pixel pitch, the spectroscopic performance of Medipix2 suffered from the charge-sharing effect and cross-pixel charge summing was proposed as a potential solution.

Medipix3 was developed to overcome the charge sharing problem and enhance count rate performance. As well as charge summing, multiple counters per pixel with variable dynamic range and continuous read-write functionality have been implemented in Medipix3 [Ballabriga et al., 2006, Ballabriga, 2009a]. Initial results from the Medipix3 detector [Tlustos, 2010] illustrated the effect of charge-summing mode on the spectral response. Both in simulated and measured spectra, the desired effect was obtained and the low energy tail was significantly reduced. Small animal imaging with materials analysis using either a statistical or physical model was suggested as a suitable application for this technology.

2.3 Spectral decomposition

Decomposition of spectral data may be applied in either the projection or reconstruction image domains and may be based on basis functions describing either the physical interaction mechanisms or the material properties. Statistical methods, requiring no a priori model, may also be used for classifying spectral images.

Spectral effects were considered theoretically by Alvarez and Macovski in 1976 [Alvarez and Macovski, 1976]. They noted that spectral data could be formed by various methods, which might now include: dual energy beams, isotope sources, tunable x-ray sources, multiple absorption filters and also spectroscopic detectors. They modelled spectral data using basis functions derived from approximations of the photoelectric and Compton effects. The model is applied in the projection image domain and the resulting photoelectric and Compton component images are characteristic of atomic number and electron density respectively. The method also eliminates beam hardening artefacts but does not correct the effects of scattering. The method assumes that there are only two basis functions from which the attenuation coefficients for all materials can be (approximately) derived and consequently the study concludes that spectral decomposition can be supported by low resolution measurements of just two energy groups. This analysis fails to consider K-edge effects which are important indicators of high Z materials such as artificial contrast agents. Furthermore, these methods do not include a forward model of the detector response and so are not directly applicable to spectral CT using spectroscopic photon counting detectors. In a recent simulation study, Alvarez [Alvarez, 2011] considered an extension of the original two function decomposition specifically for spectroscopic detectors. The requirement to include the response function of the detector is accommodated by a combination of empirical calibration and interpolation. Although K-edges from high Z materials were not included within this study, the author argues that the method could readily be extended to include basis functions for such materials.

K-edge effects of contrast agents such as iodine were specifically considered by Schlomka et-al [Schlomka et al., 2008]. They experimentally demonstrated decomposition of photoelectric, Compton and iodine component images using a micro CT system incorporating a commercially available energy discriminating CdTe line array detector. In another study, Firsching [Firsching et al., 2008] completely replaced the photoelectric and Compton components in favour of a set of material specific basis functions. Both of these methods are applied in the projection domain and require a detailed detector response function that is difficult to measure accurately.

Statistical methods such as principal component analysis (PCA) avoid the need for a physical model of the detector response and analyse multi dimensional data directly for significant patterns or correlations. PCA has been successfully applied to spectral projection and reconstructed images [Butzer et al., 2008, Butler et al., 2009, Butzer, 2009]. The method assumes that the spectral data vary linearly with some unknown basis functions and determines the most significant subset of these directly from the measurement data. As a consequence, PCA and other statistical methods may be used to classify structures within an image by their spectroscopic properties, but they cannot identify specific materials nor determine their quantities.

Several quantitative decomposition methods have been applied in the reconstruction image domain. Brooks [Brooks, 1977] decomposed the spectral data into photoelectric and Compton images, and a third spectral component describing the properties of the x-ray beam. Heismann et-al [Heismann et al., 2003] decomposed the data into density and atomic number and finally Liu et-al [Liu et al., 2009] used Heismann's result as an additional input to their own material decomposition method and derived mass fractions within mixed solutions. These approaches all use forward models of the spectrum but none consider the spectroscopic response of the detector; they were developed with clinical scale dual energy CT in mind and assumed the detector to be an ideal absorber.

The fundamental characteristic that all these approaches utilize is the intrinsic dimensionality of the energy dependent material attenuation coefficients. This is sometimes assumed to be just two, with one component representing the photoelectric effect and the other the Compton effect. This is approximately true only for materials of low atomic number ($Z \leq 20$) that have no K-edge within the measurement region. Furthermore, in a recent theoretical study [Bornefalk, 2012] of the number of components required to represent the attenuation coefficients of an arbitrary low Z material ($Z \leq 20$), it was concluded that, although there are indeed two very dominant effects, the intrinsic dimensionality of the attenuation data is at least four.

2.4 Preclinical research applications

Spectral CT using high resolution spectroscopic photon counting detectors is able to provide multi-energy datasets from a single acquisition using a standard x-ray tube. Researchers have identified improved image quality (reduction of artefacts), K-edge imaging (artificial contrast identification) and enhanced intrinsic tissue contrast (soft tissue imaging) as potential advantages of spectral CT [Schlomka et al., 2008, Butler et al., 2008a, Butler et al., 2008b, Shikhaliev and Fritz, 2011]. At the micro CT scale, these advantages can be applied to preclinical research involving small animal models of disease and ex vivo biological specimens [Anderson et al., 2010].

A substantial amount of work utilizing the K-edges of contrast materials has been done demonstrating the ability of spectral CT technology to distinguish contrast materials from body tissues by their attenuation spectrum [Roessl and Proksa, 2007, Feuerlein et al., 2008, Schlomka et al., 2008, Firsching et al., 2009, Cormode et al., 2010, Bulte, 2010]. Comparatively little research has been done into the potential advantages of applying spectral CT to soft tissue imaging without contrast agents. Most K-edge imaging involves relatively high energy x-ray photons and consequently requires high Z detector materials such as CdTe. Soft tissues, on the other hand, show most contrast at low photon energies and can be successfully imaged using sensor layers of low atomic number such as silicon. The application of spectral CT using Medipix3 with a silicon sensor layer to preclinical soft tissue imaging would seem to be appropriate. Material differentiation and contrast enhancement of tissues without the need to administer artificial contrast agents would provide a useful means of monitoring the status of animal models during longitudinal studies and allow the non-destructive characterization of excised human tissues.

The MARS research group [1] have identified preclinical research into nanoparticle agents, atherosclerosis, and fatty liver disease as key health research areas for the application of spectral CT with spectroscopic photon counting detectors. High-Z nanoparticle contrast materials such as gold [Hainfeld et al., 2006] are now available. They are highly opaque and overcome some of the toxicity problems associated with traditional contrast agents such as iodine. The K-edge of gold is 81 keV and, in the form of nanoparticles, can be used for in vivo functional imaging. The proposed research into enhanced imaging of specimens and models of atherosclerosis and fatty liver disease does not involve the use of artificial contrast agents, but instead, aims to utilize intrinsic differences in soft tissue attenuation by methods that are the subject of this thesis.

2.4.1 Atherosclerosis

Atherosclerosis is hardening of the arteries characterized by the deposition of calcified plaques on the inner artery wall. The plaques may contain various amounts of lipid and are capped by collagenous fibrous material. Some plaques are stable whereas others are prone to rupture. Unstable plaques that rupture can cause cardiovascular events and strokes [Bhatt et al., 2006, Falk et al., 1995, Naghavi and Falk, 2010]. The morphology and composition of the plaque evolves as the disease progresses and thus could potentially serve to indicate cases at risk of rupture. In particular, lipid content, cholesterol crystals, haemorrhage, and the presence of a thin fibrous cap have been suggested as markers for vulnerable plaques [Kolodgie et al., 2003].

Leber et-al [Leber et al., 2004] compared the performance of multi-detector spiral CT (MDCT) against intracoronary ultrasound (ICUS) for the analysis of coronary plaque composition. The MDCT results correlated well with those

---

[1] The MARS research group is a collaboration of scientists, and engineers associated with the Universities of Otago and Canterbury, Christchurch, New Zealand. The goal of the team is to work with local industry to develop a commercial spectral CT scanner.

of ICUS. Almost all calcified plaques were correctly identified. The MDCT CT numbers correlated with ICUS hyper- and hypo-echoic results. In particular the researchers noted that large lipid cores presenting low echogenicity on ICUS could be detectable with MDCT.

Computed spectral tomography with synchrotron radiation has also been assessed for its potential to detect vulnerable plaques [Langheinrich et al., 2004, Langheinrich et al., 2007, Langheinrich et al., 2009]. It was found that synchrotron based micro CT could provide information on the morphology of the vessel wall equivalent to that provided by histology. Using two beam energies and 2 μm voxels, the detection of iron deposits in haemorrhaged lesions was reported. However, due to the small size of deposits, the ability to distinguish iron from the surrounding material reduces as voxel size increases.

Wang et-al [Wang et al., 2011a] used a clinical dual energy CT system to study a method for distinguishing iron from calcium in atherosclerotic plaques. Building upon earlier work on material decomposition [Liu et al., 2009], they used a limited number of calibration samples to derive a dual energy calibration matrix and applied this to plaques harvested from pig arteries with artificially induced lesions. They did not report the measurement uncertainties associated with their method, nevertheless, a successful result limited to iron concentrations greater than 1.5% by weight was reported. However, they note that this greatly exceeds the actual concentrations (~0.01% by weight) found in human plaques [Stadler et al., 2004] and clinical applications are not currently feasible. They propose that animal studies with micro CT systems might provide a suitable research platform for the technique.

2.4.2 Fatty liver disease

The metabolic syndrome (MetS) is a common condition that currently receives much attention from health researchers. Different organizations (e.g. National Cholesterol Education Program (NCEP) Adult Treatment Panel III (ATP III), World Health Organization (WHO)) use varied, but similar, definitions. The condition is typically diagnosed by the presence of some or all of the following risk factors: abdominal obesity, elevated triglycerides, reduced high density lipids (HDL), increased blood pressure, and insulin resistance. The clinical outcomes of MetS are primarily an increased risk of cardiovascular disease (CVD), and secondarily, an increased risk of type 2 diabetes [Grundy et al., 2004, Reilly and Rader, 2003].

The fat content of the liver has been proposed as an additional indicator of the metabolic syndrome. Ndumele et-al [Ndumele et al., 2011] studied hepatic steatosis, obesity and MetS as independent and associated risk factors for CVD as indicated by increased C-reactive protein (CRP) levels. Hepatic steatosis was found to be positively associated with the risk of both MetS and CVD.

Non alcoholic fatty liver disease (NAFLD) is a spectrum of conditions that may progress to cirrhosis and liver failure in some cases [Angulo, 2002]. In normal patients, consuming low levels of alcohol, NAFLD has been defined as the condition that exists at liver fat levels greater than ∼4–10% [Kotronen and Yki-Jarvinen, 2008, Hoenig et al., 2010]. However, partly due to the ethical considerations of studying liver fat in humans, the pathogenesis is poorly understood.

Animal studies of the metabolic syndrome indicate that the role of non-alcoholic liver steatosis is both passive and active [Den Boer et al., 2004]. Triglycerides accumulating in the liver serve as an indicator of MetS and also promote insulin resistance leading to type 2 diabetes. In predictive models of MetS it has been found that liver fat percentage is superior to abdominal obesity as an indicator of the disease.

Non-invasive methods such as ultrasound, magnetic resonance imaging and spectroscopy (MRI/MRS) and (contrast enhanced and unenhanced) computed tomography have been considered as candidate techniques for quantitative longitudinal studies of fatty liver disease [Longo et al., 2005, Kodama et al., 2007, Qayyum et al., 2009]. Although well established for severe cases, the ability to distinguish fatty liver at moderate levels is controversial. MRI is the the best performer of these methods whereas contrast-enhanced CT was found to be a poor method, perhaps due to the confounding effect of the contrast agent and sensitivity to the timing of administration and measurement. Unenhanced CT showed some promise: it was relatively insensitive but could be limited by the presence of iron and glycogen in the liver. The research suggests that some limitations may be overcome by the use of dual-energy CT. An early study by [Stephens et al., 1977] showed CT to be useful in defining lesions and fatty infiltration but incapable of detecting diffuse hepatic disease. Later, [Hecht, 1982] confirmed the ability of CT to measure the onset and reversal of severe fatty infiltration (as a result of alcoholic disease).

Computed tomography has been used to study the fatty liver condition in rabbits. Kawata et-al studied fatty liver using standard CT [Kawata et al., 1984]. Rabbits in the experimental group were intravenously fed with fat and the effects measured by CT and compared with a control group. At the end of the study the livers were excised and the fat contents analysed biochemically. The liver fat content of the untreated group was 2% by weight and comprised mostly phospholipids. The liver fat content of the most-treated group was 6% by weight consisting mostly of triglycerides and some cholesterol. Increases in triglycerides and cholesterol in the liver were associated with a significant reduction in CT number (-14.9 HU ± 5.1 HU). However, the sensitivity of the method was limited and very careful measurements were required to achieve statistically significant results. Wang et-al [Wang et al., 2003] studied fatty liver in rabbits using dual energy CT. They found significant negative correlations between the CT numbers measured at 90 keV and 120 keV and the liver fat volume percentage measured by histology. Also the difference in CT number ($\Delta H = CT_{120\mathrm{keV}} - CT_{90\mathrm{keV}}$) was positively correlated with fat content and found to be more stable than measures using either $CT_{90\mathrm{keV}}$ or $CT_{120\mathrm{keV}}$

alone. The limit of detection was in the range 5–10% fat by volume.

To date there have been no quantitative studies published of liver fat content in small animals using spectral CT with spectroscopic photon counting detectors. An early pilot study [Berg et al., 2009] aimed to experimentally extract the attenuation curves from spectroscopic CT scans of blended fat and liver. Although the basic trends observed were qualitatively correct, problems were encountered which prevented accurate quantitative work. In the case of the MARS-CT system using Medipix3 with a silicon sensor layer, it is expected that its low energy measurement range will provide greater contrast and hence better sensitivity than the clinical energies used in the studies above.

2.5 Summary and conclusions

1. Hounsfield's invention signalled a paradigm shift in diagnostic radiology. Clinical CT is now a very mature and widely used technology. Future developments may include the adoption of new measurement principles such as spectral CT and volumetric, quantitative imaging techniques.

2. Dual energy spectral CT is currently the most commonly used form of spectral CT. It can be used clinically to distinguish certain material types but returns only two spectral components. The standard dual energy implementation uses two source–detector systems arranged at 90° and space constraints can be a problem, particularly in micro CT applications.

3. Micro CT is used for many preclinical research applications. Compared with clinical CT, the development of micro CT has been driven by different requirements, namely contrast and spatial resolution. However, for in vivo small animal imaging, image quality and spatial resolution are limited by dose constraints. Spectral CT with spectroscopic photon counting detectors is a candidate for improving imaging performance

without incurring prohibitive dose penalties.

4. The Medipix family of photon counting detectors are developed out of high energy physics at CERN for medical applications. They represent the state of the art in pixelated spectroscopic detectors. Medipix3 is the latest and most advanced model currently available. Small animal and specimen imaging is a suitable platform for applying this technology.

5. Decomposition of spectral data may be applied in either the projection or reconstruction image domains and may return component images based on fundamental interaction mechanisms or material properties. Decomposition methods applied in the projection domain are typically more rigorous and allow for both image decomposition and correction of polychromatic artefacts. However, accurate response functions are required and these are generally difficult to obtain for spectroscopic photon detectors. An empirical calibration method has recently been proposed to solve this problem. To date, decomposition methods in the reconstruction image domain have typically been based on forward models of the system that neglect the detector response and are thus not well suited to systems using spectroscopic photon counting detectors.

6. The MARS research group have adopted the Medipix detector family as its underpinning technology for research into spectral imaging. They have identified improvements in image quality, K-edge imaging of contrast agents, and improved soft tissue contrast as three key technical development areas. These technical improvements can be applied to preclinical research in areas such as functional imaging with nanoparticle contrast agents, atherosclerosis, and the metabolic syndrome (MetS).

7. Atherosclerosis is hardening of the arteries characterized by the deposition of calcified plaques on the inner artery wall. Some plaques are

unstable and prone to rupture causing cardiovascular events and strokes. The morphology and composition of the plaque can potentially serve as a marker for vulnerable plaques at risk of rupture. The morphology and composition of atherosclerotic plaques have been analysed with clinical CT and dual energy CT using human subjects and large animal models. Limited success was achieved at this scale. However, very high resolution spectral CT studies using synchrotron radiation have been effective and the results suggest that analysis by spectral micro CT may be feasible.

8. Fatty liver disease is an indicator of the metabolic syndrome (MetS). It has been studied with both standard and dual energy CT with some success, especially in severe cases. However, the current limits of detection do not allow the onset of the disease to be studied. Comprehensive small animal models of MetS including the fatty-liver disease component are becoming available and provide an ideal opportunity for studies using spectral CT with photon counting detectors.

Chapter 3

X-ray imaging

This chapter describes the physical processes of x-ray imaging and introduces the Medipix3 detector. The first two sections provide atomic level descriptions of the interaction mechanisms responsible for x-ray production and attenuation. The next section describes the use of attenuation coefficients for calculating the effect of bulk materials on a narrow beam of x-ray photons. The physical principles, materials and basic operating modes of x-ray detectors are then described and the physical properties of scintillator and semiconductor detectors are compared. Following a description of the main features of the Medipix3 x-ray detector, the chapter concludes with a summary of the main points.

3.1 Electron interactions

Electrons interact with matter primarily by Coulomb interactions with orbital electrons and atomic nuclei [Groom and Klein, 2000]. Most of the interaction energy is lost as heat. Some interactions with orbital electrons can produce characteristic x-rays. Interactions with atomic nuclei can result in the production of bremsstrahlung x-rays.

Table 3.1: Characteristic x-ray emission energies and relative intensities (in parentheses) for some common materials. Calcium is commonly found in biological tissues whereas molybdenum, rhodium and tungsten are often used as x-ray target materials. The characteristic emissions from indium and other similar materials may serve as convenient energy calibration lines for spectroscopic systems. Retrieved from [Thompson et al., 2001].

Element	$K_{\alpha 1}$ /keV	$K_{\alpha 2}$ /keV	$K_{\beta 1}$ /keV	$K_{\beta 2}$ /keV	$K_{\beta 3}$ /keV
20 Ca	3.692 (100%)	3.688 (50%)	4.013 (13%)	–	–
42 Mo	17.479 (100%)	17.374 (52%)	19.608 (15%)	19.965 (3%)	19.590 (8%)
45 Rh	20.216 (100%)	20.074 (53%)	22.724 (16%)	23.173 (4%)	22.699 (8%)
49 In	24.210 (100%)	24.002 (53%)	27.276 (17%)	27.861 (5%)	27.238 (9%)
74 W	59.318 (100%)	57.982 (58%)	67.244 (22%)	69.067 (8%)	66.951 (11%)

3.1.1 Characteristic x-rays

When an electron interacts with an orbital electron the energy transfer results in either the excitation or ionization of the target atom. Electronic rearrangement then occurs to fill the shell vacancy and either a characteristic x-ray or Auger electron is emitted from the atom. Auger emission is a competitive process to x-ray emission and the fluorescence yield describes the probability of an x-ray emission following an ionization event. The energy of the x-ray emission is determined by the difference in initial and final atomic energy levels. The emission lines are typically labelled according to the Siegbahn notation system which groups the emissions by wavelength and intensity. See Figure 3.1 and Table 3.1.

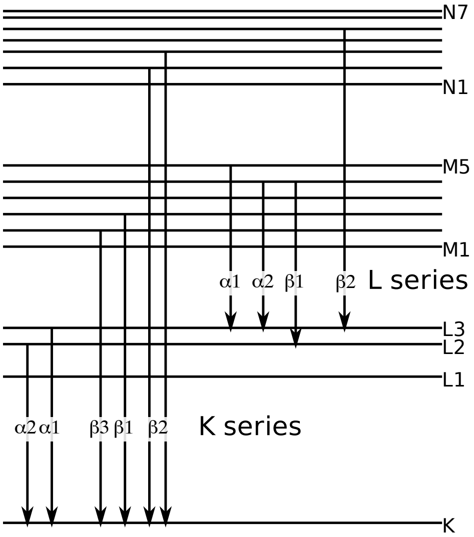

Figure 3.1: Energy level transitions associated with the emission of characteristic x-ray. For example, following a K shell vacancy the most probable transition is from the L3 level to the K shell and these are labelled $K_{\alpha 1}$ in the Siegbahn notation system. Siegbahn notation was invented before the quantum origin of characteristic x-rays was undertood and the lines are grouped according to wavelength in order of decreasing intensity ($K_{\alpha 1}$, $K_{\alpha 2}$, $K_{\beta 1}$, $K_{\beta 2}$, $K_{\beta 3}$, ...).

3.1.2 Bremsstrahlung

Bremsstrahlung is produced during deceleration of a charged particle in a strong electric field such as that of an atomic nucleus. The effect increases with energy and is a primary means of x-ray production.

Differential cross section

Bethe and Heitler [Bethe and Heitler, 1934] first derived the differential cross-section for bremsstrahlung with respect to the energy $h\nu$ of the photon radiation produced:

$$\Phi = \sigma_0 Z^2 \frac{T}{h\nu} \frac{p_f}{p_i} B \tag{3.1}$$

where $\sigma_0 = r_0/137$ is the product of the classical electron radius and the fine structure constant, T is the kinetic energy of the incident electron, p_i and p_f are the initial and final momenta of the incident electron, Z is the atomic number of the medium and B is a dimensionless function of $h\nu/T$. Thus, bremsstrahlung intensity increases with the atomic number of the target and the kinetic energy of the incident electron.

Energy spectrum

The bremsstrahlung number density spectrum for a thin target (where the thickness of the target is much less than the mean free path of the electron) is directly proportional to the cross-section:

$$N(h\nu) = \int \Phi(h\nu, T)\frac{d(h\nu)}{T} \tag{3.2}$$

The approximation of a thick target as a succession of thin targets, treatment of $h\nu\Phi$ as a constant and the use of the Thomson-Whiddington approximation [Whiddington, 1912] for the penetration of electrons with inital kinetic energy T_0 into a thick target leads to Kramers' Law [Kramers, 1923] for the unfiltered bremsstrahlung spectrum:

$$N(h\nu) \propto Z\left(1 - \frac{h\nu}{T_0}\right) \tag{3.3}$$

The bremsstrahlung intensity is thus greatest at low photon energies and has a maximum equal to the kinetic energy of the incident electrons.

3.2 Photon interactions

3.2.1 Photoelectric absorption

Photoelectric absorption is the process by which an incident photon interacts with an absorber atom and completely disappears (is absorbed) causing an energetic photoelectron to be ejected from the atom. This is an atomic interaction that does not occur with free electrons.

For x-rays of sufficient energy the most probable interaction is with electrons of the K-shell. The photoelectron has energy equal to the difference in the energy of the incident photon $h\nu$ and the binding energy of the shell E_b.

$$E_{e^-} = h\nu - E_b \tag{3.4}$$

Electronic rearrangement then occurs and the shell vacancy is filled either by a free electron or one from a higher electronic shell. This process is accompanied by the emission of one or more characteristic x-rays.

Because of the effect of multiple shells, there is no simple analytical expression for the probability of photoelectric absorption over all energies E and all atomic numbers Z. Scofield published a comprehensive treatment for the photoelectric effect for all shells [Scofield, 1973]. A reasonable approximation for the interaction probability per atom is:

$$\tau \propto Z^{4\rightarrow 5}/E^{3\rightarrow 4} \tag{3.5}$$

Thus the photoelectric effect is most significant at low energies and increases rapidly with increasing atomic number Z.

3.2.2 Elastic scattering

Elastic scattering is the scattering of a photon by a charged particle, such as an electron, without energy transfer. If the electron is bound to an atom it is called Rayleigh scattering. In this process the incident photon interacts with the electric field of the scattering particle causing it to re-emit radiation of the same energy as the incident particle. The electron does not carry away any recoil energy. Thus the photon is elastically scattered.

The Rayleigh scattering cross section σ_{R} includes the cooperative effect of all electrons in the atom and its calculation involves tabulated form factors [Chantler, 2000].

$$\sigma_{\mathrm{R}} = \pi {r_0}^2 \int_{-1}^{1} \left(1 + \cos^2\theta\right) F d\theta \tag{3.6}$$

where r_0 is the classical electron radius and F is the form factor function of atomic number Z. Rayleigh scattering increases with Z and is most significant at small angles but is generally a weak effect.

3.2.3 Compton scattering

Compton scattering is the interaction of a photon with the electric field of a free electron. The photon is deflected from its path and the electron recoils taking with it some of the original photon energy. Unlike elastic scattering, Compton scattering requires a relativistic description.

Energy dependence of the scattering angle

From simultaneous conservation of both energy and momentum we can write the following relationship between the energy of the scattered photon and the angle of scattering [Compton, 1923]:

$$\frac{h\nu'}{h\nu} = (1 + \alpha\ (1 - \cos\theta))^{-1} \tag{3.7}$$

where $h\nu$ is the incident photon energy, $h\nu'$ is the scattered photon energy and $\alpha = \frac{h\nu}{m_0 c^2}$ is the ratio of photon energy to electron rest mass. This term appears in the Klein-Nishina formula for the differential scattering cross-section.

Klein-Nishina formula

The Klein-Nishina formula gives the differential scattering cross-section σ_C per solid angle Ω in terms of the energy of the incident photon $h\nu$ and the scattering angle θ. The Klein-Nishina formula for Compton scattering off a single electron can be written:

$$\frac{d\sigma_\mathrm{C}}{d\Omega} = \frac{1}{2}{r_0}^2 \left(\frac{h\nu}{h\nu'}\right)^2 \left(\frac{h\nu}{h\nu'} + \frac{h\nu'}{h\nu} - 1 + \cos^2\theta\right) \tag{3.8}$$

A plot of the differential cross-section for a range of initial energies from $\alpha = 0.01$ to $\alpha = 100$ (5.11 keV to 51.1 MeV) as a function of scattering angle is shown in Figure 3.2. The weak angular dependence at low photon energies is a feature exploited by some scatter correction algorithms [Glover, 1982, Ohnesorge et al., 1999].

The cross-section per atom integrated over all angles is given by:

$$\sigma = 2\pi Z \int_0^\pi \frac{d\sigma_\mathrm{C}}{d\Omega} \sin\theta d\theta \tag{3.9}$$

The Klein-Nishina formula is an important component of forward models of the x-ray interaction process and is used by a number of spectral decomposition algorithms [Alvarez and Macovski, 1976, Schlomka et al., 2008].

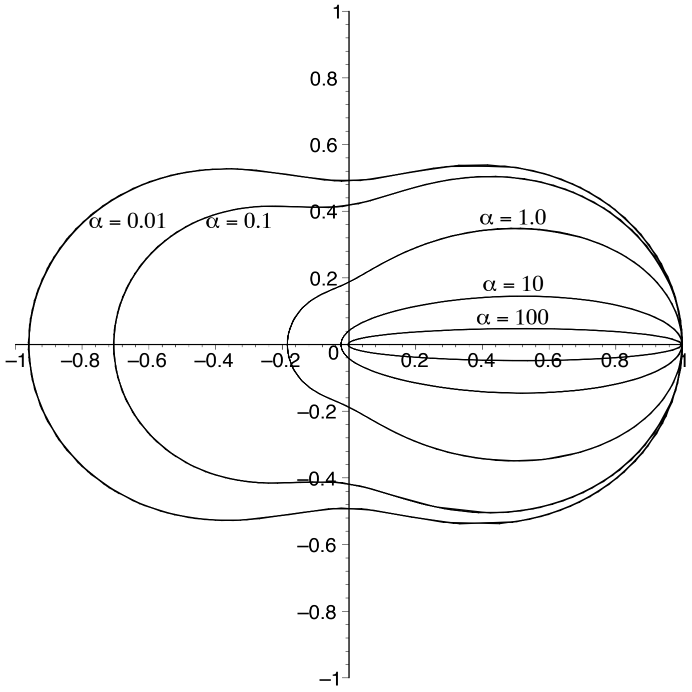

Figure 3.2: A polar plot of the number of photons incident from the left scattered into a unit solid angle. Initial energies from $\alpha = 0.01$ to $\alpha = 100$ (5.11 keV to 51.1 MeV) are shown. At the higher energies scattering is predominantly in the forward direction.

3.2.4 Pair production

Pair production is the relativistic conversion of a high energy photon into an electron and positron pair. It is a threshold effect that does not occur for photon energies below twice the rest mass of the electron (1.02 MeV) and it is not generally significant below several MeV. The effect takes place in the Coulomb field of the nucleus.

The excess kinetic energy available to the particles is given by the difference in photon energy and twice the electron rest mass:

$$T = h\nu - 2m_0c^2 \tag{3.10}$$

The cross section κ for pair production has a similar form to that for bremsstrahlung described earlier. Pair-production also varies approximately with the square of atomic number Z and inversely with the excess energy T. The energy threshold ($2m_0c^2 = 1.02$ MeV) for pair production is outside the diagnostic energy range (10–150 keV) and this mechanism is therefore not relevant here.

3.3 Attenuation coefficients

For a narrow beam of x-rays passing through a material there is a fixed probability μ per unit length t of interacting with the material and either being absorbed or scattered out of the beam. Thus the initial intensity I_0 of a beam is reduced exponentially according to Beer's Law:

$$I = I_0 \exp(-\mu t) \tag{3.11}$$

and the mean free path between interactions is:

$$\int_0^\infty t \exp(-\mu t) \mu dt = \frac{1}{\mu} \tag{3.12}$$

Because the linear attenuation coefficient varies with the density of the material, it is often more convenient to divide through by material density and work with mass attenuation coefficients $\frac{\mu}{\rho}$:

$$\frac{\mu}{\rho} = (\tau + \sigma_{\mathrm{R}} + \sigma + \kappa)\frac{N_{\mathrm{A}}}{A} \tag{3.13}$$

where $(\tau + \sigma_{\mathrm{R}} + \sigma + \kappa)$ is the sum of atomic cross sections and $\frac{N_{\mathrm{A}}}{A}$ is the ratio of the Avogadro constant to the atomic mass.

The mixture rule [Jackson and Hawkes, 1981] states that atoms contribute to the interaction effects independently and that the physical form of the material is not important. It has been found to be accurate except within $\sim$1 keV of absorption edges. Thus the mass attenuation coefficient of a compound or mixture is given by the sum of $i = 1 \cdots N$ independent components weighted by the partial mass fractions w_i:

$$\frac{\mu}{\rho} = \sum_i w_i \left(\frac{\mu}{\rho}\right)_i \tag{3.14}$$

The mass attenuation coefficients for all the main interaction processes have been calculated by a variety of sources and published as a scientific database [Berger et al., 1998]. The database tables may be used to calculate the x-ray interaction probabilities for any element, mixture or compound.

Figure 3.3(a) shows the contributions of the individual interaction mechanisms to the total attenuation coefficient for iron. The total attenuation coefficient of iron is compared to some other common materials in Figure 3.3(b). It can be seen that the curves for each material are different and measurement of the attenuation properties of a tissue comprising these components may yield information about the partial densities of each component. This is the principle exploited by spectral CT to distinguish biological tissues. However, the ability to differentiate and quantify the material components will depend upon the energy range considered. Where the mass attenuation coefficient curves for two given component materials are parallel, their partial densities cannot be determined from attenuation data for a composite material as one component curve can be reproduced from a multiple of the other. Thus, over the full diagnostic energy range (10–150 keV), fat, water, calcium and iron are distinguishable by their mass attenuation properties. However, if data from only a restricted energy range is available, or is measured with poor resolution, then material differentiation will be compromised.

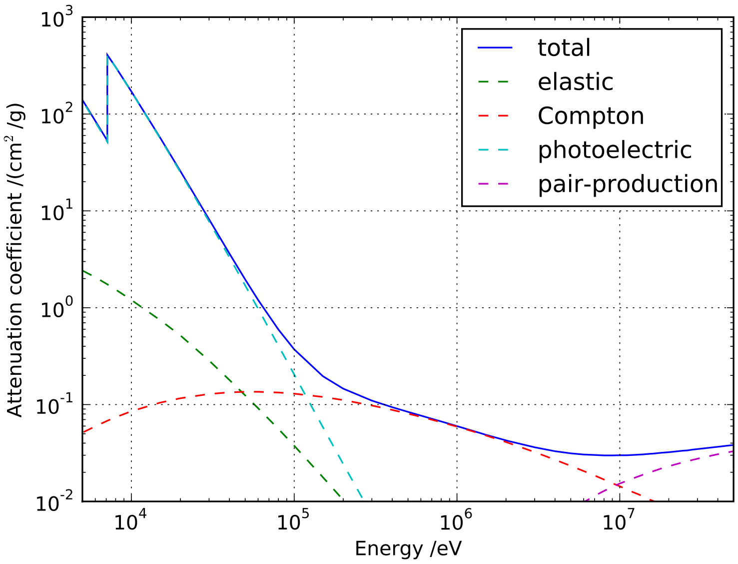

(a)

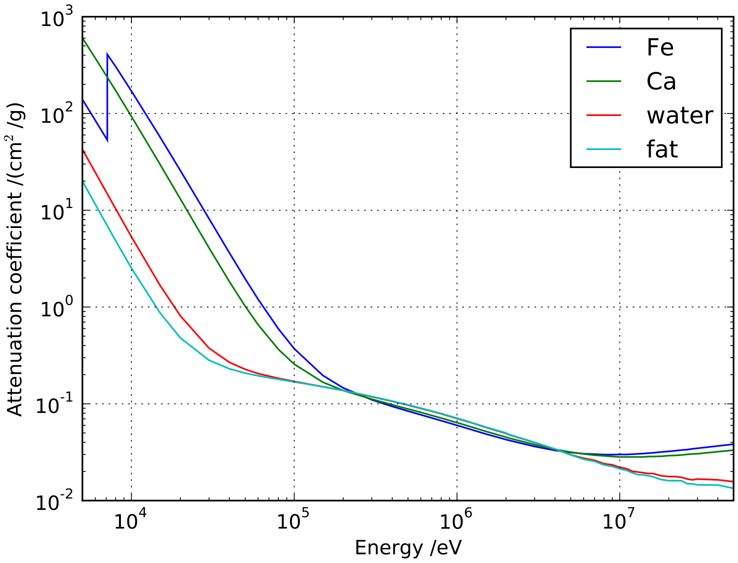

(b)

Figure 3.3: (a) A plot of photon interaction components for iron. The photoelectric effect is dominant in the low energy x-ray region. Compton scattering is dominant in the mid-energy region. Pair production is not significant below several MeV. (b) A plot of the total attenuation coefficients for iron and other common materials. The cross sections converge in the region where the Compton effect dominates and diverge in the regions where photoelectric and pair production dominate.

3.4 Detectors

3.4.1 Detector types

Digital imaging x-ray detectors must convert the incident x-ray flux into an electronic signal for processing. The conversion process can be direct or indirect. Indirect converters typically produce light by scintillation that is converted by other means into an electronic charge. Direct converters produce an electronic charge directly from the x-ray interaction event.

Figure 3.4 shows the electronic band diagram for an activated scintillator (indirect conversion detector) and a semiconductor (direct conversion detector). Activated scintillators include an activation species which creates sites within the forbidden gap making transitions from the conduction band to the valence band more probable. Under normal conditions, the valence band is full and the conduction band is empty. When an x-ray interaction occurs in the detector, an electron-hole pair is created by the promotion of an electron to the conduction band. The free electron migrates to a fluorescence site and returns to the valence band via an intermediate level created by the activation species. This produces a light emission with wavelength suitable for transmission through the detector to a collector, such as a photodiode, where an electronic charge is created.

A semiconductor detector is constructed as a diode and a reverse bias applied to create a depletion region free of charge. When an x-ray interaction occurs in the detector an electron-hole pair is created by the promotion of an electron to the conduction band. In the case of the semiconductor detector the charge is collected directly under the influence of the applied electric field.

Examples of indirect conversion detectors include inorganic crystals such as CsI(Tl) and ceramic scintillators such as
Gd_2O_2S(Tl) (GOS). This ceramic scintillator is commonly used in commercial systems for x-ray radiography and tomography. Some properties of common

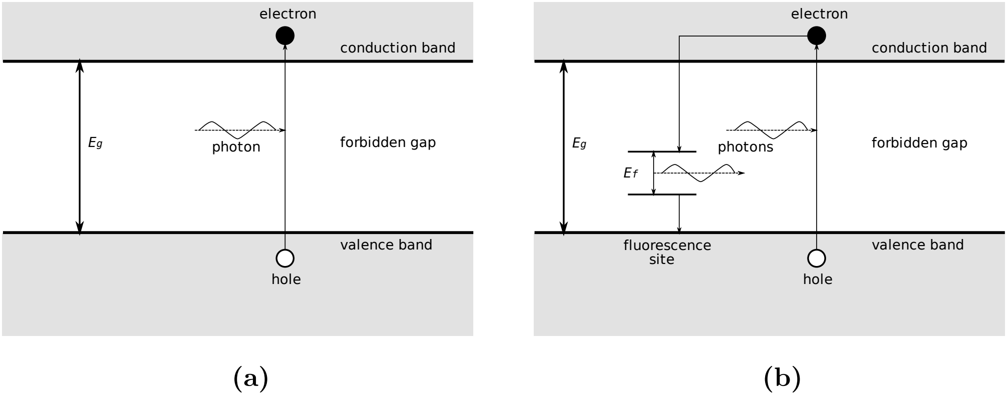

Figure 3.4: (a) The band gap diagram for a direct conversion x-ray detector. A photon with energy greater than the band gap E_g creates an electron-hole pair by promoting a valence electron to the conduction band. The mobile electronic charge is collected under the influence of an electric field. (b) The band gap diagram for an indirect conversion x-ray detector. After the electron-hole pair is created by the incident photon, the free electron returns to the valence band via an intermediate level created by the presence of an activation species. The scintillator is transparent to the fluorescence photon which is collected and converted to an electronic signal by a device such as a photodiode.

scintillators are given in Table 3.2. Direct conversion semiconductor detector materials include Si, GaAs and CdTe. The charge can be collected as either electrons or holes. These compound semiconductor materials are used in a variety of detectors including the Medipix family of pixelated photon counting detectors. Some properties of common semiconductor materials are given in Table 3.3. Figure 3.5 compares the linear attenuation coefficients for some common scintillators and semiconductors.

3.4.2 Signal processing

The signal from the detector sensor material may be processed using current mode or pulse mode electronics. Because the charge created by the incident radiation is proportional to the energy deposited, detectors operating in current mode are sometimes referred to as energy integrating. Energy integrating detectors measure the total energy deposited in the detector in a given in-

Table 3.2: Some properties of common scintillator materials. The scintillation efficiency is the charge to scintillation photon conversion ratio. The light yield is the number of scintillation photons per unit energy interaction. Compiled from [Knoll, 2000, Greskovich and Duclos, 1997, van Eijk, 2003].

Material	Z_{eff}	Density /(g.cm^{-3})	Decay constant /μs	Scintillation efficiency	Light yield /(γ/MeV)
NaI(Tl)	~51	3.67	0.23	11 %	40000
CsI(Tl)	~54	4.51	1	12 %	52000
Gd_2O_2S	~61	7.34	1000	15 %	60000

Table 3.3: Some properties of common semiconductor materials. The charge mobility is given for both electrons and holes. For Ge the semiconductor properties are given at 77 K as this material requires cooling due to its narrow bandgap. The properties of the other materials are given at 300 K. Compiled from [Knoll, 2000].

Material	Z_{eff}	Density /(g.cm^{-3})	Electron and hole mobility /(cm^2/Vs)	Bandgap /eV	Energy per charge pair /eV
Si	14	2.33	1350 480	1.12	3.61
Ge (77 K)	32	5.32	3.6×10^4 4.2×10^4	0.74	2.98
CdTe	~50	6.06	~1000 ~65	1.47	4.43
GaAs	~32	5.35	~8500 ~400	1.42	4.2

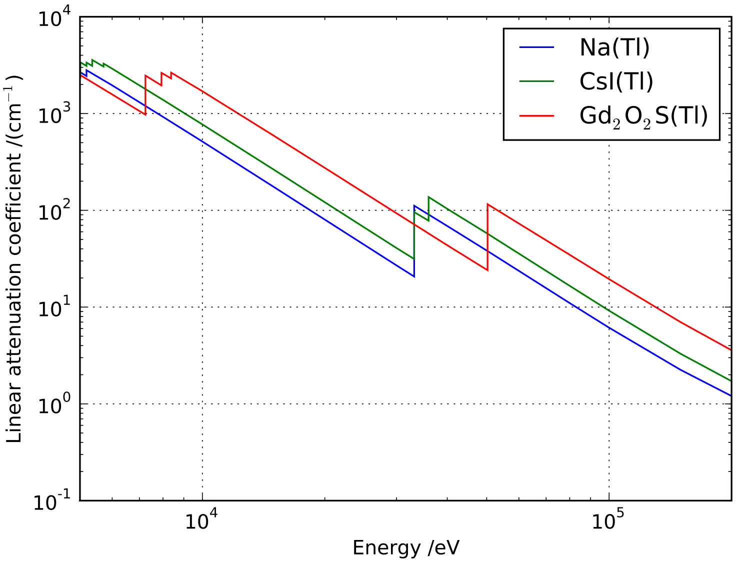

(a)

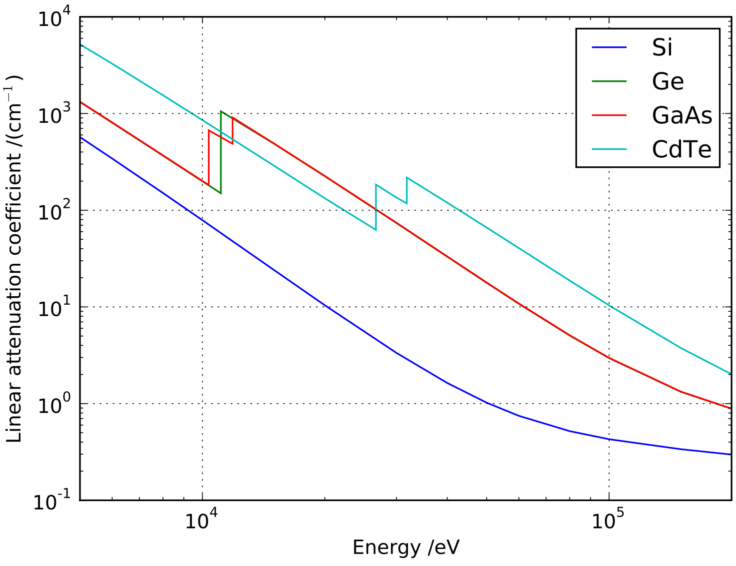

(b)

Figure 3.5: (a) The linear attenuation coefficients for some common scintillators. (b) The linear attenuation coefficients for some common semiconductors. The mean free path at 100 keV for the scintillators is ∼1 mm. Amongst the semiconductors only CdTe has a mean free path comparable to those of the scintillators.

terval (current $\propto$ charge per unit time). Information about the distribution of energies and the number of events is not retained. In contrast, pulse mode systems process each event individually by momentarily integrating the charge deposited and then measuring the height of the resulting pulse before the signal is discharged. Typically, the height of the pulse is proportional to the integrated charge and may thus be used to determine the energy deposited for each event. This mode of operation is sometimes referred to as spectroscopic photon counting mode. Although each event is processed individually, the incident flux within a given interval is usually summarized by the number of counts and distribution of energies.

Detector materials such as $Gd_2O_2S(Tl)$ have a slow response time per event ($\sim$milliseconds) and are therefore not suitable for use as spectroscopic photon counting detectors. However, semiconductors and other scintillators materials with a fast response ($\sim$microseconds) may be operated in photon counting mode.

3.4.3 Medipix3

A Medipix3 detector [Ballabriga et al., 2010, Ballabriga et al., 2011] is a hybrid photon counting device comprising a CMOS ASIC bump bonded to a monolithic semiconductor sensor layer. It is the latest and most sophisticated member of the Medipix family of spectroscopic photon counting detectors from the Medipix collaboration, CERN. The Medipix3 ASIC contains analogue and digital circuitry for processing individual pulses collected from the direct conversion sensor layer. Medipix3 was designed to improve upon the Medipix2 detector by correcting spectroscopic performance defects and enhancing count rate capability. It also provides additional modes of operation, multiple counters per pixel, and greater control over threshold adjustment. Available sensor materials include silicon, CdTe and GaAs. A single Medipix3 has an imaging area of only 14.02×14.02 mm^2 but can be tiled on 3 sides to form a $2\times n$ array.

Fine pitch pixel x-ray detectors suffer from charge sharing [Campbell et al., 2008]. The charge released in the sensor by the x-ray interaction disperses as it is collected. Thus, the charge may be allocated across several pixels and spectroscopic performance is distorted. Medipix3 includes a special charge summing mode that uses summing and arbitration circuits to correct this effect. For every event, arbitration logic compares the charge at each pixel within a local cluster and allocates the summed response of the cluster to the single pixel contributing the maximum charge.

During production, the Medipix3 can be bump bonded in either fine pitch or spectroscopic mode (Table 3.4). In fine pitch mode, the Medipix3 has 256×256 pixels arranged in a square matrix with a pitch of 55 μm. Each pixel includes analogue circuitry to integrate and shape the incoming charge and digital circuitry to count the individual pulses. Two pulse-height discriminators per pixel are provided in fine pitch mode. In spectroscopic mode, the bump bonding is done at a pitch of 110 μm. This allocates eight pulse-height discriminators per pixel. Devices configured in spectroscopic mode are not yet available.

In operation, the Medipix3 is controlled and configured by a set of 25 global DACs (Table A.1) and 13-bits of a 24-bit control register applied at the pixel level (Table A.2). The global DACs set chip-wide current and voltage levels that bias the analogue circuitry and provide global current sources for adjusting pixel thresholds. The pixel configuration bits are used to set the counter bit depth, threshold equalization adjustment and high or low gain individually for each pixel.

The available features of the Medipix3 should be considered in the context of each application. For example, charge summing mode is designed to improve spectroscopic performance. This may prove to be important for soft tissue imaging in the absence of K-edges where subtle variations in attenuation data may need to be measured. For future work with live animal models, the

Table 3.4: Medipix3 configuration options and operating modes. Compiled from [Ballabriga, 2009a].

Pixel configuration	Operating mode	Thresholds
Fine pitch mode (55 μm pixel pitch)	Single pixel mode	2
	Charge summing mode	
Spectroscopic mode (110 μm pixel pitch)	Single pixel mode	8
	Charge summing mode	

Pixel mode	Counting range	Counters
1-bit	1	2
4-bit	15	2
12-bit	4095	2
24-bit	16,777,215	1

availability of multiple counters per pixel may be used to acquire spectroscopic data at reduced dose. However the use of eight counters per pixel requires bump bonding in spectroscopic mode, and would consequently be associated with a loss of spatial resolution that may not be acceptable to applications that require detailed imaging of specimen morphology.

3.5 Summary and conclusions

1. X-ray photon beams may be produced by the interaction of high energy electrons with matter. The energy of most interactions is lost as heat. Some interaction events can produce characteristic x-rays by ionization or bremsstrahlung x-rays by deceleration in the Coulomb field of a nucleus. X-rays produced by atomic ionization events have energies that are characteristic of the electronic binding energies. In contrast, bremsstrahlung interactions produce a continuum of x-rays with low energy photons being produced preferentially. Bremsstrahlung production is most effective for electrons with high kinetic energies interacting with

high Z target materials.

2. In the diagnostic energy range, photon interactions are dominated by the photoelectric and Compton effects. Photons are completely absorbed by the photoelectric effect resulting in the ejection of a bound electron from an atom which may be accompanied by the emission of a characteristic x-ray. There is no simple expression for the photoelectric effect for all atoms, however it is strongly dependent on atomic number and reduces rapidly with energy. The photoelectric effect is dominant at low energies ($< 10^5$ eV). Compton scattering involves the transfer of energy from the incident photon to a recoil electron. The photon is not absorbed but loses energy and is scattered. The Compton effect increases with atomic number and reduces slowly with energy. It is dominant at mid-energies ($\sim 10^5$–10^7 eV).

3. Beer's law applies to the passage of a narrow beam of radiation through matter and states that the intensity of the beam reduces exponentially with the product of path length and the linear attenuation coefficient. It is convenient to divide by material density and work with mass attenuation coefficients. The mixture rule can be used to calculate the effective mass attenuation coefficient of a compound or elemental mixture. The mass attenuation coefficient of the mixture is given by a linear combination of the components. The mass attenuation coefficients for most materials converge in the region where the Compton effect dominates ($\sim 10^5$–10^7 eV) and diverge in the regions where the photoelectric and pair production effects dominate.

4. X-ray detectors may convert the energy deposited directly or indirectly into a measurable charge. Scintillators are indirect converters that first transform the energy deposited into visible light before creating a measurable signal at a light collector using a device such as a photodiode.

Semiconductor detectors are direct converters that operate under a reverse bias and collect the charge directly under the influence of the applied electric field. Ceramics such as $Gd_2O_2S(Tl)$ and inorganic crystals such as CsI(Tl) are examples of high Z scintillators. CdTe is an example of a semiconductor with a high effective atomic number similar to that of inorganic scintillators. However, in some applications Si is preferred despite its low atomic number due to other characteristics such as better homogeneity and charge mobility.

5. X-ray detectors may be operated in pulse mode or current mode. Current mode devices provide a signal proportional to the integral of energy deposited over some given time interval. Pulse mode devices process each interaction event individually. Pulse mode is used for spectroscopic photon counting detectors such as Medipix.

6. Medipix3 is the latest and most sophisticated member of the Medipix family of spectroscopic photon counting detectors. Medipix3 was designed to improve upon the Medipix2 detector by correcting spectroscopic performance defects and enhancing count rate capability.

7. Medipix3 is highly configurable and the available options should be considered for each application. Medipix3 charge summing mode is designed to improve spectroscopic performance by eliminating the charge sharing effect and may be important for quantitative soft tissue imaging. For work with live animal models the availability of multiple counters per pixel could be used to maximize information retrieved for a given dose. Spectroscopic mode may not be suitable for some applications that require detailed imaging of specimen morphology.

Chapter 4

Tomography

This chapter describes the theory and practice of computed tomography. The material in the early sections of this chapter was derived from some of the many publications available that review tomographic measurement principles and algorithms [Kak and Slaney, 2001, Yaroslavsky, 2003, Kalender, 2001, Goldman, 2007, Turbell, 2001]. The basic theory for obtaining cross sectional reconstructions from parallel projections at multiple angles is given. The reconstruction algorithm is extended to alternative geometries such as fan beam and cone beam. Practical aspects of standard tomography such as detectors, sources and image artefacts are then discussed. Finally, spectral CT is introduced and a numerical simulation is developed that can be used to predict some aspects of its performance. The main conclusions of this chapter are then summarized.

4.1 Introduction

The first practical CT system [Hounsfield, 1973] comprised a single scintillating detector and source arranged on a translating bed that could rotate around the object. This is known as a translate and rotate geometry. The system was a head scanner and used algebraic reconstruction techniques on a 128×128

matrix. It produced a map of attenuation coefficient normalized to water (a unit now known as the Hounsfield unit or HU). The impact of the ability to produce cross-sectional images of anatomical features with a $\sim 100\times$ increase in tissue contrast afforded by this new measurement technique was immediate and developments followed rapidly. In 1974 Ledley [Ledley et al., 1974] developed a whole body scanner using convolution algorithms for reconstruction. The second generation of scanners included multiple detectors placed opposite a single source to improve the overall acquisition time. However, this partial fan beam was not sufficient for full coverage of the object and so the translate-rotate mechanism was retained. The transition to full fan beam geometry came with the third generation of scanner. These were much faster and provided full coverage of the object without the need for the translate mechanism. Full body fan beam systems became available in 1976 and developments aimed at improving scan speeds continued. For a while, fourth generation systems using a fixed ring of detectors provided the ultimate in fast imaging. With the introduction of slip-ring technology, multi-slice systems and spiral scanning [Kalender, 1994], the third generation configuration was adopted as standard and remains so today. Multi-slice CT with sub-second scan times per rotation are now the norm in clinical CT.

Tomographic reconstructions of the spatial distribution of an object's attenuation coefficient using x-ray attenuation projections have their basis in Beer's attenuation law and the Fourier slice theorem. Rather than inverse Fourier methods, practical reconstruction algorithms usually use filtered-backprojection [Ramachandran and Lakshminarayanan, 1971] [Feldkamp et al., 1984]. These are fast, robust and, in the case of parallel and fan beam geometries, are mathematically equivalent to the exact Fourier methods. However, the energy dependence of the attenuation coefficient is not accommodated within standard reconstruction algorithms. The *effective* attenuation coefficient that is actually reconstructed depends upon the spectrum of the x-ray source and the response characteristics of the x-ray detector [Rutherford et al., 1976].

In 1977 Brooks [Brooks, 1977] studied the relationship between the CT number of a material and the x-ray spectrum of the interrogating flux. In the normalized Hounsfield scale, the CT numbers for air and water are not energy dependent. The energy dependence of other materials is reduced but not eliminated. Brooks noted this as both a problem and an opportunity. He solved the problem by including an x-ray beam quality factor to account for spectroscopic differences between measurement systems. He exploited the opportunity by decomposing the measured CT number into photoelectric and Compton components, thereby elegantly characterizing the material. Brooks suggested that only two spectral measurements were required to characterize each material. This presupposes that the energy dependence of the photoelectric effect is the same for all materials and that there are no K-edges within the energy region of interest. Where this assumption is invalid, an alternative decomposition basis and a greater number of spectral measurements will be required to characterize the material.

Practical x-ray CT systems use bremsstrahlung x-ray tubes that produce a continuous spectrum with a maximum energy determined by the accelerating voltage. In this case, Beer's law does not hold exactly and artefacts result from the use of the polyenergetic x-ray beams [Herman, 1979]. Compton and, to a lesser extent, coherent scattering within the object further complicates the system response producing additional reconstruction artefacts [Stonestrom and Macovski, 1976, Glover, 1982]. In standard CT systems, physical filters and software corrections are employed to reduce the effects of polyenergetic x-ray sources and scattering within the object.

For small animal and specimen imaging, development has been driven, predominantly, by the desire for improved contrast to noise ratio and spatial resolution rather than scanning speed [Ritman, 2007]. This has led to the widespread use of micro focus x-ray tubes and alternative high resolution detector technology such as flat panel detectors with amorphous silicon and CCD camera readout systems together with the adoption of cone beam geometry [Paulus et al., 2000, Kim et al., 2005, Ross et al., 2006, Zhu et al., 2009, Wang et al., 2011b]. In small animal models, a voxel resolution of $\sim(100\ \mu\text{m})^3$ is required for scale equivalence to human CT. To achieve an acceptable contrast to noise ratio at this high spatial resolution the radiation dose must be greatly increased. This places practical limits on spatial resolution achievable with live animal imaging [Ford et al., 2003, Ritman, 2007]. For in-vitro specimen imaging, radiation dose is not a concern and voxel sizes of $(< 50\ \mu\text{m})^3$ are readily achievable. In both cases the application of new techniques and novel technology may bring benefits in terms of tissue contrast and resolution that are not possible with standard CT.

In contrast to standard systems, spectral CT systems are designed to emphasize and exploit energy dependent differences in attenuation. The reported benefits of spectral CT include increased image contrast [Lehmann et al., 1981, Giersch et al., 2004, Carramate et al., 2011], artefact corrections [Alvarez and Macovski, 1976, Shikhaliev, 2005], and material discrimination and quantification [Roessl and Proksa, 2007, Schlomka et al., 2008, Feuerlein et al., 2008].

The different modes of spectral CT in common use are based upon controlling either the x-ray source spectrum or x-ray detector response characteristics to sample the attenuation coefficient of the object across different energy ranges. With the development of sophisticated spectroscopic photon counting detectors, such as the Medipix family [Campbell et al., 1998, Llopart et al., 2002, Ballabriga et al., 2006], the quantity of spectral data available from CT measurements has been greatly increased. However, the utility of the additional spectral data is not obvious. Following a description of the theory and practice of standard computed tomography, this chapter introduces spectral CT and develops a simple numerical model for characterizing some aspects of its performance.

4.2 Theory

Where Beer's law holds, x-ray attenuation measurements correspond to line integral projections of the attenuation coefficient along the x-ray path. The Fourier slice theorem relates the 1D Fourier transforms of these line integral projections with the 2D Fourier transform of the spatial distribution of the attenuation coefficient.

Although inverse Fourier methods can, in principle, be used to determine the spatial distribution of attenuation coefficient, practical reconstruction algorithms usually use filtered-backprojection (FBP) methods. These are fast, robust and, in the case of parallel and fan beam geometries, are also exact in the sense that, with unlimited measurement accuracy and sampling resolution, the reconstruction tends to the true spatial distribution of the attenuation coefficient. Exact FBP methods also exist for cone beam geometry [Defrise and Clack, 1994], however it is the approximate FDK method [Feldkamp et al., 1984] that is most commonly used.

Results from clinical CT measurements are usually not displayed as effective attenuation coefficient but rather in a system of derived values called CT numbers measured in Hounsfield units [Hounsfield, 1973]. These are effective attenuation coefficients normalized to those of water and rescaled so that $CT_{\text{water}} = 0$ and $CT_{\text{air}} = -1000$. In these units, the effect of the energy dependence of the attenuation coefficient of body tissues is reduced, allowing CT values from similar systems to be directly compared.

4.2.1 Line integral projection

Neglecting effects such as scattering and beam hardening, the projection signal S of a narrow beam of x-rays through an object is related to the line integral of the attenuation coefficient along the ray path L as follows:

$$\int_L \mu(x,y)dl = -\ln\frac{S}{S_0} \tag{4.1}$$

where S is the attenuated projection, S_0 is the unattenuated projection and $\mu(x,y)$ is the spatial distribution of the attenuation coefficient.

Acquiring multiple parallel projections a over multiple angles θ produces samples of the radon transform:

$$P(\theta,a) = -\ln\frac{S(\theta,a)}{S_0(a)} \tag{4.2}$$

The samples $P(\theta,a)$ may be arranged as a sinogram image with row indices corresponding to discrete angles and columns corresponding to individual detector elements (Figure 4.2).

4.2.2 Fourier slice theorem

The Fourier slice theorem states that the 1D Fourier transform (F_1) of the parallel projection of a 2D object is equal to a 1D radial slice of the 2D Fourier transform (F_2) where the slice is taken in a direction parallel to that of the projection. Thus the 2D Fourier transform of an object can be built by taking the 1D Fourier transform of each row θ of the sinogram:

$$\mathrm{F}_2\left(\mu(x,y)\right) = \mathrm{F}_1\left(P(\theta,a)\right) \tag{4.3}$$

In principle, the cross-section can now be obtained by taking the 2D Fourier inverse of the accumulated 2D transform:

$$\mu(x,y) = \mathrm{F}_2^{-1}\left[\mathrm{F}_1\left(P(\theta,a)\right)\right] \tag{4.4}$$

However, in practice, numerical errors that occur during the interpolation from

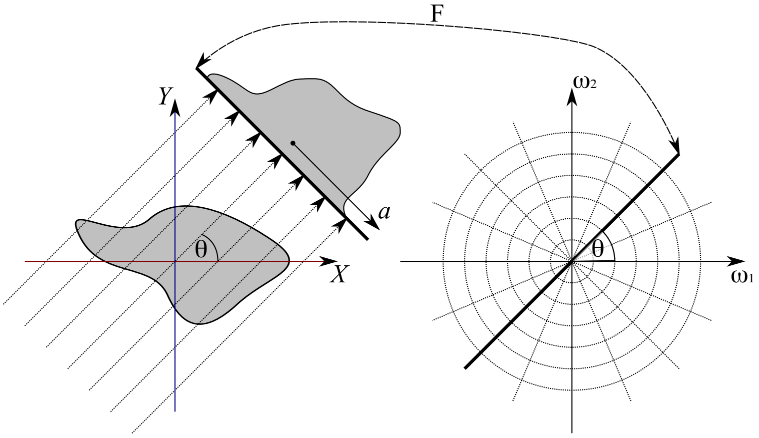

Figure 4.1: The Fourier slice theorem. The parallel beam of x-rays pass through the object and intersect the detector at equidistant points along its axis a. The 1D Fourier transform of the projection through the object at angle θ gives the corresponding radial slice of the 2D Fourier transform of the object cross section.

the radial coordinate system of the 2D samples and the regular grid required for the inverse Fourier transform produce large scale artefacts in the reconstruction. Therefore, the Fourier slice theorem is not used directly. Instead, the algorithm of choice is filtered backprojection. Filtered backprojection algorithms exist for each of the commonly used geometrical arrangements.

4.2.3 Filtered backprojection

Parallel geometry

The parallel geometry depicted in Figure 4.1 was used in the first generation of CT scanners. In practice, a single source and detector were placed opposite each other on a translating bed. The detector-source arrangement was translated to acquire a set of parallel line integral measurements for each of a series of rotational projection angles.

Filtered backprojection of parallel projection data consists of two steps: filtering of the sinogram data and backprojection of the filtered data into the reconstruction image plane. Filtering is actually a convolution which, in the

Fourier domain, is implemented by multiplication with a ramp filter or similar (Figure 4.2):

$$\bar{P}(\theta, a) = P(\theta, a) * g(a) \tag{4.5}$$

$$\mu(x, y) = \int_0^{2\pi} \bar{P}(\theta, a(x, y)) d\theta \tag{4.6}$$

where $a(x, y) = xcos(\theta) + ysin(\theta)$.

In the Fourier domain the ideal (Ram-Lak) ramp filter is given by the magnitude of the frequency. It may be modified by other filters such as Butterworth and Hamming to provide some noise smoothing:

$$\text{Ram-Lak: } g(\omega) = |\omega| \tag{4.7}$$

$$\text{Butterworth: } g(\omega) = |\omega| \cdot \frac{1}{1 + \frac{\omega}{\omega_c}^{2p}} \tag{4.8}$$

$$\text{Hamming: } g(\omega) = |\omega| \cdot \left(0.54 + 0.46 \cos\left(\pi \frac{\omega}{\omega_c}\right)\right) \tag{4.9}$$

where ω_c is the cut-off frequency and k and p are filter control parameters. There are many other filters that are in common use to, for example, enhance bone contrast or suppress soft tissue noise.

Fan-beam geometry

Fan beam geometry (Figure 4.3) was used in a limited sense in the second generation of CT scanners and more completely in the third. The second generation used a single x-ray source with multiple detectors arranged in a partial fan to collect the data. A translate-rotate mechanical motion was still required for complete coverage of the object. In third generation scanners a single source was placed opposite a large number of adjacent detectors each arranged to view the source along a different ray path through the object. The number of detectors was sufficient for complete coverage of the object. Either an equiangular or linear array of detectors may be used resulting in slightly different reconstruction algorithms.

The parallel beam FBP algorithm is extended to an equiangular fan beam geometry using geometrical factors and a modified ramp filter [Ramachandran and Lakshminarayanan, 1971, Herman et al., 1976]. This arrangement was for many years the standard arrangement used for clinical CT. For systems using a linear detector array, the ramp filter is unmodified and it is only necessary to introduce geometrical pre-weighting and backprojection factors to account for the divergent beam:

$$\bar{P}(\beta, a) = \left(P(\beta, a) \frac{R}{\sqrt{R^2 + a^2}} \right) * g(a) \tag{4.10}$$

$$\mu(x, y) = \int_0^{2\pi} \frac{R^2}{U(x, y, \beta)^2} \bar{P}(\beta, a(x, y, \beta)) d\beta \tag{4.11}$$

where U is the distance between the source and reconstruction voxel projected onto the optical axis:

$$U(x, y, \beta) = R + x \cos \beta + y \sin \beta$$

Cone-beam geometry

The parallel and fan-beam reconstruction methods described above are 2D algorithms that reconstruct a single slice of an object from 1D projections of a 2D source. Small animal and specimen micro CT systems usually employ a flat 2D detector illuminated by a 3D conical source of x-rays (Figure 4.4). This arrangement is efficient and provides the data for 3D volume reconstructions directly without translation of the object through the gantry.

The 2D fan-beam algorithm was extended to 3D by Feldkamp, Davis and Kress with the introduction of their FDK algorithm [Feldkamp et al., 1984]. The pre-weighting factor now depends on both the cone angle κ and the fan angle γ:

$$\bar{P}(\beta,a,b) = \left(P(\beta,a,b)\frac{R}{\sqrt{R^2+a^2+b^2}} \right) * g(a) \tag{4.12}$$

$$\mu(x,y) = \int_0^{2\pi} \frac{R^2}{U(x,y,\beta)^2}\bar{P}(\beta,a(x,y,\beta),b(x,y,z,\beta))d\beta \tag{4.13}$$

The backprojection geometrical factor U is the same as for the fan-beam geometry:

$$U(x,y,\beta) = R + x\cos\beta + y\sin\beta$$

The FDK method uses the same 1D ramp filter as the fan-beam reconstruction. Exact cone-beam methods [Defrise and Clack, 1994] require a 2D filtering step and the FDK method is therefore only approximate except at the vertical beam centre. However, the reconstruction artefacts are generally acceptable, and the FDK method is the most commonly used algorithm for reconstructing cone-beam data.

4.2.4 Image display

Standard x-ray CT systems reconstruct the spatial distribution of the attenuation coefficient $\mu(x,y)$ at some effective energy that is characteristic of the system. However, the attenuation values are strongly energy dependent and are not therefore particularly convenient for comparative purposes in clinical applications. Images used in clinical CT are derived from the effective attenuation coefficient normalized to water. This reduces the energy dependence of the result and allows CT images to be compared across systems. Following standard practice, CT numbers are effective attenuation values within a voxel scaled so that by definition $CT_{\text{water}} = 0$ and $CT_{\text{air}} = -1000$:

$$CT = 1000\ \text{HU}\frac{\mu - \mu_{\text{air}}}{\mu_{\text{water}} - \mu_{\text{air}}} \tag{4.14}$$

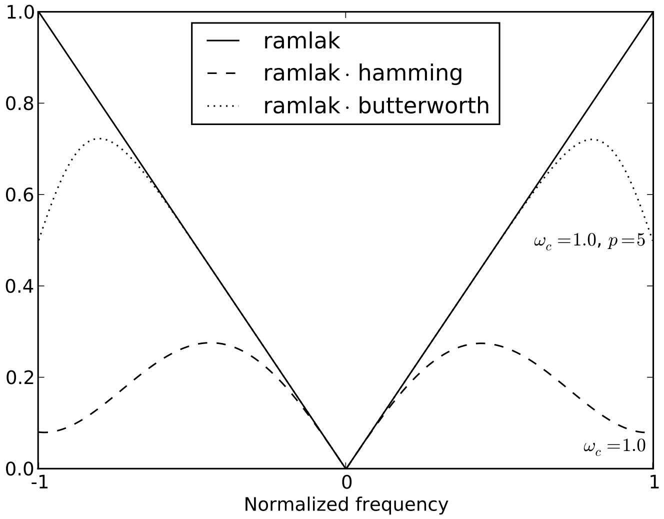

(a) Various reconstruction filters

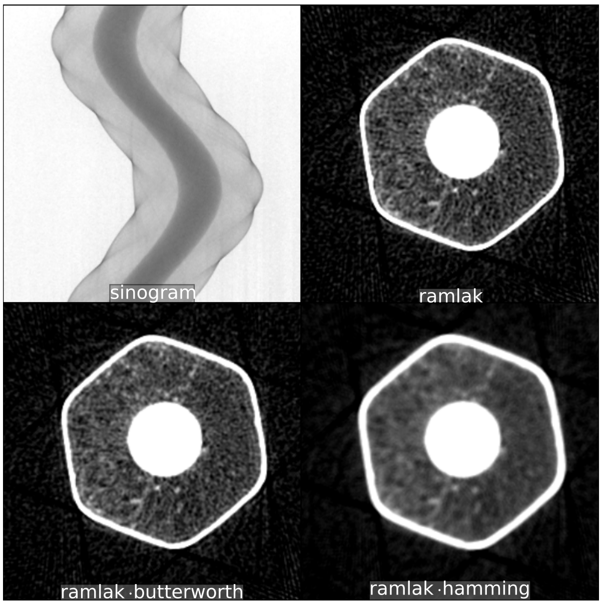

(b) Sinogram and reconstructed images

Figure 4.2: Tomographic reconstruction of a pencil using filtered backprojection and various reconstruction filters. The ramp filter (ramlak) is ideal for high resolution reconstructions of high contrast objects. Modified ramp filters can be used to reconstruct smoother images. The Hamming filter (hamming) is a low pass filter designed to improve the appearance of low contrast features. The Butterworth filter (butterworth) provides some smoothing but preserves most of the spatial resolution by filtering mainly the highest frequencies.

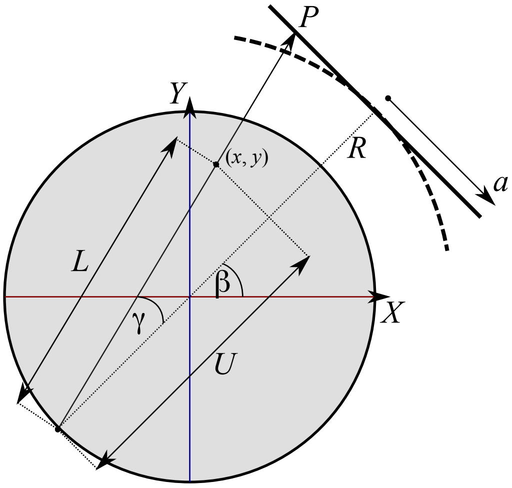

Figure 4.3: Fan beam geometry. The 2D object distribution is represented in the X–Y plane. The projection angle is β and the fan angle is γ. The x-ray fan beam emerges from a single point opposite either an equiangular (dashed) or linear (solid) detector array that records the data for the projection P.

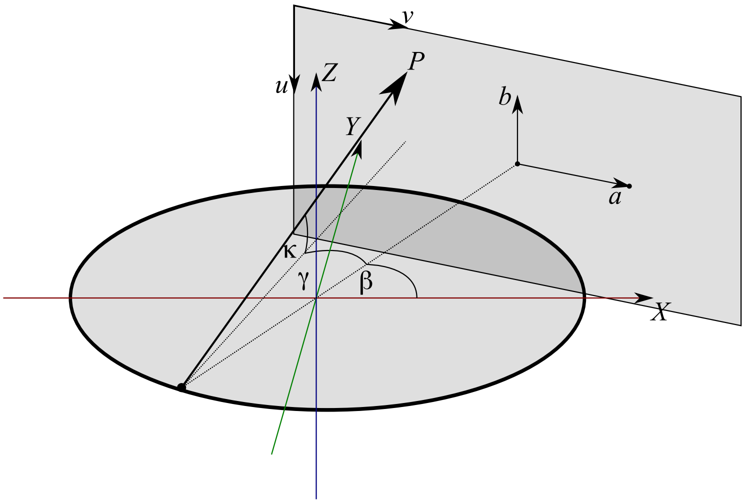

Figure 4.4: Cone beam geometry. The object coordinate axes are X, Y, and Z. The detector's physical coordinates are a, b and the pixel row and column coordinates are u, v. The projection rotation angle is β and the fan and cone angles are γ and κ respectively. The x-ray cone beam emerges from a single point source opposite the detector and is projected through the object to form each sample P.

Figure 4.5 shows the attenuation coefficients for some clinically relevant materials scaled to HU. See also Table 4.1 for the composition of some clinical materials. The energy dependence of the CT number is quite obvious at low energies. At the higher energies used for diagnostic purposes, the energy dependence of the CT number is greatly reduced.

The range of CT numbers measurable on a standard CT system is typically represented by 4096 grey scale values (covering the interval [-1024, 3071] HU). This far exceeds the inherent capability of the human eye and most display systems. Therefore images are usually windowed to represent the materials of interest with the greatest contrast.

Although the energy dependence of the CT number has long been recognized, standard radiological practice does not incorporate effective energy information within the display and reporting of results. This is of little consequence for standard CT systems since these are designed and operated to minimize the effect of spectral differences. However, spectral CT systems are designed to enhance and exploit the energy dependence of the attenuation coefficient. In this context the Hounsfield Unit is not particularly suitable for display purposes, being neither a fundamental unit nor an energy independent derivative [Hurrell et al., 2012].

Table 4.1: Elemental mass composition of some clinical tissues [ICRU, 1988].

Tissue	Elemental composition (percentage by mass)					Density /g.cm^{-3}
	H	C	N	O	Others	
Adipose	11.4	59.8	0.7	27.8	0.1 Na, 0.1 S, 0.1 Cl	0.950
Blood	10.2	11.0	3.3	74.5	0.1 Na, 0.1 P, 0.2 S, 0.3 Cl, 0.2 K, 0.1 Fe	1.060
Liver	10.2	13.9	3.0	71.6	0.2 Na, 0.3 P, 0.3 S, 0.2 Cl, 0.3 K	1.060
Cortical bone	3.4	15.5	4.2	43.5	0.1 Na, 0.2 Mg, 10.3 P, 0.3 S, 22.5 Ca	1.920
Average soft tissue	10.1	11.1	2.6	76.2	-	1.000

4.3 Practice

4.3.1 Mechanical arrangements

Clinical CT systems comprise two main components: the patient bed and the rotating gantry. The rotating gantry contains the (usually) single x-ray source opposite a fan beam array of detector elements. In standard clinical CT the detectors are usually of the solid state $Gd_2O_2S(Tl)$ (GOS) scintillator type [van Eijk, 2003]. An anti-scatter collimator aligned to view the source and eliminate radiation from other directions may be placed directly in front of the detector array. The power to the x-ray unit is delivered via slip-rings that eliminate cables and allow continuous rotation. The patient bed delivers the patient through the rotating gantry in a continuous movement to achieve the helical scan. See Figure 4.6.

Small animal and specimen imaging systems operate on similar principles to clinical scanners but at much smaller scales. In the case of small animals such as mice, a resolution of $\sim(100\ \mu\text{m})^3$ is required to provide a similar level of detail as found in human CT [Ritman, 2007]. This implies a reconstruc-

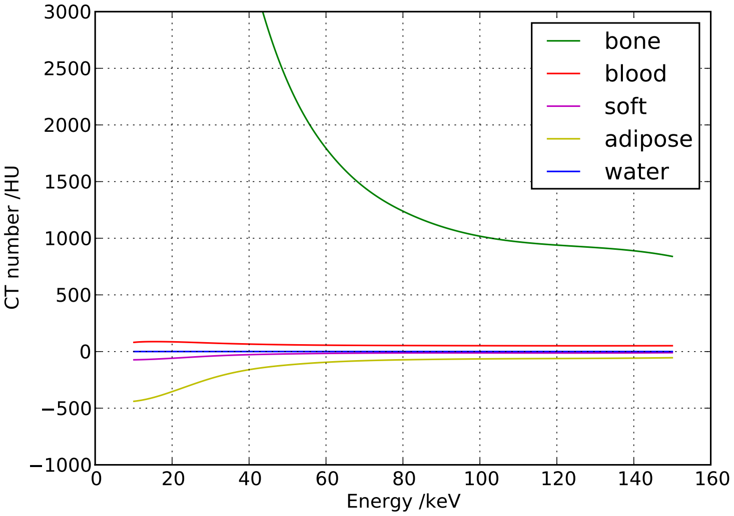

(a) CT numbers for clinical materials

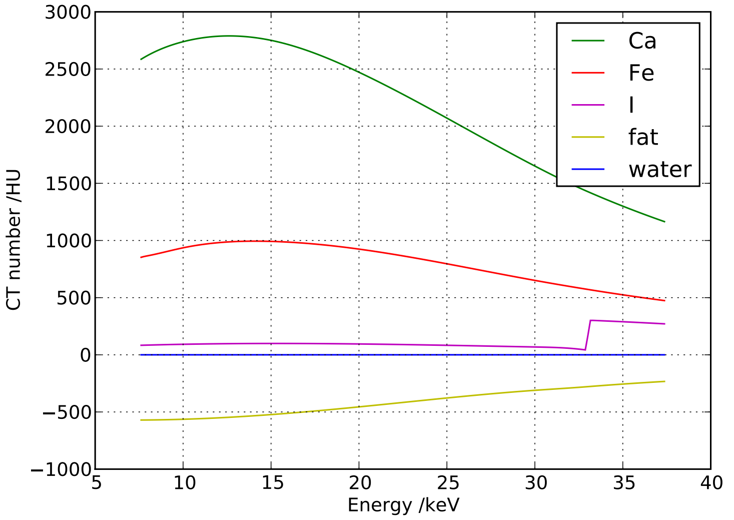

(b) CT numbers for surrogate materials

Figure 4.5: The attenuation coefficients [Berger et al., 1998] for various materials scaled to Hounsfield units. (a) CT numbers for clinical materials (compact bone, blood, soft-tissue and fat) plotted over the diagnostic imaging energy range. (b) CT numbers for surrogate materials (2 M calcium chloride, 0.4 M ferric nitrate, 0.01 M iodine and fat) plotted over an energy range appropriate for small animal and specimen imaging.

tion matrix of 1000 × 1000 voxels for a field of view $FOV \sim 100$ mm and hence a pixel pitch of ∼50 μm depending on the geometrical magnification factor. (The geometrical magnification factor is given by the ratio of source–to–detector and source–to–object distances $M = \frac{SDD}{SOD}$.) In-vitro specimen imaging systems typically operate at a still smaller scale. However, scale distinctions in computed tomography are somewhat arbitrary and both types of system may be referred to as micro CT [Kalender, 2001, Bartling et al., 2007].

Small animal imaging CT systems, in particular, may be regarded as scaled down versions of clinical units [Bartling et al., 2007]. Because of the requirement to maintain the condition of the live animal and eliminate unwanted movement during the scan, the animal is placed on a platform about which the x-ray and detector gantry rotate. To maintain comparable imaging resolution micro-focus x-ray tubes are commonly used which have a focal spot size ∼5–50 μm. The small focal spot limits the amount of power that can be delivered and hence the x-ray fluxes are insufficient for rapid scanning. Typical scan times are several minutes for these systems. The small size of the object requires the use of much softer x-ray spectra to maintain image contrast [Paulus et al., 2000]. Consequently alternative detector technology and sensor layer materials may be used including: phosphor screens, amorphous selenium (a-Se) amorphous silicon (a-Si) panels, crystalline silicon (Si) and CdTe layers and others coupled to photodiodes, CCD cameras or direct conversion electronics [Yaffe and Rowlands, 1997, Goertzen et al., 2004]. Specimen imaging systems typically differ somewhat from small animal systems. Because of the relaxed dose and physiological constraints, designers may elect to use a fixed x-ray source and detector unit with a rotating specimen stage. Greater imaging resolution can be achieved using reduced focal spot sizes, finer pitch detector pixels, higher magnification and longer imaging times. Two dimensional flat panel detector technology is often used in both small animal and specimen imaging. This implies a cone beam geometry and the use of 3D volume

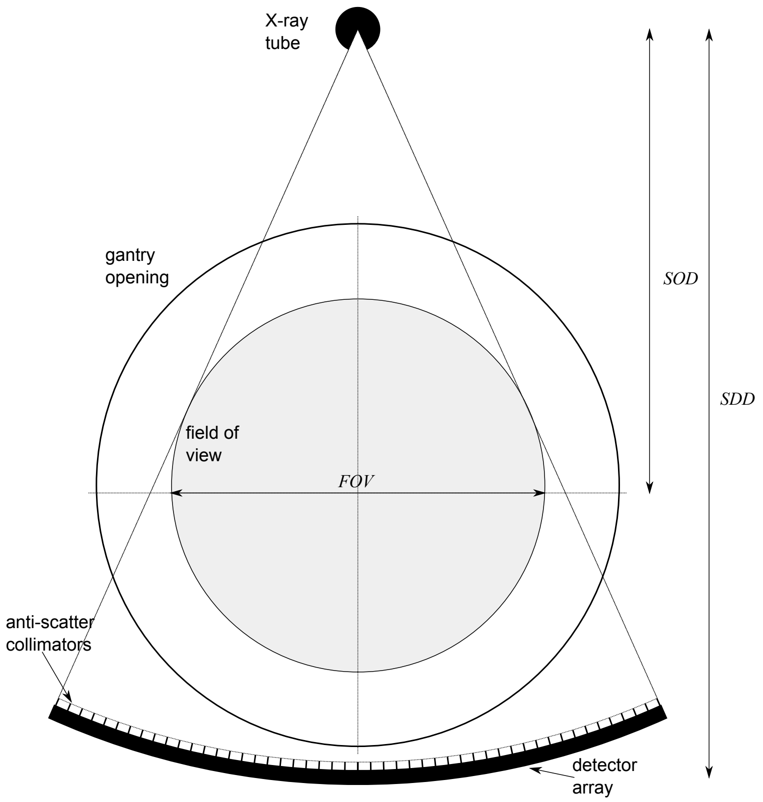

Figure 4.6: A simplified diagram of the frontal view of a clinical CT system fan beam geometry (adapted from [Kalender, 2001]). The field of view is typically $FOV \sim 500$ mm whereas the source–to–object and source–to–detector distances are typically $SOD \sim 600$ mm and $SDD \sim 1000$ mm respectively. In comparison, a small animal CT system might use a flat panel detector (without anti-scatter collimation) in a cone beam geometry with $FOV \sim 100$ mm.

reconstruction algorithms such as the FDK algorithm.

4.3.2 X-ray sources

The source of x-rays for clinical and the vast majority of micro CT systems is a type of particle accelerator known as an x-ray tube. The modern x-ray tube is based on that developed in 1913 by Coolidge [Coolidge, 1913]. An electrically heated wire filament (cathode) releases electrons that are accelerated towards a positively charged target (anode). The interaction of electrons within the target produce both characteristic and bremsstrahlung x-rays. See Figure 4.7.

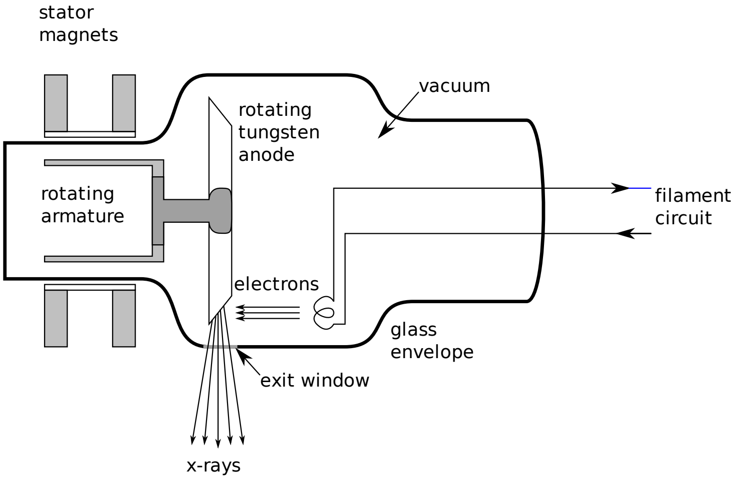

Figure 4.7: Simplified diagram of an x-ray tube (adapted from [Hendee and Ritenour, 2002].) Electrons are thermionically emitted from the cathode and accelerated towards the rotating anode target. X-rays are produced (primarily) by bremsstrahlung and emitted approximately orthogonally to the electron beam.

The cathode filament is usually made from tungsten because of its high melting point. Since the production of x-rays is more efficient in materials with a high Z number, tungsten ($Z = 74$) is also often used as the anode material. Nevertheless x-ray production is an inherently inefficient process and rotating anodes are usually used to assist with heat dissipation. Molybdenum may be used as the base material for the anode because of its high heat capacity. Molybdenum and rhodium are sometimes used as the target material where low energy x-rays are required (e.g. for breast imaging).

In micro CT systems the requirement for a small focal spot compromises flux output. The heat dissipation characteristics are such that the maximum power that can be handled by a tube is approximately proportional to the diameter of its focal spot [Flynn et al., 1994]. Thus micro focus x-ray tubes are usually of rather limited output compared with clinical devices and this extends the length of time required to scan an object at high resolution.

4.3.3 Detectors

Clinical CT systems typically use ceramic scintillators such as $Gd_2O_2S(Tl)$ (GOS) as the sensor elements within the detector arrays. As discussed in Chapter 3, these provide good stopping power and a fast response. Previously, high pressure xenon ion chambers were favoured. These were well suited to providing a homogeneous array of detecting elements in the fan beam geometry. However, a particular advantage of solid state scintillator detectors is the ease with which multi-row arrays can be built and xenon detectors are now largely obsolete within CT. Multi-slice diagnostic CT systems now incorporate up to 64 rows of scintillator elements within the fan beam detector array. Pixel sizes in modern clinical scanners are typically 1.0 mm or less (although the array structure is not necessarily isotropic). The sensitivity to scattered radiation is reduced by absorption septa placed between the detector elements.

Small animal and specimen imaging micro CT systems may use 1D solid state detectors in a fan beam geometry or 2D flat panel detectors in a cone-beam geometry. Most flat panel detectors are phosphor coated CCD cameras or amorphous silicon readout panels. In some applications anti-scatter grids manufactured from layers of a high Z material such as lead or tungsten with a low Z radiolucent spacing material such as plastic or aluminium may be placed directly in front of the detector array to prevent scattered radiation from reaching the detector elements.

Unlike human CT, the requirement for short scan times is not as demanding in small animal and (especially) in-vitro specimen imaging applications. The use of charge integrating detectors is therefore not always necessary. Pulse mode semiconductors may be used to eliminate electronic noise and, in some cases, provide energy discrimination. However, the fine pixel pitch causes a particular problem for direct conversion detectors known as charge sharing [Mathieson et al., 2002, Campbell et al., 2008]. This limits the spectroscopic performance in most cases. Advanced signal processing possible with hybrid detectors (sensor layer + CMOS ASIC) such as Medipix3 can be used to restore spectroscopic performance by summing the dispersed charge back into a single pixel. However, the small size of state-of-the art hybrid detectors can be a limitation. The Medipix2 and Medipix3 detectors have an imaging size of only 14 mm × 14 mm. For small animal imaging applications this implies a need for multi-detector arrays or move–and–tile scan protocols (or both) [Pfeiffer, 2004].

4.3.4 Artefacts

Polychromaticity

Reconstruction algorithms assume that the projection measurement data represents the line integral of the values to be reconstructed. In the case of a polyenergetic x-ray flux such as that produced by bremsstrahlung x-ray tubes, the interactions within the object being scanned successively remove the low energy component of the spectrum. The effective attenuation coefficient thus varies with the progress of the beam through the object and the final projection is not a simple line integral. This is the beam hardening effect.

There are two effects of beam hardening on the reconstructed image. The first is cupping that occurs in relatively homogeneous objects of large diameter. The increase in beam energy results in an artificial reduction in the measured attenuation coefficient near the centre of large objects. The second is the appearance of streaks between dense parts of the object. As the object rotates the dense parts will periodically align with the beam. When this occurs the mean energy of the beam is artificially increased as it traverses the intervening region and once again the reconstructed attenuation coefficient is artificially reduced.

If the x-ray beam is prefiltered as it leaves the tube, the degree of hardening that occurs within the object is reduced. In clinical systems a bowtie filter can be employed to increase the degree of prefiltering at the edges of the beam in accordance with the reduced path length through the periphery of the patient. For software correction of residual beam hardening, a calibrated correction curve can be determined by measuring the projection correction factors that are required to eliminate cupping in a cylindrical phantom [Herman, 1979].

To avoid beam hardening artefacts in small animal and high contrast specimen images, some prefiltering will be required. The diameter of a mouse is ∼30 mm and an effective beam energy of ∼25 keV will provide maximum contrast resolution [Paulus et al., 2000]. An aluminium filter of thickness ∼1–2 mm will remove most of the x-ray spectrum below 15 keV and may represent an appropriate level of filtering for small rodents.

Scatter

Scattering is another important interaction mechanism that is not included in the assumptions upon which the reconstruction algorithms are based. The line integral formulation is derived from Beer's Law which is based on total attenuation and does not include the effects of scattering *into* the detector. Thus when an attenuating object is placed into the beam the x-ray flux at the detector is both decreased by attenuation from material within the ray path (primary signal) and increased by scatter into the beam of extraneous x-rays (secondary signal).

When scanning low Z soft tissues the secondary signal due to scatter is often negligible and no effect is observed. However, if the secondary signal is significant, effects similar to those seen with beam hardening can be observed. That is, both streaks and cupping can occur due to scattering.

In clinical fan beam CT anti-scatter collimation is used to absorb the secondary x-rays before they reach the detectors. Anti-scatter grids can be used in flat panel systems to reduce the amount of scattered radiation reaching the detector. However, these also reduce the geometric efficiency and are not suitable for move-and-tile based systems. For cone beam systems such as the MARS-CT, scattering in soft tissues may be sufficiently reduced through the use of an air gap [Sorenson and Floch, 1985]. Where it is not possible to prevent or sufficiently minimize the secondary scatter, software corrections can be used [Glover, 1982]. Noting that the angular distribution of Compton scattering is slowly varying, a simple and often effective approach is to apply a constant offset to the projection signal before reconstruction.

Ring artefacts

Where inter-pixel variations exist they give rise to a constant source of projection error in the data recorded by that pixel. Since each pixel is backprojected at a constant radius for all projection angles, these inhomogeneities appear as rings in the reconstructed image. Xenon detector arrays were relatively homogeneous due to their construction as multiple electrodes within a single pressurized chamber. In contrast, solid state detectors are a collection of discrete elements and thus they are in principle more prone to inhomogeneities. Frequent calibration of the electronics and measurement of the pixel gain as well as dedicated ring correction software are required to eliminate rings from the reconstructed images.

The Medipix detectors used in the MARS-CT system are highly sophisticated hybrid devices. Although the sensor layer is monolithic, separate analogue and digital signal processing electronics are provided for each pixel. Thus the stability and homogeneity of the hybrid electronics will impact directly on image quality. The Medipix3 is the latest in the series of detectors from the Medipix collaboration and its performance is still being investigated. To achieve good CT image quality, measurement protocols may need to include frequent detector calibrations and image processing may require dedicated ring filtering algorithms.

4.4 Spectral CT

4.4.1 Introduction

There are four main methods for acquiring spectral CT data:

1. Sequential scan, single-source, single detector. In this mode of operation a standard CT system is used to acquire projection data sequentially at two or more x-ray tube voltages.

2. Dual-source, dual detector. In this mode a pair of source-detector systems are incorporated within a single system. Each source-detector arrangement is designed to acquire data at a different tube voltage.

3. Single-source, dual-layer detector. This mode uses a pair of detectors and a single source. The detectors are arranged in layers so that the front layer acquires data from the full continuum whereas the rear layer acquires higher energy data from the filtered spectrum.

4. Single-source, spectroscopic detector. A spectroscopic detector capable of acquiring data above multiple energy thresholds or within multiple energy bins is used with a single broad spectrum energy source.

Methods 1 and 2 control the energy of the interrogating x-ray beam and measure the total exit signal using a detector with a fixed energy response. Methods 3 and 4 measure the exit spectrum of a fixed interrogating beam using an energy sensitive detector arrangement. Method 4 is the most sophisticated and relies upon state of the art detector technology such as the Medipix family. These detectors provide a great deal of spectroscopic data, however they are also prone to specific sources of error such as charge-sharing. It is not immediately clear how spectral CT with spectroscopic detectors will perform in practice. A simple numerical model can help reveal some basic characteristics of the method.

4.4.2 Numerical simulation

X-ray source

There are a number of semi-empirical and analytical models for accurately estimating the x-ray emission from a standard x-ray tube [Reed, 1975, Birch and Marshall, 1979, Ebel et al., 1989, Tucker et al., 1991, Poludniowski, 2007, Poludniowski and Evans, 2007]. These sophisticated algorithms accurately describe both the bremsstrahlung and characteristic emissions from the tube. For our purposes, noting that the characteristic emissions are strongly suppressed by beam filtration, the relatively simple method developed by Kramers [Kramers, 1923] is sufficient. According to Kramers' Law, the number distribution of the unfiltered bremsstrahlung spectrum as a function of photon energy $E = h\nu$ is:

$$N(E) \propto Z\left(1 - \frac{E}{T_0}\right) \tag{4.15}$$

where Z is the atomic number of the target and $T_0 \propto V$ is the kinetic energy of the electron beam (proportional to the accelerating voltage).

Projection signal

Ignoring photon scattering, the projection signal is due to the combination of photon emission and attenuation (in the beam filters and the object), convolved with the detector response. Writing the cumulative transmission after attenuation from all intervening materials as a factor $\Phi(E)$, the detector response function as $R(E, E_0)$ and the number density of x-rays emitted at energy E_0 as $N(E_0)$, the energy dependent signal density $S(E)$ is the convolution of detector response and transmitted x-ray flux integrated over all emission energies:

$$S(E) = \int_{E_0=0}^{T_0} R(E, E_0)\Phi(E_0)N(E_0)\, dE_0 \tag{4.16}$$

where:

$$\begin{aligned} \Phi(E) &= \exp \sum_{\text{all materials}} -\mu(E)t \\ R(E, E_0) &= G(E, E) * Q(E, E_0) * (1 - \exp(-\mu_{\mathrm{D}}(E_0)D) \end{aligned}$$

and μ and t are the attenuation coefficient and thickness for each material and μ_{D} and D are the detector interaction coefficient and thickness respectively. The detector response includes convolution with a charge sharing function Q described in Appendix B and Gaussian resolution function G.

The detector electronics typically accumulates its responses above a lower threshold or within a finite energy bin in which case the recorded signal is the integral of $S(E)$ above or between appropriate limits respectively:

$$S = \int_{E_{\mathrm{L}}}^{E_{\mathrm{U}}} S(E)\, dE \tag{4.17}$$

Discrete approximation

To perform numerical calculations we can approximate the spectral response integral as a matrix multiplication. A discrete approximation $\mathbf{s} = [s_j]$ for the energy dependent spectral response $S(E)$ is:

$$\mathbf{s} = \mathbf{R} \cdot \mathbf{f} \tag{4.18}$$

where the detector response matrix and exit flux are:

$$\begin{aligned} R_{j,i} &= R(E_j, E_i) \\ f_i &= \Phi(E_i)N(E_i) \end{aligned}$$

and E_i and E_j are appropriate samples of the x-ray emission and detection energy intervals.

Spectroscopic response

Figure 4.8 shows simulated spectroscopic responses for a Medipix3 detector in the open beam of an x-ray tube at 50 kVp. The Medipix3 detector is modelled as a 300 μm silicon layer with an energy resolution of 2 keV FWHM. (An approximation for the combined effect of electronic [Ballabriga et al., 2010] and statistical contributions.) Responses are plotted both with and without the charge sharing tail (simulating single pixel mode SPM and charge summing mode CSM respectively). Two levels of x-ray filtration are modelled (0.6 mm and 1.8 mm aluminium equivalent). The same arbitrary scale is used for all responses. The effect of charge sharing is to erroneously increase the low energy count rate at the expense of the high energy response. The additional filtration increases the mean energy of the signal.

Spectral CT response

The CT numbers for various materials are estimated by comparing the spectral response S after transmission through a small unit length of each material with those calculated after transmission through the same lengths of air and water. Figure 4.9 shows simulated CT numbers obtained using responses (a) in SPM (model includes the charge sharing tail) and (b) in CSM (model excludes the charge sharing tail). Once again the Medipix3 detector is modelled as a 300 μm silicon layer with an energy resolution of 2 keV FWHM. The contrast between materials is generally greatest at low energies. The K-edge of iodine is at 33.2 keV and its CT number therefore increases around this value. Charge sharing reduces the contrast between materials in SPM.

Contrast resolution

Contrast resolution is the ability to distinguish small deviations in CT number that occur with a small change in effective density or path length [Paulus et al., 2000, Kalender, 2001]. This depends on both the pixel noise present in the reconstructed image and the attenuation coefficient of the material at the effective energy of the x-ray beam.

The attenuation coefficient measured by the CT system is proportional to the logarithm P of the normalized detector signal S:

$$P = -\ln \frac{S}{S_0} \tag{4.19}$$

Assuming the pixel noise in the reconstructed image is Poisson and that $\sigma_{S_0} \ll \sigma_S$ then the uncertainty in P is given by:

$$\sigma_P = \frac{\sigma_S}{S} = \frac{1}{\sqrt{S}} \tag{4.20}$$

Writing the contrast resolution as the ratio of uncertainty σ_P to the rate of change in P with path length t gives:

$$\begin{aligned} C = \frac{\sigma_P}{\frac{dP}{dt}} &= -\frac{S}{\frac{dS}{dt}} \cdot \sqrt{\frac{1}{S}} && (4.21) \\ &= -\frac{\sqrt{S}}{\frac{dS}{dt}} && (4.22) \end{aligned}$$

In terms of the numerical model defined above, the energy dependent contrast resolution is:

$$c_j \propto \frac{\sqrt{s_j}}{s'_j} \tag{4.23}$$

where:

$$\mathbf{s}' = \mathbf{R} \cdot \mathbf{f}'$$

$$f'_i = -\mu(E_i) f_i$$

Figure 4.10 shows the simulated contrast to noise ratio measured in SPM and CSM for water phantoms of various diameters up to 50 mm. The x-ray spectrum was calculated using Kramers' Law and an assumed accelerating voltage of 50 kVp. Intrinsic filtration of 0.6 mm and 1.8 mm aluminium equivalent thickness was modelled. In SPM the contrast resolution is maintained at very low energies due to the presence of the charge sharing tail. At high energies the contrast resolution is noticeably worse in SPM than CSM due to the loss of signal to charge sharing. The benefit of reduced filtration (0.6 mm aluminium) is most noticeable for the 1 mm and 10 mm diameter phantoms. At larger diameters, the loss of contrast resolution caused by the use of 1.8 mm aluminium filtration is less significant. Thus for mouse sized (∼30 mm diameter) specimens, the anticipated reduction in beam hardening artefacts provided by additional prefiltering may be justified.

The overall results of the simulation agree in general terms with previous work describing contrast resolution for a monoenergetic x-ray source [Paulus et al., 2000]. For both SPM and CSM there is bin energy at which the contrast resolution is an optimum. The optimum energy increases with the diameter of the soft tissue specimen but for the simulated 50 kVp x-ray beam is typically ∼15–25 keV.

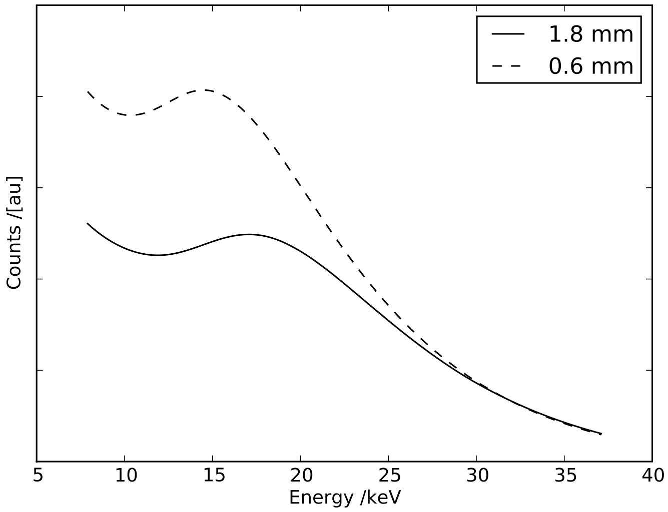

(a) Simulated open beam response in SPM.

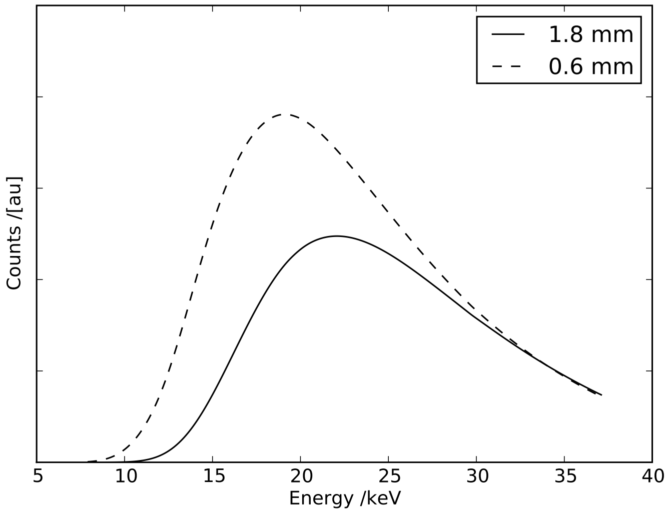

(b) Simulated open beam response in CSM.

Figure 4.8: Simulated open beam responses for a Medipix3 with 300 μm silicon sensor layer operating in (a) SPM and (b) CSM. The x-ray tube was simulated with 0.6 and 1.8 mm Al filtering and an accelerating voltage of 50 kVp. The same arbitrary scale is used for all cases.

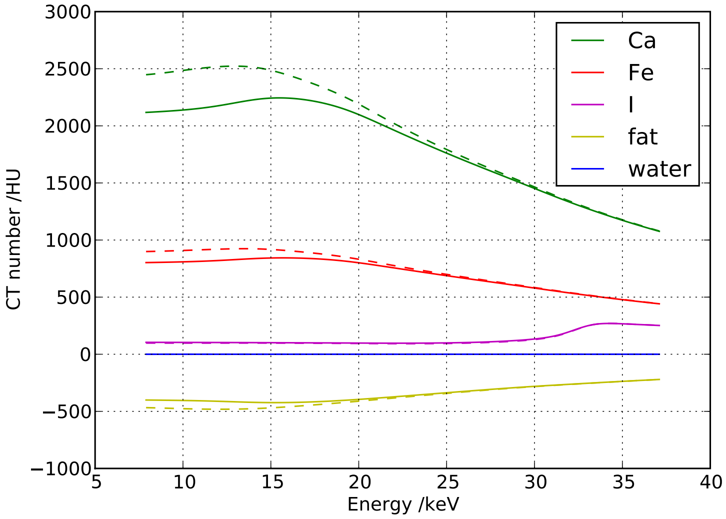

(a) Energy bin response in SPM

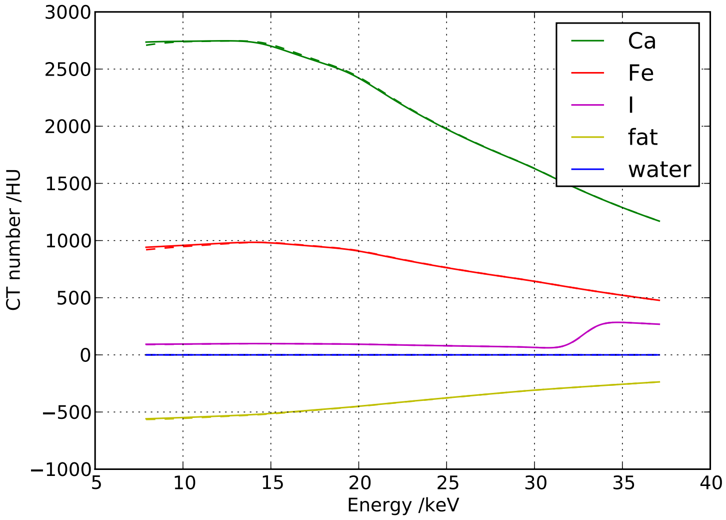

(b) Energy bin response in CSM

Figure 4.9: Simulated CT responses for a Medipix3 with 300 μm silicon sensor layer operating in (a) SPM and (b) CSM for a range of clinically relevant surrogate materials (2 M calcium chloride, 0.4 M ferric nitrate, 0.01 M iodine and fat). In both cases the x-ray source was simulated at 50 kVp with 1.8 mm Al filtration (solid lines) and with 0.6 mm Al filtration (dashed lines).

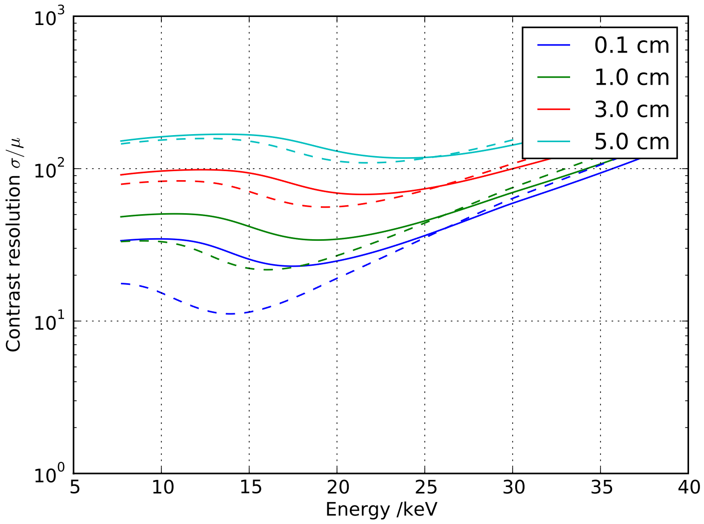

(a) Contrast resolution SPM

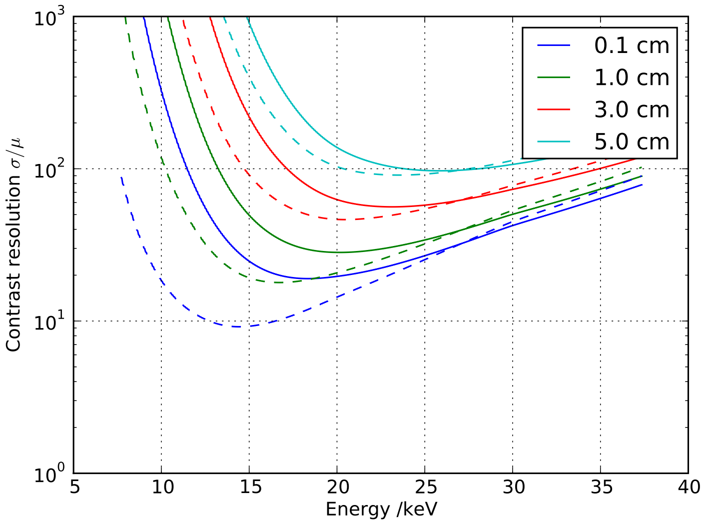

(b) Contrast resolution in CSM

Figure 4.10: Simulated contrast resolution curves for a Medipix3 with 300 μm silicon sensor layer measuring a range of water phantoms in (a) SPM and (b) CSM. In both cases the x-ray source was simulated at 50 kVp with 1.8 mm Al filtration (solid lines) and with 0.6 mm Al filtration (dashed lines).

4.5 Summary and conclusions

1. The Fourier slice theorem allows a 2D spatial distribution to be reconstructed from 1D line integrals collected at multiple projection angles. Historically, many different data collection geometries have been employed which may be broadly categorized as either parallel beam, fan beam or cone beam.

2. The most commonly used reconstruction algorithms are of the filtered backprojection type. These algorithms are fast, robust and mathematically equivalent to the exact Fourier method for parallel and fan beam geometries. The FDK filtered backprojection algorithm is usually used for cone beam geometries. It is exact at the vertical beam centre and approximate elsewhere.

3. In attenuation based x-ray tomography, the value that is reconstructed is the effective attenuation coefficient. It is specific to the spectral properties of the system and is strongly energy dependent. In clinical CT, the attenuation coefficient is usually normalized to water and expressed as a CT number in Hounsfield units.

4. Physical effects such as beam hardening and x-ray scattering and electronic effects such as pixel inhomogeneity, can produce artefacts that impair the quality of the reconstructed images. X-ray beam prefiltering and measurement geometry can be adjusted to minimize these physical effects. Systems based on solid state detector arrays are, in principle, more susceptible to electronic effects that produce ring artefacts. Frequent calibration can reduce the effects of electronic variations. Software corrections can be used to correct residual physical and electronic artefacts.

5. Spectral CT utilizes energy dependent projection data and aims to enhance contrast, reduce artefacts, improve material differentiation and

aid quantification. The different modes of spectral CT may be classified according to whether the x-ray beam or detector characteristics are controlled. Spectral CT with spectroscopic photon counting detectors relies upon state of the art detector technology such as Medipix3. Medipix3 is the latest and most sophisticated detector from the Medipix collaboration and is designed to mitigate charge sharing effects and allow simultaneous counting in multiple energy bins.

6. The CT number spectra for several clinically relevant materials measured with Medipix3 have been simulated numerically in SPM and CSM. The simulated CT number spectra are comparable with the normalized monoenergetic attenuation coefficients with agreement improving through the application of CSM.

7. Simulations of contrast resolution in SPM and CSM indicate that, for small animals and specimens, optimum performance is obtained at relatively low energies (15–25 keV) and will be enhanced through the use of charge summing mode.

Chapter 5

Evaluating Medipix3

This chapter evaluates a prototype MARS camera with Medipix3 for use as an x-ray imaging detector. Electronic stability, image quality and spectroscopic performance are evaluated. The on-chip temperature sensor is calibrated and examples of spectroscopic projection images are presented. The candidate presented material from this chapter at the *International Workshop on Radiation Imaging Detectors (2010)* in Cambridge, UK and prepared a corresponding article for publication in the *Journal of Instrumentation* [Ronaldson et al., 2011a].

5.1 Introduction

The Medipix family of x-ray imaging detectors are developed by an international collaboration led by designers at CERN. The collaboration aims to apply detector technology developed in support of high energy physics to medical imaging. Medipix3 is the latest and most advanced in this series of photon counting detectors and has been made available for testing and evaluation.

Medipix3 [Ballabriga et al., 2006, Ballabriga et al., 2010] extends the capabilities of earlier detectors by including additional operating modes and configuration options. The pixels of traditional photon counting detectors, such as Medipix2 [Llopart et al., 2002], operate individually without using information from their neighbours. This is called *single pixel mode* (SPM). Traditional photon counting detectors suffer from the charge sharing effect whereby charge dispersion during collection causes multiple pixels to simultaneously count a portion of the total input signal, thereby degrading spectroscopic performance [Campbell et al., 2008]. To mitigate this effect, Medipix3 includes pixel summing and arbitration circuitry that first sums the response from adjacent pixels and then allocates the result to the pixel contributing the largest share of the charge. This is called *charge summing mode* (CSM).

Medipix3 also provides multiple readout counters per pixel (Table 3.4). In *fine pitch mode* the 55 μm × 55 μm pixels of the sensor and readout layers are arranged in a one-to-one mapping with two readout counters per detector pixel. In *spectroscopic mode*, four Medipix3 readout pixels are mapped to one 110 μm × 110 μm sensor pixel thereby providing eight readout counters per pixel.

A Medipix3 x-ray imaging detector configured in fine pitch mode with a silicon sensor layer has been incorporated into a prototype MARS camera for characterization and testing. This x-ray camera comprises custom-built readout electronics and software libraries designed for the Medipix family of detectors [Doesburg et al., 2009]. The MARS research team intends to use the Medipix family of detectors as the underpinning technology within the x-ray camera and spectral CT systems it is developing. The aim of this chapter is to evaluate a prototype MARS camera incorporating the Medipix3 for image quality and stability prior to use within the MARS-CT systems.

5.2 Materials and methods

5.2.1 Equipment

A 256×256 pixel Medipix3 bump-bonded to a 300 μm thick silicon sensor layer was used for this work (see Figure 5.1). It was connected to a prototype MARS camera readout via an external SCSI cable and cooled by ambient air only. The prototype MARS camera was controlled by the locally developed `libMars` C library and Python interface (Appendix C). A second MARS camera incorporating a Medipix3 chip within a sealed enclosure was used for investigations of the on-chip temperature sensor. For all measurements, the Medipix3 was operated in high gain mode as appropriate for the low energy range of the silicon sensor.

For spectroscopic measurements, the MARS camera unit was used as a standalone device. A Kevex PSX11-150-75 mini-focus x-ray tube (Thermo Fisher Scientific, Scotts Valley, CA) with tungsten anode and 0.13 mm beryllium window was used within a shielded enclosure for spectroscopic calibration and a 1.7 GBq ^{241}Am radioactive source was used to provide the incident flux for additional bench tests. For the projection scanning measurements, the detector and samples were mounted within a prototype MARS-CT system. The MARS-CT was equipped with a Source-Ray SB-80-1K x-ray tube (Source-Ray Inc, Ronkonkoma, NY) with tungsten anode and 1.8 mm of aluminium (equivalent) intrinsic filtration.

5.2.2 Threshold equalization

In operation, the Medipix3 is controlled and configured by a set of 25 global DACs (Table A.1) and 13-bits of a 24-bit control register applied at the pixel level (Table A.2). The global DACs apply bias voltages and currents at the chip level and are typically used to bias the analogue circuitry. They also supply signal offset currents (Threshold0–Threshold7) that effectively adjust

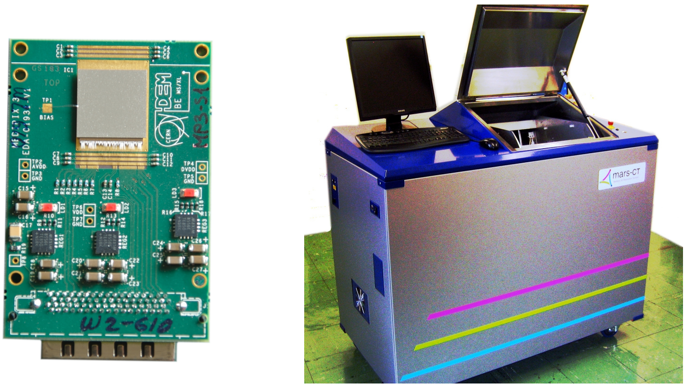

Figure 5.1: The Medipix3 detector with 300 μm thick silicon sensor layer and the MARS-CT system incorporating the MARS camera and Source-Ray SB-80-1K x-ray tube.

the counter thresholds to set the minimum pulse height that can be counted. However, due to manufacturing variations, the counter thresholds vary from pixel to pixel and the response of the detector to a uniform flux is inconsistent across the chip. Before acceptable images can be acquired it is necessary to equalize the counter thresholds so that each pixel is sensitive to pulses of the same minimum height.

Two global current sources (one positive and one negative) and 5 adjustment bits per pixel counter are available for relative adjustment of the counter thresholds. The negative current source is set by ThresholdN and may be applied at the pixel-level to any counter threshold using a switch selected by one of the 5 adjustment bits. The positive current source is set by DACpixel and some fraction $(\frac{0}{15} \cdots \frac{15}{15})$ of this may be applied to each counter threshold using the remaining 4 adjustment bits.

The equalization process adopted for the work in this chapter was based on that proposed by the chip designers [Ballabriga, 2009a]. The intrinsic electronic noise of the chip is used to find counter threshold adjustment masks in both single-pixel mode (SPM) and charge-summing mode (CSM). Prior to equalization in SPM, all pixels were switched on and a null adjustment mask applied. A sequence of threshold scans[1] were used to inform the selection of, firstly, the negative current adjustment bit, and secondly, the positive current adjustment bits, such that the counter thresholds were equalized, as far as possible, just above the electronic noise floor. After equalization, malfunctioning pixels and those with an equalized counter threshold greater than some acceptable limit were inhibited using the `MaskBit`.

The equalization procedure for CSM was similar to that for SPM except that equalization was performed sequentially for four sets of pixels, each set comprising corresponding members of local clusters of 2×2 pixels. The remaining 75% of pixels were switched off during each part of the process to eliminate arbitration and ensure that the effects of pixel threshold adjustments would be correctly observed in the corresponding pixel counters. The four parts of the CSM configuration mask were then combined.

The effectiveness of the equalization process was examined by measuring the flat field pixel count histogram in SPM and CSM. A successful equalization should yield a count distribution that is approximately uniform across all pixels. This was tested in SPM and CSM by illuminating the chip with a 50 kVp flat-field. The pixel responses were averaged over one hundred frames and normalized and flat field pixel count histograms were computed. Test images were then acquired and examined to assess post-equalization image quality.

The spatial characteristics of image noise were quantified by measuring the noise power spectra[2] (NPS) [Rossmann, 1962, Williams et al., 1999] in SPM and CSM. The 2D noise power spectrum was calculated individually from the central region of one hundred flat-field frames and the average over the full data set used to determine the 1D NPS by averaging over both image axes.

---

[1] A threshold scan is acquired by incrementing the global counter threshold DAC, say `Threshold0`, through its range (0–511) and acquiring an image frame from the chip at each threshold setting.

[2] The noise power spectrum quantifies the noise per unit spatial frequency. For pixels counting data independently and uniformly the noise power spectrum should be flat.

5.2.3 Temporal stability

The ability of the chip to acquire repeatable measurements depends upon the stability of the bias signals supplied by the global DACs. The `libMars` Python interface was used to monitor the output of the global DACs during a continuous series of threshold scans of the intrinsic noise in SPM and CSM. The observed output levels were plotted for a period of approximately 40 minutes after power-on from a cold state and examined for unwanted variations.

For a stable detector the counts y observed during repeated measurements under identical conditions are expected to follow a Poisson distribution. This was investigated with the detector exposed to a flat-field x-ray source. The MARS camera was left idle after power-on to reach a stable operating temperature. A set of 100 repeated measurements were then taken and the sample variance to mean ratio calculated. For a Poisson process, this dispersion index is expected to follow a reduced χ^2 distribution with $N-1$ degrees of freedom where N is the number of samples. That is:

$$\frac{s^2}{\bar{y}} \sim \frac{\chi^2_{N-1}}{N-1} \tag{5.1}$$

where s^2 and $\bar{y}$ are the sample variance and mean. The observed results for the variance to mean ratio were compared graphically with the reduced χ^2 distribution with $N-1$ degrees of freedom.

5.2.4 Temperature calibration

Medipix3 provides sensor outputs (band-gap-output and band-gap-temperature) for monitoring the on-chip temperature. A version of the MARS camera incorporating the Medipix3 within a sealed enclosure was used to investigate the properties of this on-chip temperature sensor. The camera was mounted within the MARS-CT cabinet and a Fluke Ti20 thermal imaging camera (Fluke Corporation, Everett, WA) used to record the effective temperature of the chip aperture periodically after power-on. The emissivity setting of the Fluke Ti20 was left at its default value of 0.98. At the same time, measurements of the `band-gap-output` (x_1) and `band-gap-temperature` (x_2) chip monitor outputs were recorded. Calibration of the net signal against effective temperature was done by linear regression:

$$T_{\text{eff}} = m\Delta x + c \tag{5.2}$$

where

T_{eff} = effective temperature in °C
$\Delta x = x_2 - x_1$
x_1 = `band-gap-output` level in mV
x_2 = `band-gap-temperature` level in mV.

5.2.5 Spectroscopy

The energy response of the MARS-Medipix3 camera system was calibrated using threshold scans of x-ray fluorescence spectra generated from indium and molybdenum samples placed within the 50 kVp x-ray beam. The spectroscopic responses in SPM and CSM were tested using a 1.7 GBq ^{241}Am sealed source placed directly in front of the chip aperture. Threshold scans were taken with the source inside its brass shielding container with the lid removed. The data were numerically differentiated to obtain the SPM and CSM spectra.

To qualitatively validate the spectroscopic imaging performance of the Medipix3, a small number n of spectral images were acquired of a high contrast test object (a USB flash disk) and a biological sample (a preserved mouse specimen injected with iodine and barium contrast media). The USB flash disk was imaged with four detector threshold settings ($n = 4$) at 50 kVp and the mouse specimen with two detector threshold settings ($n = 2$) at 80 kVp. The image data were used to form a set of spectroscopic vectors (one n-vector per pixel). The spectroscopic pixel data were analysed and categorized using a self-organizing map[3] (SOM). A colour was assigned to each pixel category and the corresponding pixels labelled accordingly to create an artificial colour-x-ray image. The image was examined to confirm that the pixels had been correctly clustered according to their expected spectroscopic properties.

5.3 Results

5.3.1 Threshold equalization

Figure 5.2 shows the counter threshold distributions and undifferentiated threshold scans of the intrinsic noise after equalization in SPM and CSM. After decreasing rapidly with increasing threshold to ∼20 DAC increments, the noise scan using the full pixel matrix diminished only slowly over the range from $\sim 20-100$ DAC increments. Masking the pixel matrix to remove those pixels with a counter threshold >12 DAC increments produced a more compact noise scan. The residual counter threshold dispersion was $\sigma \approx 3$ DAC increments ($\equiv$ 420 eV $\equiv$ 120 e^- at current settings). A similar pattern is observed after equalization in CSM except that the counter threshold distribution and noise scans were approximately twice as wide. The residual counter threshold dispersion in CSM was $\sigma \approx 6$ DAC increments ($\equiv$ 840 eV $\equiv$ 230 e^- at current settings).

The SPM flat field histogram (Figure 5.3) was approximately normally distributed and tightly clustered about the mean. However the CSM flat field histogram was widely dispersed and strongly skewed. These results are reflected in the test images of a USB flash disk (Figure 5.4(a) and (b)). The SPM test image shows little evidence of fixed pattern noise unlike the CSM test

---

[3] The self-organizing map [Kohonen, 1990], is an unsupervised learning algorithm which in this case was configured to categorize pixels according to their spectroscopic vectors.

image which is of poor quality and shows a high degree of bias towards certain pixels. The noise characteristics in SPM and CSM are quantified in the noise power spectra of the open beam test images (Figure 5.4(c)–(e)). The SPM and CSM spectra show a sharp increase at the highest frequency. Apart from this, the SPM noise power spectrum is flat, whereas that for CSM increases with increasing frequency.

5.3.2 Temporal stability

A number of DAC outputs showed evidence of unwanted variation (Figure 5.5). The outputs from the `Cas` and `FBK` DACs showed the most significant variation and this was greatest in the period immediately after power-on. In SPM the DAC outputs stabilized after a few minutes. In CSM although the rate of variation quickly reduced, the `Cas` and `FBK` output levels continued to change throughout the monitoring interval (∼40 minutes).

Figure 5.6 shows the dispersion index (variance/mean ratio) distribution for repeated measurements under identical conditions. For the series of SPM measurements the observed dispersion index distribution was in good agreement with the theoretical χ^2 distribution expected from Poisson counting statistics. However the dispersion index distribution for the CSM measurements was positively skewed with respect to that expected from a purely Poisson process.

5.3.3 Temperature calibration

Figure 5.7 shows the MARS camera within the MARS-CT scanner and a view of the chip aperture acquired with the thermal imaging camera. The thermal image taken approximately two hours after power-on clearly distinguishes the hotter chip aperture from the cooler body of the MARS camera and the surrounding environment. The linear calibration of the on-chip temperature sensor is given in Figure 5.8. There is a good correlation ($R^2 = 0.987$) between effective temperature and the net sensor output.

5.3.4 Spectroscopy

The SPM and CSM pulse height spectra for measurements of the ^{241}Am source placed directly in front of the chip aperture are shown in Figure 5.9. The main gamma emission at 60 keV and the x-ray fluorescence peaks generated in the brass shielding container are clearly visible in both SPM and CSM. The application of CSM improved the quality of the spectra by reducing the low energy continuum caused by charge-sharing effects.

The results of spectroscopic imaging of the USB flash disk and analysis by SOM are shown in Figure 5.10. Pixels corresponding to similar material types have been correctly clustered into similar categories. In particular, the solder material (containing Sn and Pb) is distinguished from the lighter copper of the electronic tracks and the plastic material used in the body of the device. Figure 5.11 shows the results of similar measurements and analysis of the mouse specimen. In this case, various biological tissues and artificial contrast media are correctly distinguished according to their spectroscopic properties.

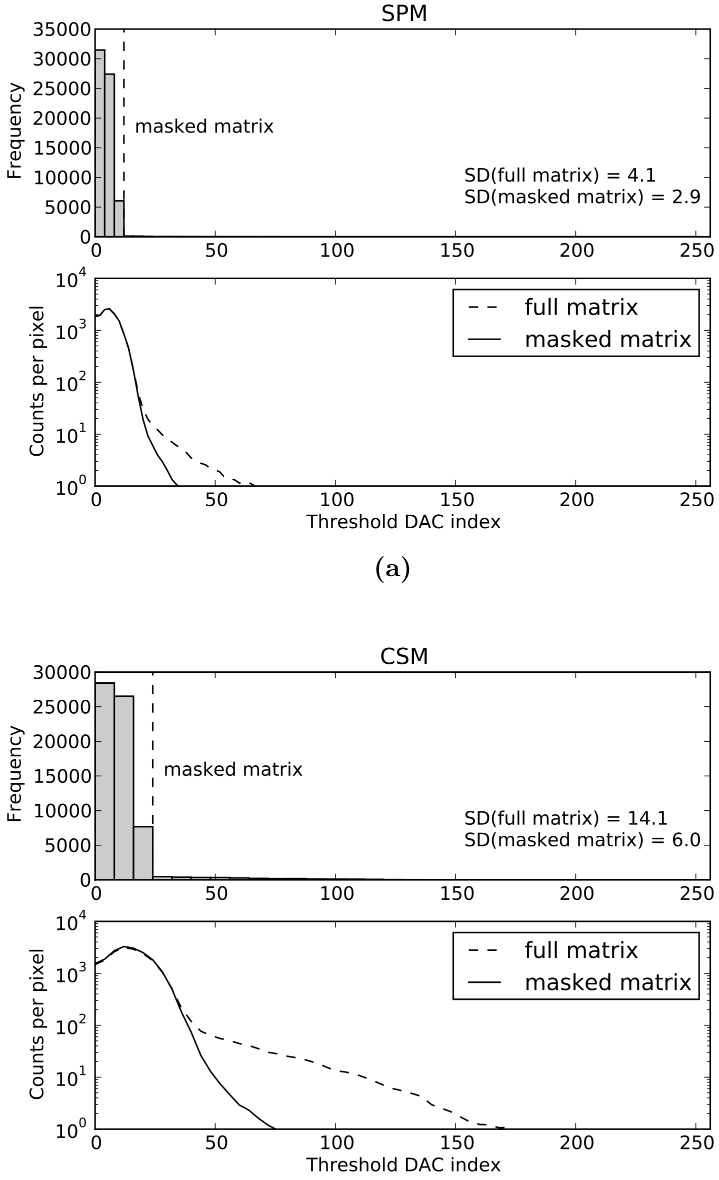

(a)

(b)

Figure 5.2: Counter threshold distributions and undifferentiated noise scans in (a) SPM and (b) CSM. In SPM, the threshold noise scan taken with the full pixel matrix is compared with that obtained when pixels with a threshold >12 DAC increments are masked (<1% of the total). In CSM, the full pixel matrix noise scan is compared with the scan obtained when pixels with a counter threshold >24 DAC increments are masked (<5% of the total).

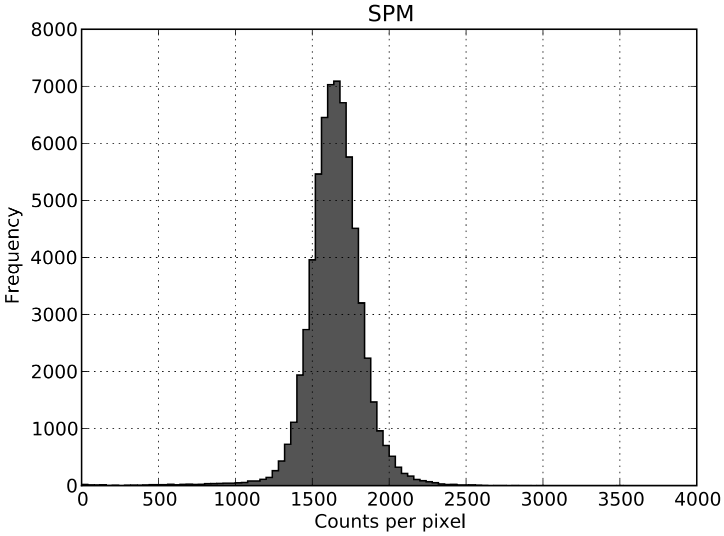

(a)

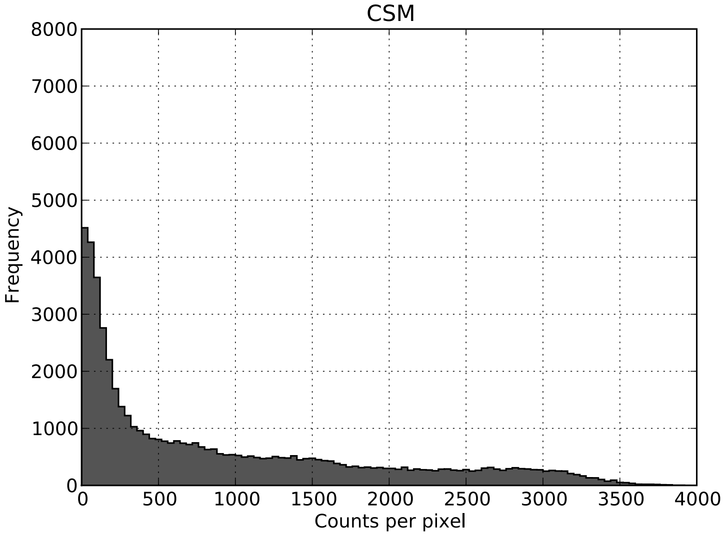

(b)

Figure 5.3: Flat field histograms showing the distributions of pixel counts measured in open beam after equalization in (a) SPM and (b) CSM. ($V = 50$ kVp; $E > 12$ keV.)

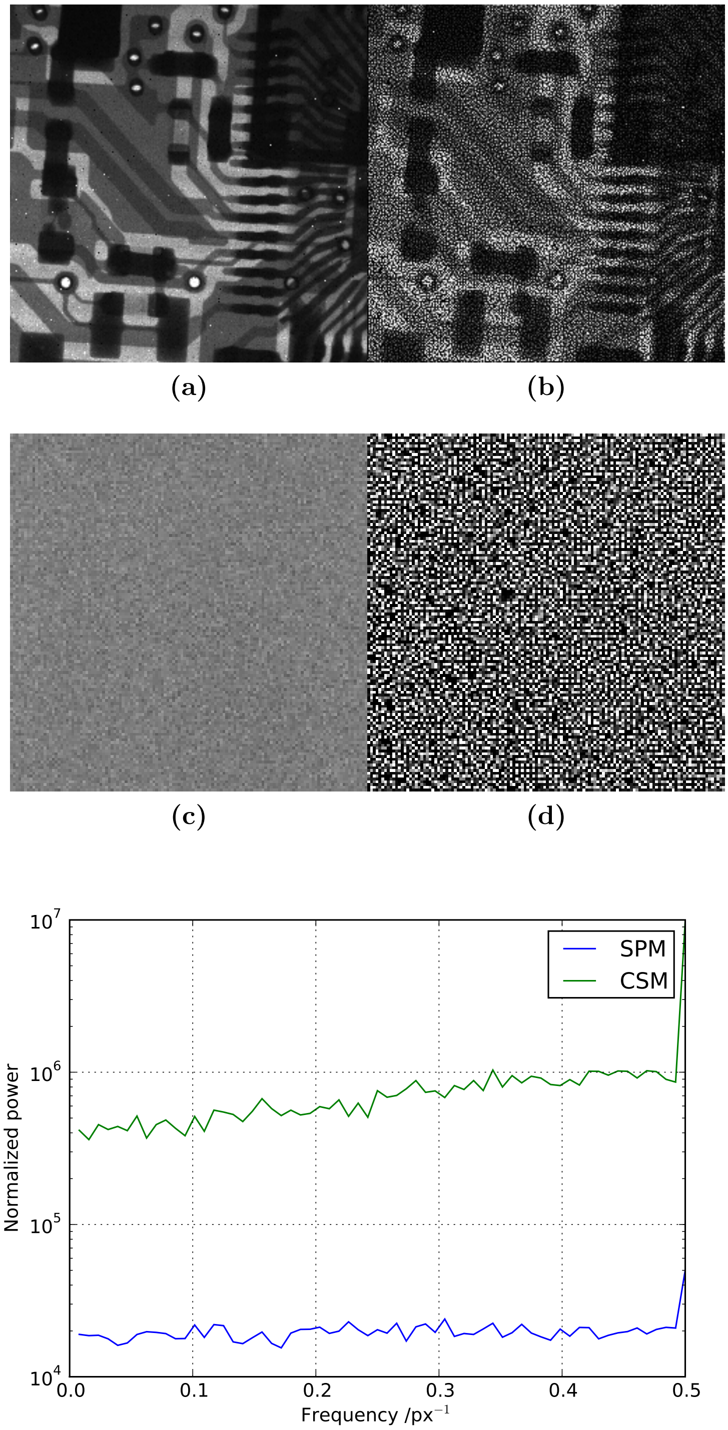

(a) (b)

(c) (d)

(e)

Figure 5.4: Test images of a USB flash disk in (a) SPM and (b) CSM. Open beam images in (c) SPM and (d) CSM and (e) the associated flat field noise power spectra. ($V = 50$ kVp; $E > 12$ keV.)

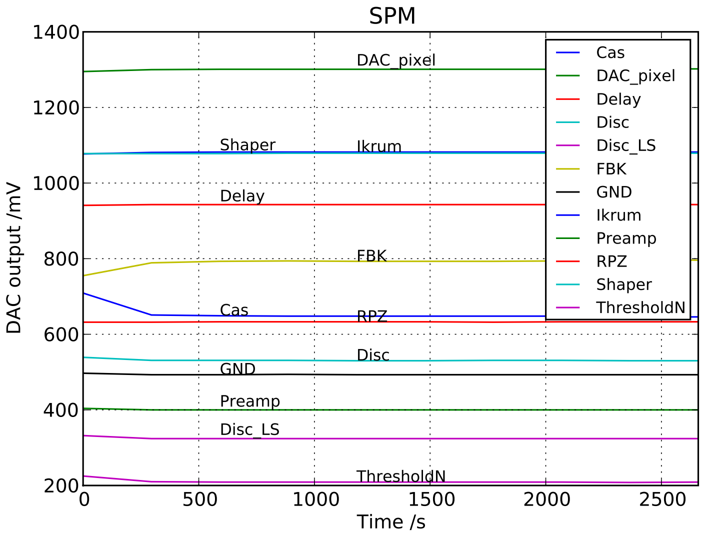

(a)

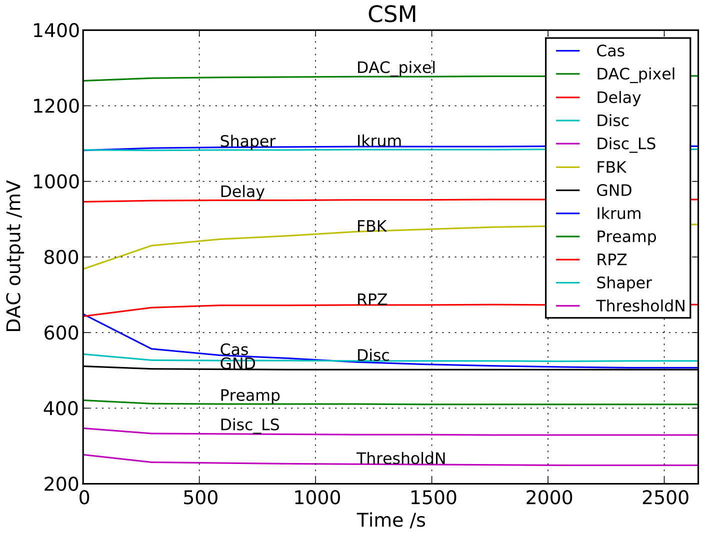

(b)

Figure 5.5: The DAC outputs of the Medipix3 in (a) SPM and (b) CSM recorded during continuous threshold scans of the intrinsic noise initiated immediately after power-on.

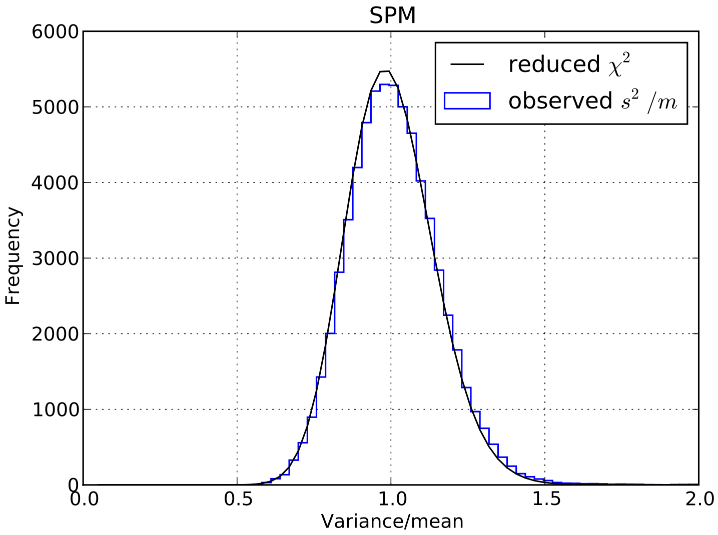

(a)

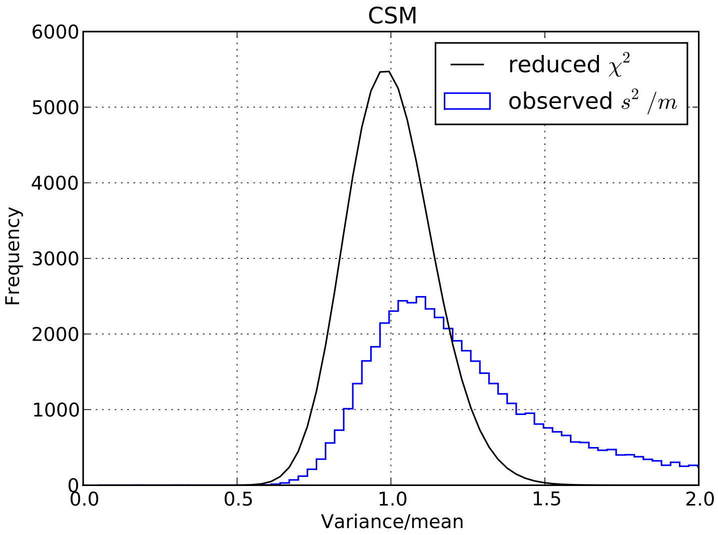

(b)

Figure 5.6: The dispersion index (variance/mean ratio) distribution calculated from 100 repeated measurements in (a) SPM and (b) CSM compared with the reduced χ^2 distributions expected from Poisson counting statistics. ($V = 50$ kVp; $E > 12$ keV.)

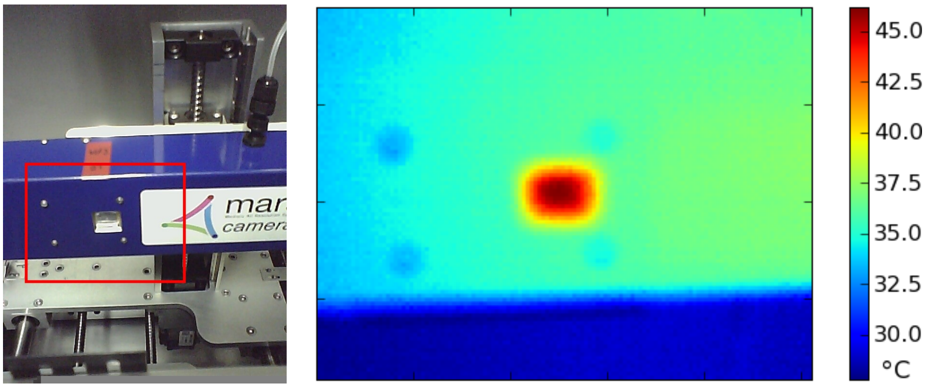

(a) **(b)**

Figure 5.7: The effective temperature of the chip aperture in the MARS camera (a) was measured with a Fluke Ti20 thermal imaging camera. The thermal image (b) was acquired after two hours of operation in CSM.

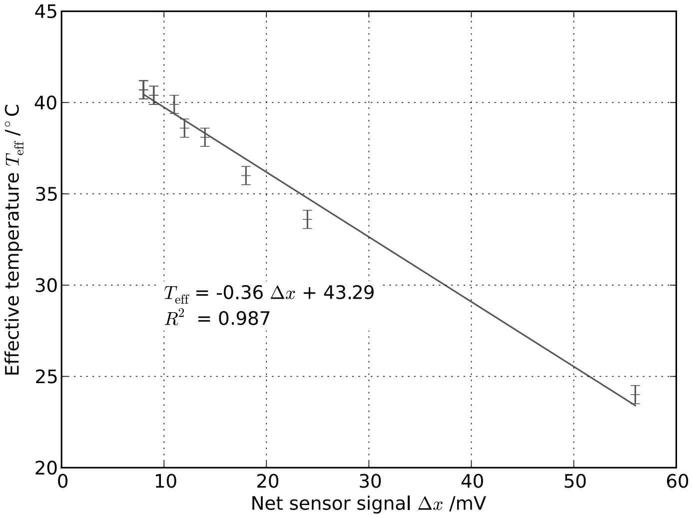

Figure 5.8: The effective temperature as a function of the net signal from the on-chip temperature sensor.

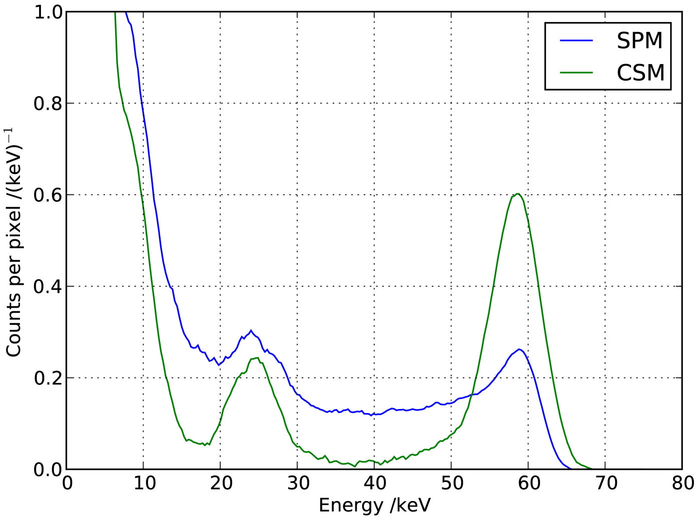

Figure 5.9: SPM and CSM spectra acquired from a 1.7 GBq ^{241}Am source. The main peak at 60 keV is clearly resolved in CSM. In SPM some of the peak contribution is redistributed into the continuum. The peaks at $\sim$25 keV are due to fluorescence x-rays generated within the brass shielding container.

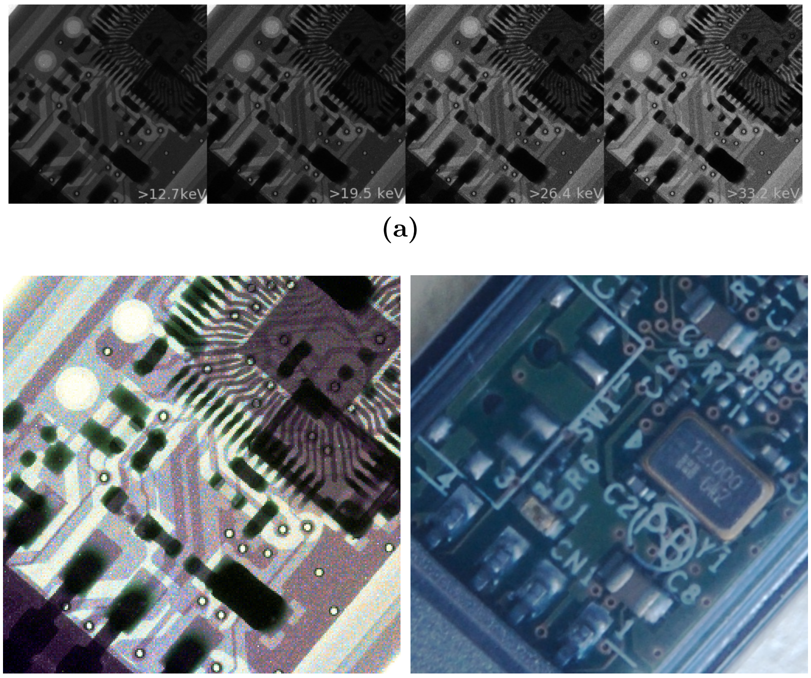

(a)

(b)

Figure 5.10: (a) A series of spectroscopic transmission images of a USB flash disk acquired with four different detector energy thresholds using a fixed x-ray tube voltage of 50 kVp. (b) An enhanced colour x-ray image derived from the individual spectroscopic images compared with a photograph of the USB flash disk. ($V = 50$ kVp; $E > 12.7, > 19.5, > 26.4, > 33.2$ keV.)

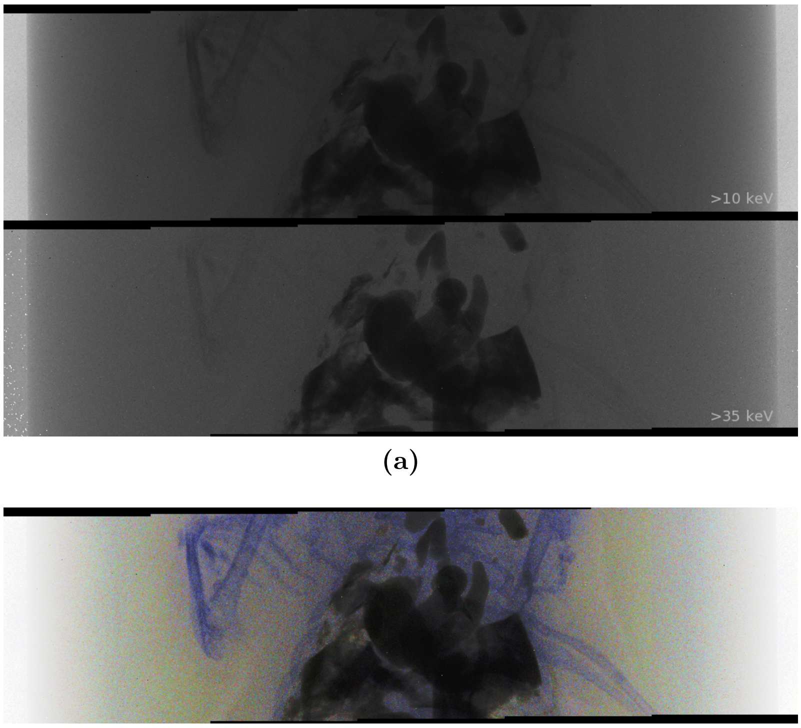

(a)

(b)

Figure 5.11: (a) Two spectroscopic transmission images of the abdominal region of a preserved mouse containing artificial contrast media and (b) an enhanced colour x-ray image derived from the same data. ($V = 80$ kVp; $E > 10, > 35$ keV.)

5.4 Discussion

The threshold equalization procedure employed for this work has enabled acceptable images to be acquired in SPM. The counter threshold distributions and integral noise scans were much improved after the equalization process. The resulting pixel count rate distribution, test images and noise power spectra for SPM were all acceptable and it is therefore likely that SPM can be used for x-ray imaging studies. However, imaging performance in CSM was poor. Although equalization improved the counter threshold distribution and integral noise scans, the resulting pixel count rate distribution, test images and noise power spectra all showed evidence of problems that would prevent high quality images from being obtained with this mode of operation. In particular, the pixel count rate distribution is widely dispersed and the test images have a highly granular appearance with neighbouring pixels showing grossly different sensitivities. This spatial correlation is reflected in the noise power spectrum which has a strong peak at the highest frequency.

For this work, acceptable performance in SPM was achieved by allowing sufficient time for stabilization within the data acquisition protocols. However, the failure of the CSM DAC output levels to stabilize within the monitoring interval, and the discrepancy between the observed and theoretical counting statistics, currently prevents the use of this mode for routine scanning operations. The analogue power consumption in CSM (15.45 μW per pixel) is higher than in SPM (8.25 μW per pixel) and the variation in DAC output levels may be related to the increased heat output. Considering the proposed MARS-CT scanner applications [Butler et al., 2008b, Walsh et al., 2011], the enclosed installation environment and high radiation fields in which the chip will operate may further exacerbate the heating effect. If cooling with ambient air is insufficient, then an alternative means of stabilizing the chip temperature such as Peltier cooling will be required.

The calibration of the on-chip temperature sensor was performed using an assumed thermal emissivity of 0.98. This value is a suitable default for many materials including the paint of the MARS camera body and the plastic cover on the chip aperture. However, the true emissivity of the chip aperture is unknown and the calibration has therefore been given in terms of *effective* temperature. Nevertheless, there is a good correlation between the on-chip temperature sensor and the effective thermal imaging temperature and it is therefore concluded that the on-chip temperature sensor is suitable for (i) monitoring the condition of the chip and (ii) providing feedback to some future method of temperature stabilization.

The global energy resolution of the detector is a function of quantum counting effects, random electronic noise and systematic effects such as residual counter threshold dispersion. In room temperature silicon, the contribution of quantum counting effects is relatively minor and random electronic noise and counter threshold dispersion are expected to dominate. After equalization, the counter threshold dispersion is fixed at the pixel level. In CSM four single-pixel channels are summed to provide each output. The counter threshold dispersion and electronic noise distributions add in quadrature giving a total CSM pulse height distribution that is approximately twice the width of that in SPM. Our measured value for residual counter threshold dispersion ($\sigma \simeq 840$ eV) implies a lower limit on the achievable CSM energy resolution of FWHM $\gtrsim 2$ keV.

The SPM spectroscopic imaging results successfully demonstrate the use of the chip for biological materials discrimination. The mouse sample was scanned sequentially using only two distinct energy thresholds but it was nevertheless possible to distinguish various material types using the spectroscopic information.

5.5 Summary and conclusions

1. The performance of the MARS-Medipix3 camera combination has been

characterized and, with some limitations, shown to be acceptable for x-ray imaging. After applying the counter threshold equalization procedure, the Medipix3 acquires visually acceptable images in SPM. However, acceptable images were not obtained in CSM. In CSM, the pixel count rate distribution was widely dispersed and the images had a granular appearance.

2. Single pixel mode gave acceptable performance in terms of energy response, image quality and stability over time. Following a warm up period to allow the global DAC outputs to stabilize, SPM performance was stable and the count rate distribution was approximately Poissonian. In charge summing mode, the DAC outputs were not stable and count rate variations were excessive.

3. Spectroscopic performance was successfully demonstrated in both SPM and CSM. Although the use of CSM impaired imaging performance, CSM improved spectroscopic performance by reducing the charge sharing continuum. Spectroscopic imaging performance was demonstrated in SPM using a USB flash disk and a preserved mouse as test objects. Material types were correctly categorized by their spectroscopic properties.

4. Although the warm up protocol produced satisfactory SPM results in this case, more robust methods of control, such as Peltier cooling, may be required for future applications. The on-chip temperature sensor may be used to provide monitoring or feedback for future temperature stabilization methods.

Chapter 6

Calibrating a Medipix3 array

This chapter describes the global DAC calibration, pixel threshold equalization and energy calibration protocols developed to configure and operate the Medipix3 array as a single large-area detector unit. The results are evaluated in terms of flat field image quality. The experimental work was done in collaboration with Rafidah Zainon in support of later research into material decomposition and the characterization of atherosclerotic plaques [Zainon et al., 2012].

6.1 Introduction

A single Medipix3 chip has a sensor layer with total sensitive area of (14.02×14.02) mm^2 [Ballabriga et al., 2006, Ballabriga et al., 2010] which in fine pitch mode is subdivided into 256×256 pixels. This is a rather small detecting area for many applications, however, the Medipix3 chip can be tiled on 3 sides to form a $2 \times n$ array. The quad Medipix3 is a 2×2 array formed from a single silicon layer bump bonded to four Medipix3 ASICs. Each Medipix3 ASIC is separated from its neighbours by approximately 100 μm.

The MARS camera [Doesburg et al., 2009] can accommodate Medipix3 chip arrays up to 2×3. The camera provides a common power supply for the chip array and an Ethernet interface for data transfer and communication. The Ethernet interface enables the global DACs and threshold equalization masks for each chip to be addressed and configured independently. A MARS camera fitted with a quad Medipix3 array, 300 μm silicon sensor layer and Peltier cooling system was obtained for testing and calibration prior to use within the MARS-CT system.

The performance of each pixel within a chip and of each chip within an array are subject to the effects of manufacturing variations. To obtain high quality images from each chip within the array it is necessary to calibrate and adjust each chip so that all pixel counters respond to the same minimum x-ray energy. To use the quad detector array effectively as a single unit, it is necessary to calibrate the spectroscopic response of each equalized chip so that the global threshold DAC indices corresponding to any desired energy level can be determined.

The Medipix3 is configured at the chip-level using 25 global DACs (see Table A.1) and at the pixel level using 13-bits of a 24-bit control register (see Table A.2). Each Medipix3 pixel has two counters. The discriminator threshold for each counter is programmable at the chip level by means of a global DAC. Due to manufacturing variations, the intrinsic level of the counter thresholds are widely distributed and thus the responses of the individual pixels to a uniform flux are not consistent across the chip. Before acceptable images can be acquired it is necessary to equalize the counter thresholds so that each pixel counter responds in a similar manner to a given x-ray flux. Two global current sources and a 5-bit pixel level adjustment are available for this purpose. Discriminator threshold equalization is achieved using a combination of global and pixel DAC adjustments.

After equalization, the relative spectroscopic responses of the individual chips can be measured using threshold scans of the open beam x-ray. The response of each chip can then be matched in software by re-mapping the threshold DAC indices. The absolute energy calibration for any single chip can be obtained by measurement of fluorescence x-rays generated from thin foils placed within the beam. The energy calibration coefficients for the remaining chips can then be calculated indirectly using the open beam threshold DAC mapping functions.

A properly configured and calibrated Medipix3 array should respond to any given x-ray source as a cohesive unit with only minimal intra- and inter-chip variations. It is proposed that, this combination of DAC adjustments and calibration operations will allow the quad Medipix assembly to be used as an integrated detector array within systems such as the MARS-CT scanner.

6.2 Materials and methods

6.2.1 Equipment

The MARS camera used for this work (Figure 6.1) included a quad Medipix3 detector bump-bonded to a 300 μm silicon sensor layer and configured in 55 μm fine-pitch mode. The MARS camera included a fan-assisted Peltier cooling system to stabilize the chip temperature. The MARS camera was controlled by the locally developed `libMars` C library and Python interface (Appendix C). For all measurements the Medipix3 was operated in single-pixel mode.

The x-ray source from a MARS-CT scanner was used to illuminate the camera during testing. The Source-Ray SB-80-1K x-ray tube (Source-Ray Inc, Ronkonkoma, NY) had a tungsten anode and included 1.8 mm of aluminium (equivalent) intrinsic filtration. The focal spot size was 33 μm and the maximum tube current and accelerating voltage were 1 mA and 80 kVp respectively.

The method for calibrating the chip array is given in three sections. Firstly, the DAC calibration procedure aims to find optimum values for ThresholdN and DACpixel so that the distribution of counter thresholds may be adjusted with

Figure 6.1: The MARS camera with quad Medipix3 detector and fan-assisted Peltier cooling system.

the maximum available resolution. Secondly, the equalization procedure aims to find the threshold adjustment configuration that minimizes the variation in counter thresholds so that all pixels respond in a similar manner to a given x-ray flux. Finally, the objective of the energy calibration protocol is to find a suitable set of linear calibration and threshold DAC mapping functions that enable the Medipix3 array to be operated as a single spectroscopic detector.

6.2.2 Setting the Global DACs

The Medipix3 has 25 global DACs (Table A.1). A number are used for testing purposes, some are not relevant to the current operating mode, and some are only set at measurement time. The remaining 12 DACs are used to bias and configure the pulse processing electronics. Half of these were set directly using their nominal index values. The GND FBK and Cas DACs were set by monitoring their voltage outputs using the ADC functions within the MARS camera. The ThresholdN and DACpixel DACs that supply the threshold adjustment currents were set by calibration against the distribution of counter thresholds. The RPZ DAC that controls the return to baseline characteristics was also set to its nominal value as the count rate per pixel was modest and further adjustment of RPZ was not necessary.

Two global current sources (one positive and one negative) and 5 adjustment bits per pixel counter are available for threshold adjustment. The negative current source is set by ThresholdN and may be applied at the pixel-level to any counter threshold using a switch selected by one of the 5 adjustment bits. The positive current source is set by DACpixel and some fraction ($\frac{0}{15} \cdots \frac{15}{15}$) of this may be applied to each counter threshold using the remaining 4 adjustment bits.

The collection of adjustment bits for the two available counters are known as `THA` (counter 0) and `THB` (counter 1). Only counter 0 was used during this work. The adjustment bits may be subdivided into `THN` and `THP` responsible for the negative and positive current adjustments respectively. The most significant `THA` bit controls the application of the negative current and the remaining four bits control the application of the positive current. That is:

$$\text{All adjustment bits: } \texttt{THA} = \texttt{THN} \text{ OR } \texttt{THP} \tag{6.1}$$

$$\text{Negative adjustment bit: } \texttt{THN} = \texttt{THA} \text{ AND } \texttt{10000} \tag{6.2}$$

$$\text{Positive adjustment bits: } \texttt{THP} = \texttt{THA} \text{ AND } \texttt{01111} \tag{6.3}$$

Setting **ThresholdN** and **DACpixel**

The values of the ThresholdN and DACpixel DACs should be just sufficient to allow the vast majority of counter thresholds to be adjusted to a common level. This was done by measuring the initial distribution of unadjusted threshold positions and the effect of each global current source on the location of the distribution. Application of each global current source to the counter thresholds was controlled by setting the relevant `THA` adjustment bits. The global DAC calibration procedure was as follows:

1. Reset the Medipix3 DACs to their nominal values. (See table A.1.)

2. Initialize the threshold equalization mask so that all pixels are counting (in high gain mode).

3. For `THA` in the list [`00000`, `10000`, `11000`]:

   (a) Set the threshold equalization mask `THA` value for all pixels.

   (b) Perform a threshold scan for 50 ms per Threshold0 setting over the range 0 to 511.

   (c) Locate the counter threshold for each pixel[1] and record the counter threshold distribution for the chip as a whole.

4. Compute the effect of `THN` and `THP` on the distribution of counter thresholds.

5. Compute the optimum values for ThresholdN and DACpixel.

The optimum values for the ThresholdN and DACpixel DACs are computed from the width of the original counter threshold distribution and the observed effects of the global current sources on the location of that distribution. The ThresholdN and DACpixel DACs translate the distribution of counter thresholds in the positive and negative directions respectively.

The changes in applied ΔThresholdN and ΔDACpixel global threshold adjustment currents are proportional to the relative value of the change in applied pixel adjustment:

$$\Delta\mathsf{ThresholdN} = \frac{\Delta\mathtt{THN}}{1} \times \mathsf{ThresholdN} \tag{6.4}$$

$$\Delta\mathsf{DACpixel} = \frac{\Delta\mathtt{THP}}{15} \times \mathsf{DACpixel} \tag{6.5}$$

and the corresponding displacements $\Delta X_{\mathtt{THN}}$ and $\Delta X_{\mathtt{THP}}$ were calculated from the observed changes in the location of the counter threshold distribution.

---

[1] The location of the counter threshold corresponds to that Threshold0 setting that returns the maximum count from a scan of the intrinsic noise.

The ratios $\frac{\Delta X_{\text{THN}}}{\Delta \mathsf{ThresholdN}}$ and $\frac{\Delta X_{\text{THP}}}{\Delta \mathsf{DACpixel}}$ are thus displacement coefficients giving the change in counter threshold distribution location per unit global current.

The intrinsic variation in counter thresholds that we wish to include within the range of threshold adjustments may be characterized by some counter threshold distribution width w. In this work the width w was set such that 99% of the counter threshold distribution was expected to be within the interval $x_0 \pm w$:

$$\mathrm{P}[x_0 - w < X < x_0 + w] \approx 0.99 \tag{6.6}$$

The optimum settings for **ThresholdN** and **DACpixel** were then calculated from the desired adjustment range w and reciprocal displacement coefficients:

$$\mathsf{ThresholdN} = w \frac{\Delta \mathsf{ThresholdN}}{\Delta X_{\text{THN}}} \tag{6.7}$$

$$\mathsf{DACpixel} = w \frac{\Delta \mathsf{DACpixel}}{\Delta X_{\text{THP}}} \tag{6.8}$$

6.2.3 Threshold equalization

The threshold equalization procedure aims to find the threshold adjustment configuration that minimizes the variation in pixel responses across the chip. An initial equalization procedure was performed using the intrinsic noise of the chip. The threshold adjustment was then refined using threshold scans of an open beam x-ray source. Ideally, after equalization, all pixels are expected to respond in a similar manner to a flat field x-ray flux. The effectiveness of the equalization was determined by inspection of the open beam threshold scans and by quantification of the flat field image inter-quartile range (IQR).

Threshold adjustment using intrinsic noise

Initial threshold adjustment was carried out using the intrinsic electronic noise of the chip using the following procedure:

1. Reset the Medipix3 DACs to their nominal values. Set the values for ThresholdN and DACpixel to their calibrated values.
2. Set the threshold equalization adjustment bits to `THA` = `10000` for all pixels.
3. For each `THA` bit from MSB to LSB:
    - (a) Toggle the `THA` bit for all pixels.
    - (b) Perform a threshold scan for 50 ms per Threshold0 setting over the range 0 to 511.
    - (c) Locate the counter threshold for each pixel[1] and discard the bit change if the counter threshold is less than a nominal target DAC value ($\gtrsim 0$).
4. Finally, identify and switch off any remaining *bad pixels*[2].

The process is illustrated in Figure 6.2. The resulting configuration mask is intended to adjust all counter thresholds to some value just above a nominal target DAC value (set just greater than zero). The effectiveness of the procedure was determined by plotting the distribution of counter thresholds after equalization and the distribution of flat field responses at a mid-range threshold value equivalent to approximately 20 keV.

Threshold adjustment using an x-ray source

The equalization procedure using an external x-ray source was applied after the noise-based procedure above. In outline, the process was similar to the noise-based procedure except that: the chip was placed in a spatially homogeneous open beam x-ray flux prior to equalization; a target response curve (counts vs. Threshold0 DAC) was determined from the median pixel response observed

---

[2] A bad pixel is defined here as one with an outlier open beam count rate, dark-field count rate, or counter thresholdvalue.

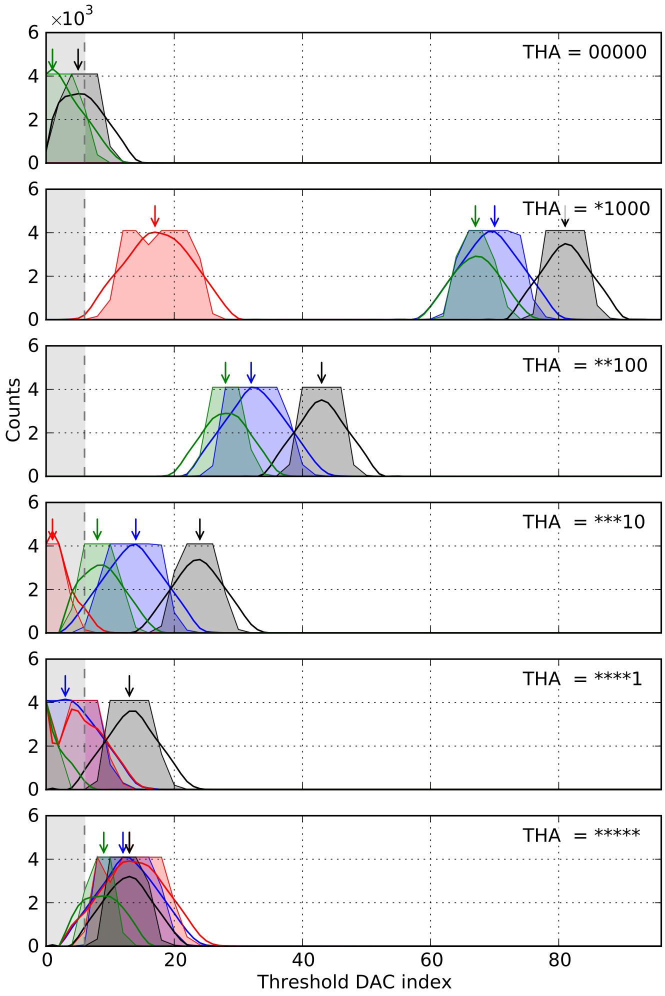

Figure 6.2: The effect of the noise-based equalization procedure on the threshold scans of four selected pixels. The raw threshold scans are shown as filled plots. Also shown is the smoothed data used to determine the counter threshold (marked with an arrow). From top to bottom, the effect of each `THA` bit from MSB to LSB was tested in turn. If the counter threshold was below the target value (grey region) then the bit change for that pixel counter was discarded, otherwise it was retained before the next bit was tested. The first panel (`THA` = 00000) shows the test of the first (most significant) bit. The final panel (`THA` = *****) shows the noise scans using the completed mask.

after performing an initial threshold scan in the open beam x-ray flux; and each adjustment bit setting was rejected or accepted according to whether or not the correlation between each pixel response curve and the target response curve increased or decreased. In full, the procedure is:

1. Place the chip in a spatially homogeneous x-ray flux.
2. Reset the Medipix3 DACs to their nominal values. Set the values for ThresholdN and DACpixel to their calibrated values.
3. Set the threshold equalization adjustment bits according to the noise equalization performed above.
4. Perform a threshold scan for 500 ms per Threshold0 setting over the range 0 to 511. Determine the target response curve as the median response over all pixels. For all pixels, calculate the correlation coefficient between observed and target response curves.
5. For each `THA` bit from MSB to LSB:
    (a) Toggle the `THA` bit for all pixels.
    (b) Perform a threshold scan for 500 ms per Threshold0 setting over the range 0 to 511.
    (c) For all pixels calculate the correlation coefficient between observed and target response curves. Accept the bit change if the correlation coefficient improves, otherwise reject it.
6. Finally, identify and switch off any remaining *bad pixels*[2].

The resulting configuration mask is intended to maximize the correlations between the individual pixel response curves and the target (median) response curve. Because the procedure acts on a wide range of threshold values, the overall pixel count rate variations at typical threshold values are expected to be less than those obtained after equalization using just the intrinsic noise. The effectiveness of the open beam equalization procedure was determined by plotting the pixel response curves and the distributions of flat field values at a mid-range threshold value ($\equiv 20$ keV).

6.2.4 Energy calibration

The energy calibration was performed in two stages. One of the chips was selected as a reference and this was calibrated directly. The other chips were calibrated indirectly by mapping their open beam responses to match that of the reference chip.

Direct calibration

A direct calibration for the reference chip was obtained by measuring the fluorescence x-rays generated from molybdenum and indium metal foils placed within the open beam. In each case a threshold scan was performed and numerically differentiated to obtain the x-ray spectrum. The threshold locations of the molybdenum and indium K_α lines at 17.5 keV and 24.2 keV were determined. The intrinsic noise was also measured by performing a threshold scan under dark field conditions to obtain a third point ($E = 0$ keV) for the linear energy calibration.

Indirect calibration

Given the energy calibration for the reference chip, the other chips of the array were indirectly calibrated by mapping their open beam responses onto that of the reference chip. In each case an undifferentiated threshold scan was performed in open beam. The coefficients of a linear mapping function were obtained by minimizing the relative difference between the mapped response

$\mathbf{y_i'}$ of each chip and that of the reference chip $\mathbf{y_0}$. That is:

$$\text{Minimize: } \chi_i^2 = |\ln(\mathbf{y_i'}) - \ln(\mathbf{y_0})|_{x_\mathrm{L}}^{x_\mathrm{U}} \tag{6.9}$$

where: $y' = y(x') = y(a_0 + a_1 x)$ is the mapped response and χ^2 is evaluated over a suitable working range which in this case was taken to be $x_\mathrm{L} = 40$, $x_\mathrm{U} = 160$. The indirect energy calibration for each chip is then given by substituting the result of the direct energy calibration into the linear mapping x' for each chip in turn:

$$x = A_0 + A_1 E \tag{6.10}$$

$$x' = A_0 a_1 + a_0 + A_1 a_1 E \tag{6.11}$$

6.3 Results

6.3.1 Global DAC calibration

The effect of ThresholdN and DACpixel currents applied via the THN and THP adjustment mask bits on the distribution of counter thresholds for chip0 is shown in Figure 6.3. The optimum values for ThresholdN and DACpixel for chip0 are estimated to be 44 and 98 respectively. The calibration results for all four chips are given in Table 6.1.

With one exception, the index value results for the chips were similar. Although the DACpixel index value for chip3 was much less than those obtained for the other chips, the voltage output level of DACpixel for chip3 was consistent with those of the other chips and thus the discrepancy in index value may be due to some manufacturing variation rather than a problem with the calibration procedure.

Table 6.1: The calibrated DAC index values and corresponding output voltage levels for ThresholdN and DACpixel.

Chip number	ThresholdN	DACpixel
0	44 (222 mV)	98 (1163 mV)
1	42 (210 mV)	100 (1164 mV)
2	40 (216 mV)	120 (1172 mV)
3	38 (215 mV)	61 (1166 mV)

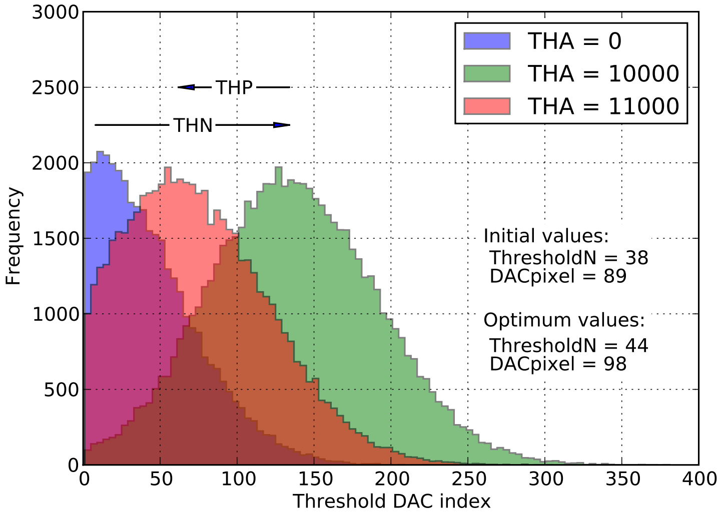

Figure 6.3: The effect of ThresholdN and DACpixel applied via the THN and THP adjustment mask bits on the distribution of counter thresholds for chip0. (Bin width = 2 DAC index values.)

6.3.2 Threshold equalization

Threshold adjustment using intrinsic noise

The distribution of counter thresholds before and after equalization using the intrinsic electronic noise is shown in Figure 6.4. After equalization, the counter thresholds are tightly clustered around a DAC target value just above zero. The flat field histograms and images acquired after equalization with the intrinsic electronic noise are shown in Figure 6.5. The pixel response IQR for the four chips ranges from 8.7% to 9.9%. The global IQR is 10.7%.

The count rate distributions for three of the four chips are similar, however the location of the distribution for `chip2` is shifted to higher values. The reason for this is unknown but the magnitude of the effect ($\sim$ 10%) is not excessive and may be within the expected range of manufacturing variations.

Threshold adjustment using an x-ray source

The open beam x-ray spectra acquired before and after equalization with an open beam x-ray source are shown in Figure 6.6. As a result of the correlation-based criterion for adjusting the bits of the threshold mask, the spectra acquired after equalization with the x-ray source show less dispersion than those acquired after equalization using only the noise-based approach.

The flat field histograms and images acquired after equalization with an open beam x-ray source are shown in Figure 6.7. The pixel response IQR for the four chips ranges from 7.0% to 7.8%. The global IQR is 9.7%. That is, the intra-chip responses are improved compared with the results after noise-based equalization but there is little change in the inter-chip variation.

6.3.3 Energy calibration

The differential spectra taken with the molybdenum and indium foils within the x-ray beam measured in SPM are shown in Figure 6.8. In both cases the

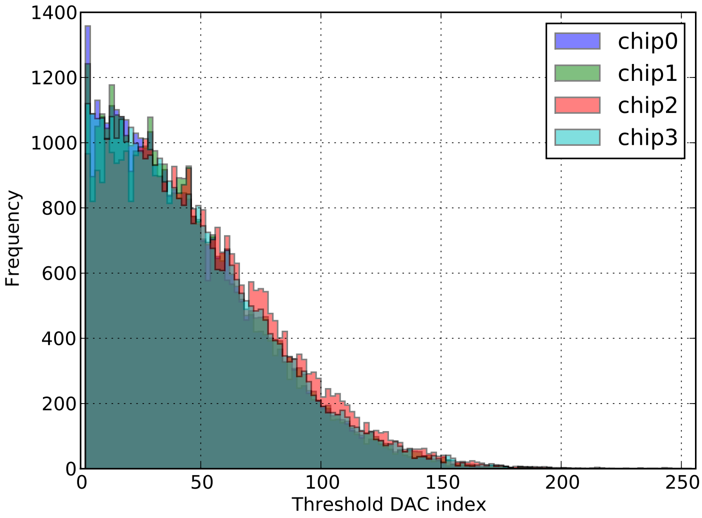

(a)

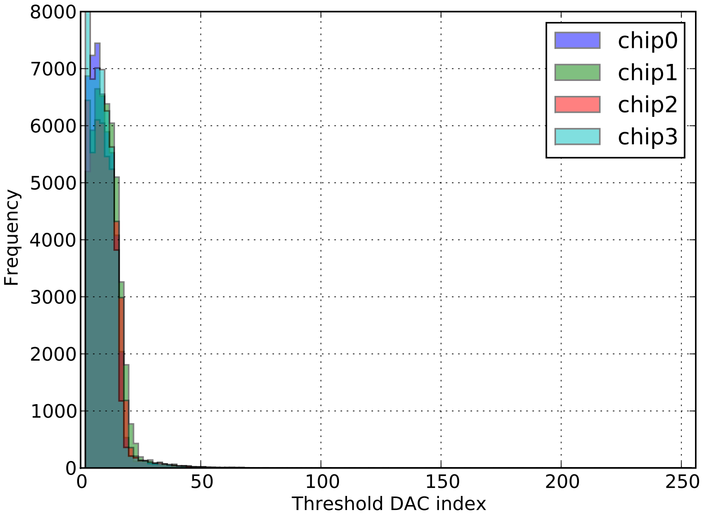

(b)

Figure 6.4: The distribution of counter thresholds (a) before and (b) after equalization using the intrinsic electronic noise. (Bin width = 2 DAC index values.)

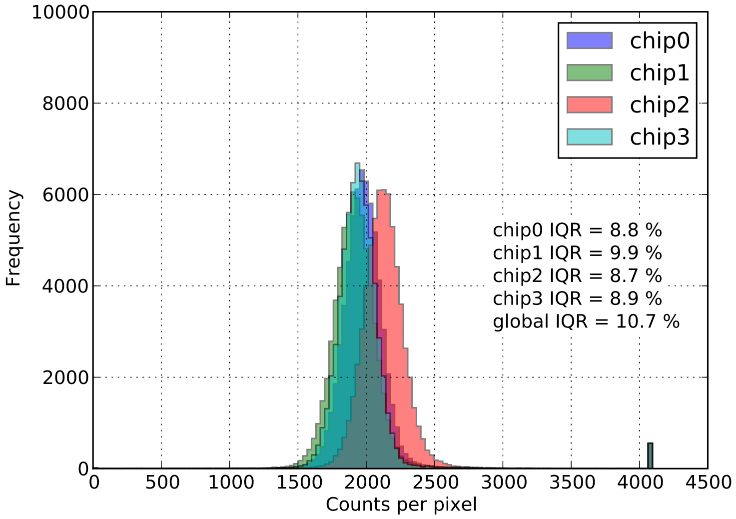

(a)

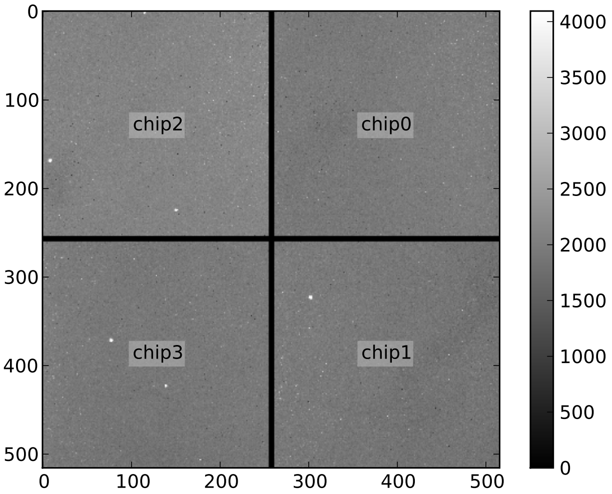

(b)

Figure 6.5: Flat field histograms (a) and images (b) measured with the quad silicon Medipix3 acquired in SPM after equalization using the electronic noise. ($V =$ 50 kVp.)

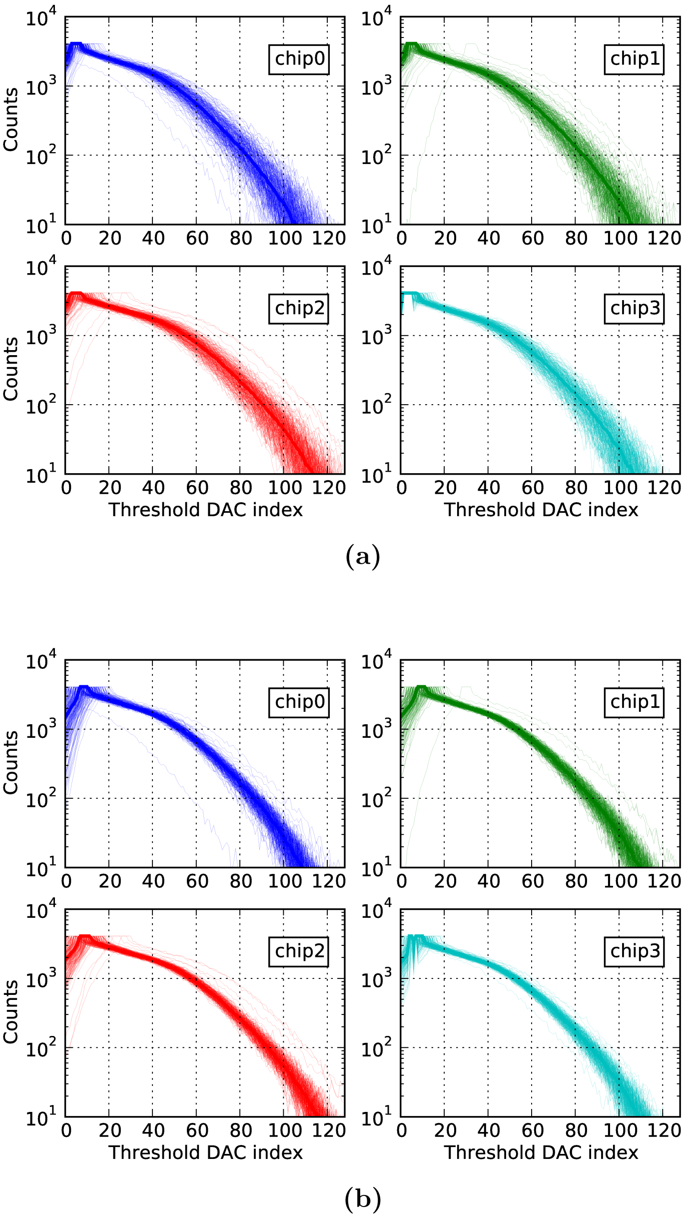

Figure 6.6: Open beam x-ray spectra from 252 pixels within a single row acquired (a) before and (b) after equalization with x-rays. (V = 50kVp.)

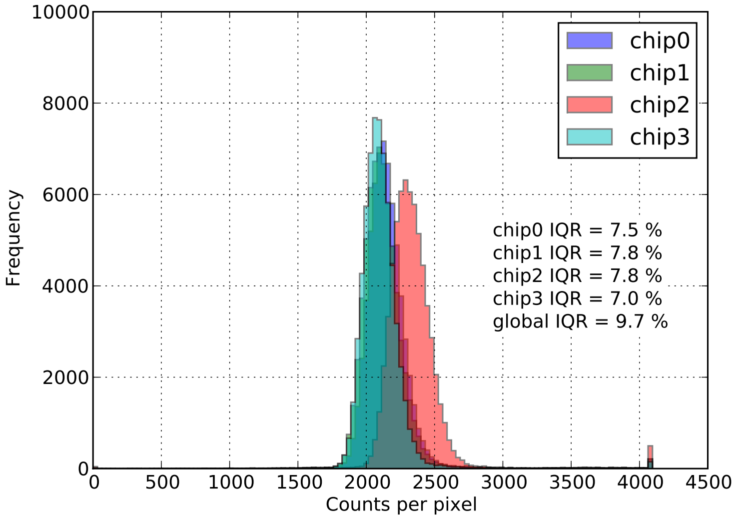

(a)

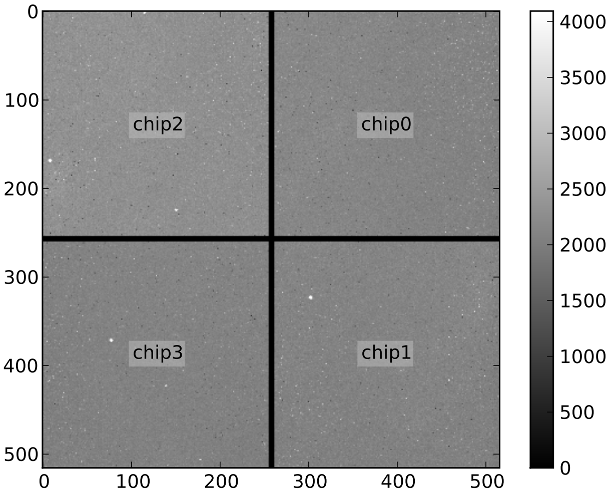

(b)

Figure 6.7: Flat field histograms (a) and images (b) measured with the quad silicon Medipix3 acquired in SPM after equalization using the open beam x-ray source. ($V = 50$ kVp.)

responses of three of the four chips are similar but that of chip2 is shifted to higher DAC index values.

The linear mappings for DAC index ($X \mapsto X'$) and energy calibrations for each chip are shown in Figure 6.9. The observed energy calibrations are approximately linear for all chips. The linear mappings matching X for each chip with chip0 were:

$$X' = 1.000X + 0.0 \tag{6.12}$$

$$X' = 1.030X - 1.2 \tag{6.13}$$

$$X' = 1.071X + 4.1 \tag{6.14}$$

$$X' = 1.027X - 3.1 \tag{6.15}$$

The direct energy calibration for chip0 and the corresponding indirect calibrations for the other chips were:

$$X' = 4.64E/\text{keV} + 16.2 \tag{6.16}$$

$$X' = 4.78E/\text{keV} + 15.5 \tag{6.17}$$

$$X' = 4.97E/\text{keV} + 21.5 \tag{6.18}$$

$$X' = 4.76E/\text{keV} + 13.5 \tag{6.19}$$

The flat field histograms and images obtained after the full equalization and calibration procedure are shown in Figure 6.10. After all adjustments and corrections, the pixel count rate IQR for the four chips ranges from 7.0% to 7.6%. The global IQR taken over all pixels in the chip array is 7.3%.

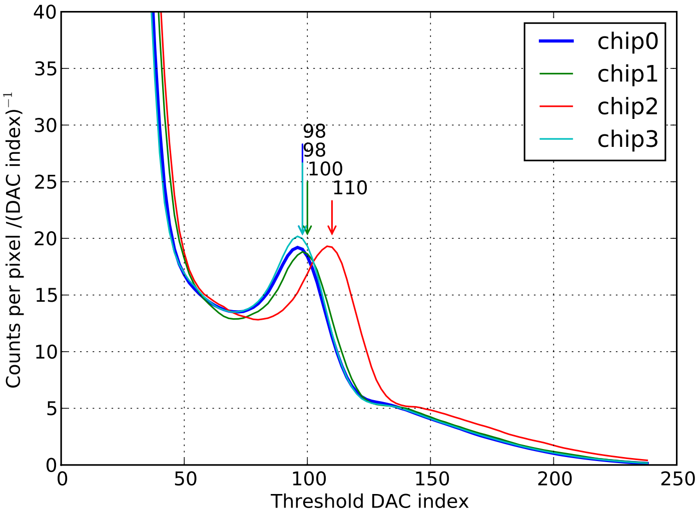

(a)

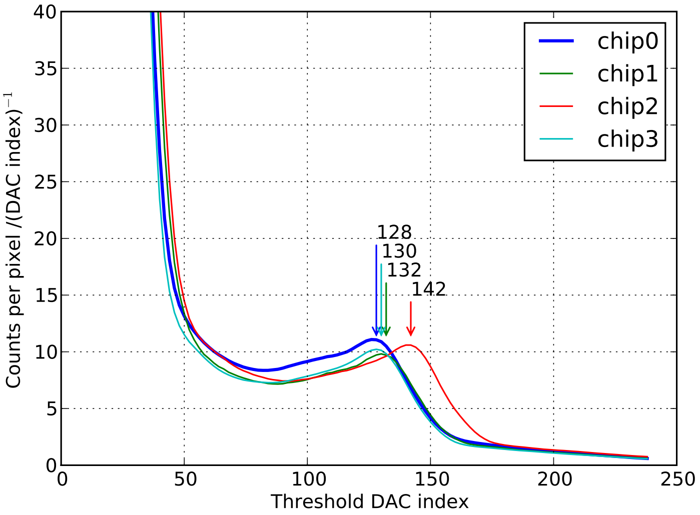

(b)

Figure 6.8: Differential spectra measured with the quad silicon Medipix3 in SPM from (a) molybdenum and (b) indium metal foils placed within the open beam. The K_α lines from indium and molybdenum are at 17.5 keV and 24.2 keV respectively. ($V = 50$ kVp.)

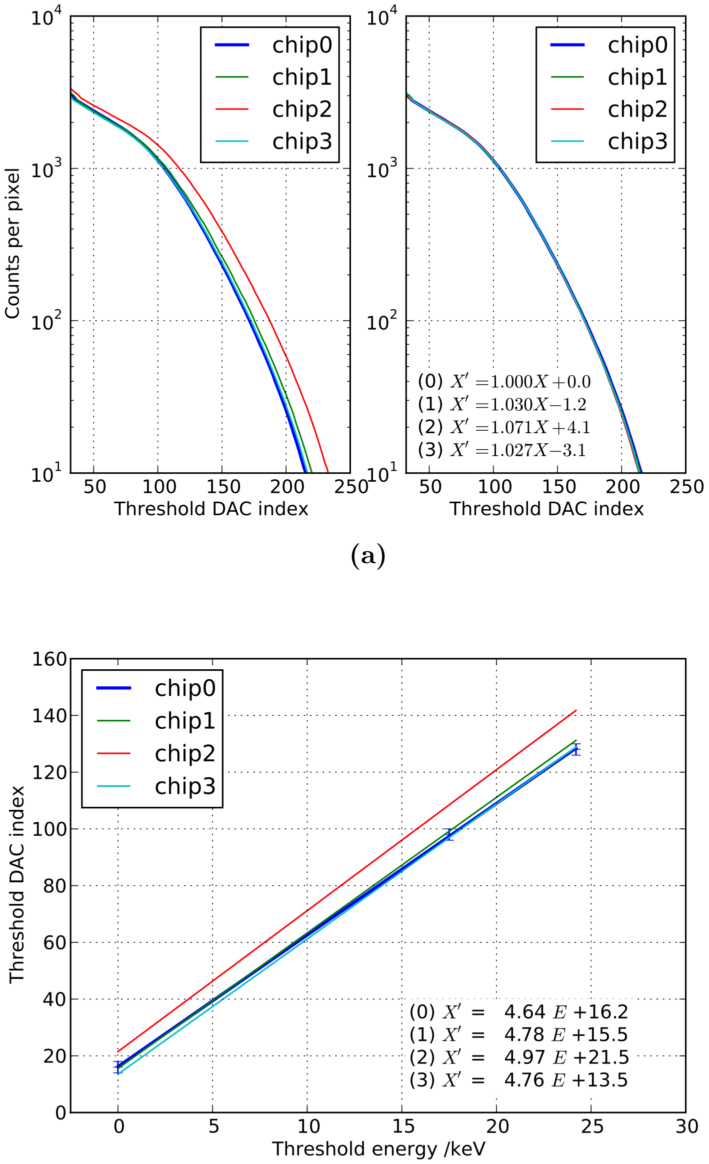

(a)

(b)

Figure 6.9: (a) Linear threshold maps obtained by matching the responses of the four chips in open beam. The unmapped responses are shown on the left and the matched responses after mapping are shown on the right. (V = 50 kVp.) (b) A linear calibration for `chip0` threshold DAC index in terms of photon energy E. Also given are indirect calibrations for the other chips obtained by combining the linear threshold maps with the energy calibration for `chip0`.

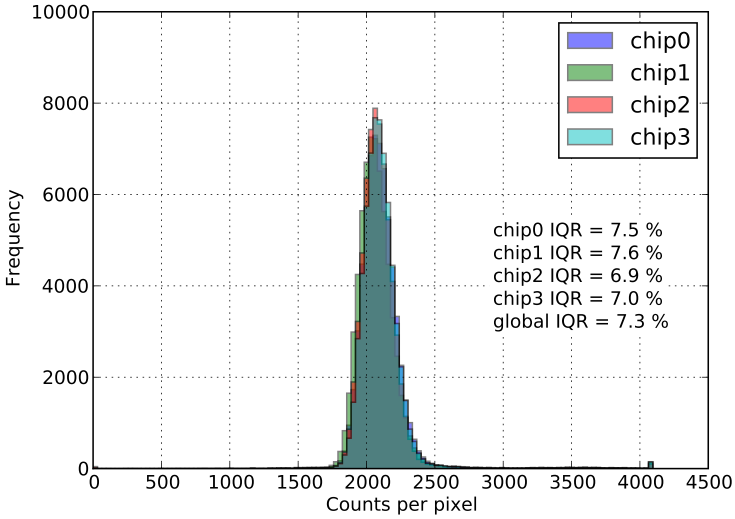

(a)

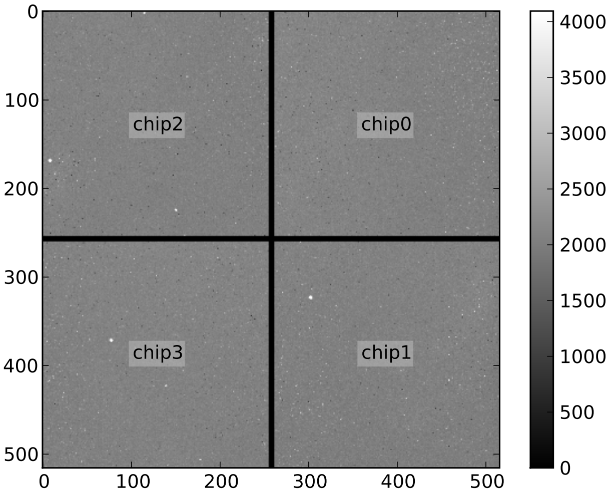

(b)

Figure 6.10: Flat field histograms (a) and images (b) for the quad silicon Medipix3 acquired in SPM after completing the full equalization and calibration procedure. ($V = 50$ kVp.)

6.4 Discussion

The method developed in this chapter for calibrating the ThresholdN and DACpixel global DACs is based on the distribution of counter thresholds and the observed effects on the location of the distribution when the global currents controlled by ThresholdN and DACpixel are applied at the pixel level. The determination of the distribution locations uses the median and is robust to the presence of outliers. The method is automatic and uses only the intrinsic noise and so can be run at any time before counter threshold equalization.

Compared with the method originally proposed by the chip designers [Ballabriga, 2009a] that exhaustively considered each of the $2^5 - 1$ possible adjustments, the method developed in this chapter for counter threshold equalization is more efficient in that each adjustment bit is considered only once. This becomes important for cases where frequent threshold adjustments are required or where multiple counters are to be used. After threshold equalization using the intrinsic noise, the counter threshold distribution for each chip is located close to zero and the widths of the distributions are much reduced compared with the unequalized case. The flat field images are of reasonable quality but can be improved further by the open beam counter threshold adjustment procedure.

Even if the noise-based counter threshold adjustment were to be perfect, the intrinsic variations in pixel gain (reported to be ∼5% [Talla, 2011]) would cause variations in pixel response at typical threshold values. The open beam x-ray equalization procedure compensates for this by matching the pixel responses over a wide range of threshold values. After adjustment of the threshold equalization using the open beam x-ray source, the variation in flat field pixel count rates for each chip is thus improved. However, the inter-chip response variations are largely unaffected and the overall response of each chip must be matched using a separate calibration procedure.

The energy calibration method developed in this chapter uses fluorescence peaks to calibrate a single chip from the array and the other chips are matched to the first using the open beam. The fluorescence peaks are quite broad and the extremely precise calibrations that would be required to match the chip responses directly using independent energy calibrations is difficult to obtain. The procedure adopted in this chapter is designed to be more precise than performing individual energy calibrations for all chips. Furthermore, for large chip arrays, this procedure will be more efficient, and periodic response matching could be carried out automatically.

In conclusion, the DAC calibration, threshold equalization, energy calibration and response mapping procedures are effective such that, after all corrections have been applied, the intra- and inter- chip variations of the Medipix3 array are reduced to a level where the individual chip responses are largely homogeneous and almost indistinguishable.

6.5 Summary and conclusions

1. Many of the Medipix3 global DACs are set using nominal values or target voltage output levels. Calibration of the ThresholdN and DACpixel global DACs is required prior to counter threshold equalization. The procedure developed in this chapter for calibrating the ThresholdN and DACpixel global DACs by observing their effect on the counter threshold distribution, is simple, effective and robust.

2. The noise-based counter threshold equalization procedure is efficient. Each threshold adjustment bit is considered in turn and the initial equalization procedure completes after only five threshold scans of the intrinsic noise. Additional adjustment of the equalization mask using the open beam x-ray source further improves the intra-chip pixel responses.

3. Direct energy calibration of a single Medipix3 chip with silicon sensor layer is possible using fluorescence x-rays generated by the interaction of an open beam x-ray source with thin metal foils of, for example, indium and molybdenum. The responses of the other chips can be precisely matched to that of the first using just the open beam x-ray source.

4. After all adjustments, calibrations and corrections described above have been completed, intra- and inter-chip variations in response are sufficiently reduced to enable the detector array to be operated as a single cohesive unit.

Chapter 7

Evaluating the performance of MARS-CT

This chapter evaluates the performance of the MARS-CT system incorporating a Medipix3 detector with silicon sensor layer against the anticipated requirements for soft-tissue imaging research. Methods for determining spatial resolution, pixel noise, uniformity, CT number linearity and the spectroscopic calibration are given and the results discussed and evaluated. This chapter is based on experimental work done in collaboration with Rafidah Zainon. A presentation based on the material in this chapter was prepared by the candidate and presented at the *IEEE Nuclear Science Symposium and Medical Imaging Conference (NSS/MIC) (2011)* in Valencia, Spain by Dr Anthony Butler on behalf of the MARS team. A corresponding paper was prepared by the candidate and published in the conference proceedings [Ronaldson et al., 2011b].

7.1 Introduction

The MARS research team in Christchurch, New Zealand has developed a spectral micro-CT scanner equipped with a MARS camera incorporating a Medipix3 detector with silicon sensor layer [Doesburg et al., 2009, Walsh et al., 2011]. It is anticipated that this technology will improve the ability to distinguish and quantify material types by the spectroscopic characteristics of their x-ray attenuation coefficients [Schlomka et al., 2008, Anderson et al., 2010].

The MARS-CT scanner will be used to study advanced imaging techniques for quantifying material components in small animal and human specimen studies of diseases such as fatty-liver [Scott et al., 2012] and atherosclerosis [Zainon et al., 2011]. The progression of fatty-liver disease is characterized by increasing levels of fat in the liver. The effective atomic number of fat is lower than that of typical parenchymal liver tissue and thus the ability to quantify fat content may be enhanced by spectroscopic x-ray measurements. Vulnerable atherosclerotic plaques (likely to rupture) are characterized by the presence of lipid and punctate iron deposits in addition to large scale calcifications [Langheinrich et al., 2007]. Identification of vulnerable plaques by their spectroscopic and morphological characteristics is a research goal of the MARS team and other researchers. Thus the performance of MARS-CT in terms of both spectroscopic response and spatial resolution is important for this research.

The aim of this work was to evaluate the performance of the MARS-CT scanner against the anticipated research requirements for spatial resolution, pixel noise, uniformity, linearity and spectroscopic performance. Ideally spatial resolution should be of the order $\sim$100 μm or better so that punctate deposits can be identified. Random and systematic uncertainties from all sources should be significantly less than the spectroscopic signals generated by materials of interest such as fat, calcium and iron.

7.2 Methods and materials

7.2.1 Equipment

The MARS-CT scanner used for this work comprised a micro-focus x-ray tube and Medipix3 detector within a rotating gantry. The Source-Ray SB-80-1K x-ray tube (Source-Ray Inc, Ronkonkoma, NY) had a tungsten anode and included 1.8 mm of aluminium (equivalent) intrinsic filtration. The focal spot size was 33 μm and the maximum tube current and accelerating voltage were 1 mA and 80 kVp respectively.

The Medipix3 detector was bump-bonded to a 300 μm silicon sensor layer and configured in 55 μm fine-pitch mode. The detector chip was mounted within a fan-cooled MARS camera readout box. The MARS camera was controlled by the locally developed `libMars` C library and Python interface (Appendix C). Due to electronic instabilities, charge summing mode was not used and all measurements were taken in single pixel mode.

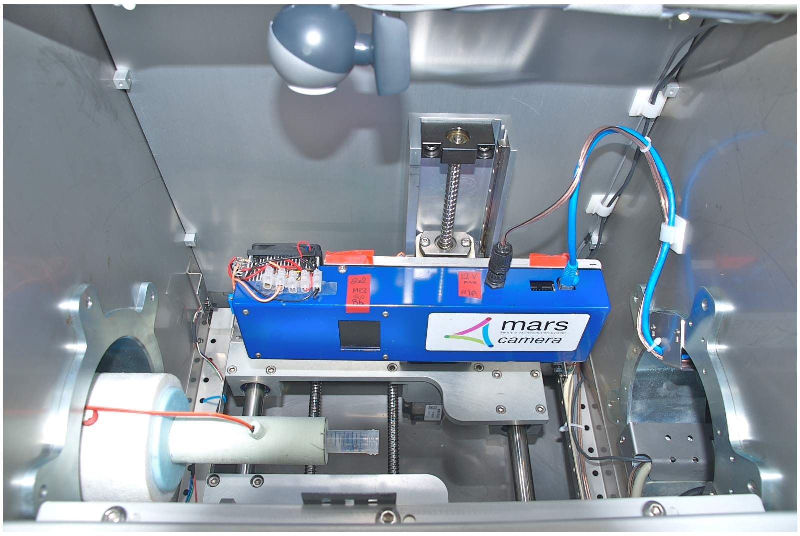

Figure 7.1: The MARS camera mounted within the scanning chamber of the MARS-CT scanner. The camera is mounted opposite the Source-Ray SB-80-1K x-ray tube.

Five phantoms were used to measure different aspects of the system performance:

- *Perspex phantom.* A cylindrical perspex phantom of diameter 10 mm with polished surfaces was used to measure the spatial resolution.
- *Large water phantom.* A large water phantom of diameter 50 mm with perspex walls of thickness 3.0 mm was used to measure the beam hardening correction coefficients.
- *Small water phantom.* A small water phantom of diameter 15 mm with polypropylene walls of thickness 1.5 mm was used to measure CT number uniformity and pixel noise.
- *Calcium chloride phantom.* A 10 mm diameter perspex phantom with 2 mm diameter inserts containing aqueous solutions of calcium chloride at concentrations of: 0.5 M, 1 M, 2 M and 5 M (74.9, 147, 294 and 735 mg.mL^{-1}) was used to measure CT number linearity with increasing material concentration.
- *Fat-CaFe multi-contrast phantom.* A 10 mm diameter perspex phantom with 2 mm diameter inserts containing: sunflower oil (fat surrogate), 3.0 mg.mL^{-1} of iodine (Ultravist 300), 50 mg.mL^{-1} of ferric nitrate, 200 mg.mL^{-1} of calcium chloride, air and water was used to measure the spectroscopic CT number responses for each material.

Two biological specimens were used to demonstrate the system performance: (i) a human femoral plaque set in resin and (ii) a euthanized mouse with kidneys enhanced with iodine contrast agent.

7.2.2 The scanning protocol

A cylindrical scanning protocol with 250 projection angles was used to scan the samples. A single Medipix3 chip has an imaging area of only 14 mm × 14 mm and, where necessary, large area projection images at each angle were acquired by moving the sensor and subsequently tiling the images in software. Flat field measurements for each sensor position were taken before and after the sample scan so that any variations in detector performance over the duration of the scan could be identified and corrected.

X-ray tube settings of $V = 50$ kVp and $I = 0.5$ mA were used together with detector exposure times chosen to give approximately 2000 counts per pixel in open beam. The MARS-CT has the facility for providing variable magnification via moveable camera and source platforms. For this work the camera and source positions were held constant to provide a magnification factor of 1.44 and a voxel size of $(38\ \mu\text{m})^3$.

7.2.3 Data processing

The raw projection data were corrected and normalized using a combination of the initial and final flat-field projection images. Where necessary, frames were stitched to form large area projections and sinograms formed from the normalized data. The sinograms were filtered [Münch et al., 2009] to reduce ring artefacts before reconstructing the CT slices using the *Octopus* commercial CT reconstruction software [Dierick et al., 2004].

For the majority of measurements beam hardening was not significant and no corrections were made. However, beam hardening was expected to become significant for larger diameter objects and therefore uniformity measurements were made in water phantoms of diameter 15 and 50 mm before and after correction using a polynomial beam hardening-correction method [Herman, 1979].

The reconstructed images from the phantom data were stacked and averaged to represent a slice thickness of 1 mm acquired over 250 projections in open beam. To minimize resolution losses in the vertical direction the biological specimen images were smoothed but not stacked nor averaged. A single reconstructed slice for each biological specimen together with the 1 mm slice averages for the phantom data were calibrated in Hounsfield Units using air and water references:

$$CT = 1000\ \mathrm{HU} \frac{\mu - \mu_{\mathrm{water}}}{\mu_{\mathrm{water}} - \mu_{\mathrm{air}}} \tag{7.1}$$

where μ is the reconstructed effective attenuation coefficient and μ_{air} and μ_{water} are the effective attenuation coefficients for air and water references. Uncertainties on the CT numbers were obtained by standard error propagation of the observed pixel noise.

7.2.4 Performance evaluation

Dose rate

Radiation dose estimates are required for future work with live animal models. The dose rate in air at the isocentre (129 mm from the x-ray source) was measured using an Unfors Xi CT ion chamber (Unfors RaySafe AB, Billdal, Sweden) for a variety of x-ray tube settings.

Spatial resolution

Spatial resolution was determined from the MTF measured at the edge of the perspex phantom. The phantom was scanned at 50 kVp and the reconstruction performed using the standard protocol without beam hardening correction. Reconstructed slices corresponding to a thickness of 1 mm were stacked and averaged. The edge profile of the perspex-air boundary was numerically differentiated and the MTF calculated from the Fourier transform of the result. The characteristic spatial resolution corresponding to a MTF of 10% was determined. The impact of the sinogram filtering algorithm on the spatial resolution was assessed by repeating the analysis without sinogram filtering and comparing the results.

Pixel noise

Scans of the 15 mm diameter water phantom were used to determine the relationship between pixel noise and exposure. CT scans were acquired with a detector threshold of 9.8 keV and a fixed tube voltage of 50 keV for a number of exposure ($Q = current \times time$) settings. The standard deviation of CT number per pixel averaged over five regions of interest (ROIs) taken from CT reconstructions corresponding to a slice thickness of 1 mm were used to evaluate the relationship between noise and exposure. The graph of σ^2 against Q^{-1} was examined to determine the relative contributions of random (quantum) and systematic effects.

Beam hardening correction

The large diameter (50 mm) water phantom was used to calibrate the beam hardening correction polynomial coefficients. The phantom was scanned with a detector threshold energy of 9.8 keV and an x-ray tube voltage of 50 kVp. The path lengths L through different portions of the phantom were calculated from the known measurement geometry and plotted against the corresponding attenuation values $Y = -\log \frac{S}{S_0}$ obtained from the normalized sinogram at the vertical beam centre. The beam hardening correction coefficients for the attenuation values were obtained from a polynomial fit through the origin [Herman, 1979]:

$$L = \sum_{i>0} a_i Y^i \tag{7.2}$$

$$\implies Y' = Y + \sum_{i>1} b_i Y^i \tag{7.3}$$

where: $b_i = \frac{a_i}{a_1}$ and Y' is the corrected attenuation value.

Uniformity

Uniformity was measured by comparing the CT numbers at the centre and peripheries of the 15 and 50 mm water phantoms. Both phantoms were scanned at 50 kVp and CT reconstructions performed with and without simple beam hardening correction. Reconstructed slices corresponding to a thickness of 1 mm were stacked and averaged. The mean CT number and standard deviation per pixel in regions of interest at the centre and near the periphery of the reconstruction were determined and compared. The CT number profile through the centre of the phantom was also determined and examined graphically.

Linearity

The calcium chloride phantom was scanned at 50 kVp with detector threshold energies of 8.0, 12.3, 16.6 and 20.9 keV. The CT number responses and standard uncertainties for ROIs over the centre of each solution insert were calculated from the reconstructed images. The relationship between signal intensity and calcium chloride concentration was determined by linear regression for each threshold energy.

Spectroscopic calibration

The Fat-CaFe multi-contrast phantom was scanned at 50 kVp with detector threshold energies of 9.8, 15.1, 20.4, 25.6, 30.9 and 36.2 keV. The CT number response and uncertainty for ROIs over the centre of each material insert were calculated from the reconstructed images. The CT number was plotted against threshold energy for each material. The ability to distinguish material types was confirmed by comparing the spectroscopic CT responses.

7.2.5 Demonstration with biological specimens

Two biological specimens were scanned to demonstrate the performance of the MARS-CT system. A human femoral artery plaque set in resin was scanned at 50 kVp with detector threshold energies of 9.8 and 23.9 keV. The CT data were vertically smoothed and scaled into Hounsfield units. Spectral data from a single slice were used to form an HSV colour composite image. The hue channel was set proportional to the normalized spectral difference and the saturation channel to the absolute spectral difference [Kriegler et al., 1969]. The sum of the two spectral images was used for the value channel. That is, hue (h), saturation (s) and value (v) are given by:

$$h \propto \frac{CT_1 - CT_2}{CT_1 + CT_2} \tag{7.4}$$

$$s \propto CT_1 - CT_2 \tag{7.5}$$

$$v \propto CT_1 + CT_2 \tag{7.6}$$

A mouse was injected with iodine contrast agent into the tail vein and euthanized a few minutes later. A CT scan of the abdominal region was taken at 50 kVp and a detector threshold of 9.8 keV. A single slice from a vertically smoothed image stack was corrected for beam hardening and the result scaled into Hounsfield units using air and water references.

7.3 Results

7.3.1 Dose rate

The dose rates measured at the isocentre are given in Table 7.1. As expected, the dose rate is proportional to the tube current and increases exponentially with voltage.

Table 7.1: Dose rates at the isocentre of MARS-CT for a variety of tube settings. The distance from the source to the isocentre was 129 mm.

Voltage /kVp	Current /mA	Dose rate /mGy.s^{-1}
35	0.10	0.09
35	0.50	0.47
35	1.00	0.92
50	0.10	0.21
50	0.50	1.04
50	1.00	2.08
80	0.10	0.46
80	0.50	2.25
80	1.00	4.50

7.3.2 Spatial resolution

The images of the MTF phantom reconstructed with and without sinogram filtering are shown in Figure 7.2a. The corresponding plots of line spread function and MTF are shown in Figure 7.2b. Without sinogram filtering the MTF falls to 10% of its maximum at a spatial frequency of 9.0 mm^{-1} equivalent to a resolution of 110 μm. The application of sinogram filtering removes the visible ring artefacts but degrades the spatial resolution. After filtering the MTF falls to 10% of its maximum at a spatial frequency of 7.3 mm^{-1} equivalent to a resolution of 140 μm.

7.3.3 Pixel noise

Figure 7.3 shows the CT pixel noise variance σ^2 measured in the small water phantom as a function of reciprocal exposure Q^{-1}. Noise variance is approximately linear ($R^2 = 0.999$) with reciprocal exposure:

$$\sigma^2 = 121.1\ \mathrm{HU}^2 + 5509.4\ \mathrm{HU}^2\mathrm{mAs} \times Q^{-1} \tag{7.7}$$

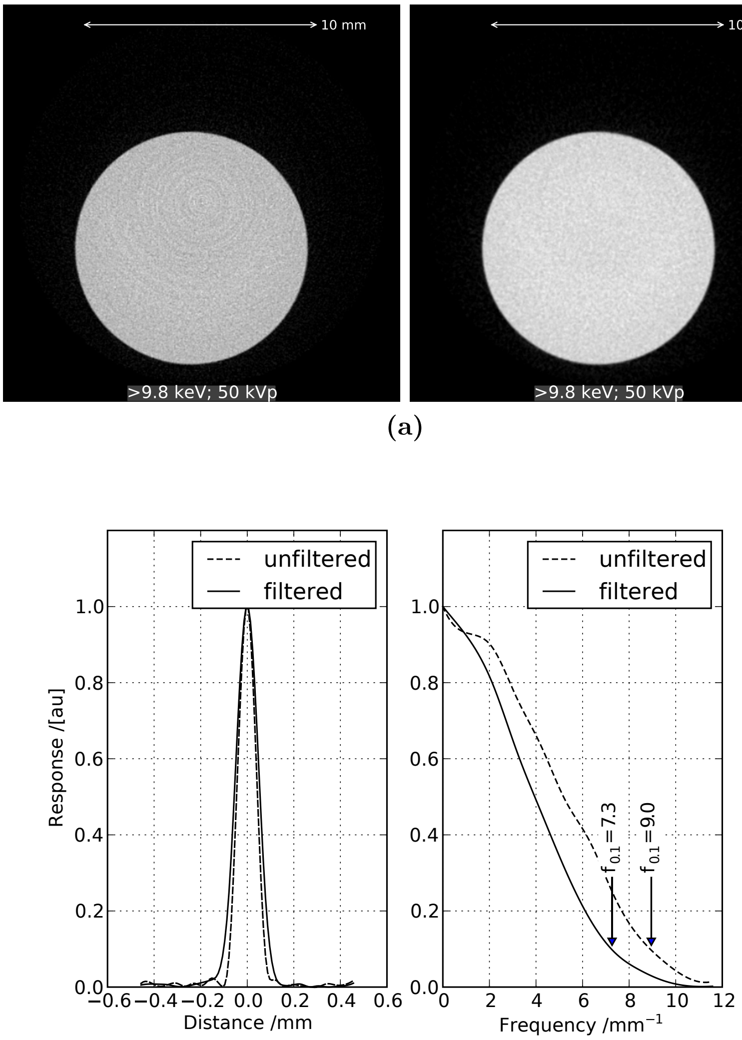

(a)

(b)

Figure 7.2: Images of the MTF phantom reconstructed without filtering (a)(left) and with filtering (a)(right). Ring artefacts visible in the unfiltered image are virtually eliminated in the filtered image. The graphs (b) show the line spread function (left) and MTF (right) for the unfiltered and filtered data measured at the edge of the perspex phantom. For the unfiltered data the MTF falls to 10% of its maximum value at a spatial frequency of 9 mm^{-1} (equivalent to a resolution of 110 μm). After filtering the MTF falls to 10% at 7.3 mm^{-1} (equivalent to a resolution of 140 μm).

The systematic noise component is estimated from the intercept:

$$\sigma_{\text{sys}} = \sqrt{121.1 \text{ HU}^2} = 11.0 \text{ HU} \tag{7.8}$$

7.3.4 Beam hardening correction

The plot of path length against attenuation value (negative logarithm of the normalized sinogram value) is shown in Figure 7.4. The polynomial correction to the attenuation values derived from the fitted curve is:

$$Y' = Y - 0.171Y^2 + 0.095Y^3 \tag{7.9}$$

7.3.5 Uniformity

Figures 7.5 and 7.6 show the CT reconstructions of the large and small water phantoms with and without beam hardening corrections together with mean CT numbers for ROIs located at their centres and peripheries. As expected, the CT number uniformity and pixel noise degraded with increasing object diameter.

For the large water phantom the range of mean CT numbers before beam hardening correction was -97.3 to +12.8 HU. After beam hardening correction the range was -32.2 to +12.0 HU. For the small water phantom the range of mean CT numbers before beam hardening correction was -23.0 to +4.8 HU. After beam hardening correction the range was -2.7 to +4.8 HU.

The error contributions due to non-uniformity for these different cases may be expressed as standard uncertainties [JCGM, 2008]. For the large water phantom (diameter = 50 mm) the standard uncertainty due to non-uniformity

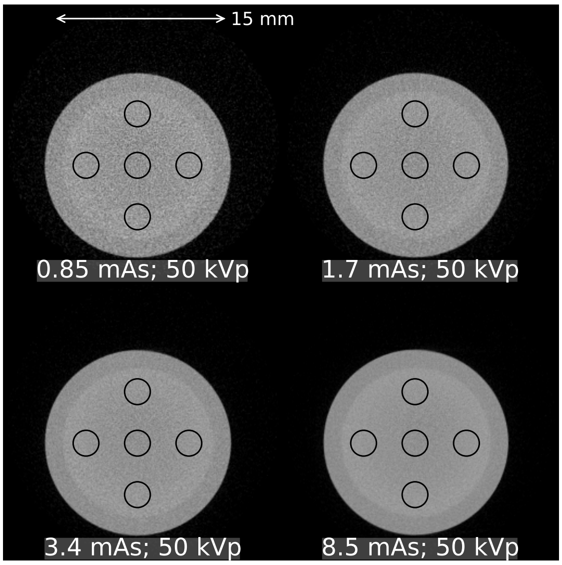

(a)

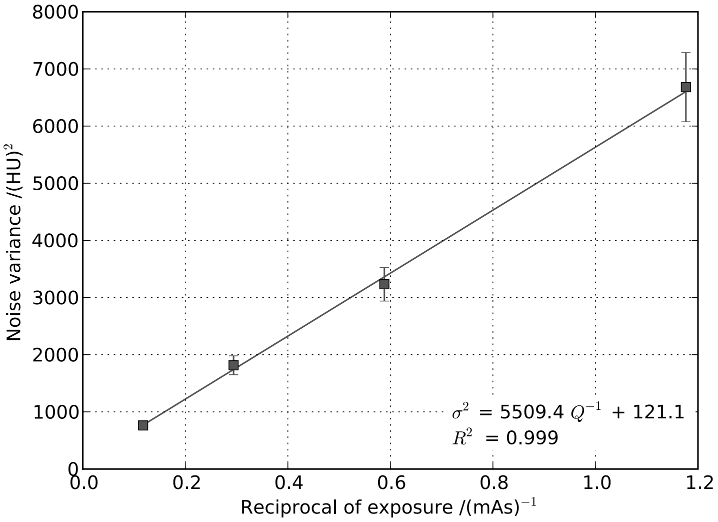

(b)

Figure 7.3: (a) CT images of a 15 mm diameter water phantom acquired at four different x-ray exposure settings. Five circular ROIs used to obtain the average pixel noise variance are marked. (b) A plot of pixel noise variance σ^2 against reciprocal exposure Q^{-1} from scans of a 15 mm diameter water phantom. (V = 50 kVp; $E > 9.8$ keV.)

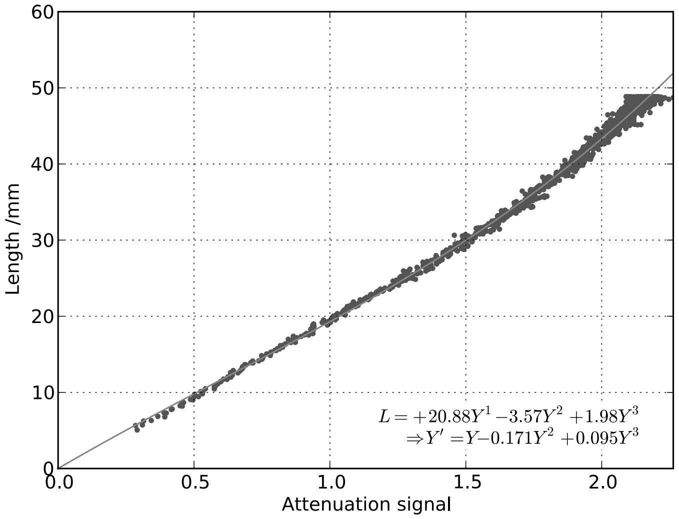

Figure 7.4: A third order polynomial fit of path length L against observed attenuation signal Y (negative logarithm of sinogram value). The derived polynomial for the corrected attenuation signal Y' is also given.

before beam hardening correction was:

$$\sigma_{\mathrm{u}} = \frac{12.8 + 97.3}{2 \cdot \sqrt{3}} \text{ HU} = 31.8 \text{ HU} \tag{7.10}$$

After beam hardening correction the standard uncertainty due to residual non-uniformity in the large water phantom was:

$$\sigma_{\mathrm{u}} = \frac{12.0 + 32.2}{2 \cdot \sqrt{3}} \text{ HU} = 12.8 \text{ HU} \tag{7.11}$$

For the small water phantom (diameter = 15 mm), the standard uncertainty due to non-uniformity before beam hardening correction was:

$$\sigma_{\mathrm{u}} = \frac{4.8 + 23.0}{2 \cdot \sqrt{3}} \text{ HU} = 8.0 \text{ HU} \tag{7.12}$$

After beam hardening correction the standard uncertainty due to residual non-uniformity in the small water phantom was:

$$\sigma_{\mathrm{u}} = \frac{4.8 + 2.7}{2 \cdot \sqrt{3}} \text{ HU} = 2.2 \text{ HU} \tag{7.13}$$

7.3.6 Linearity

The CT reconstructions of the calcium linearity phantom at four detector threshold energies are shown in Figure 7.7 together with plots of the CT number responses against the concentration of calcium chloride. Regression analysis indicates that for all threshold energies the system is linear ($R^2 \geq 0.998$) up to 294 mg.ml^{-1} corresponding to a CT number of approximately 2000 HU. Beyond this concentration the CT number response is underestimated.

7.3.7 Spectroscopic response

The CT reconstructions of the multi-contrast phantom and the measured relationship between CT number and detector threshold energy for each material are shown in Figure 7.8. The spectroscopic responses to the materials tested were characteristic of those materials and consistent with their energy dependent attenuation coefficients. At low energies interactions are dominated by the photoelectric effect and the contrast between materials with different effective atomic numbers is greatest. At higher energies the relative contribution of the Compton interaction component increases and the contrast between materials reduces. In the case of iodine, the CT number increases with energy threshold due to the influence of the K-edge at 33.2 keV. The standard uncertainty on each data point calculated by propagation of the observed errors was $\sim$10 HU and thus the spectroscopic responses are clearly measurable above the various sources of measurement uncertainty

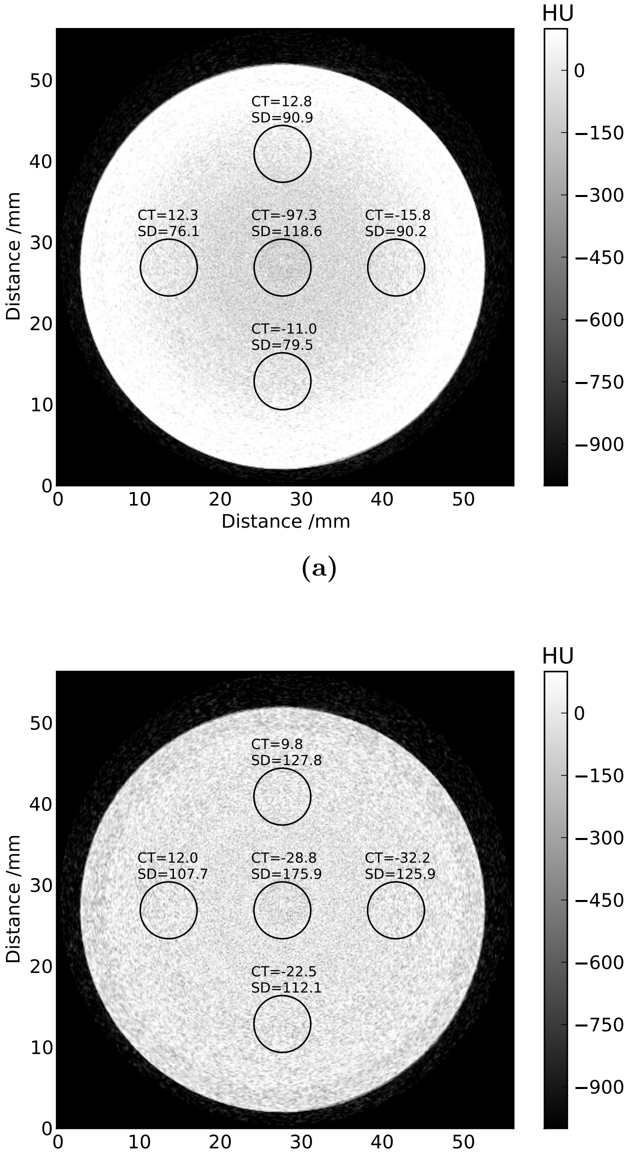

(a)

(b)

Figure 7.5: CT response uniformity (a) before and (b) after beam hardening correction measured at the centre and near the periphery of a 50 mm diameter water phantom. ($V = 50$ kVp; $E > 9.8$ keV.)

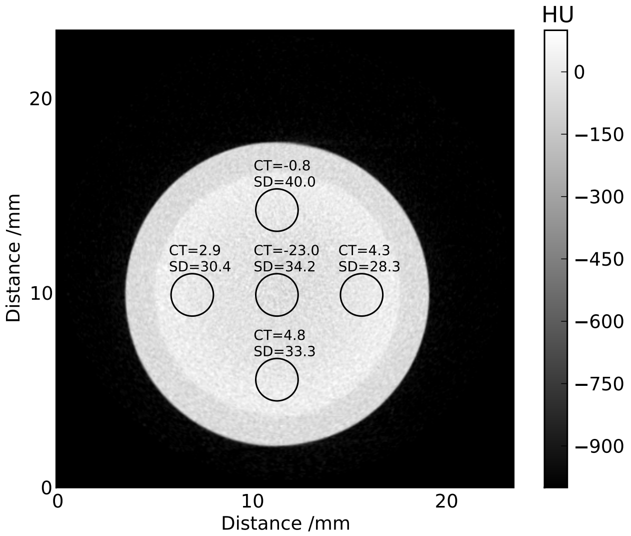

(a)

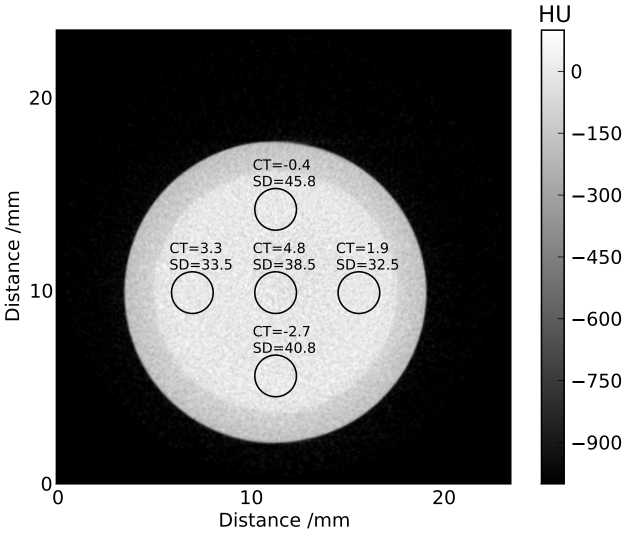

(b)

Figure 7.6: CT response uniformity (a) before and (b) after beam hardening correction measured at the centre and near the periphery of a 15 mm diameter water phantom. ($V = 50$ kVp; $E > 9.8$ keV.)

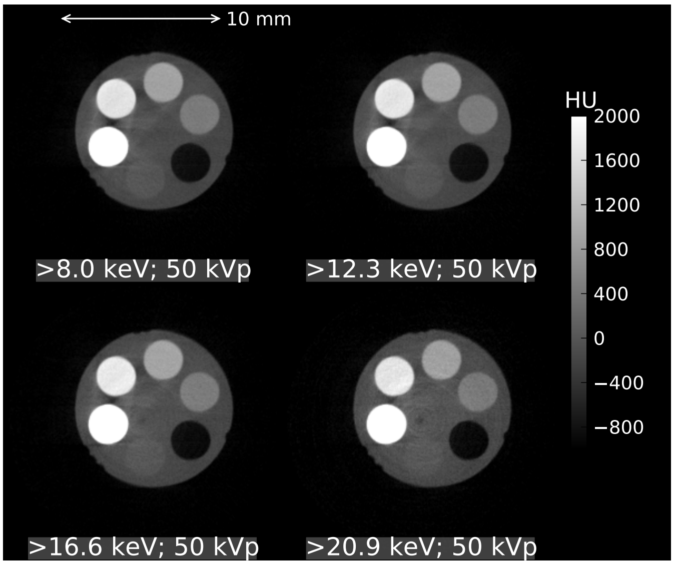

(a)

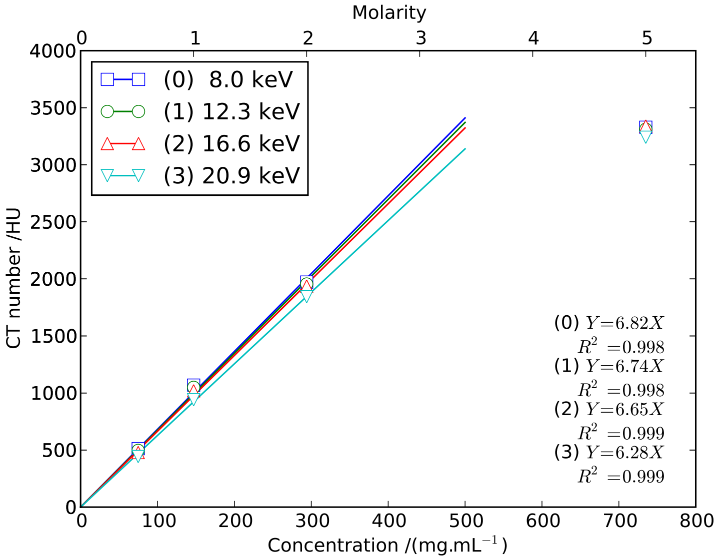

(b)

Figure 7.7: (a) Spectral CT reconstructions images of a 15 mm diameter perspex phantom containing air, water and calcium chloride at a range of concentrations up to 5 M (735 mg.mL^{-1}); and (b) the measured CT numbers Y as a function of calcium chloride concentration X. Linear fits through the origin are given based on data up to 300 mg.mL^{-1}.

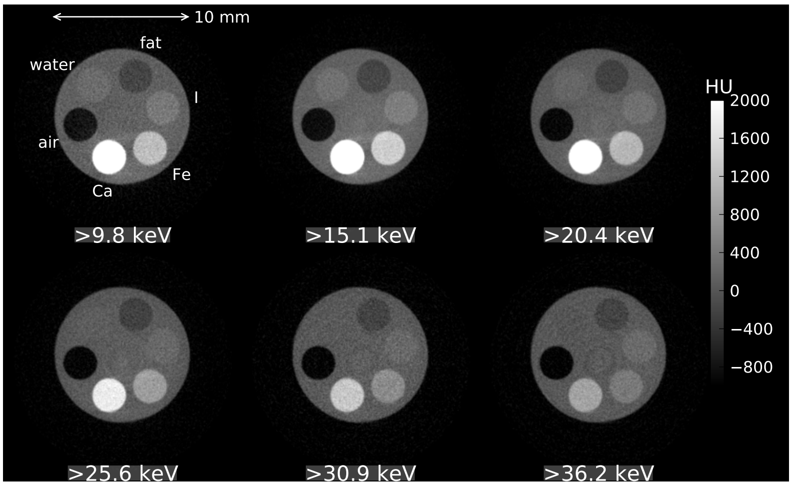

(a)

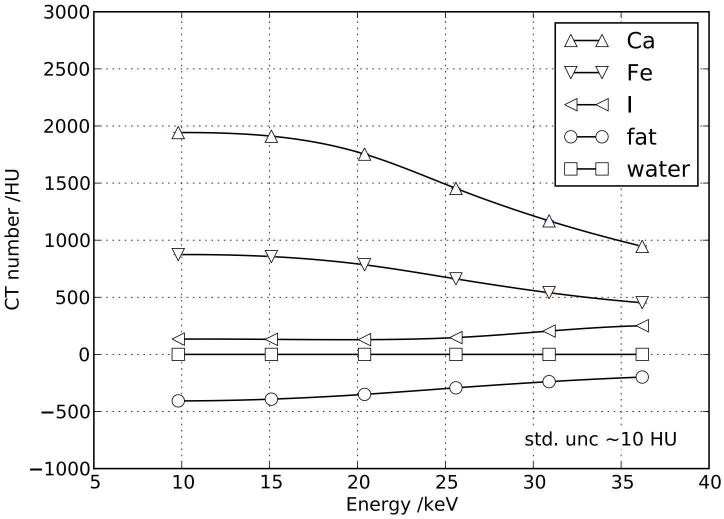

(b)

Figure 7.8: (a) Spectral CT reconstructions using different energy thresholds. The perspex phantom contained 2 M calcium chloride, 0.4 M ferric nitrate, 0.01 M iodine, fat surrogate (sunflower oil), water and air. (b) The spectral CT numbers for each basis material plotted against the detector threshold energies. The standard uncertainties for each data point are ~10 HU.

7.3.8 Biological images

Figures 7.9 and 7.10 show single slice CT images of a human femoral artery plaque in resin and the abdominal region of a euthanized mouse with kidneys enhanced using iodine contrast agent.

The plaque was scanned with two detector threshold energies and these were used to form the HSV colour composite image. The hue channel was set to the normalized spectral difference so that materials with the same spectroscopic properties would be represented with the same hue regardless of density. The calcified region of the plaque is clearly distinguishable by hue from the rest of the specimen. Likewise, the perspex wall of the phantom can be distinguished by hue from the resin within the main body of the phantom.

The mouse was scanned at a single energy. Polynomial beam hardening correction was applied and the result scaled into Hounsfield units using a water reference. The image of the mouse is free from obvious artefacts and the iodine enhanced kidneys and regions of fat surrounding them are clearly visible against the soft tissue of the bulk of the abdomen. Highly attenuating regions such as those of greatest iodine concentration and the spinal column have CT numbers in excess of 2000 HU (beyond the linear range of the system).

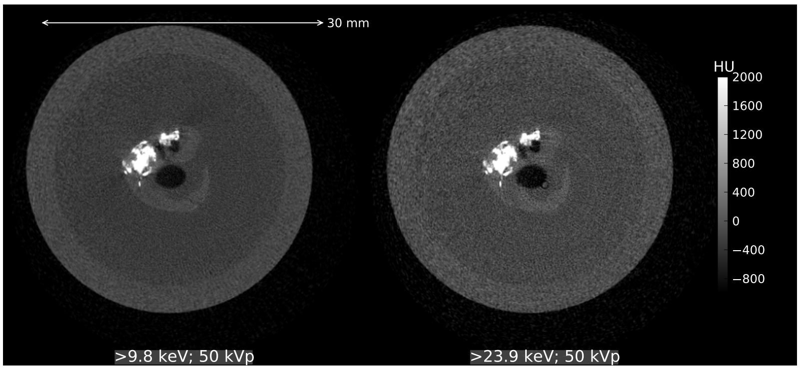

(a)

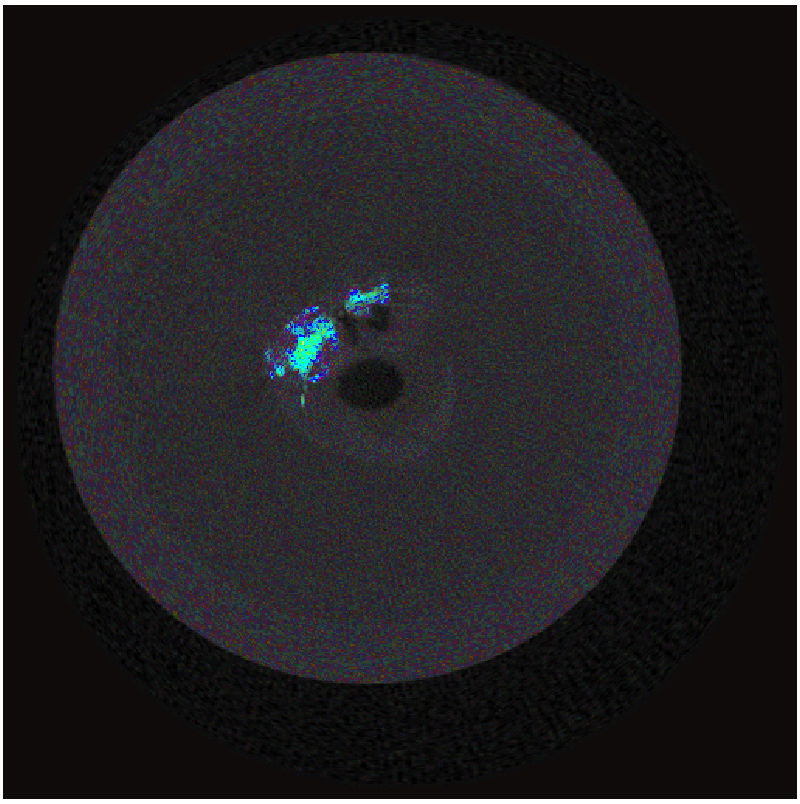

(b)

Figure 7.9: (a) CT images of a femoral artery plaque in resin scanned with two detector threshold energies. (b) A hue, saturation, and value colour composite formed from the spectral data using the normalized spectral difference as the hue channel.

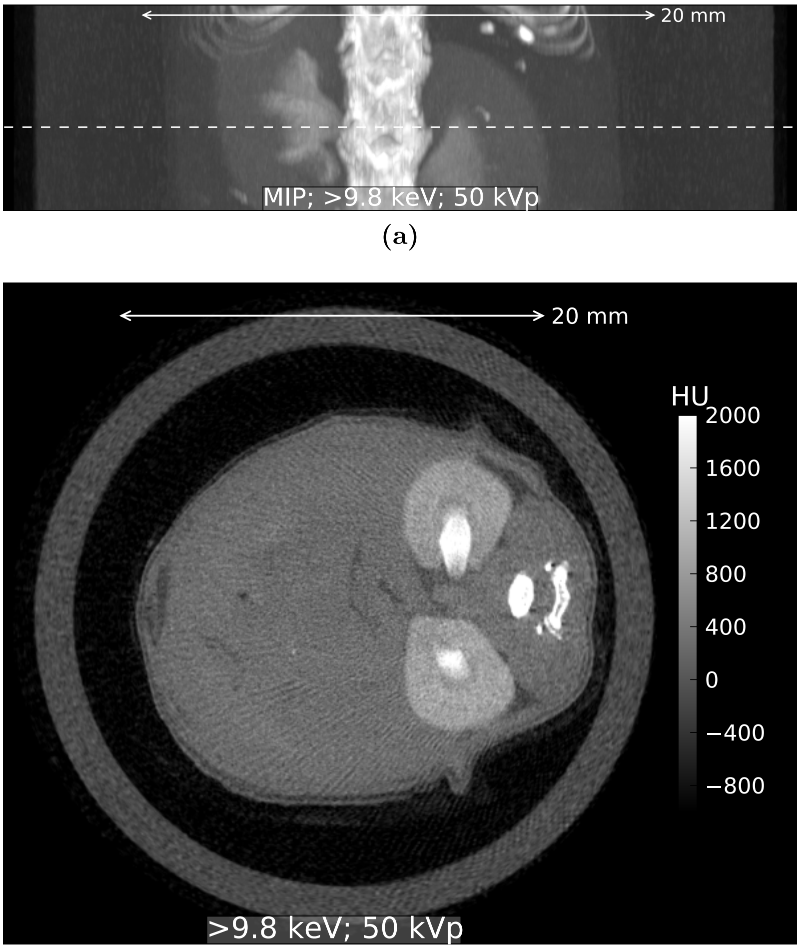

(a)

(b)

Figure 7.10: (a) Maximum intensity projection image through the mouse showing the location of the axial slice through the kidneys (dashed line). (b) Axial CT image (after beam hardening correction) of the abdominal region of a mouse showing kidneys enhanced with iodine contrast agent.

7.4 Discussion

This study has shown that the performance of MARS-CT, in terms of spatial resolution, pixel noise, uniformity, linearity and spectroscopic response, is adequate for soft tissue imaging research. The various sources of measurement uncertainty have been quantified using phantoms and the performance of the system demonstrated with biological specimens.

Firstly, the spatial resolution of the system (110 μm) is sufficient to allow imaging of most objects within small animal models and human specimens. However, some fine structures such as small calcifications and iron deposits may be too small to resolve with this system [Langheinrich et al., 2009]. The use of the sinogram filtering algorithm slightly degrades the spatial resolution (140 μm) although for most applications the improvement in image quality will outweigh the cost in spatial resolution.

Secondly, statistical pixel noise particularly affects the ability to detect low contrast materials [Lin et al., 1993, Du et al., 2007, Zarb et al., 2011]. The amount of random quantum noise present in the reconstructed image depends on scan parameters such as exposure and ideally other sources of error should be relatively insignificant [Kalender, 2001]. The general form of the relation between pixel noise and exposure obtained from our results (Figure 7.3) concur with the established result that image noise is inversely related to the square root of exposure Q [Judy et al., 1977, Lin et al., 1993, McNitt-Gray, 2006]. For low exposure measurements the contribution from random quantum effects will dominate the total noise of the system. However, the systematic contribution will limit the performance of the MARS-CT at higher exposures to $\gtrsim$10 HU.

Thirdly, uniformity of response with spatial position is required for quantitative work. Ideally, for any given material, the same attenuation coefficient should be recorded regardless of the measurement position within a reconstructed slice. However, effects such as beam hardening and scattering can cause cupping artefacts in the reconstructed slices and require specific corrections to the data prior to reconstruction [Herman, 1979, Glover, 1982]. For the MARS-CT system the standard uncertainty due to response non-uniformity increases with the diameter of the phantom but for applications involving small samples up to $\sim$15 mm in diameter will be relatively insignificant ($\lesssim$10 HU). For larger samples and specimens such as intact mice, cupping artefacts are likely to be present that will require correction for quantitative work.

Fourthly, linearity is important for quantitative applications involving opaque materials such as the analysis of calcium and iron deposits in atherosclerotic plaque [Langheinrich et al., 2007, Hyafil et al., 2007]. These specific tasks require the measurement of accurate CT numbers across a wide range of opacities. The linear range of the MARS-CT system operated at 50 kVp extends to approximately 2000 HU which is adequate for most soft-tissue materials. However, the CT numbers of more highly attenuating materials may not be accurately measured by the system in its current configuration. Alternative sensor layers and higher tube voltages could be investigated for applications involving high-Z or especially dense materials.

Finally, the spectroscopic responses to clinically relevant reference materials within the multi-contrast test phantom were characteristic of those materials and consistent with their energy dependent attenuation coefficients. It is therefore expected that a spectroscopic basis for the discrimination and quantification of material components within soft tissue specimens and small animal models can be established.

Performance limitations noted in this study include cupping artefacts observed in the large water phantom, and the presence of streak artefacts between some high contrast objects (see Figure 7.7). Streak and cupping artefacts can both be caused by beam hardening or scattering [Glover, 1982, Joseph and Spital, 1982]. For this work, beam hardening has been reduced through prefiltering of the x-ray beam with 1.8 mm aluminium equivalent filtering and scattering has been limited by the use of an air gap [Sorenson and Floch, 1985]. This has proved effective for sample diameters up to ∼15 mm water equivalent and for calcium concentrations up to ∼1 mol.L^{-1}. Beyond these values, additional data correction methods may be required for quantitative work.

Despite the limitations discussed above, the performance of the MARS-CT is currently adequate for our soft-tissue imaging research requirements. The performance has been demonstrated using biological specimens and good quality images free from obvious artefacts have been obtained. The combined benefits of the spatial and energy resolution offered by this system will enable material differentiation and quantification methods to be developed and tested.

7.5 Summary and conclusions

1. The radiation dose rate at the isocentre has been measured for a variety of x-ray tube settings. At the usual operating values of 50 kVp and 500 μA, the dose rate at the isocentre is 1 mGy.s^{-1}. The dose rate increases linearly with tube current and exponentially with tube voltage.

2. The spatial resolution of the MARS-CT has been measured using a purpose built phantom and is 110 μm. With the addition of sinogram filtering this is slightly degraded to 140 μm.

3. Pixel noise in the reconstructed images has been measured in water phantoms for a range of tube settings and, as expected, is inversely related to the square root of exposure. At high exposures systematic noise contributions dominate and limit the measurement uncertainty to $\gtrsim$10 HU.

4. Uniformity has been measured in water phantoms of diameter up to 50 mm and, as expected, uniformity and noise deteriorate with increasing sample diameter. Without correction, the standard uncertainty due

to non-uniformity in the 15 mm diameter water phantom is ∼8 HU. Beam hardening corrections are required for scans of water phantoms of diameter >15 mm. Polynomial beam hardening corrections have been successfully demonstrated in scans of water phantoms up to 50 mm diameter.

5. The linearity of CT number with increasing material concentration has been measured using calcium chloride solutions. In its current configuration, using a silicon sensor layer and a tube voltage of 50 kVp, the MARS-CT system response is linear up to ∼2000 HU. Beyond this value the CT number is underestimated. Alternative sensor layers and higher tube voltages may be required for applications involving high-Z or especially dense materials.

6. The spectroscopic responses have been measured for a set of clinically relevant reference materials within a multi-contrast phantom and have been found to be characteristic of those materials and consistent with their energy dependent attenuation coefficients. The contrast between materials is greatest at low energies and the characteristic changes in CT number response are clearly measurable above the various sources of measurement uncertainty.

Chapter 8

Quantifying material composition

This chapter presents the theory and experimental evaluation of a constrained least squares method for material decomposition and quantification. The experimental work was done in collaboration with Rafidah Zainon. Portions of this chapter were presented by Rafidah Zainon at the *International Conference on Biomedical Engineering and Biotechnology (2011)* in Shanghai, China [Zainon et al., 2011] and by the candidate at the *Radiological Society of North America (RSNA) Scientific Assembly and Annual Meeting (2011)* in Chicago, USA [Ronaldson et al., 2011c]. A journal manuscript has been prepared by the candidate from the material in this chapter.

8.1 Introduction

At energies relevant to diagnostic CT, x-rays interact predominantly by a combination of the photoelectric and Compton effects. The photoelectric effect varies with material density and atomic number according to $\sim \frac{\rho}{A}Z^4$. The Compton effect varies according to $\sim \frac{\rho}{A}Z$. Both effects are energy dependent and thus spectral decomposition becomes possible with the acquisition of CT data over at least two energy ranges.

Spectral decomposition may be applied in either the projection or reconstruction image domains and may be based on functions describing either the physical interaction mechanisms or the material properties. Alvarez and Macovski [Alvarez and Macovski, 1976], working in the projection image domain, and Brooks [Brooks, 1977] working in the reconstruction image domain, showed that spectral CT measurements could be decomposed into basis images representing the relative contributions of the photoelectric and Compton effects. Both methods used two spectral CT measurements to produce two component images.

Recent advances in detector technology have stimulated research into spectral CT using spectroscopic photon counting detectors. This form of spectral CT is able to provide multi-energy datasets from a single acquisition using a standard x-ray tube operated at a single accelerating voltage. A recent simulation study [Alvarez, 2011] implemented an empirical calibration for spectroscopic photon counting detectors in the projection domain to determine spectral basis components in the absence of K-edges. Other projection domain spectral decomposition methods [Schlomka et al., 2008, Firsching et al., 2008] that specifically consider K-edge materials rely upon accurate modelling of the detector response.

The various methods for spectral decomposition all derive their basis from the intrinsic dimensionality of the energy dependent material attenuation coefficients. This is sometimes assumed to be just two, with one component representing the photoelectric effect and the other the Compton effect. However, this approximation is valid only for materials of low atomic number that have no K-edge within the measurement region. Furthermore, in a recent study [Bornefalk, 2012] of the number of components required to represent the attenuation coefficients of an arbitrary low Z material ($Z \leq 20$), it was concluded that, although there are indeed two very dominant effects, the intrinsic dimensionality of the attenuation data is at least four. It is therefore anticipated that higher-dimensional spectroscopic data sets may improve the ability to quantify the composition of clinically relevant materials [Schlomka et al., 2008, Anderson et al., 2010, Shikhaliev and Fritz, 2011].

The purpose of this work is to develop a spectral CT method for material quantification and to determine if spectral CT with Medipix3 has the potential to quantify fat, calcium and iron in soft tissues within small animal models and surgical specimens of diseases such as fatty-liver (metabolic syndrome) and unstable atherosclerosis. Accurate quantification of fat in liver and lipid, iron and calcium in atherosclerotic plaque to determine if it is stable or unstable, would allow treatments to be tested and monitored in vivo in animal models [Anderson et al., 2010].

The proposed method for material quantification is constrained least squares [Tarantola, 2005]. A volume constraint on the bulk tissue matrix (comprising water and fat) is incorporated and prior constraints are placed on the credible concentrations of materials dispersed or dissolved therein (e.g. calcium, iron, iodine). The method is applied in the reconstruction image domain by calibration against phantoms containing known materials. With this approach the effects of arbitrary materials, and K-edges are included where necessary, but the requirement for an accurate forward model of the detector response is avoided.

The MARS-CT scanner incorporating a MARS camera with Medipix3 spectroscopic photon counting detector [Ballabriga et al., 2006, Doesburg et al., 2009] has been calibrated experimentally with phantoms containing known solutions of clinically relevant materials. A linear basis for material decomposition was established by spectroscopic calibration and a set of credible prior distributions from the literature. The potential of the proposed method for quantifying different sets of materials was evaluated in terms of information entropy and degrees of freedom. The measurement performance has been evaluated quantitatively using mouse and atheroma equivalent phantoms and demonstrated qualitatively using ex-vivo biological specimens. This chapter describes the theory of the proposed material quantification technique and presents the experimental methods and results from the analysis of phantoms and biological samples.

8.2 Theory

In this section the mathematical theory of a constrained least squares method for material decomposition is described and *entropy* and *degrees of freedom* are introduced as measures of the effectiveness of the measurement. These measures may be used to compare potential measurement configurations [Rodgers, 1996] or select between competing systems [Engelen and Stephens, 2004] on the basis of information retrieved.

8.2.1 CT numbers and attenuation coefficients

Computed tomography reconstructs the effective attenuation coefficient μ distribution within the interior of the measured object. This is a function of the x-ray spectrum and detector response characteristics as well as of the object being examined. Reconstructed images are often scaled to CT numbers (in Hounsfield units) to enhance differences between body tissues and to enable direct comparison of measurements from different CT scanners:

$$CT = 1000\frac{\mu - \mu_{\text{water}}}{\mu_{\text{water}} - \mu_{\text{air}}} \tag{8.1}$$

We can transform the CT number measurements into values that are directly proportional to the attenuation coefficients of the unknown materials. For $\mu_{\text{air}} \approx 0$ we obtain:

$$y = 1 + \frac{CT}{1000} \approx \frac{\mu}{\mu_{\text{water}}} \tag{8.2}$$

From the mixture rule [Jackson and Hawkes, 1981], we write the effective linear attenuation coefficient of a combination of material components $x_i,\ i = 1 \ldots M$ as the sum of the attenuation coefficients for the individual components:

$$y = \frac{\sum_i \mu_i x_i}{\mu_{\text{water}}} \tag{8.3}$$

and we seek a method for estimating the components x_i given a spectral calibration for μ_i/μ_{water} and spectral measurements y.

8.2.2 Constrained least squares

The following analysis applies equally to vectors formed from CT numbers taken over regions of interest within the spectral CT images and those formed per pixel.

Measuring the CT numbers of a set of material components $i = 1 \ldots M$ at multiple energies $j = 1 \ldots N$ allows us to write a linear equation for the transformed measurement variables $[y_j]$ in terms of the (unknown) composition $[x_i]$ and a spectroscopic calibration $[A_{j,i}]$ with errors ϵ which we will assume follow a Gaussian distribution:

$$\mathbf{y} = \mathbf{A} \cdot \mathbf{x} + \epsilon \tag{8.4}$$

We will represent the composite soft tissue material as some bulk tissue matrix within which other components may be dissolved or dispersed. The elements of $\mathbf{x}$ corresponding to components of the bulk tissue matrix will be written as dimensionless volume fractions. The other elements represent the concentrations of additional dispersed or dissolved components. Either number or mass concentrations may be used. We will later use number concentrations (molarity in mol.L^{-1}).

We can augment the measurement expression above with additional linear equations. For example, to constrain the sum of volume fractions for the bulk tissue components $[x_i] \in V$, we write the following augmented measurement equation:

$$\begin{bmatrix} y_1 \\ \vdots \\ y_N \\ 1 \end{bmatrix} = \begin{bmatrix} A_{1,1} & \cdots & A_{1,M} \\ \vdots & \ddots & \vdots \\ A_{N,1} & \cdots & A_{N,M} \\ \delta_1 & \cdots & \delta_M \end{bmatrix} \cdot \begin{bmatrix} x_1 \\ \vdots \\ x_M \end{bmatrix} + \begin{bmatrix} \epsilon_1 \\ \vdots \\ \epsilon_N \\ \epsilon_{N+1} \end{bmatrix} \tag{8.5}$$

where $\delta_i = 1$ if $x_i \in V, 0$ otherwise.

The probability density function $f(\mathbf{y})$ for the augmented measurement response may be written in terms of a χ^2 cost function:

$$f(\mathbf{y}) \propto \exp\left(-\frac{1}{2}\chi^2_{\mathrm{Y}}\right) \tag{8.6}$$

$$\chi^2_{\mathrm{Y}} = (\mathbf{y} - \mathbf{A}\mathbf{x})^{\mathsf{T}} \cdot \mathbf{C}_{\mathrm{Y}}{}^{-1} (\mathbf{y} - \mathbf{A}\mathbf{x}) \tag{8.7}$$

where $\mathbf{C}_{\mathrm{Y}}$ is the covariance matrix of the augmented measurement error distribution. Those elements of $\mathbf{C}_{\mathrm{Y}}$ representing the variations in spectral CT responses can be determined by direct characterization of the MARS-CT system. The additional variance term representing the variation in the sum of partial volume fractions due to, for example, non-ideal mixing may be estimated from reference data [Kaye and Laby, 1995]. Finding composition estimates $[\hat{x}_i]$ that maximize the measurement likelihood is then equivalent to minimizing the χ^2 cost function [Tarantola, 2005]. However, if the parameters are unbounded, negative results can be obtained for concentrations and volume fractions. To ensure a physically valid result we can incorporate some prior knowledge of the credible distributions of model parameters.

Independently of any measurement, we can place lower bounds on the valid ranges of concentration and volume, and reasonable estimates of the upper bounds in biological materials can be obtained from relevant literature. We assume that after a suitable transformation $\mathrm{M} : [x_i] \mapsto [m_i]$ each credible distribution can be approximately represented as a Gaussian. For positively constrained physical quantities, it is convenient to express $[x_i]$ as unconstrained variables $[m_i]$ through the lognormal distribution with an additional cost function defined as follows [Tarantola, 2005]:

$$\chi^2_{\mathrm{M}} = \mathbf{m}^{\mathsf{T}} \cdot {\mathbf{C}_{\mathrm{M}}}^{-1} \cdot \mathbf{m} \tag{8.8}$$

where:

$$\mathbf{m} = \left[\ln \frac{x_i}{\beta_i}\right]$$
$$\mathbf{C}_{\mathrm{M}} = \mathrm{diag}\left[\gamma_i^2\right]$$

and $[\beta_i]$ and $[\gamma_i]$ are location and scale dispersion parameters defining the credible distributions for the model components. The model components are assumed to vary independently and thus $\mathbf{C}_{\mathrm{M}}$ is diagonal.

We wish to obtain an estimate $\hat{\mathbf{x}}$ of the composition that is consistent with both the prior and the augmented measurement data. This is done by minimizing the combined cost function [Tarantola, 2005]:

$$\chi^2(\mathbf{x}) = \chi^2_{\mathrm{M}}(\mathbf{m}) + \chi^2_{\mathrm{Y}}(\mathbf{x}(\mathbf{m})) \tag{8.9}$$

$$\hat{\mathbf{m}} = \operatorname{argmin} \chi^2\left(\mathbf{m}\right) \tag{8.10}$$

$$[\hat{x}_i] = \left[\beta_i e^{\hat{m}_i}\right] \tag{8.11}$$

The posterior covariance matrix $\mathbf{P}$ for the estimated composition is then obtained from the inverse Hessian matrix evaluated numerically around the estimate $\hat{\mathbf{x}}$ [Tarantola, 2005]:

$$\mathbf{P} \approx \left[\frac{\partial^2 \chi^2}{\partial x^2}\right]_{\hat{\mathbf{x}}}^{-1} = \left(\operatorname{diag}\left[\hat{x}_i^{-1}\right] \left[\frac{\partial^2 \chi^2}{\partial m^2}\right]_{\hat{\mathbf{m}}} \operatorname{diag}\left[\hat{x}_i^{-1}\right]\right)^{-1} \tag{8.12}$$

The effectiveness of any measurement may be quantified by the reduction in information entropy H and by the increase in effective number of degrees of freedom (d.f.) of the system. The information entropy is a logarithmic measure of the volume of the uncertainty covariance $\mathbf{P}$ and is given by [Rodgers, 1996]:

$$H = \frac{1}{2} \log(\det(\mathbf{P})) \tag{8.13}$$

The effective d.f. for the fitted composition measures the number of components recovered by the measurement and is approximated by the trace of the *hat* matrix [Ye, 1998]:

$$\nu \approx \left[\frac{\partial \hat{y}}{\partial y}\right]_{\hat{\mathbf{x}}} = \operatorname{tr}\left(\mathbf{A}\mathbf{P}\mathbf{A}^{\mathsf{T}}\, \mathbf{C}_{\mathrm{Y}}{}^{-1}\right) \tag{8.14}$$

8.2.3 Measurement uncertainties

The variance on the measurement result is given by the diagonal of the posterior covariance matrix $\mathbf{P}$. The variance estimates depend upon the model and covariances $\mathbf{C}_{\mathrm{M}}$ and $\mathbf{C}_{\mathrm{Y}}$. The validity of the model and covariances can be tested by comparing the χ^2 value for the result with its expected distribution $\chi^2 \sim \chi^2(N + M + 1)$. In cases where the χ^2 value is excessive, we may reject the fitted result, otherwise we accept the result with uncertainties given by:

$$[\sigma_i{}^2] = \operatorname{diag}(\mathbf{P}) \tag{8.15}$$

8.3 Methods and materials

8.3.1 Spectral CT system

The MARS-CT scanner used for this work comprised a micro-focus x-ray tube and a Medipix3 detector within a rotating gantry. The Source-Ray SB-80-1K x-ray tube (Source-Ray Inc, Ronkonkoma, NY) had a tungsten anode and included 1.8 mm of aluminium (equivalent) intrinsic filtration. The focal spot size was 33 μm and the maximum tube current and accelerating voltage were 1 mA and 80 kVp respectively. For this study, all images were acquired at 50 kVp.

Some preliminary work was done using a single Medipix3 detector, however the majority of this work including all phantom studies and biological specimen imaging was done with a quad (2×2) detector array with a total imaging area of approximately 28 mm × 28 mm. Both the single and quad Medipix3 photon counting detectors were bump bonded onto a 300 μm thick silicon sensor layer in 55 μm fine-pitch configuration. Due to electronic instabilities noted in Chapter 5, charge summing was not used and all measurements were taken in single pixel mode.

The x-ray spectrum at 50 kVp and the interaction coefficients for silicon are shown in Figure 8.1. This spectrum was selected to give good soft tissue contrast for small (mouse sized) specimens [Paulus et al., 2000]. The silicon detector was selected due to the availability of high quality sensor layers in this material and provides adequate performance at the relatively low photon energies of the 50 kVp spectrum where the photoelectric effect is dominant.

Each sample was scanned at 50 kVp using 250 projection angles. Where necessary, the field of view at each angle was extended by moving the detector array. Projection images were acquired at each position by stepping the detector threshold through a sequence of energy levels and acquiring an image at each setting. Flat field measurements for each sensor position and energy bin

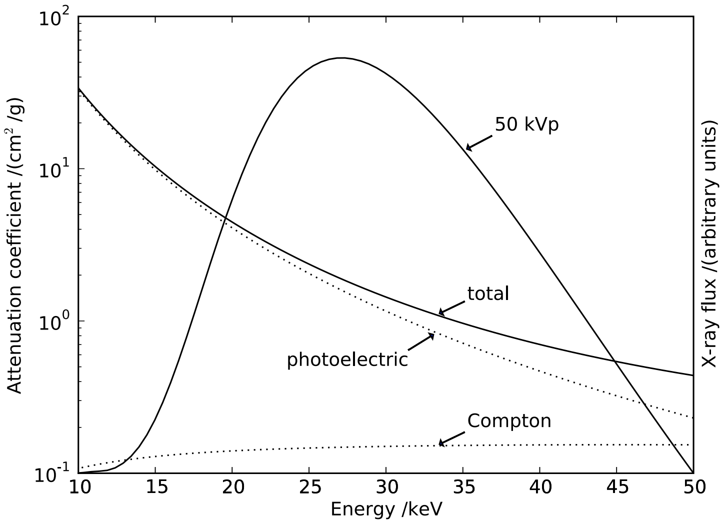

Figure 8.1: The photoelectric, Compton and total mass attenuation coefficients for silicon are shown (left axis) together with a simulation of the output from the x-ray tube at 50 kVp with 1.8 mm aluminium filtration (right axis).

were taken before and after the sample scan so that any variations in detector performance over the duration of the scan could be identified and corrected.

After scanning, the raw projection data were corrected and normalized using a combination of the initial and final flat field projection images. Interpolation was used to replace missing or erroneous image data. Energy bin images were created using the net signal between detector thresholds. Sinograms were formed from the normalized projection data and filtered [Münch et al., 2009] to reduce ring artefacts before the CT data were reconstructed using the *Octopus* commercial CT reconstruction software [Dierick et al., 2004]. All reconstructions were made using an isotropic voxel size of approximately 40 μm^3.

8.3.2 Spectroscopic calibration

A perspex phantom of 10 mm diameter with 2 mm diameter inserts containing ferric nitrate (0.4 M $Fe(NO_3)_3(aq)$), calcium chloride (2.0 M $CaCl_2(aq)$), fat surrogate (sunflower oil), iodine (0.01 M $I_2(aq)$), air and water was used to evaluate the spectroscopic CT number response for different materials. The ferric nitrate and calcium chloride solutions were prepared by dissolution and dilution. The iodine solution was prepared by dilution of Ultravist 300 contrast agent (Bayer Schering Pharma, Berlin). Sunflower oil was chosen as a suitable fat surrogate because of its high triglyceride content.

The calibration phantom was scanned at 50 kVp with detector threshold energies of 9.8, 15.1, 20.4, 25.6, 30.9 and 36.2 keV. The CT number and standard deviation for each material were measured in Hounsfield units (HU) for an ROI placed manually over each solution insert. The relationship between CT number and detector threshold energy was examined graphically.

Response matrix

The spectroscopic CT numbers for each calibration material were transformed as described above to give attenuation coefficients relative to water for each energy bin. For fat surrogate (sunflower oil) and water the relative attenuation coefficients represent the attenuation due to the volume fractions of the bulk tissue components:

$$A_{j,i} = 1 + \frac{CT_{j,i}}{1000} \text{ for } i \in \{\text{water, fat}\} \tag{8.16}$$

where $CT_{j,i}$ is the CT number for material i at energy j.

For the aqueous solutions of $CaCl_2$, $Fe(NO_3)_3$ and I_2 the attenuation due to water was subtracted and the result scaled to give the relative attenuation coefficient per unit concentration of the dissolved species alone. These terms represent the additional attenuation due to material dispersed or dissolved within the bulk tissue matrix:

$$A_{j,i} = \frac{1}{C_i}\frac{CT_{j,i}}{1000} \text{ for } i \notin \{\text{water, fat}\} \tag{8.17}$$

where C_i is the molar concentration (moles per unit volume) of the dissolved species in the calibration solution.

A volume conservation constraint was included by setting y_{N+1} and the corresponding elements of $[A_{N+1,i}]$ to unity (see Equation 8.5). The variance on the constraint was set to represent a nominal uncertainty of 5% in the sum of volume fractions due to non-ideal mixing.

$$y_{N+1} = 1, C_{\mathrm{Y}N+1,N+1} = 0.05^2 \tag{8.18}$$

$$A_{N+1,i} = 1 \text{ for } i \in \{\text{water, fat}\} \tag{8.19}$$

$$A_{N+1,i} = 0 \text{ otherwise} \tag{8.20}$$

Response matrices were assembled from $N = 6$ spectral calibration measurements for particular measurement scenarios by selecting columns of $[A_{j,i}]$ to represent the following sets of unknowns: (i) $i \in \{$I, fat, water$\}$; (ii) $i \in \{$Ca, Fe, water$\}$; (iii) $i \in \{$Ca, fat, water$\}$; (iv) $i \in \{$fat, water$\}$.

Input data covariance

The input data covariance was written as the combination of random (quantum) and systematic effects [Ford et al., 2003]. The random noise component per unit exposure was determined from the covariance $\mathbf{C}_{\mathrm{ran}}$ observed in the reconstructed water region of interest. An estimate of the covariance due to systematic effects $\mathbf{C}_{\mathrm{sys}}$ was obtained from the systematic uncertainties reported in Chapter 7. The overall covariance on the input data was obtained from:

$$\mathbf{C}_{\mathrm{Y}} = \mathbf{C}_{\mathrm{sys}} + k\mathbf{C}_{\mathrm{ran}} \tag{8.21}$$

where k is inversely proportional to exposure × volume of ROI.

8.3.3 Performance assessment

The potential performance of the system was assessed hypothetically using the calibration data above and a priori distributions designed to encompass all credible values of the model components.

Estimating the prior

In contrast to methods such as unconstrained linear least squares, this method requires a credible prior to be specified by the experimenter. This is a subjective process. However, the prior merely formalizes the experimenter's performance requirements in terms of what is already known independently of any measurement and enables the potential for improving this state of knowledge to be quantified in context. Regarding its effect on the decomposition, the prior reduces the impact of measurement noise on the estimates, acting as a regularization operator that is sometimes used in least squares methods to prevent overfitting. The χ^2 goodness of fit test is included as a check on both the validity of the prior and the performance of the measuring system.

The a priori distributions should be compatible with the ranges of credible values for the model components. This will vary by application according to the component materials being investigated and their typical concentrations within biological tissues. The distributions for the components contain only positive values and, with the exception, of the water component are positively skewed. The lognormal distribution with location and scale parameters β_i and γ_i is therefore appropriate:

$$\mathbf{m} = \left[\ln \frac{x}{\beta_i}\right], \mathbf{C}_\mathrm{M} = \operatorname{diag}\left[\gamma_i^2\right] \tag{8.22}$$

To estimate location and scale parameters for each component we consider the relative abundance of the materials. Water is the major component of the bulk tissue matrix and fat a relatively minor component. Of materials likely to be dispersed within the bulk tissue matrix, calcium is the most abundant and is found in atherosclerotic plaques [Rahdert et al., 1999, Thiam et al., 2004] in concentrations up to $\sim$ 10 mol.L^{-1}. Iron, as a result of intraplaque haemorrhage, may be found within plaques [Rahdert et al., 1999, Thiam et al., 2004, Stadler et al., 2004] in lesser concentrations up to $\sim$ 10 mmol.L^{-1}. Iodine is a (potentially toxic) artificial contrast agent used in concentrations just sufficient to highlight selected tissues. Thus the following parameters define a prior encompassing all credible distributions for these materials:

$$\beta_i = 0.1 \text{ mol.L}^{-1}, \gamma_i = \ln 10 \text{ for } i \in \{\text{Ca, Fe, I}\} \tag{8.23}$$

$$\beta_i = 1.0, \gamma_i \sim \infty \text{ for } i \in \{\text{fat, water}\} \tag{8.24}$$

Note that the units of $[\beta_i]$ match those of $[x_i]$ whereas the elements of $[\gamma_i]$ are dimensionless. The prior distributions for the water and fat components allow any positive value; the volume constraint is sufficient to limit the positive ranges of these bulk tissue components. This prior is based on bounding cases, and contains minimal information about the model parameters. If necessary the distributions can be adjusted for particular applications.

Entropy and degrees of freedom

As described above, information entropy and degrees of freedom (d.f.) provide measures of the overall uncertainty and number of independent components retrieved by the measurement. The change in information entropy and d.f. were calculated at $[\hat{x}_i] = [\beta_i]$ using up to six energy bins in sequence. For each scenario, the expected covariance matrix $\mathbf{P}$ after measurement was calculated using the appropriate response matrix $\mathbf{A}$ and the input data covariance matrix $\mathbf{C}_\mathrm{Y}$ formed from the combination of errors established during calibration. The additional term in the input covariance matrix $\mathbf{C}_\mathrm{Y}$ corresponding to the variation in the sum of partial volumes was set to 0.05^2 to allow for variations in density due to non-ideal mixing. For comparison, the analysis was also performed without a volume constraint by setting the same term to a large value $\gg 1$. The information retrieved after each successive energy bin was added to the measurement data set, was examined graphically by plotting the cumulative values of entropy and degrees of freedom.

8.3.4 Phantom studies

Calcium concentration

A perspex phantom of 10 mm diameter with 2 mm diameter inserts containing water, sunflower oil (fat surrogate), and aqueous solutions of calcium chloride at concentrations of 1, 0.5, 0.25 and 0.125 M was used to investigate the ability of spectral CT to quantify the calcium concentration. The solutions were prepared by diluting a stock solution of 1 M $CaCl_2$ and the phantom scanned at 50 kVp with four detector threshold energies: 10, 16, 22 and 28 keV. Spectral CT images were reconstructed using energy bin projections formed from the net signal between thresholds. The spectral data were decomposed into calcium, fat and water basis images using the constrained least squares decomposition technique described above. A volume constraint on the water and fat content was applied. An informative prior based on the credible distributions for this application was set as follows:

$$\beta_i = 0.01 \text{ mol.L}^{-1}, \gamma_i = \ln 10, \text{ for } i \in \{\text{Ca}\} \tag{8.25}$$

$$\beta_i = 0.01, \gamma_i = \ln 10 \text{ for } i \in \{\text{fat}\} \tag{8.26}$$

$$\beta_i = 1.0, \gamma_i \sim \infty \text{ for } i \in \{\text{water}\} \tag{8.27}$$

This prior reflects the expectation that the atheroma and liver tissues will typically be dominated by the water component but that fat and calcium may potentially be present in large quantities.

The measured calcium concentrations were obtained using the spectral CT averages taken over each material insert. The measured results were plotted against the nominal concentrations. The appropriateness of the model and the validity of the measurement results were tested by calculating the χ^2 goodness-of-fit statistic for each case and comparing the result with the 99% upper critical value for the χ^2 distribution.

Fat mass fraction

A series of phantoms were prepared by blending lean ovine liver with known amounts of fat. The mixtures were loaded into polypropylene containers of 15 mm diameter. A PVC reference tube was also placed into each phantom as a surrogate for calcium. The phantoms were scanned and the material decomposition performed using the same protocol as for the calcium chloride phantom above.

The fat and water components were obtained using the spectral CT averages over a common region of interest. The results were adjusted for density and normalized to total mass to obtain the fat mass fraction for each phantom. The fat mass fraction results for all phantoms were plotted against the nominal values. The χ^2 goodness-of-fit statistics were calculated for each case and compared with an acceptable limit given by the 99% upper critical value for the χ^2 distribution.

8.3.5 Demonstration with biological samples

The material decomposition method was applied to two ex-vivo human atherosclerotic plaques [Zainon, 2012] and a transgenic mouse [Scott et al., 2012]. These biological samples were chosen as they contained easily recognizable regions of calcium and fat within background soft tissue.

The ex-vivo atherosclerotic plaques were prepared for imaging by freezing and manual cutting with a microtome blade. A cooling chamber was used to maintain their temperature near 0°C for the duration of the scans. The specimens were scanned using the same protocol as for the phantom studies. The transgenic mouse was euthanized before imaging and placed within a polypropylene container for scanning. The xiphoid cartilage was used as a marker to locate the abdominal region of interest and the specimen was scanned at 50 kVp with three detector threshold energies: 10, 16 and 22 keV. The spectral data were decomposed into calcium, fat and water basis images using the constrained least squares decomposition technique described above.

The scanning of animal and human tissue was approved by regional Ethics committees: Animal Ethics (University of Otago Animal Ethics Approval C8/07) and Human Ethics (URB/07/02/001).

8.4 Results

8.4.1 Spectroscopy

The CT spectra from all energy bins for each material ($CaCl_2$, $Fe(NO_3)_3$, I_2, fat and water) are shown in Figure 8.2. Except for a small increase in both contrast and random noise at low energies, the spectroscopic responses from the energy bins used in this chapter are similar to those obtained from the signals above energy thresholds obtained previously (Figure 7.8).

8.4.2 Performance assessment

The information entropy and degrees of freedom (d.f.) after a sequence of up to six measurements at different energies determined with and without a volume conservation constraint are given in Figure 8.3. Three d.f. for the {I, fat, water} case are recovered after four spectral measurements without the volume constraint (Figure 8.3a) and after three measurements with the volume constraint (Figure 8.3b). In the case of {Ca, fat, water} the final d.f. is partially

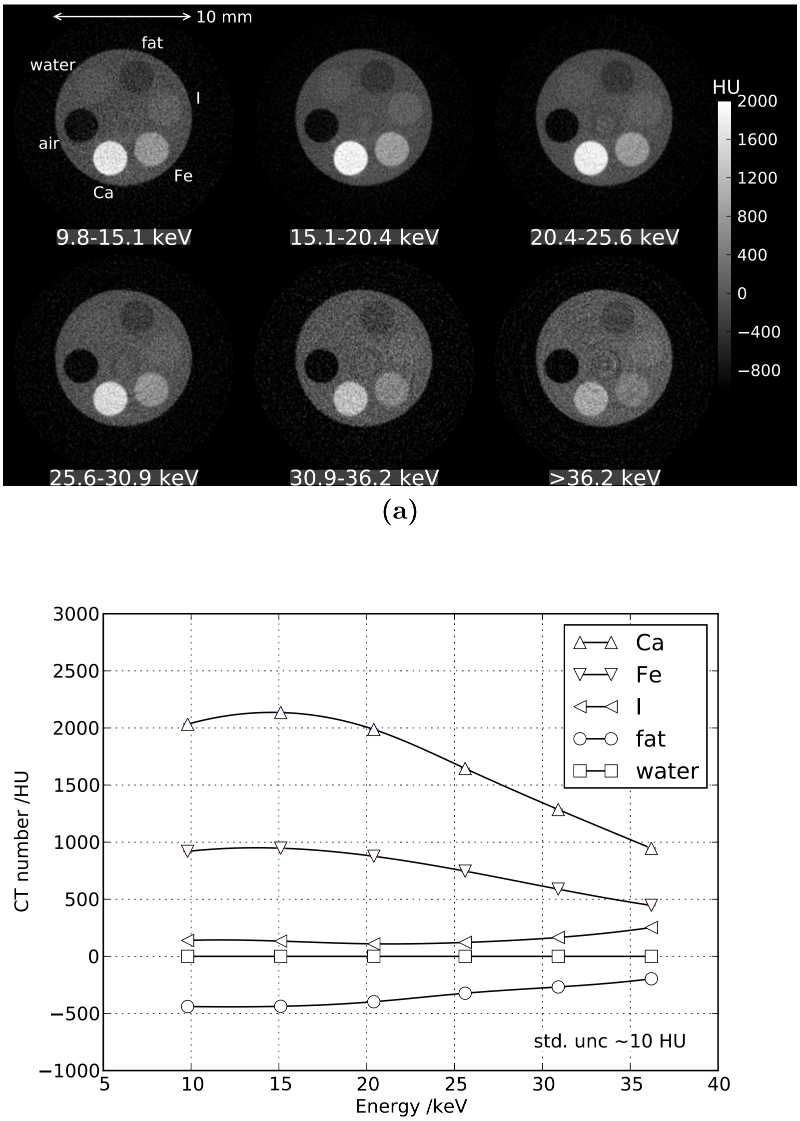

(a)

(b)

Figure 8.2: (a) Spectral CT reconstructions of a perspex phantom containing 2 M calcium chloride, 0.4 M ferric nitrate, 0.01 M iodine, fat surrogate (sunflower oil), water and air. (b) The spectral CT numbers for each basis material plotted for a range of detector threshold energies.

recovered whereas only two d.f. are recovered for {Ca, Fe, water}. For the measurement of {fat, water} two d.f. are recovered after three spectroscopic measurements without the volume constraint but are recovered immediately when the volume constraint is included. In all cases the information entropy improves continuously with additional spectroscopic measurements and is further improved by the use of a volume constraint. The benefit of the volume constraint is greatest where only a few spectroscopic measurements have been made.

8.4.3 Phantom studies

The spectral CT and material component images for the calcium chloride phantom are given in Figure 8.4. Figure 8.5 shows the calcium concentrations measured by spectral CT plotted against the nominal values. There is a good correlation ($R^2 = 0.990$) between the measured and nominal values over the full range of concentrations. The 99% critical value for the $\chi^2(8)$ goodness of fit test statistic is 20.8. The observed χ^2 value is less than the critical value for all measurements.

The spectral CT and material component images for a fat and liver phantom containing 34 % fat by weight are shown in Figure 8.6. The polypropylene container walls appear bright in the fat component image. The PVC tubing appears bright in the calcium image. Figure 8.7 shows the fat mass fractions measured by spectral CT plotted against the nominal values. There is a good correlation ($R^2 = 0.985$) between the measured and nominal values over the full range of fat contents. The 99% critical value for the $\chi^2(8)$ goodness of fit test statistic is 20.8. The observed χ^2 value is less than the critical value for all measurements except that of the phantom containing 100% fat indicating some minor incompatibility in the data and model for this result.

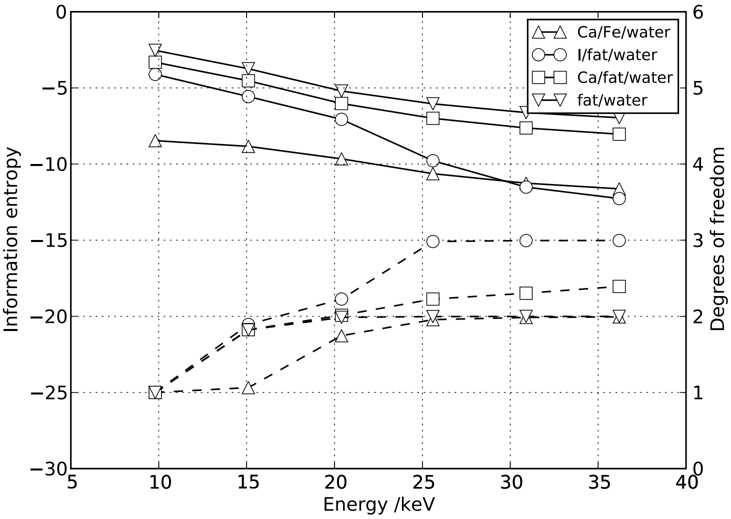

(a)

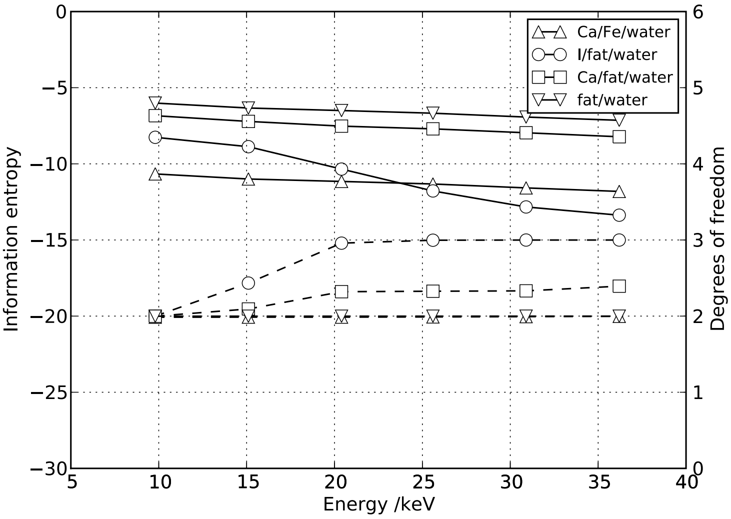

(b)

Figure 8.3: (a) The information entropy (solid lines) and degrees of freedom (dashed lines) retrieved by a sequence of spectral CT measurements for four sets of materials analysed without a volume conservation constraint. (b) The information entropy and degrees of freedom after analysis with a volume conservation constraint on fat and water. The use of the volume constraint reduces entropy and returns the available d.f. with fewer measurements.

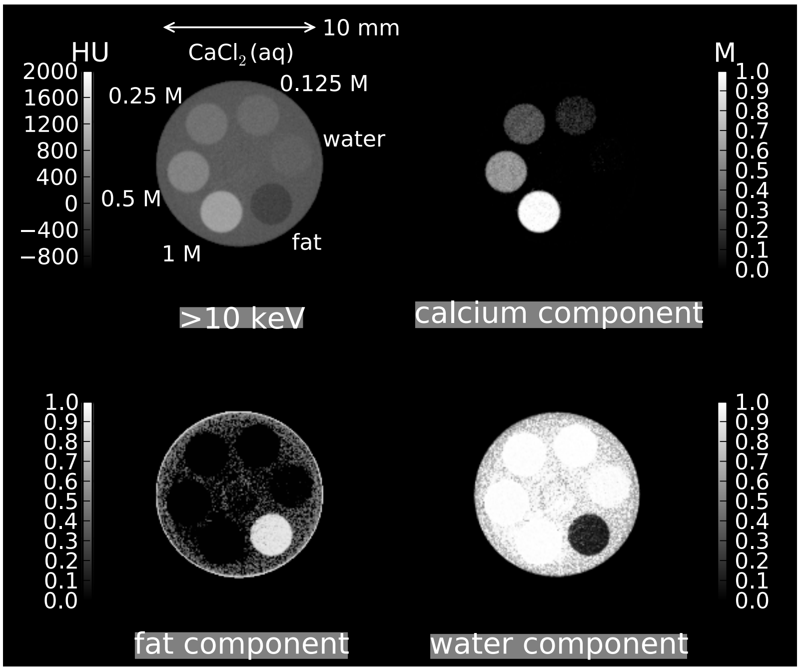

Figure 8.4: A single energy spectral CT image of the calcium chloride phantom and material component images for calcium, fat and water obtained from the analysis of spectral data. The calcium component image is displayed in units of number concentration (mol.L^{-1}). The images for fat and water are in units of volume fraction.

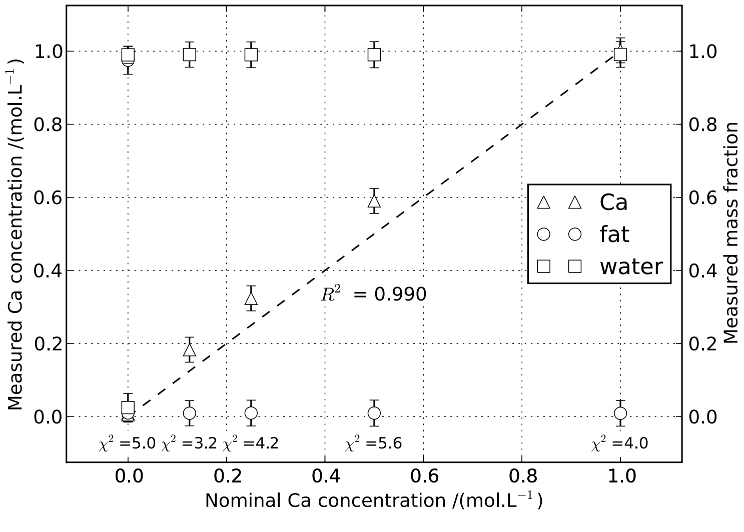

Figure 8.5: The calcium concentration measured by spectral CT plotted against the nominal value for each calcium chloride phantom insert. The correlation coefficient for calcium is $R^2 = 0.990$. The mass fractions of fat and water are also plotted and remain approximately constant.

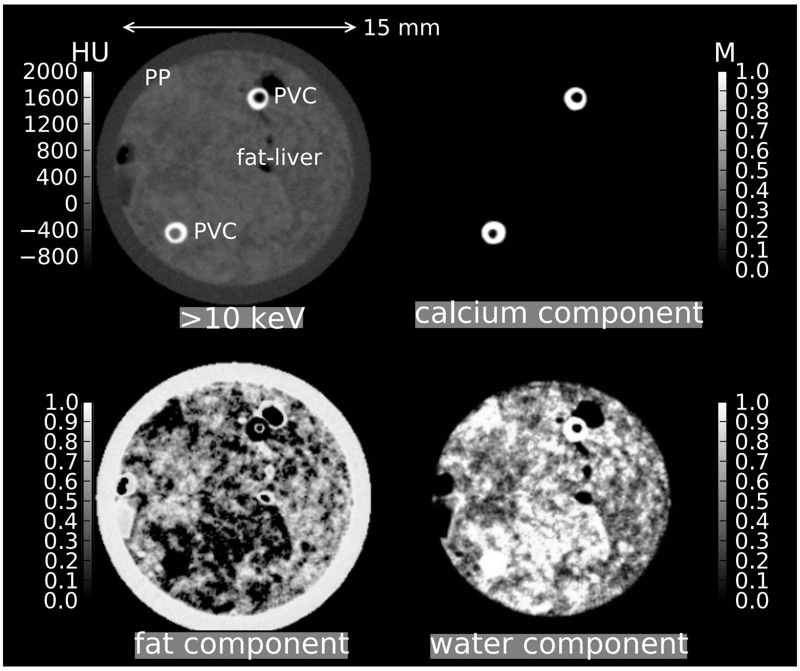

Figure 8.6: A single energy spectral CT image of a fat and liver phantom and material component images for calcium, fat and water obtained from the analysis of spectral data. The calcium component image is displayed in units of number concentration (mol.L^{-1}). The images for fat and water are in units of volume fraction. This phantom contained 34 % fat by weight.

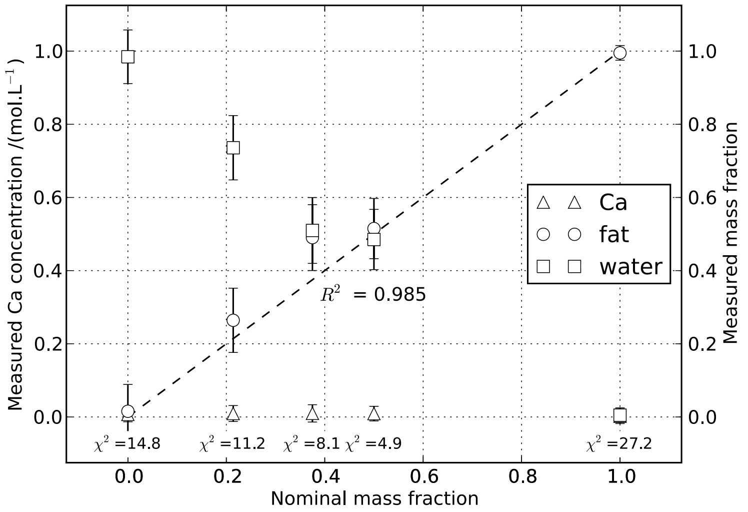

Figure 8.7: The fat mass fraction measured by spectral CT for each fat and liver phantom plotted against the nominal values. The correlation coefficient is $R^2 = 0.985$. The mass fraction of water and the concentration of calcium are also plotted. The mass fraction of water is negatively correlated with that of fat whereas the concentration of calcium is approximately zero for all measurements.

8.4.4 Demonstration with biological samples

Spectral CT and material component images for the human atherosclerotic plaques and the transgenic mouse are given in Figures 8.8 and 8.9. The calcifications in the atherosclerotic plaques and the bones of the mouse are represented in the calcium component images. The polypropylene containers appear bright in the fat component images in all cases.

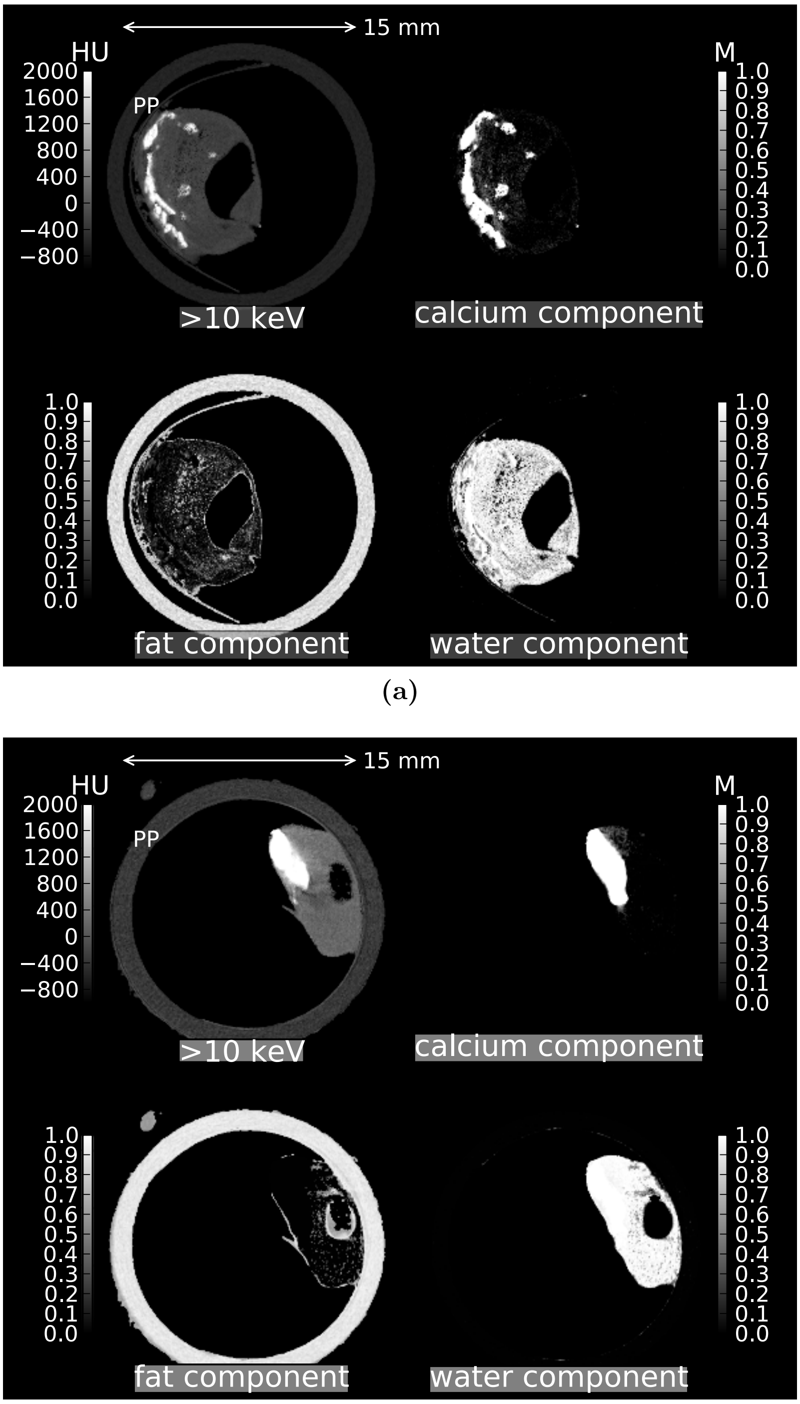

(a)

(b)

Figure 8.8: Single energy spectral CT images of two human atherosclerotic plaques and corresponding material component images for calcium, fat and water obtained from the analysis of spectral data. The images are transverse slices through regions containing calcium, lipid and water-like components. The calcium component images are displayed in units of number concentration (mol.L^{-1}). The images for fat and water are in units of volume fraction.

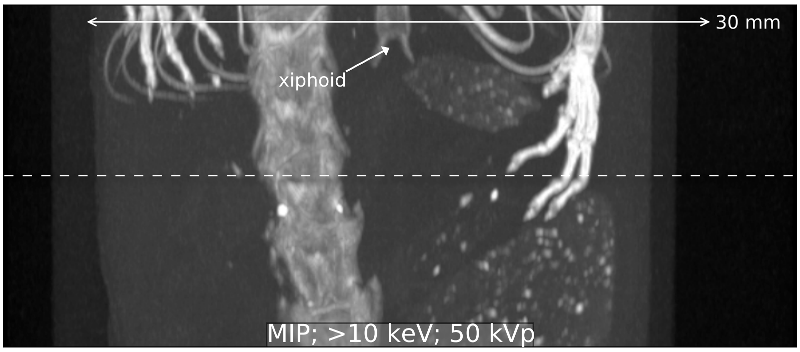

(a)

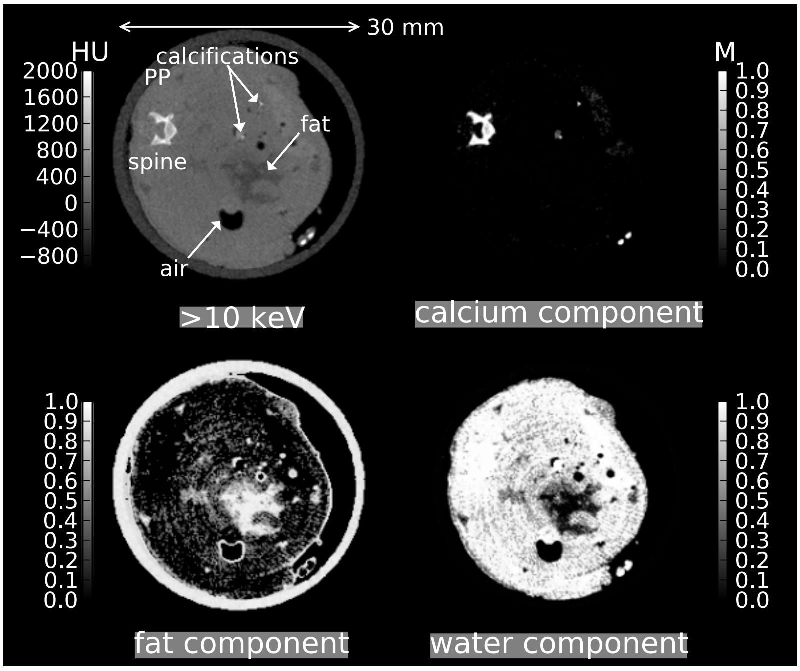

(b)

Figure 8.9: A single energy spectral CT image of a transgenic mouse and material component images for calcium, fat and water obtained from the analysis of spectral data. The images are axial slices located just below the ribs and contain regions of calcium, fat and water-like soft tissue. The calcium component image is displayed in units of number concentration (mol.L^{-1}). The images for fat and water are in units of volume fraction.

8.5 Discussion

In this study a material decomposition method using constrained least squares has been applied to spectral CT measurements using up to six energy bins. The method was applied in the reconstruction image domain to a series of phantoms representing materials relevant to preclinical soft tissue imaging applications. Soft tissue imaging without the use of artificial contrast agents precludes the use of K-edge imaging and the aim of this work was to determine the feasibility of quantitative material decomposition using only the intrinsic characteristics of the soft tissue attenuation coefficients.

In the absence of K-edges, it is sometimes assumed that the dimensionality of the energy dependent attenuation coefficients for soft tissues is just two [Alvarez and Macovski, 1976, Brooks, 1977]. Bornefalk [Bornefalk, 2012] has shown that although there are two dominant components, the intrinsic dimensionality of the attenuation coefficients for low Z materials is at least four. Therefore, it is expected that two material components should be relatively easy to resolve but that additional components would be much harder to distinguish. This is confirmed by the analysis of information entropy and degrees of freedom.

The information entropy and degrees of freedom (d.f.) measures obtained from the analysis of the calibration matrix for soft tissue components indicate that, in some cases, it may be possible to distinguish up to three components, particularly with the assistance of prior constraints and by assuming volume conservation. However, in general, the presence of K-edges within or adjacent to the measurement region will be required to distinguish three or more components. For {I, fat, water} the full number of d.f. is returned after four spectral measurements both with and without the use of a volume constraint. However for {Ca, Fe, water} the analysis is unable to return more than two d.f. even with the use of six energies and a volume constraint. Spectroscopically, iodine is distinct from the soft materials both because of the greater contribution of the photoelectric effect at low energies and the presence of a K-edge at 33.2 keV. In contrast, Ca and Fe are spectroscopically quite similar and neither material has a K-edge within the energy region of interest. Thus, to distinguish Fe from Ca within soft tissues may require the use of additional spectroscopic data or constraints such as mass conservation [Liu et al., 2009]. The information retrieved from the analysis of {Ca, fat, water} is intermediate, indicating some limited ability to independently quantify the components of this set.

The limitations of this study include the use of artificial phantoms rather than biological materials and the exclusion of scattering and beam hardening effects. Firstly, the method was calibrated with phantoms containing known mixtures and solutions, and selected bases representing calcium, fat and water. Thus, for typical biological specimens, fat represents those tissues with the lowest effective atomic number and calcium those with the highest. Because of the volume constraint and the positivity requirement of the prior, all bulk tissues will be decomposed as either fat or water or some mixture of the two and materials of higher effective atomic number than water dispersed within the matrix will be represented by an equivalent amount of calcium. Thus, in the case of the fat and liver phantoms, the PVC inserts were represented in the calcium component image but had no visible effect on the fat or water components. Similarly, although polypropylene was not within the basis set, it was represented within the fat component images as its effective atomic number is most similar to that of fat. The decomposition of the various biological tissues within the plaque and mouse specimens was also consistent with this interpretation. Secondly, beam hardening has been limited through prefiltering of the x-ray beam, and scattering through the use of an air gap [Sorenson and Floch, 1985]. Residual beam hardening and scattering may both produce streak and cupping artefacts in reconstructed images [Glover, 1982, Joseph and

Spital, 1982]. For applications involving large diameter or opaque objects, the effects of scattering and beam hardening may be reduced by data preprocessing corrections [Herman, 1979, Glover, 1982, Ohnesorge et al., 1999].

8.6 Summary and conclusions

1. The work presented in this chapter shows that spectral CT can effectively quantify certain sets of three materials in soft tissues using the proposed method of constrained least squares, and that the efficacy of the method improves with the use of appropriate volume constraints.

2. The use of degrees of freedom and entropy as measures of the effectiveness of the decomposition measurement has been demonstrated. These measures indicate that, for measurements taken using the Medipix3 detector and silicon sensor layer, iron and calcium are practically indistinguishable when present together within soft tissues. For the soft tissue materials considered here, little benefit is obtained from the use of more than four energy bins.

3. The quantification of calcium, fat and water components within soft tissues has been performed in mouse and atheroma equivalent phantoms and demonstrated within biological samples. The quantification results obtained from spectral CT were in good agreement with the nominal values. The decomposition of the various biological tissues within the plaque and mouse specimens was consistent with their expected composition.

Chapter 9

Ex-vivo quantification of fat in mice liver

This chapter applies the quantitative method developed in Chapter 8 to a preclinical study of the fatty liver condition in mice. The fat content of a series of excised mice livers is quantified by spectral CT with Medipix3 and the results compared with those of biochemical analysis. The experimental work was done in collaboration with Dr Nicola Scott and Rafidah Zainon. Special thanks are due to Dr Elzbieta Hiszczynska-Sawicka for performing the biochemical analyses of the liver samples.

9.1 Introduction

The use of spectral CT with spectroscopic photon counting detectors for preclinical research involving small animal models of disease and biological specimens is a promising potential application of this novel technology [Butler et al., 2008b, Anderson et al., 2010]. A substantial amount of work utilizing the K-edges of contrast materials has been done demonstrating the ability of the technology to distinguish contrast materials from body tissues by their attenuation spectra [Roessl and Proksa, 2007, Feuerlein et al., 2008, Schlomka et al., 2008, Firsching et al., 2009, Cormode et al., 2010, Bulte, 2010]. Comparatively little research has been done into the potential of spectral CT applied to soft tissue imaging without contrast agents. Material differentiation and quantification of tissues by spectral CT would provide a useful means of monitoring the status of animal models during longitudinal studies and allow the non-destructive characterization of excised human tissues.

The metabolic syndrome (MetS) is a common condition that currently receives much attention from health researchers. Different organizations use varied, but similar, definitions. The condition is typically diagnosed by the presence of some or all of the following risk factors: abdominal obesity, elevated triglycerides, reduced HDL, increased blood pressure, and insulin resistance. The clinical outcomes of MetS are primarily an increased risk of cardiovascular disease (CVD), and secondarily, an increased risk of type 2 diabetes [Grundy et al., 2004, Reilly and Rader, 2003]. The fat content of the liver has been proposed as an additional indicator of the metabolic syndrome.

In normal patients, consuming low levels of alcohol, non-alcoholic fatty liver disease can be defined as the condition that exists at liver fat levels greater than ∼4–10% [Kotronen and Yki-Jarvinen, 2008, Hoenig et al., 2010]. The extreme eventual outcomes of fatty liver disease are cirrhosis, CVD and type-2 diabetes, however, partly due to the ethical considerations of studying liver fat in humans, the pathogenesis is poorly understood. Consequently, animal models provide a valuable means of studying the disease.

Animal studies of the metabolic syndrome indicate that the role of non-alcoholic liver steatosis is both passive and active [Den Boer et al., 2004]. Triglycerides accumulating in the liver serve as an indicator of MetS and also promote insulin resistance leading to type 2 diabetes. In predictive models of MetS it has been found that liver fat percentage is superior to abdominal obesity as an indicator of the disease [Hoenig et al., 2010]. However, the methods available for measuring liver fat percentage are either of limited ability, or destructive, and therefore not suitable for longitudinal studies. Non-invasive methods such as ultrasound and magnetic resonance imaging and spectroscopy (MRI/MRS) may be used in longitudinal studies, however these are insensitive and expensive respectively [Qayyum et al., 2009]. The fatty liver condition in rabbits has been studied using both clinical CT [Kawata et al., 1984] and dual energy CT [Wang et al., 2003]. In both cases the CT measures were associated with the fat content of the liver, however the methods were unable to provide statistically significant results below ∼6–10% fat by volume.

To date there are no published studies of liver fat content in small animals using spectral CT with spectroscopic photon counting detectors. An early pilot study [Berg et al., 2009] aimed to experimentally extract the attenuation curves from spectroscopic CT scans of blended fat and liver. Although the basic trends observed were qualitatively correct, problems were encountered which prevented accurate quantitative work. In the case of the MARS-CT system using Medipix3 with a silicon sensor layer, it is expected that the low energy measurement range will provide greater contrast and hence better sensitivity than the clinical energies used in the studies above.

Recently Scott et al [Scott et al., 2012] reported on the generation of a new transgenic mouse strain (MetS-Tg) that displays all the principal characteristics of human MetS. Compared with wild type mice, central obesity, atherosclerosis, hypertension and fatty liver tendencies of the transgenic mice all increased and HDL decreased as with the human condition. Scott et al characterized the liver fat content by histology. For longitudinal studies involving these and other mice models, a non-invasive method for analysing liver fat content is required.

A spectral CT study of the lipid content of the excised livers of twelve wild type (WT) and twelve double-knockout (dKO) MetS-Tg mice is now described. The objective of this work is to demonstrate the ability of spectral CT with Medipix3 to quantitatively assay the fat content of mice liver and thereby enable the development of in vivo methods suitable for longitudinal studies of small animal models.

A future study is envisaged whereby the liver fat content of a population of mice would periodically be assayed in vivo by spectral CT from the onset of the fatty liver condition and throughout its progression. At the end of the study the fat mass fractions of the livers of the euthanized mice would be determined by biochemical analysis. The spectral CT method would be calibrated against the biochemical method and the fat mass fraction results from both methods combined to provide a complete description of the liver condition throughout the course of the study. If a limit of detection for fat content of ∼4–10% by weight were achievable with spectral CT then non-invasive classification of the onset of MetS at the level proposed by [Hoenig et al., 2010] would become feasible.

9.2 Methods and materials

9.2.1 Sample preparation and biochemical analysis

Twelve wild type (WT) and twelve double-knockout (dKO) transgenic mice of ages 4–22 months were euthanized. The mice livers were harvested, weighed, and stored at −80°C prior to scanning. For scanning, the livers were defrosted and loaded into polypropylene sample containers. Scanning was performed following the protocol described below. The livers were then returned to the −80 °C freezer awaiting biochemical analysis.

Biochemical analysis of the total lipid content was performed by extraction with hexane under the assumption that only the lipid component would be soluble in the organic solvent. A sample of each liver was weighed and then homogenized with water. The lipid was extracted using hexane and the hexane–lipid solution dried under liquid nitrogen. The lipid mass fraction for each liver was determined by weighing the dried remainder:

$$m_1 = \frac{w_{\text{lipid}}}{w_{\text{liver}}} \tag{9.1}$$

where w_{liver} and w_{lipid} are the weights of the liver sample and lipid remainder respectively.

9.2.2 Spectral CT scanning

The MARS-CT scanner used for this work comprised a micro-focus x-ray tube and Medipix3 detector within a rotating gantry. The Source-Ray SB-80-1K x-ray tube (Source-Ray Inc, Ronkonkoma, NY) had a tungsten anode and included 1.8 mm of aluminium (equivalent) intrinsic filtration. The focal spot size was 33 μm and the maximum tube current and accelerating voltage were 1 mA and 80 kVp respectively. All biological specimen imaging was done with a quad (2 × 2) detector array having a total imaging area of approximately 28 mm × 28 mm. The x-ray tube was operated at 50 kVp and 500 μA for all measurements and the source to object and source to detector distances were 129 mm and 198 mm respectively. The quad Medipix3 photon counting detector with 300 μm thick silicon sensor layer was configured in 55 μm fine-pitch mode and operated in single pixel mode for all acquisitions.

The scanning programme extended over several days. Following the methods developed in Chapter 6, the Medipix3 chips were equalized and an energy calibration was done at the beginning of each day. Samples were then scanned over the remainder of the day without re-calibration.

Each sample was scanned at 50 kVp using 250 projection angles and four detector threshold energies. Projection images were acquired at each position by stepping the detector threshold through a sequence of energy levels and acquiring an image at each setting. Flat field measurements for each sensor position and energy were taken before and after the sample scan so that any variations in detector performance over the duration of the scan could be identified and corrected.

After scanning, the raw projection data were corrected and normalized using a combination of the initial and final flat field projection images. Interpolation was used to replace missing or erroneous image data. Sinograms were formed from the normalized projection data and filtered [Münch et al., 2009] to reduce ring artefacts before the CT data were reconstructed using the *Octopus* commercial CT reconstruction software [Dierick et al., 2004]. All reconstructions were made using an isotropic voxel size of approximately 40 μm^3.

9.2.3 Spectroscopic analysis

The fat mass fraction was determined using the method of Chapter 8 adjusted to suit the particular requirements of this application. A spectroscopic calibration matrix and a prior comprising credible distributions for the materials of interest were used for the material quantification analysis, and the input data were corrected for systematic variations using an additional system response normalization protocol.

Calibration matrix

A spectroscopic calibration matrix, containing effective attenuation coefficients relative to water, for calcium, fat and liver, together with a volume conservation constraint on the total volume of fat and liver was constructed:

$$\begin{bmatrix} y_1 \\ \vdots \\ y_N \\ 1 \end{bmatrix} = \begin{bmatrix} A_{1,\mathrm{Ca}} & A_{1,\mathrm{fat}} & A_{1,\mathrm{liver}} \\ \vdots & \vdots & \vdots \\ A_{N,\mathrm{Ca}} & A_{N,\mathrm{fat}} & A_{N,\mathrm{liver}} \\ 0 & 1 & 1 \end{bmatrix} \cdot \begin{bmatrix} x_{\mathrm{Ca}} \\ x_{\mathrm{fat}} \\ x_{\mathrm{liver}} \end{bmatrix} + \begin{bmatrix} \epsilon_1 \\ \vdots \\ \epsilon_N \\ \epsilon_{N+1} \end{bmatrix} \tag{9.2}$$

The calibration coefficients for calcium were per unit concentration $/(\mathrm{mol.L}^{-1})$ whereas those for fat and liver were per unit volume fraction (dimensionless).

The effective attenuation coefficients relative to water for fat and calcium were obtained by direct spectroscopic calibration as described in Chapter 8. The effective attenuation coefficients for liver relative to water were obtained using numerical estimates of the attenuated projection signals obtained by the methods of Chapter 4:

$$A_{j,\mathrm{liver}} = \frac{\hat{\mu}_{j,\mathrm{liver}}}{\hat{\mu}_{j,\mathrm{water}}} = \frac{\log \hat{y}_{j,\mathrm{liver}}}{\log \hat{y}_{j,\mathrm{water}}}$$

where the estimated projection signals $\hat{y}_{j,i}$ per unit lengths of water and liver were obtained by numerical simulation (Equations 4.16–4.18) using NIST attenuation coefficients [Berger et al., 1998] and the ICRU44 composition for liver (Table 4.1).

Estimating the prior

A prior comprising the following credible distributions of the liver tissue components was defined:

$$\beta_i = 0.001\ \mathrm{mol.L}^{-1}, \gamma_i = \ln 10,\ \text{ for } i \in \{\mathrm{Ca}\} \tag{9.3}$$

$$\beta_i = 0.01, \gamma_i = \ln 10 \text{ for } i \in \{\mathrm{fat}\} \tag{9.4}$$

$$\beta_i = 1.0, \gamma_i \sim \infty \text{ for } i \in \{\mathrm{liver}\} \tag{9.5}$$

This prior reflects the expectation that the liver tissues will typically be dominated by the water-based liver tissue component but that fat may potentially be present in large quantities. High Z materials represented by calcium may be present in only small amounts.

Input data covariance

The input data covariance was calculated from the combination of random (quantum) and systematic effects [Ford et al., 2003]. The random noise component per unit exposure was determined from the covariance $\mathbf{C}_{\text{ran}}$ observed in the water region of interest of the calibration phantom. An estimate of the covariance due to systematic effects $\mathbf{C}_{\text{sys}}$ was obtained from the characterization measurements reported in Chapter 7. The overall covariance on the input data was then obtained from:

$$\mathbf{C}_{\text{Y}} = \mathbf{C}_{\text{sys}} + k\mathbf{C}_{\text{ran}} \tag{9.6}$$

with k inversely proportional to exposure × volume of ROI. Because of the large regions of interest used to obtain the CT numbers for the liver samples, the covariance matrix was dominated by the systematic component. The nominal standard uncertainty on the volume conservation constraint was set to 2%:

$$y_{N+1} = 1, C_{Y_{N+1,N+1}} = 0.02^2 \tag{9.7}$$

Response normalization

Relative effective attenuation values for each sample averaged over a region of interest of area ∼1 cm^2 and depth ∼1 mm were measured and corrected for variations in system performance using the relative effective attenuation values for the polypropylene (PP) sample container as a reference:

$$k_j = \frac{\bar{y}_{j,\text{PP}}}{y_{j,\text{PP}}} \tag{9.8}$$

$$\mathbf{y}' = \text{diag}[k_j] \cdot \mathbf{y} \tag{9.9}$$

$$\mathbf{C}'_{\text{Y}} = \text{diag}[k_j] \cdot \mathbf{C}_{\text{Y}} \cdot \text{diag}[k_j] \tag{9.10}$$

where $y_{j,\mathrm{PP}}$ is the measured sample attenuation value for polypropylene at energy j and $\bar{y}_{j,\mathrm{PP}}$ is the effective attenuation value for polypropylene at energy j averaged over all sample measurements.

Fat mass fraction

The material composition was determined by the constrained least squares method of Chapter 8 using the corrected input data $\mathbf{y}'$ and $\mathbf{C}'_{\mathrm{Y}}$. The fat mass fraction for each sample was calculated from the measured partial volumes and nominal densities of fat and liver:

$$m_2 = \frac{x_{\mathrm{fat}}\rho_{\mathrm{fat}}}{x_{\mathrm{fat}}\rho_{\mathrm{fat}} + x_{\mathrm{liver}}\rho_{\mathrm{liver}}} \tag{9.11}$$

where:

$$\rho_{\mathrm{fat}} = 0.92 \text{ g.cm}^{-3}$$
$$\rho_{\mathrm{liver}} = 1.06 \text{ g.cm}^{-3}$$

9.2.4 Measurement biases and detection limits

The Pearson correlation coefficient R^2 and corresponding P value were calculated to confirm the existence of a linear association between the biochemical and spectral CT analysis methods. Representing the underlying relationship between the results of spectral CT (m_2) and those of biochemical extraction (m_1) as $\hat{Y}$ upon $\hat{X}$ allows the measurement biases and detection limits to be determined by ordinary least products (OLP) linear regression[1] [Ludbrook,

---

[1] Ordinary least squares (OLS) linear regression was not applicable in this case because the biochemical fat mass fractions were not fixed quantities.

2010]:

$$\hat{Y} = \hat{a}_0 + \hat{a}_1 m_1 \tag{9.12}$$

$$\hat{X} = \frac{m_2 - \hat{a}_0}{\hat{a}_1} \tag{9.13}$$

$$\hat{a}_1 = \frac{SD(m_2)}{SD(m_1)} \tag{9.14}$$

$$\hat{a}_0 = \bar{m}_2 - \hat{a}_1 \bar{m}_1 \tag{9.15}$$

The 95% confidence intervals $[a_{i-}, a_{i+}]$ on the regression coefficients were determined by bootstrapping the regression using the fitted residuals [Stine, 1989]. The confidence limits are then the 2.5% and 97.5% percentiles of the bootstrap distribution of coefficients. The existence of bias between the methods was tested by examining the confidence intervals (CI) for the regression coefficients. In cases where the CI for the intercept does not include zero then some constant bias can be assumed. In cases where the CI for the slope does not include unity some proportional bias can be assumed.

The detection limits for the spectral CT fat quantification method were determined from the prediction interval for the regression. The 90% prediction interval was obtained by bootstrapping the regression using the residuals as described above including additional terms ϵ_X and ϵ_Y representing the biochemical and spectral CT measurement errors:

$$\epsilon_X \sim N(0, \hat{\sigma}_X^2) \tag{9.16}$$

$$\epsilon_Y \sim N(0, \hat{\sigma}_Y^2) \tag{9.17}$$

$$\text{where: } \hat{\sigma}_X^2 = \frac{1}{N-2} \sum (m_1 - \hat{X})^2 \tag{9.18}$$

$$\hat{\sigma}_Y^2 = \frac{1}{N-2} \sum (m_2 - \hat{Y})^2 \tag{9.19}$$

The 90% prediction limits are then the 5% and 95% percentiles of the distribution of predicted responses.

Two detection limits were calculated [Currie, 1968]. The critical level Y_C is defined as that measurement (m_2) which, if obtained, would be regarded as significant at a level α (false positive rate). The limit of detection X_D is defined as the amount of substance necessary to be present so that the probability of failing to record a fat mass fraction measurement of at least Y_C is a small value β (false negative rate). These definitions may be written:

$$P(X > 0|Y = Y_C) = 1 - \alpha \tag{9.20}$$

$$P(Y > L_C|X = X_D) = 1 - \beta \tag{9.21}$$

where α and β are the risks of false positive and false negative errors and may be set to convenient small values.

Based on the method of Hubaux and Vos [Hubaux and Vos, 1970], the critical level Y_C in units of m_2 was calculated from the upper prediction limit at zero mean signal. The amount of substance X_D in units of m_1 required to generate a signal at or above the critical level was obtained by projecting the intersection of $Y = Y_C$ and the lower prediction limit onto the X axis.

9.2.5 Radiation dose

From the previous measurements of dose rate in air at the isocentre (Table 7.1), the relevant dose rate and overall sample scanning time were used to estimate the total radiation dose accumulated in the excised samples. The potential radiation dose for future live animal studies was estimated by considering the current scanning time and that which could potentially be saved if two counters were used and if the x-ray source emissions were inhibited during gantry motion (or, equivalently, if the detectors acquired a signal continuously during gantry motion).

9.3 Results

9.3.1 Spectroscopic analysis

The spectroscopic calibration matrix is given in Table 9.1. The first row contains the volume conservation coefficients for the basis materials. The remainder of the table contains the attenuation coefficients relative to water at each energy. The attenuation coefficient units for calcium are per molar concentration whereas those for fat and liver tissue are per unit volume fraction. The attenuation coefficients for liver were calculated using the numerical approximation of Chapter 4 and exceed those of water mainly due to its slightly higher density ($\rho_{\text{liver}} = 1.06$ g.cm^{-3}).

The relative error in the spectral CT attenuation values for the polypropylene containers is shown in Figure 9.1. The variations in attenuation values are correlated between energies and are typically less than ±1%.

The fat mass fractions obtained from spectral CT are given in Table 9.2 and plotted against the results of the biochemical analysis in Figure 9.2. The P values for all of the χ^2 goodness-of-fit test statistics are consistent with the model assumptions and the results are therefore accepted as valid. As expected, the MetS-Tg (dKO) results are clustered towards the upper end of the fat mass range whereas the wild type (WT) results are clustered towards the lower end of the range. There is a significant correlation ($R^2 = 0.72$, $P < 0.001$) between the methods.

Table 9.1: The elements of the calibration matrix. The first row contains the volume conservation constraint coefficients. The remainder of the table contains the effective attenuation coefficients relative to water. The attenuation coefficients for liver exceed those of water mainly due to its slightly higher density.

Energy /keV	A_{Ca} /mol.L^{-1}	A_{fat}	A_{liver}
	0.000	1.000	1.000
10	0.856	0.669	1.076
16	0.856	0.672	1.075
22	0.744	0.706	1.072
28	0.606	0.757	1.067

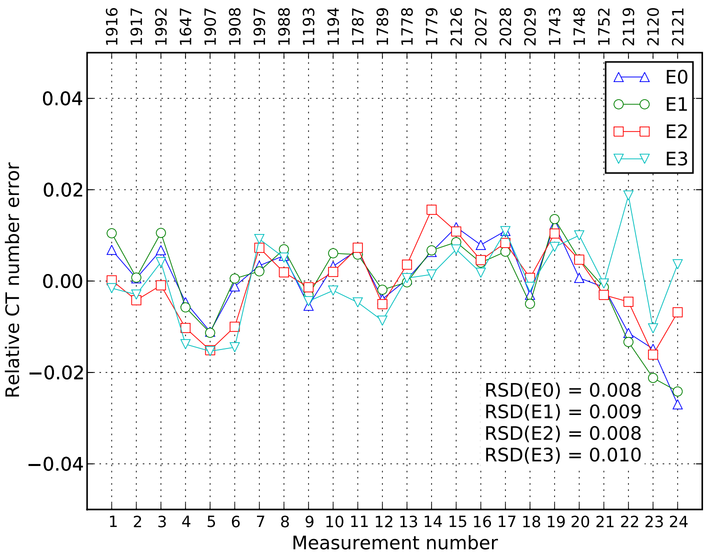

Figure 9.1: The relative errors in polypropylene CT number for each energy plotted against measurement sequence number (bottom axis) and mouse ID (top axis). The relative standard deviations $RSD(E)$ are given for the CT responses at each energy.

9.3.2 Measurement biases and detection limits

The OLP regression coefficients and their 95% confidence intervals were:

$$a_0 = -0.05 \tag{9.22}$$

$$[a_{0-}, a_{0+}] = [-0.07, -0.03] \tag{9.23}$$

$$a_1 = 1.36 \tag{9.24}$$

$$[a_{1-}, a_{1+}] = [1.10, 1.70] \tag{9.25}$$

The 95% confidence interval for the intercept a_0 does not include zero and the confidence interval for the slope a_1 does not include unity and thus there is evidence at the 5% level for both constant and proportional bias between the methods. The regression line may be used to map the results of one method onto the scale of the other.

From Figure 9.2 the fat mass fraction critical level $Y_C = 0.03$ is given by the upper prediction limit at zero mean signal. The limit of detection, being that fat mass fraction necessary to generate a detectable signal, is given by the intersection of $Y = Y_C$ and the lower 90% prediction limit and is $X_D = 0.08$. That is, a fat mass fraction above 8%, as measured by biochemistry, will be detectable by the method of spectral CT.

9.3.3 Radiation dose

From Table 7.1 the dose rate measured at the isocentre at the current settings was 1.04 mGy.s^{-1}. The total scanning time per sample was 2850 s. Thus, the total accumulated dose per sample was 2850 × 1.04 mGy.s^{-1} = 3.0 Gy.

The total scanning time comprised time for 314 acquisitions (250 projection angles and 64 flat field frames) over four energy thresholds plus time for gantry

Table 9.2: Biochemical (m_1) and spectral CT (m_2) mass fraction results for fat in liver. Estimated standard uncertainties (u) and goodness-of-fit statistics (χ^2) with corresponding P values are given for each CT result.

ID	Genotype	m_1	m_2	u	χ^2	P
1916	dKO	0.066	0.025	0.051	6.9	0.551
1917	dKO	0.073	0.045	0.051	4.3	0.832
1992	dKO	0.058	0.016	0.035	4.4	0.822
1647	WT	0.029	0.007	0.015	5.9	0.655
1907	WT	0.028	0.005	0.009	4.8	0.783
1908	WT	0.037	0.007	0.015	4.7	0.786
1997	dKO	0.081	0.086	0.050	5.2	0.737
1988	dKO	0.068	0.041	0.053	7.0	0.531
1193	WT	0.068	0.008	0.018	5.7	0.677
1194	WT	0.059	0.012	0.031	6.7	0.565
1787	dKO	0.060	0.032	0.052	5.4	0.719
1789	dKO	0.057	0.011	0.026	4.9	0.766
1778	dKO	0.067	0.029	0.053	8.1	0.421
1779	dKO	0.121	0.116	0.050	8.0	0.434
2126	WT	0.035	0.008	0.017	9.0	0.342
2027	WT	0.065	0.010	0.021	11.7	0.165
2028	WT	0.049	0.008	0.020	9.0	0.341
2029	WT	0.037	0.009	0.024	7.3	0.501
1743	dKO	0.069	0.036	0.052	6.9	0.545
1748	dKO	0.024	0.011	0.024	4.4	0.821
1752	dKO	0.051	0.008	0.015	7.7	0.468
2119	WT	0.043	0.006	0.011	3.3	0.913
2120	WT	0.036	0.005	0.009	5.6	0.697
2121	WT	0.052	0.004	0.007	2.5	0.963
MEAN	WT	0.045	0.008	0.016	6.4	0.616
SD	WT	0.013	0.002	0.007	2.5	0.232
MEAN	dKO	0.066	0.038	0.043	6.1	0.637
SD	dKO	0.021	0.031	0.013	1.4	0.154
MEAN	ALL	0.056	0.023	0.030	6.2	0.626
SD	ALL	0.021	0.027	0.017	2.0	0.197

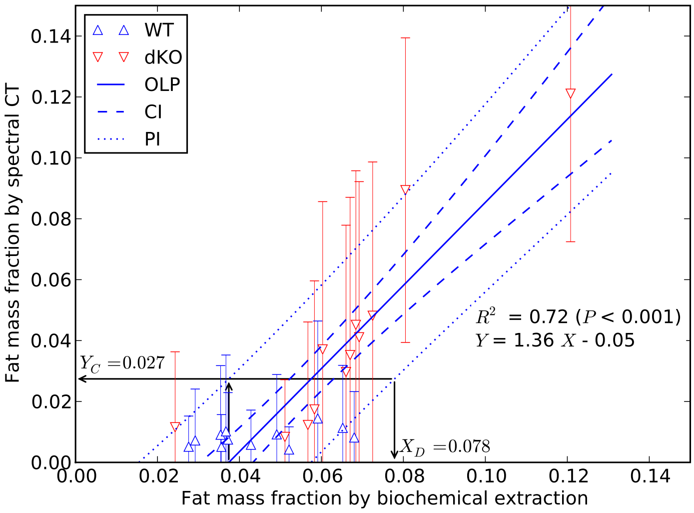

Figure 9.2: Fat mass fraction results by spectral CT plotted against those of biochemical extraction. The wildtype (WT) and double knockout (dKO) genotypes are indicated by the blue and red markers respectively. The OLP regression is shown (blue solid line) together with the 90% confidence interval for the regression (blue dashed lines) and the 90% prediction interval (blue dotted lines). The critical level is that signal just significant above the spectral CT background and is denoted Y_C. The limit of detection X_D is the minimum quantity required to produce a detectable signal.

movements. The acquisition times for each energy were 0.6, 0.7, 1.5, and 4.0 s, amounting to a total acquisition time of 2135 s. That is, the x-ray beam utilization was ∼75% and the total dose could be reduced by 25% if the x-ray output was inhibited during gantry movement or if data were acquired continuously during gantry rotation. If two counters per pixel were used then the acquisition time would drop by a further factor of $\frac{0.7+4.0}{0.6+0.7+1.5+4.0} = 69\%$ resulting in a potential minimum accumulated dose of approximately 1.6 Gy.

9.4 Discussion

This study has shown that fat in excised livers can be quantified by spectral CT with Medipix3. Although the study is limited to ex vivo quantification, it can, nevertheless, be inferred from the current result that in vivo quantification of fat in mice livers is feasible at the required detection limits.

The ex vivo CT mass fraction results and biochemical data are strongly correlated ($R = 0.72, P < 0.001$). However, the 95% confidence interval for the OLP intercept does not contain the origin and the 95% confidence interval for the slope does not contain unity and we must therefore conclude that there is some significant bias between the methods. The sources of bias may include errors in the spectroscopic calibration, spectral artefacts, and deficiencies in the method used for biochemical analysis. Further work may reduce these effects at source, nevertheless, it is likely that some bias between the methods will remain. Following the OLP regression analysis procedure used in this chapter it is possible to eliminate the bias between methods by calibrating one against the other.

With the MARS-CT scanner configuration used for this study, the limit of detection X_D for liver fat mass fraction is approximately 8% and thus fat in mice livers containing at least this amount will be detectable by spectral CT. This potentially allows the onset and progression of the disease to be studied non-destructively. However, for in vivo studies, the effects of radiation dose on the living specimen must also be considered together with those of increased specimen size on imaging performance.

Both the random and systematic uncertainties will be adversely affected by increases in specimen size. The photon count rate at the detector will reduce and the random noise contribution to the reconstructed data will increase. At the same time, larger specimens may cause an increase in the magnitude of scattering and beam hardening artefacts. It should also be noted that the diameter of an adult mouse is ∼30 mm and this is too large to be imaged by a single acquisition using the current 2×2 quad chip. At the current geometrical magnification, a chip array of at least 4×1 will be required.

The increase in random noise due to the reduction in primary signal with increased specimen size is not of particular concern and recovering signal losses by increasing the x-ray flux need not be considered. The fatty liver analysis is done on the basis of the signal contained within large regions of interest and it is therefore systematic errors that dominate; the method can tolerate a substantial increase in the random noise component. The systematic effects due to specimen size are of greater concern and include, predominantly, the physical effects of scattering and beam hardening.

Scattering and beam hardening corrections have not been considered in this study of excised livers because the sample sizes are sufficiently small that these effects can be neglected. In addition, beam hardening has been limited by prefiltering of the x-ray beam and scattering by the use of an air gap. Although these methods may not be sufficient for larger sample sizes, other well established data preprocessing methods exist [Herman, 1979, Glover, 1982, Ohnesorge et al., 1999] for correcting these effects.

Although the current total radiation dose estimate of 3.0 Gy is rather high compared with the $LD_{50}(30)$ for a mouse of ∼7 Gy [Sato et al., 1981], potential improvements in scanning protocol may reduce this to ∼1.6 Gy. As mentioned above, a chip array of at least 4×1 is required to image a mouse with a single acquisition as assumed for this dose estimate. These dose estimates apply to the tissue within the x-ray beam and are not necessarily total body doses. Collimation of the beam, so that only the tissue being imaged is irradiated, will minimize the total effective dose to the mouse.

Finally, there are a number of technological improvements to be implemented that will further enhance the performance of spectral CT with Medipix3 for fatty liver quantification and ensure that in vivo studies are feasible. The

Medipix3 design is being revised to eliminate electronic defects seen with the version used here. The revised Medipix3 detector should have better temporal stability and will include an improved implementation for charge summing. These improvements will, firstly, reduce the non-quantum sources of error and, secondly, improve the spectroscopic signal to noise ratio. Both are factors that should directly benefit this application. Considering all of these issues together with the current performance levels for excised liver, it is concluded that in vivo quantification of fat in liver by spectral CT with Medipix3 is feasible at the levels required for monitoring the onset and progression of fatty liver disease.

9.5 Summary and conclusions

1. The work presented in this chapter shows that spectral CT can effectively quantify the fat content of excised livers. Considering this result together with the impact of both the limitations of this ex vivo study and the potential for improved performance offered by forthcoming revisions to the Medipix3 detector, it is concluded that in vivo quantification of fat in mice livers down to useful levels by spectral CT is feasible.

2. Some bias exists between the biochemical and spectral CT methods for fat quantification. There are several possible contributory factors including the spectroscopic calibration, spectral artefacts, and deficiencies in the method for biochemical analysis. Any bias that remains after the various sources of error have been minimized can be corrected by calibrating one method against the other.

3. The limit of detection for quantifying the fat mass fraction of excised livers was found to be 8%. This limit is influenced by systematic error contributions such as non-quantum electronic effects. Extrapolating the current result to in vivo studies requires that systematic errors are

controlled and corrected where possible.

4. Electronic error contributions are currently controlled through methods within the measurement protocol such as flat field correction, frequent adjustments of the threshold equalization and energy calibration, as well as system normalization measurements. These methods, or their equivalent, should remain as part of the measurement procedure even though the demands for such measures may reduce as the detector design is revised and improved.

5. The physical effects of beam hardening and scattering have been limited by prefiltering of the x-ray beam and the use of an air gap. These methods may not be sufficient for larger or more opaque samples, and other well established data preprocessing methods may be implemented as necessary to ensure that in vivo studies with spectral CT are successful.

Chapter 10

Conclusion

This chapter summarizes the main results and conclusions of the thesis and assesses whether the overall aim of the thesis has been achieved. The chapter concludes with a discussion of how the work may be extended.

10.1 Summary

In *Chapter 2* it was noted that, within clinical computed tomography, spectral CT is implemented almost exclusively in the form of dual energy CT using standard energy integrating scintillator detectors. Currently, spectroscopic photon counting detectors are not able to meet clinical requirements for size, stability and throughput. However, the demands of preclinical imaging are less severe, and spectroscopic photon counting detectors such as those of the Medipix family are more easily applied to this area.

Researchers within the MARS group are currently studying the application of spectral CT preclinical research in areas such as: functional imaging with nanoparticles, characterization of atherosclerotic plaques and longitudinal studies of mice models of human diseases such as fatty liver (metabolic syndrome). The application of improved methods based on spectral CT to these areas will have widespread clinical benefits.

Spectral decomposition may be applied in either the projection or reconstruction image domains. Traditional methods represent the spectral data as photoelectric and Compton interaction components. Where K-edges are present these methods fail and material bases must be used instead. For preclinical applications using spectroscopic photon counting detectors, projection domain decomposition methods require an accurate model of the detector response. Compton scattering, fluorescence and charge sharing processes within the detector make this difficult to obtain. In comparison, reconstruction domain methods are relatively simple to implement and are based on empirical calibration. A calibrated reconstruction domain method is therefore preferable for preclinical applications with Medipix3.

Chapter 3 reviewed some basic aspects of x-ray interactions and imaging. The main interaction processes relevant to this work are the photoelectric and Compton effects. These are energy dependent and characteristic of each element but virtually independent of chemical form. For soft tissues ($Z \leq 20$) there are no absorption edges within the relevant energy range and thus the attenuation curves for these materials are often represented by just two basis functions. However, this is an approximation, and it is reported that the intrinsic dimensionality of the attenuation coefficients for soft tissues is at least four.

The principles of computed tomography and spectral CT were reviewed in the first part of *Chapter 4*. The value reconstructed by computed tomography is the effective attenuation coefficient. It is dependent on the composition of the object being scanned and the spectral properties of the system. These dependencies provide the basis for decomposing spectral data sets into physical, empirical or material components.

The second part of *Chapter 4* simulated the measurement of effective attenuation curves by spectral CT with Medipix3. Measurements of the effective attenuation coefficients for clinically relevant materials were simulated in both single pixel and charge summing modes. The simulations indicated that, in principle, spectral CT with Medipix3 would provide a good measure of the energy dependent attenuation coefficients, particularly when operated in charge summing mode.

A prototype x-ray camera incorporating Medipix3 was developed by the MARS research group. The performance of the prototype MARS-Medipix3 camera was experimentally characterized in *Chapter 5*. The counting distribution in single pixel mode was approximately Poissonian and high quality images were obtained. However, in charge summing mode temperature related electronic instabilities and pixel allocation biases were observed that prevented high quality imaging. Nevertheless, it was possible to demonstrate that charge summing mode improves spectroscopic performance as intended by the designers. It was concluded that the performance of the MARS-Medipix3 camera operating in single pixel mode would be acceptable for tomographic imaging but that some form of forced cooling was advisable to improve electronic stability. The candidate presented the material in *Chapter 5* at the *International Workshop on Radiation Imaging Detectors (2010)* in Cambridge, UK and prepared a corresponding article for publication in the *Journal of Instrumentation* [Ronaldson et al., 2011a].

A MARS camera incorporating a quad Medipix array with Peltier cooling was configured and calibrated in *Chapter 6*. This chapter developed and tested new methods for calibrating the global DACs and equalizing the pixel thresholds. Energy calibration of the chip array was performed using fluorescence x-rays generated by the interaction of the open beam source with thin metal foils and the responses of the individual chips matched using the open beam. It was concluded that these methods enabled the Medipix array to be operated as a homogeneous large area imaging device.

In *Chapter 7* the x-ray camera was installed in the MARS-CT system and the performance of the system characterized in terms of various standard measures. Spatial resolution was 110 μm. The CT number noise variance was found to be inversely related to exposure but was not quantum limited. The spectroscopic performance was also measured using a phantom containing clinically relevant materials. The experimental results for spectroscopic CT number were in good agreement with the simulations of *Chapter 4*. In single pixel mode, the use of energy bins provided slightly better contrast than total counts over threshold. Because of the problems with stability and pixel allocation noted earlier, all measurements were performed in single pixel mode and charge summing mode was not tested experimentally. A presentation based on the material in this chapter was prepared by the candidate and presented at the *IEEE Nuclear Science Symposium and Medical Imaging Conference (NSS/MIC) (2011)* in Valencia, Spain by Dr Anthony Butler on behalf of the MARS team. The candidate prepared a corresponding paper for publication in the conference proceedings [Ronaldson et al., 2011b].

The potential for quantifying biological soft tissue materials by spectral CT with Medipix3 was assessed in *Chapter 8* using the MARS-CT system. The spectroscopic calibrations for iron, calcium, fat and water were analysed in terms of information entropy and degrees of freedom. It was found that spectral measurements with MARS-CT as configured were insufficient to distinguish iron from calcium within soft tissues. Calcium, fat and water components were successfully quantified in mouse and atheroma equivalent phantoms and the ability to distinguish these materials was demonstrated qualitatively in biological specimens. The candidate presented the material in *Chapter 8* at the *Radiological Society of North America Scientific Assembly and Annual Meeting (2011)* in Chicago, USA and has prepared a corresponding manuscript for publication [Ronaldson et al., 2012].

In *Chapter 9*, the spectral decomposition method was applied to a study of the fat content of excised mice livers. The fat mass fractions of the livers from twelve wild type and twelve transgenic mice were quantified by spectral CT and the results compared with those of biochemical analysis. The correlation was statistically significant and a fat mass fraction limit of detection of 8% was reported. Although there were some limitations with the ex vivo study, the results were sufficient to affirm the feasibility of spectral CT for in vivo monitoring of the fatty liver condition in mice.

In addition to the presentations and publications mentioned above, this thesis has contributed to the research of the MARS team through other work as described in *Academic Contributions* provided on page xv.

10.2 Discussion and conclusions

The aim of this thesis was to assess the feasibility for enhancing preclinical soft tissue imaging by spectral CT with Medipix3. The thesis has been investigated through development and characterization of the MARS-CT system and the feasibility of enhanced soft tissue imaging affirmed by the development and validation of a practical method for material decomposition in the image reconstruction domain.

The limitations of this study include electronic issues with the Medipix3 detector that have adversely affected imaging performance in single pixel mode and prevented experimental investigation of charge summing mode. Although the performance of Medipix3 in single pixel mode is adequate in most respects, non-quantum systematic effects dominate the overall measurement uncertainties. Spectroscopic performance in charge summing mode is much improved over single pixel mode. Unfortunately, technical limitations with this first version of Medipix3 prevent the use of charge summing mode for spectral imaging. It is expected that improvements in chip design will address these problems, and later versions of Medipix3 will provide improved performance in single pixel mode and enable spectral CT with charge summing mode to be tested experimentally.

The spectral decomposition method developed for this thesis is simple and flexible. The soft tissue applications that are the focus of this thesis do not have K-edges available within the spectrum, and spectral imaging methods must be able to detect more subtle characteristics. Traditional methods for spectral decomposition based on just two empirical or physical components are unable to do this. Other published methods use an arbitrary number of material bases but are implemented in the projection domain and thus require an accurate forward model of the detection process. This is difficult to obtain. Therefore this work has implemented material decomposition through practical calibration in the reconstruction image domain. This implementation includes a novel method (in this area) for assessing the effectiveness of spectral CT in terms of the information retrieved by the measurement.

Analysis of the information content of the attenuation spectra indicates that, as expected, the presence of K-edges will significantly enhance the detectability of higher Z materials. For soft tissue materials, spectral information from the current system is insufficient by itself to distinguish many biological materials. For some current applications, this has been resolved by imposing constraints based on the physical properties of the materials being examined. Thus, with volume constraints on the bulk materials of the soft tissue matrix, and prior distributions that require positivity for all components, calcium, fat and water within soft tissues may be quantified down to useful levels.

Although developed for soft tissue applications, the method is quite general and in principle could be applied to other areas such as functional imaging with nanoparticles. Imaging of artificial contrast agents relies upon the detection of absorption edges from high Z materials such as gold. For gold, the K-edge is at 80 keV and alternative sensor materials such as CdTe would be required. It is a strength of the reconstruction image domain calibration method that the response of any arbitrary detector type can be included in the spectroscopic calibration without requiring any modification to the technique.

10.3 Outlook

10.3.1 Preclinical applications

Limitations with the currently available technology were encountered during this study that could be addressed by further work. Also, some aspects of the current work are sufficiently general that the scope could easily be extended to include other application areas.

Due to instabilities and biases associated with the current design of Medipix3, it has not been possible to experimentally assess the impact of charge summing mode on the performance of spectral CT imaging. It is expected that, when available, charge summing mode will improve spectroscopic imaging performance and thereby increase intrinsic soft tissue contrast. An important piece of future work is therefore to experimentally measure the soft tissue imaging performance in charge summing mode with the revised version of Medipix3.

Finally, the material decomposition method developed here has been applied to soft tissues in the absence of K-edges. It is, however, a sufficiently general method that K-edge imaging should be possible with little or no modification. Although practical work in this thesis has been restricted to the silicon sensor layer, the method of calibration is applicable to other sensor materials such as CdTe and GaAs. Therefore extension of the experimental work to include alternative sensor materials and other preclinical research areas such as functional imaging with nanoparticle contrast agents is recommended.

10.3.2 Potential for clinical application

In this work it has been shown, albeit on a small scale, that spectral CT can be used to improve soft tissue imaging and quantify various material components. In principle, similar methods could be applied to clinical spectral CT so that it would become more competitive with MRI for soft tissue imaging whilst maintaining the benefits of higher spatial resolution. Other researchers are working on the application of spectral CT to functional imaging problems using novel molecular contrast agents [Popovtzer et al., 2008, Cormode et al., 2010, Pan et al., 2010]. Using these contrast agents, clinical spectral CT could enable metabolic imaging investigations without the need for local access to sources of radiopharmaceuticals and hence high resolution functional imaging studies would become more widely available than they are at present.

There are, of course, many technical obstacles to be overcome before spectral CT with fine pitch spectroscopic photon counting detectors can be applied to human-scale clinical CT. These include the development of spectroscopic sensor layers with physical and mechanical properties suitable for clinical imaging, as well as engineering developments necessary to cope with the increased count rates. These challenges are already being investigated [Roessl et al., 2008, Taguchi et al., 2009, Barber et al., 2010, Shikhaliev and Fritz, 2011] and we may eventually see spectral CT systems with fine pitch spectroscopic photon counting detectors providing enhanced soft tissue and functional imaging information for clinical diagnosis. The development route may include other imaging modes, such as planar radiography and body-part CT scanning, and it will be interesting to see what range of benefits can be extracted from the use of this technology.

Appendix A

Medipix3 configuration

Medipix3 is a hybrid detector ASIC comprising 256 × 256 readout channels and may be bump-bonded to various sensor layers such as Si, GaAs or CdTe. At manufacture, the chip may be configured either in fine pitch mode by bump-bonding every readout channel to provide a pixel pitch of 55 μm, or, in spectroscopic mode by bump bonding alternate rows and columns of channels to provide a pixel pitch of 110 μm. Each readout channel contains two 12-bit counters and two programmable thresholds. Thus, in spectroscopic mode a total of eight counters can be used simultaneously. The selection of pixel pitch is made at manufacture, after this, the user is able to configure the chip for operation using 25 global DACs and individually adjust the configuration of each pixel using 13-bits of a 24-bit control register.

The global DACs (Table A.1) bias the analogue circuitry and control chip-wide functions such as the discriminator levels for the counters. Each Medipix3 readout channel has two counters giving a total of up to eight counters per pixel when configured in spectroscopic mode. The discriminator threshold for each counter is programmable at the chip level by means of a global DAC (Threshold0–Threshold7).

The pixel DACs (Table A.2) are used to configure each readout channel. Configurable properties include the selection of low or high gain and the application of an adjustment current for counter threshold equalization. Due to manufacturing variations, the intrinsic level of the counter thresholds are widely distributed and thus the responses of the individual pixels to a uniform flux are not consistent across the chip. Before acceptable images can be acquired it is necessary to equalize the intrinsic counter thresholds so that each pixel counter responds in a similar manner to a given x-ray flux. The ThresholdN and DACpixel global DACs and a 5-bit pixel level adjustment for each counter (THA and THB) are available for this purpose. Where necessary, the operation of any pixel may be inhibited by setting a mask bit.

Table A.1: The nominal index values and functions for each of the 25 Medipix3 global DACs. Compiled from [Ballabriga, 2009b, Ballabriga, 2009a, Talla, 2011].

ID	Nominal value (CSM)	Nominal value (SPM)	Function
Threshold0	–	–	Set counter threshold.
Threshold1	511	511	Set counter threshold.
Threshold2	511	511	Set counter threshold.
Threshold3	511	511	Set counter threshold.
Threshold4	511	511	Set counter threshold.
Threshold5	511	511	Set counter threshold.
Threshold6	511	511	Set counter threshold.
Threshold7	511	511	Set counter threshold.
ThresholdN	128	64	Set the negative threshold adjustment current.
DAC_pixel	255	128	Set the positive threshold adjustment current.
Preamp	128	128	Bias the preamp. Controls the current output of the preamplifier stage. With increasing Preamp, the shaper output gain initially increases then reaches a plateau.
Ikrum	8	8	Set the Ikrum current. Controls the maximum leakage current sink and return to zero characteristics. Noise increases with Ikrum.
Shaper	255	255	Bias the shaper circuit. Controls the current output of the first order semi-Gaussian shaping stage. Gain increases with increasing Shaper (and also temperature).

continues on next page

continued from previous page

ID	Nominal value (CSM)	Nominal value (SPM)	Function
Disc	255	255	Bias the discriminator.
Disc_LS	180	180	Bias the discriminator.
Delay	128	128	Controls the discriminator pulse output width.
TP_BufferIn	128	128	For testing.
TP_BufferOut	128	128	For testing.
RPZ	128 (640 mV)	128 (640 mV)	Set pole-zero compensation. Reduces analogue pulse over/under-shoot and improves bandwith.
GND	64 (520 mV)	64 (520 mV)	Set the ground reference value for the preamplifier CSA.
TP_REF	128	128	For testing.
FBK	128 (800 mV)	128 (800 mV)	Bias the preamplifier feedback reset path. The voltage V_{fbk} is pulled high with increasing temperature.
Cas	128 (650 mV)	128 (650 mV)	Bias the pixel cascade circuit. The voltage V_{Cas} is pulled low with increasing temperature. Variations in V_{Cas} affect the zero threshold location - most significantly when pole-zero compensation is activated. An external DAC must be used.
TP_REFA	255	255	For testing.
TP_REFB	255	255	For testing.

Table A.2: The pixel DAC configuration bits and their position within the 24-bit configuration register. Reproduced from [Ballabriga, 2009b].

ID	Domain	Position	Function
TestBit	Analogue	15	Set to 1 for testing. Set to 0 for normal use with sensor layer.
GainMode	Analogue	8	Configure the shaper gain mode. Set to 0 to operate in HGM.
MaskBit	Digital	21	Set to 1 to mask (disable) the pixel.
THA<0:3>	Analogue	17, 5, 6, 19	Positive current threshold adjustment bits for the 4-bit DAC associated with counter 0.
THA4	Analogue	7	Set to enable the negative current adjustment associated with the 4-bit DAC associated with counter 0.
THB<0:3>	Analogue	18, 22, 20, 16	Positive current threshold adjustment bits for the 4-bit DAC associated with counter 1.
THB4	Analogue	4	Set to enable the negative current adjustment associated with the 4-bit DAC associated with counter 1.

Appendix B

Charge sharing model

Fine-pitch pixelated detectors operating in single pixel mode suffer from a phenomenon known as charge sharing. The localized charge created in the sensor layer of the detector by a photon interaction, disperses as it migrates during the collection process. Some portion of the charge is therefore erroneously allocated to the neighbouring pixels (Figure B.1(a)).

The magnitude of the charge sharing effect depends upon the ratio of pixel pitch to the width of the charge distribution. We will assume that the charge cloud distribution is a 3-dimensional Gaussian $G(x, y)$ with characteristic width σ_Q. The width of the charge cloud depends upon the collection time and hence on the depth of the initial interaction and the strength of the collecting electric field. For 300 μm silicon based Medipix3 detectors, a characteristic width of ∼7 μm is typical [Ballabriga, 2009a, Zeller, 2009] and, for simplicity, we will model the charge sharing process using this constant characteristic width.

We can rescale the pixel coordinates (x, y) to be in units of this characteristic width:

$$r = \frac{x}{\sqrt{2}\sigma_Q} \tag{B.1}$$

$$s = \frac{y}{\sqrt{2}\sigma_Q} \tag{B.2}$$

Considering the closest pixel boundaries in the positive r and s directions, the proportion of a Gaussian charge cloud $G(x, y)$ shared across a boundary defined by two orthogonal limits $(r > R, s > S)$ is:

$$Q(R,S) \propto \int_R^\infty \int_S^\infty e^{-r^2-s^2} ds\, dr \tag{B.3}$$

$$= 1/4\,\pi\ (\mathit{erf}\ (S)\ \mathit{erf}\ (R) - \mathit{erf}\ (S) - \mathit{erf}\ (R) + 1) \tag{B.4}$$

Considering the primary pixel as four equal quadrants, the majority of charge is lost across the boundary with the three pixels abutting the quadrant in which the charge was initially created. In Figure B.1(a) this is the boundary of pixel E with pixels F, B and C. We will assume that charge lost to the further boundaries is negligible by comparison.

Considering the right pixel boundary R, the total charge lost is $Q(R, 0)$. Similarly the total charge lost across the upper pixel boundary is $Q(0, S)$ and the charge common to both integrals is $Q(R, S)$. Thus the secondary, tertiary and quaternary charges lost from pixel E to pixels F, B and C respectively are proportional to:

$$Q_2 = Q(R,0) - Q(R,S) \tag{B.5}$$

$$Q_3 = Q(S,0) - Q(R,S) \tag{B.6}$$

$$Q_4 = Q(R,S) \tag{B.7}$$

and the primary, unshared charge is proportional to:

$$Q_1 = \pi - (Q_1 + Q_2 + Q_3) \tag{B.8}$$

The effect of charge-sharing in single-pixel mode is significant for pixels F, B and C for Q anywhere in the upper-right quadrant of pixel E. Whenever the charge is deposited below the diagonal $r = s$ (as shown) then pixel F will receive the secondary charge whilst pixels B and C receive the tertiary and quaternary charge proportions respectively. Whenever the charge is deposited above this diagonal the roles of B and F are reversed. Aggregating the secondary, tertiary and quaternary effects of primary charge deposition Q occurring in a uniformly sampled region over the upper-right quadrant gives the charge-sharing tail (Figure B.1(b)).

In charge-summing mode, the boundary defining the region where charge is lost is shifted from the edge of the primary pixel to the outer perimeter of the group of nine pixels with the primary pixel located at the centre. That is, the integration limits are all increased by δ_P/σ_Q and the lost charge is negligible in all practical cases.

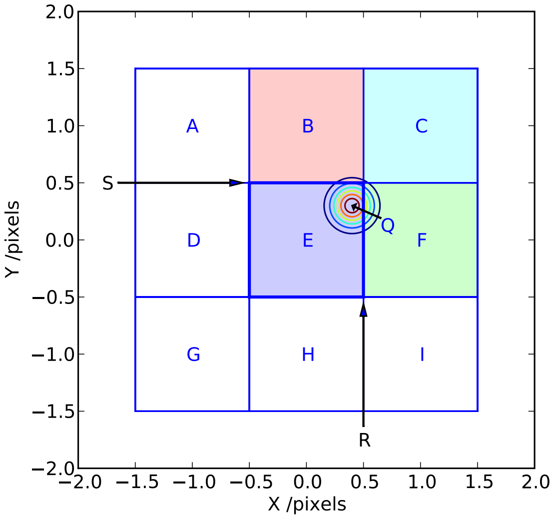

(a)

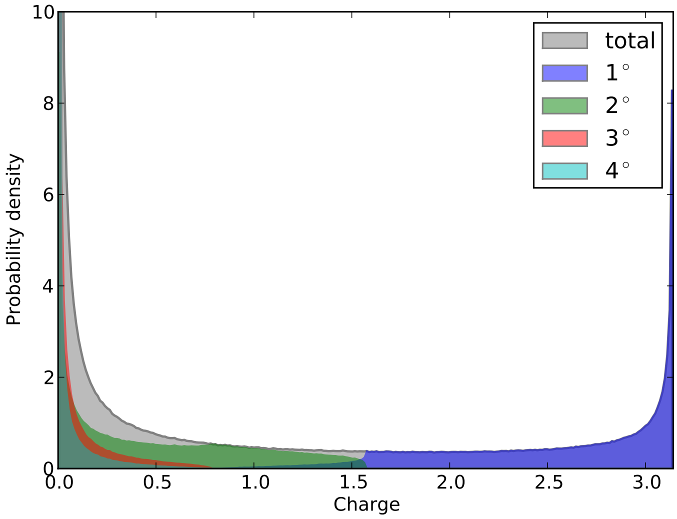

(b)

Figure B.1: (a) A charge Q is created near the boundary of pixel E. The charge spreads across the boundaries R and S as it is collected so that portions are allocated to pixels F, B and C. (b) The distributions of charges (1°, 2°, 3°, 4°) allocated to the primary pixel and its neighbours for a charge $Q = \pi$ created at a random location within the primary pixel. The total probability distribution for allocating a given charge to any pixel is also given. The ratio of pixel pitch to characteristic charge width is assumed to be $\frac{55}{7}$.

Appendix C

`libMars` software library

The `libMars` C library is a locally developed software toolkit for interfacing with the MARS camera and CT gantry subsystems. The library functions are divided into two groups, one for handling interactions with the MARS camera and Medipix detector and the other for controlling the CT gantry and associated hardware. The C library includes a Python interface with separate modules providing methods for MARS camera and CT gantry control as described in Tables C.1 and C.2 respectively. It is being actively developed to incorporate new methods suitable for use with the latest Medipix detectors.

Table C.1: Methods of the `libmarscamera_py` Python interface. These methods enable control of and communication with the MARS camera anb Medipix detectors.

Method	Description
acquire(devID, chipID, acquire_time)	Acquires an image from the detector. Buffers the image within libmars, nothing is returned.
close(id)	Finish with a readout.
downloadMask(devID, chipID)	Downloads a mask from the readout.
find() → int	Locates all new readouts. Returns the number found.

continues on next page

continued from previous page

Method	Description
getAttribute(devID, attribute) → int	Gets an attribute value from the readout.
getChipAttribute(devID, chipID, attribute) → int	Gets a chip specific attribute.
getChipCount(devID) → int	Gets the number of detectors attached to the readout.
getChipType(devID, chipID) → int	Gets the type of chip. Medipix 2: 0, MXR: 1, Timepix 2: 2, Medipix 3: 3.
getDac(devID, chipID, DAC_name) → int	Gets a DAC value.
getHV(devID, chipID) → double	Gets the high voltage reading.
getImage(devID, chipID) → array	Retrieves the(decoded) image from the detector.
getImageSize() →(xDim, yDim)	Gets the size(x,y) of the image from the camera.
getPolarity(devID) → int	Gets the High voltage polarity.
loadConfig(devID, chipID, mask)	Loads the mask onto the detector.
loadConfigFile(devID, chipID, filename)	Loads a CSV mask from file onto detector.
resetChip(devID, chipID)	Resets a detector.
setAttribute(devID, attribute, value)	Sets an attribute value on the readout.
setChipAttribute(devID, chipID, attribute, value)	Sets a chip specific attribute.
setChipType(devID, chipID, type)	Changes the detected type of the chip. This will change the behaviour of the chip. See getChipType.
setDac(devID, chipID, DAC_name, value)	Sets a DAC value.
setHV(devID, value)	Sets the high voltage.
setPolarity(devID, polarity)	Sets the high voltage polarity.

Table C.2: Methods of the `libmarsct_py` Python interface. These methods enable control of and communication with the MARS CT gantry and associated hardware.

Method	Description
caliTemps()	Calibrates the temperature sensors into the EEPROM on the motor controller. Since this is in the EEPROM it only needs to be done once. All three sensors must be at room temperature when this is called for it to work correctly. See also getTemps and zeroTemps.
describeMotor() → string	Returns a string describing the motor controller. See also getFirmware and getSerial.
getAllPos() →(rotation, sample, sensor, xray, camera)	Gets the positions of all 5 motors at once. See also getPos and getViewPos.
getCabinetLock() → boolean	Gets the state of the cabinet lock.
getCompileTime() → string	Gets the date and time the motor controller was compiled.
getFirmware() → string	Requests the firmware description as a string from the motor controller EEPROM. See also setFirmware and getSerial.
getGantryVersion() → version	Gets the version of the gantry attached to a MARS4 motor controller.
getGoto() →(rotation, sample, sensor, xray, camera)	Gets the goto positions of all the motors. See also move and setGoto.
getLamp() → boolean	Gets the state of the lamp.
getPos() →(rotation, sensor, sample)	Gets the position of the main motor controllers, in stepper motor steps. See also getViewPos.
getRotationDriveParam() → float	Gets the parameters for the rotation drive movement. See also setRotationDriveParam, startRotationDrive and startRotationAndSampleDrive.

continues on next page

continued from previous page

Method	Description
getSampleDriveParam() → float	Gets the parameters for the sample drive movement. See also setSampleDriveParam, startSampleDrive and startRotationAndSampleDrive.
getSampleSpeed() → float	Gets the current speed of the sample drive in mm/s. See also setSampleSpeed.
getSerial() → string	Requests the serial number as a string from the motor controller EEPROM. See also setSerial and getFirmware.
getTemps() →(temp1, temp2, temp3) or(temp1, temp2)	Reads from the three temperature sensors in the cabinet. MARS-CT4 has 3 temperatures but MARS-CT3 has only 2. See also caliTemps.
getViewPos() →(source, camera)	Gets the position of the x-ray source and camera stages, in stepper motor steps. These positions determine the magnification. See also getPos.
initIndividualMotor(motorName)	Initializes only one of the motor axes. Possible motor names are 'sample', 'sensor', 'rotation', 'camera' and 'xray'. See also initMotors.
initMotors()	(Re)initializes all 5 motor axes. See also initIndividualMotor.
lampOff()	Turns the lamps off.
lampOn()	Turns the lamps on.
lockCabinet()	Locks the cabinet.
motorFind()	Tries to find a motor controller. Returns nothing. See also motorFindAndInit.
motorFindAndInit()	Finds and then initializes the motor controller. See also motorFind.
move()	Moves all the motors to the goto positions previously set. See also setGoto.

continues on next page

continued from previous page

Method	Description
setAllPos(rotation, sample, sensor, xray, camera)	Sets the positions of all 5 motors at once. See also setPos and SetViewPos.
setFirmware(firmwareString)	Sets a string in the EEPROM for this motor controller firmware description. Maximum length is 80 characters + NULL termination. See also getFirmware and setSerial.
setGoto(rotation, sample, sensor, xray, camera)	Sets the goto positions of all the motors. These will later be moved to with the move command. See also move and getGoto.
setPos(rotation, sensor, sample)	Sets the position of the main motor controllers, in stepper motor steps. See also getPos and setViewPos.
setRotationDriveParam(speed, rotPos)	Sets the parameters for a rotation drive. Where the motor gets moved to rotPos at the given speed. See also getRotationDriveParam, startRotationDrive and startRotationAndSampleDrive.
setSampleDriveParam(speed, samPos)	Sets the parameters for a sample drive. Where the motor gets moved to samPos at the given speed(in mm/s). See also getSampleDriveParam, startSampleDrive and startRotationAndSampleDrive.
setSampleSpeed(speed)	Sets the speed of the sample drive in mm/s. Must be between 0.005 and 50. See also getSampleSpeed.
setSerial(serialString)	Sets a string in EEPROM for this motor controller serial number. Maximum length is 30 characters + NULL termination. See also getSerial and setFirmware.

continues on next page

continued from previous page

Method	Description
setViewPos(source, camera)	Gets the position of the x-ray source and camera stages, in stepper motor steps. These positions determine the magnification. See also getViewPos and setPos.
startRotationAndSampleDrive()	Starts the drive movements for both the rotation and the sample axes. Both movements are performs to previous definitions of what they should be. See also setRotationDriveParam, setSampleDriveParam, startRotationDrive and startSampleDrive.
startRotationDrive()	Starts the rotation drive movement based on what has previously been defined. See also setRotationDriveParam, startSampleDrive, startRotationAndSampleDrive.
startSampleDrive()	Starts the sample drive movement based on what has previously been defined. See also setSampleDriveParam, startRotationDrive, startRotationAndSampleDrive.
stopMotors()	Stops all motors that are currently moving.
unlockCabinet()	Unlocks the cabinet.
xrayCheckFault(id) → boolean	Checks the specified X-ray controller to see if it has detected a fault. True means a fault has been detected. See also xrayResetFault.
xrayCleanup()	Closes all connections to X-ray sources.
xrayDescribe(id) → string	Returns a string describing the specified X-ray controller.
xrayFind() → int	Finds all X-ray sources. Returns the number of sources found.

continues on next page

continued from previous page

Method	Description
xrayGetA(id) → double	Gets the current(A) setting on the specified X-ray controller. See also xrayGetV.
xrayGetV(id) → double	Gets the voltage(V) setting on the specified X-ray controller. See also xrayGetA.
xrayOff(id)	Switches the specified X-ray controller off.
xrayOn(id)	Switches the specified X-ray controller on.
xrayResetFault(id)	Resets the fault flag on the specified X-ray controller. See also xrayCheckFault.
xraySetA(id, newCurrent)	Sets the current(A) on the specified X-ray controller. See also xraySetV.
xraySetV(id, newVoltage)	Sets the voltage(V) on the specified X-ray controller. See also xraySetA.
zeroTemps()	Zeroes the calibration table in EEPROM for the temperature controllers. See also getTemps and caliTemps.

Bibliography

[Alvarez, 2011] Alvarez, R. E. (2011). Estimator for photon counting energy selective x-ray imaging with multibin pulse height analysis. *Medical Physics*, 38(5):2324–2334.

[Alvarez and Macovski, 1976] Alvarez, R. E. and Macovski, A. (1976). Energy-selective reconstructions in x-ray computerised tomography. *Physics in Medicine and Biology*, 21(5):733.

[Anderson et al., 2010] Anderson, N., Butler, A., Scott, N., Cook, N., Butzer, J., Schleich, N., Firsching, M., Grasset, R., de Ruiter, N., Campbell, M., et al. (2010). Spectroscopic (multi-energy) CT distinguishes iodine and barium contrast material in mice. *European Radiology*, 20(9):2126–2134.

[Angulo, 2002] Angulo, P. (2002). Nonalcoholic fatty liver disease. *New England Journal of Medicine*, 346(16):1221.

[Anton et al., 2007] Anton, G., Durst, J., Firsching, M., Giersch, J., Korn, A., Mitschke, M., Niederlohner, D., and Pfeiffer, F. (2007). Imaging theory for x-ray pixel detectors. *Nuclear Inst. and Methods in Physics Research, A*, 563(1F):116–123.

[Badea et al., 2008] Badea, C. T., Drangova, M., Holdsworth, D. W., and Johnson, G. A. (2008). In vivo small-animal imaging using micro-CT and digital subtraction angiography. *Physics in Medicine and Biology*, 53(19):R319.

[Ballabriga, 2009a] Ballabriga, R. (2009a). *The Design and Implementation in 0.13 micron CMOS of an Algorithm Permitting Spectroscopic Imaging with High Spatial Resolution for Hybrid Pixel Detectors*. PhD thesis, CERN.

[Ballabriga, 2009b] Ballabriga, R. (2009b). The Medipix3 manual. Technical report, CERN.

[Ballabriga et al., 2011] Ballabriga, R., Blaj, G., Campbell, M., Fiederle, M., Greiffenberg, D., Heijne, E. H. M., Llopart, X., Plackett, R., Procz, S., Tlustos, L., Turecek, D., and Wong, W. (2011). Characterization of the Medipix3 pixel readout chip. *Journal of Instrumentation*, 6(01):C01052.

[Ballabriga et al., 2006] Ballabriga, R., Campbell, M., Heijne, E., Llopart, X., and Tlustos, L. (2006). The Medipix3 prototype, a pixel readout chip working in single photon counting mode with improved spectrometric performance. In *IEEE Nuclear Science Symposium Conference Record, 2006*, volume 6.

[Ballabriga et al., 2010] Ballabriga, R., Campbell, M., Heijne, E., Llopart, X., Tlustos, L., and Wong, W. (2010). Medipix3: A 64k pixel detector readout chip working in single photon counting mode with improved spectrometric performance. *Nuclear Instruments and Methods in Physics Research Section A: Accelerators, Spectrometers, Detectors and Associated Equipment*, 633:S15–S18.

[Barber et al., 2010] Barber, W., Nygard, E., Wessel, J., Malakhov, N., Wawrzyniak, G., Hartsough, N., Gandhi, T., and Iwanczyk, J. (2010). Fast photon counting CdTe detectors for diagnostic clinical CT: dynamic range, stability, and temporal response. In *SPIE Medical Imaging*, pages 76221E–76221E. International Society for Optics and Photonics.

[Barnes et al., 1985] Barnes, G., Sones, R., Tesic, M., Morgan, D., and Sanders, J. (1985). Detector for dual-energy digital radiography. *Radiology*, 156(2):537–540.

[Bartling et al., 2007] Bartling, S., Stiller, W., Semmler, W., and Kiessling, F. (2007). Small animal computed tomography imaging. *Current Medical Imaging Reviews*, 3(1):45–59.

[Bates and Peters, 1971] Bates, R. and Peters, T. (1971). Towards improvements in tomography. *NZJ Sci*, 14:883.

[Berg et al., 2009] Berg, K., Carr, J., Clark, M., Cook, N., Anderson, N., Scott, N., Butler, A., Butler, P., and Butler, A. (2009). Pilot Study to Confirm that Fat and Liver can be Distinguished by Spectroscopic Tissue Response on a Medipix-All-Resolution System-CT (MARS-CT). In *AIP Conference Proceedings*, volume 1151, page 106.

[Berger et al., 1998] Berger, M., Hubbell, J., Seltzer, S., Chang, J., Coursey, J., Sukumar, R., and Zucker, D. (1998). XCOM: Photon cross sections database. *NIST Standard Reference Database*, 8:87–3597.

[Bethe and Heitler, 1934] Bethe, H. and Heitler, W. (1934). On the stopping of fast particles and on the creation of positive electrons. *Proceedings of the Royal Society of London. Series A*, 146(856):83.

[Bhatt et al., 2006] Bhatt, D., Steg, P., Ohman, E., Hirsch, A., Ikeda, Y., Mas, J., Goto, S., Liau, C., Richard, A., Röther, J., et al. (2006). International prevalence, recognition, and treatment of cardiovascular risk factors in outpatients with atherothrombosis. *JAMA: the Journal of the American Medical Association*, 295(2):180–189.

[Birch and Marshall, 1979] Birch, R. and Marshall, M. (1979). Computation of bremsstrahlung x-ray spectra and comparison with spectra measured with a Ge(Li) detector. *Physics in Medicine and Biology*, 24(3):505.

[Bornefalk, 2012] Bornefalk, H. (2012). XCOM intrinsic dimensionality for low-Z elements at diagnostic energies. *Medical Physics*, 39(2):654.

[Brooks, 1977] Brooks, R. (1977). A quantitative theory of the Hounsfield unit and its application to dual energy scanning. *Journal of Computer Assisted Tomography*, 1(4):487.

[Bulte, 2010] Bulte, J. (2010). Science to Practice: Can CT Be Performed for Multicolor Molecular Imaging? *Radiology*, 256(3):675.

[Butler et al., 2008a] Butler, A., Anderson, N., Tipples, R., Cook, N., Watts, R., Meyer, J., Bell, A., Melzer, T., and Butler, P. (2008a). Bio-medical X-ray imaging with spectroscopic pixel detectors. *Nuclear Inst. and Methods in Physics Research, A*, 591(1):141–146.

[Butler et al., 2009] Butler, A., Cook, N., Schleich, N., Butzer, J., Bones, P., and Butler, P. (2009). Processing of Spectral X-ray Data Using Principal Components Analysis. In *Prague, Czech Republic: 11th International Workshop on Radiation Imaging Detectors (iWoRiD 2009)*, volume 28.

[Butler et al., 2008b] Butler, P., Bell, A., Butler, A., Cook, N., Reinisch, L., Butzer, J., and Anderson, N. (2008b). Applying CERN's detector technology to health: MARS Biomedical 3D spectroscopic x-ray imaging. In *International Symposium on Peaceful Applications of Nuclear Technologies in the GCC Countries*. University of Canterbury.

[Butzer et al., 2008] Butzer, J., Butler, A., Butler, P., Bones, P., Cook, N., and Tlustos, L. (2008). Medipix Imaging-evaluation of datasets with PCA. In *23rd International Conference Image and Vision Computing New Zealand (IVCNZ08)*. University of Canterbury.

[Butzer, 2009] Butzer, J. S. (2009). MARS-CT: Biomedical spectral x-ray imaging with medipix. Master's thesis, University of Canterbury.

[Cameron et al., 2004] Cameron, A., Shaw, J., Zimmet, P., et al. (2004). The metabolic syndrome: prevalence in worldwide populations. *Endocrinology and metabolism clinics of North America*, 33(2):351.

[Campbell et al., 2008] Campbell, M., Heijne, E., Holý, T., Idárraga, J., Jakůbek, J., Lebel, C., Leroy, C., Llopart, X., Pospíšil, S., Tlustos, L., and Vykydal, Z. (2008). Study of the charge sharing in a silicon pixel detector by means of alpha-particles interacting with a Medipix2 device. *Nuclear Instruments and Methods in Physics Research Section A: Accelerators, Spectrometers, Detectors and Associated Equipment*, 591(1):38 – 41.

[Campbell et al., 1998] Campbell, M., Heijne, E., Meddeler, G., Pernigotti, E., and Snoeys, W. (1998). A readout chip for a 64x64 pixel matrix with 15-bit single photon counting. *Nuclear Science, IEEE Transactions on*, 45(3):751 –753.

[Carmi et al., 2005] Carmi, R., Naveh, G., and Altman, A. (2005). Material separation with dual-layer CT. In *Nuclear Science Symposium Conference Record, 2005 IEEE*, volume 4, pages 3–pp. IEEE.

[Carramate et al., 2011] Carramate, L. F. N. D., Oliveira, C. A. B., Silva, A. L. M., da Silva, A. M., dos Santos, J. M. F., and Veloso, J. F. C. A. (2011). Energy weighting technique in quantum computed tomography using a MPGD. *Journal of Instrumentation*, 6(02):C02002.

[Chantler, 2000] Chantler, C. (2000). Detailed tabulation of atomic form factors, photoelectric absorption and scattering cross section, and mass attenuation coefficients in the vicinity of absorption edges in the soft x-ray (Z= 30-36, Z= 60-89, E= 0.1 keV-10 keV), addressing convergence issues of earlier work. *Journal of Physical and Chemical Reference Data*, 29(4):597.

[Compton, 1923] Compton, A. (1923). A quantum theory of the scattering of X-rays by light elements. *Physical Review*, 21(5):483–502.

[Coolidge, 1913] Coolidge, W. (1913). A powerful Roentgen ray tube with a pure electron discharge. *Physical Review*, 2(6):409–430.

[Cormack, 1963] Cormack, A. (1963). Representation of a function by its line integrals, with some radiological applications. *Journal of Applied Physics*, 34(9):2722–2727.

[Cormack, 1964] Cormack, A. (1964). Representation of a function by its line integrals, with some radiological applications. II. *Journal of Applied Physics*, 35(10):2908–2913.

[Cormode et al., 2010] Cormode, D., Roessl, E., Thran, A., Skajaa, T., Gordon, R., Schlomka, J., Fuster, V., Fisher, E., Mulder, W., Proksa, R., et al. (2010). Atherosclerotic Plaque Composition: Analysis with Multicolor CT and Targeted Gold Nanoparticles. *Radiology*.

[Currie, 1968] Currie, L. A. (1968). Limits for qualitative detection and quantitative determination. application to radiochemistry. *Analytical Chemistry*, 40(3):586–593.

[Davies and Woolf, 1993] Davies, M. and Woolf, N. (1993). Atherosclerosis: what is it and why does it occur? *British Heart Journal*, 69(1 Suppl):S3–S11.

[Defrise and Clack, 1994] Defrise, M. and Clack, R. (1994). A cone-beam reconstruction algorithm using shift-variant filtering and cone-beam backprojection. *Medical Imaging, IEEE Transactions on*, 13(1):186–195.

[Delpierre et al., 2007] Delpierre, P., Basolo, S., Berar, J.-F., Bordesoule, M., Boudet, N., Breugnon, P., Caillot, B., Chantepie, B., Clemens, J., Dinkespiler, B., Hustache-Ottini, S., Meessen, C., Menouni, M., Morel, C., Mouget, C., Pangaud, P., Potheau, R., and Vigeolas, E. (2007). XPAD: A photons counting pixel detector for material sciences and small-animal imaging. *Nuclear Instruments and Methods in Physics Research Section A: Accelerators, Spectrometers, Detectors and Associated Equipment*, 572(1):250 – 253.

[Den Boer et al., 2004] Den Boer, M., Voshol, P., Kuipers, F., Havekes, L., and Romijn, J. (2004). Hepatic steatosis: a mediator of the metabolic syndrome. lessons from animal models. *Arteriosclerosis, thrombosis, and vascular biology*, 24(4):644–649.

[Dierick et al., 2004] Dierick, M., Masschaele, B., and Hoorebeke, L. V. (2004). Octopus, a fast and user-friendly tomographic reconstruction package developed in labview®. *Measurement Science and Technology*, 15(7):1366.

[Doesburg et al., 2009] Doesburg, R., Clyne, M., van Leeuwen, D., Cook, N., Butler, P., and Butler, A. (2009). Fast Ethernet Readout for Medipix Arrays with MARS-CT. In *IEEE Nuclear Science Symposium*. University of Canterbury.

[Du et al., 2007] Du, L. Y., Umoh, J., Nikolov, H. N., Pollmann, S. I., Lee, T.-Y., and Holdsworth, D. W. (2007). A quality assurance phantom for the performance evaluation of volumetric micro-CT systems. *Physics in Medicine and Biology*, 52(23):7087.

[Ebel et al., 1989] Ebel, H., Ebel, M., Wernisch, J., Poehn, C., and Wiederschwinger, H. (1989). Quantification of continuous and characteristic tube spectra for fundamental parameter analysis. *X-ray Spectrometry*, 18(3):89–100.

[Engelen and Stephens, 2004] Engelen, R. and Stephens, G. (2004). Information content of infrared satellite sounding measurements with respect to CO2. *Journal of Applied Meteorology*, 43(2):373–378.

[Falk et al., 1995] Falk, E., Shah, P., and Fuster, V. (1995). Coronary plaque disruption. *Circulation*, 92(3):657–671.

[Feldkamp et al., 1984] Feldkamp, L., Davis, L., and Kress, J. (1984). Practical cone-beam algorithm. *Journal of the Optical Society of America A*, 1(6):612–619.

[Feuerlein et al., 2008] Feuerlein, S., Roessl, E., Proksa, R., Martens, G., Klass, O., Jeltsch, M., Rasche, V., Brambs, H., Hoffmann, M., and Schlomka, J. (2008). Multienergy photon-counting K-edge imaging: Potential for improved luminal depiction in vascular imaging. *Radiology*, 249(3):1010.

[Firsching et al., 2009] Firsching, M., Butler, A., Scott, N., Anderson, N., Michel, T., and Anton, G. (2009). Contrast agent recognition in small animal CT using the Medipix2 detector. *Nuclear Instruments and Methods in Physics Research Section A: Accelerators, Spectrometers, Detectors and Associated Equipment*, 607(1):179–182.

[Firsching et al., 2008] Firsching, M., Takoukam Talla, P., Michel, T., and Anton, G. (2008). Material resolving x-ray imaging using spectrum reconstruction with Medipix2. *Nuclear Inst. and Methods in Physics Research, A*, 591(1):19–23.

[Flohr et al., 2006] Flohr, T., McCollough, C., Bruder, H., Petersilka, M., Gruber, K., Su*β*, C., Grasruck, M., Stierstorfer, K., Krauss, B., Raupach, R., et al. (2006). First performance evaluation of a dual-source CT (DSCT) system. *European Radiology*, 16(2):256–268.

[Flynn et al., 1994] Flynn, M., Hames, S., Reimann, D., and Wilderman, S. (1994). Microfocus x-ray sources for 3D microtomography. *Nuclear Instruments and Methods in Physics Research Section A: Accelerators, Spectrometers, Detectors and Associated Equipment*, 353(1-3):312–315.

[Ford et al., 2003] Ford, N., Thornton, M., and Holdsworth, D. (2003). Fundamental image quality limits for microcomputed tomography in small animals. *Medical Physics*, 30:2869.

[Giersch, 2005] Giersch, J. (2005). Medical quantum x-ray imaging with 2D detectors. *Nuclear Instruments and Methods in Physics Research Section A: Accelerators, Spectrometers, Detectors and Associated Equipment*, 551(1):125 – 138. Proceedings of the E-MRS Fall Meeting 2004, Symposium D - Applications of Linear and Area Detectors for X-Ray and Neutron Diffraction and Spectroscopy.

[Giersch et al., 2004] Giersch, J., Niederlöhner, D., and Anton, G. (2004). The influence of energy weighting on X-ray imaging quality. *Nuclear Instruments and Methods in Physics Research Section A: Accelerators, Spectrometers, Detectors and Associated Equipment*, 531(1-2):68–74.

[Glover, 1982] Glover, G. (1982). Compton scatter effects in CT reconstructions. *Medical Physics*, 9:860.

[Goertzen et al., 2004] Goertzen, A. L., Nagarkar, V., Street, R. A., Paulus, M. J., Boone, J. M., and Cherry, S. R. (2004). A comparison of x-ray detectors for mouse CT imaging. *Physics in Medicine and Biology*, 49(23):5251.

[Goldman, 2007] Goldman, L. (2007). Principles of CT and CT technology. *Journal of Nuclear Medicine Technology*, 35(3):115–128.

[Gong et al., 2004] Gong, X., Vedula, A. A., and Glick, S. J. (2004). Microcalcification detection using cone-beam CT mammography with a flat-panel imager. *Physics in Medicine and Biology*, 49(11):2183.

[Goshen et al., 2008] Goshen, L., Sosna, J., Carmi, R., Kafri, G., Iancu, I., and Altman, A. (2008). An iodine-calcium separation analysis and virtually non-contrasted image generation obtained with single source dual energy MDCT. In *Nuclear Science Symposium Conference Record, 2008. NSS'08. IEEE*, pages 3868–3870. IEEE.

[Greskovich and Duclos, 1997] Greskovich, C. and Duclos, S. (1997). Ceramic scintillators. *Annual Review of Materials Science*, 27(1):69–88.

[Groom and Klein, 2000] Groom, D. and Klein, S. (2000). Passage of particles through matter. *The European Physical Journal C - Particles and Fields*, 15:163–173. 10.1007/BF02683419.

[Grundy et al., 2004] Grundy, S., Brewer, H., Cleeman, J., Smith, S., Lenfant, C., et al. (2004). Definition of metabolic syndrome. *Circulation*, 109(3):433–438.

[Hainfeld et al., 2006] Hainfeld, J., Slatkin, D., Focella, T., and Smilowitz, H. (2006). Gold nanoparticles: a new x-ray contrast agent. *British Journal of Radiology*, 79(939):248–253.

[Hecht, 1982] Hecht, H. (1982). Computed Tomographic Demonstration of Rapid Changes in Fatty Infiltration of the Liver. *Radiology*, 142:691–692.

[Heismann et al., 2003] Heismann, B., Leppert, J., and Stierstorfer, K. (2003). Density and atomic number measurements with spectral x-ray attenuation method. *Journal of Applied Physics*, 94:2073.

[Hendee and Ritenour, 2002] Hendee, W. and Ritenour, E. (2002). *Medical Imaging Physics*. John Wiley and Sons.

[Henrich et al., 2009] Henrich, B., Bergamaschi, A., Broennimann, C., Dinapoli, R., Eikenberry, E., Johnson, I., Kobas, M., Kraft, P., Mozzanica, A., and Schmitt, B. (2009). Pilatus: A single photon counting pixel detector for x-ray applications. *Nuclear Instruments and Methods in Physics Research Section A: Accelerators, Spectrometers, Detectors and Associated Equipment*, 607(1):247 – 249.

[Herman et al., 1976] Herman, G., Lakshminarayanan, A., and Naparstek, A. (1976). Convolution reconstruction techniques for divergent beams. *Computers in Biology and Medicine*, 6(4):259–262.

[Herman, 1979] Herman, G. T. (1979). Correction for beam hardening in computed tomography. *Physics in Medicine and Biology*, 24(1):81.

[Hoenig et al., 2010] Hoenig, M., Cowin, G., Buckley, R., McHenery, C., and Coulthard, A. (2010). Liver fat percent is associated with metabolic risk factors and the metabolic syndrome in a high-risk vascular cohort. *Nutrition & Metabolism*, 7.

[Hounsfield, 1973] Hounsfield, G. (1973). Computerized transverse axial scanning (tomography): Part 1. Description of system. *British Journal of Radiology*, 46(552):1016.

[Hubaux and Vos, 1970] Hubaux, A. and Vos, G. (1970). Decision and detection limits for calibration curves. *Analytical Chemistry*, 42(8):849–855.

[Hurrell et al., 2012] Hurrell, M. A., Butler, A. P. H., Cook, N. J., Butler, P. H., Ronaldson, J. P., and Zainon, R. (2012). Spectral Hounsfield units: a new radiological concept. *European Radiology*, 22(5):1008–1013.

[Hyafil et al., 2007] Hyafil, F., Cornily, J., Feig, J., Gordon, R., Vucic, E., Amirbekian, V., Fisher, E., Fuster, V., Feldman, L., and Fayad, Z. (2007). Noninvasive detection of macrophages using a nanoparticulate contrast agent for computed tomography. *Nature Medicine*, 13(5):636–641.

[ICRU, 1988] ICRU (1988). ICRU44 - Tissue substitutes in radiation dosimetry. Technical report, ICRU.

[Jackson and Hawkes, 1981] Jackson, D. F. and Hawkes, D. (1981). X-ray attenuation coefficients of elements and mixtures. *Physics Reports*, 70(3):169 – 233.

[Jakůbek, 2009] Jakůbek, J. (2009). Semiconductor pixel detectors and their applications in life sciences. *Journal of Instrumentation*, 4(03):P03013.

[JCGM, 2008] JCGM (2008). Evaluation of measurement data guide to the expression of uncertainty in measurement JCGM 100: 2008 (GUM 1995 with minor corrections). Technical report, JCGM: BIPM, IEC, IFCC, ILAC, ISO, IUPAC, IUPAP and OIML.

[Johnson et al., 2007] Johnson, T., Krauß, B., Sedlmair, M., Grasruck, M., Bruder, H., Morhard, D., Fink, C., Weckbach, S., Lenhard, M., Schmidt, B., et al. (2007). Material differentiation by dual energy CT: initial experience. *European Radiology*, 17(6):1510–1517.

[Joseph and Spital, 1982] Joseph, P. and Spital, R. (1982). The effects of scatter in x-ray computed tomography. *Medical Physics*, 9:464.

[Judy et al., 1977] Judy, P., Balter, S., Bassano, D., McCullough, E., Payne, J., and Rothenberg, L. (1977). AAPM report No. 1 phantoms of performance evaluation and quality assurance of CT scanner. *Chicago, Illinois: AAPM.*

[Kak and Slaney, 2001] Kak, A. and Slaney, M. (2001). *Principles of computerized tomographic imaging.* Society for Industrial and Applied Math, Philadelphia.

[Kalender, 2005] Kalender, W. (2005). CT: the unexpected evolution of an imaging modality. *European Radiology Supplements*, 15:21–24.

[Kalender et al., 1986] Kalender, W., Perman, W., Vetter, J., and Klotz, E. (1986). Evaluation of a prototype dual-energy computed tomographic apparatus. I. Phantom studies. *Medical Physics*, 13:334.

[Kalender, 1994] Kalender, W. A. (1994). Technical foundations of spiral CT. *Seminars in Ultrasound, CT, and MRI*, 15(2):81 – 89. Spiral CT.

[Kalender, 2001] Kalender, W. A. (2001). *Computed Tomography.* Publicis Corporate Publishing, Erlangen.

[Kappler et al., 2009] Kappler, S., Grasruck, M., Niederlöhner, D., Strassburg, M., and Wirth, S. (2009). Dual-energy performance of dual-kVp in comparison to dual-layer and quantum-counting CT system concepts. In *Proc. SPIE*, volume 7258, page 725842.

[Kawata et al., 1984] Kawata, R., Sakata, K., Kunieda, T., Saji, S., Doi, H., and Nozawa, Y. (1984). Quantitative evaluation of fatty liver by computed tomography in rabbits. *American Journal of Roentgenology*, 142(4):741–746.

[Kaye and Laby, 1995] Kaye, G. and Laby, T. (1995). *Tables of Physical & Chemical Constants (16th edition 1995). 3.6.3 Densities of aqueous solutions. Kaye & Laby Online. Version 1.0 (2005).* National Physical Laboratory (Great Britain).

[Kim et al., 2005] Kim, H., Lee, S., Cho, M., Lee, S., and Cho, G. (2005). Use of a flat-panel detector for microtomography: a feasibility study for small-animal imaging. *Nuclear Science, IEEE Transactions on*, 52(1):193–198.

[Knoll, 2000] Knoll, G. (2000). *Radiation Detection and Measurement.* Wiley, New York.

[Kodama et al., 2007] Kodama, Y., Ng, C., Wu, T., Ayers, G., Curley, S., Abdalla, E., Vauthey, J., and Charnsangavej, C. (2007). Comparison of CT methods for determining the fat content of the liver. *American Journal of Roentgenology*, 188(5):1307–1312.

[Kohonen, 1990] Kohonen, T. (1990). The self-organizing map. *Proceedings of the IEEE*, 78(9):1464–1480.

[Kolodgie et al., 2003] Kolodgie, F., Gold, H., Burke, A., Fowler, D., Kruth, H., Weber, D., Farb, A., Guerrero, L., Hayase, M., Kutys, R., et al. (2003). Intraplaque hemorrhage and progression of coronary atheroma. *New England Journal of Medicine*, 349(24):2316–2325.

[Kotronen and Yki-Jarvinen, 2008] Kotronen, A. and Yki-Jarvinen, H. (2008). Fatty liver: a novel component of the metabolic syndrome. *Arteriosclerosis, thrombosis, and vascular biology*, 28(1):27.

[Kramers, 1923] Kramers, H. (1923). On the theory of X-ray absorption and of the continuous X-ray spectrum. *Philosophical Magazine Series 6*, 46(275):836–871.

[Kriegler et al., 1969] Kriegler, F., Malila, W., Nalepka, R., and Richardson, W. (1969). Preprocessing transformations and their effects on multispectral recognition. In *Remote Sensing of Environment, VI*, volume 1, page 97.

[Langheinrich et al., 2004] Langheinrich, A., Bohle, R., Greschus, S., Hackstein, N., Walker, G., von Gerlach, S., Rau, W., and Hölschermann, H. (2004). Atherosclerotic Lesions at Micro CT: Feasibility for Analysis of Coronary Artery Wall in Autopsy Specimens. *Radiology*, 231(3):675.

[Langheinrich et al., 2009] Langheinrich, A., Kampschulte, M., Crö*ß*mann, C., Moritz, R., Rau, W., Bohle, R., and Ritman, E. (2009). Role of Computed Tomography Voxel Size in Detection and Discrimination of Calcium and Iron Deposits in Atherosclerotic Human Coronary Artery Specimens. *Journal of Computer Assisted Tomography*, 33(4):517.

[Langheinrich et al., 2007] Langheinrich, A., Michniewicz, A., Sedding, D., Lai, B., Jorgensen, S., Bohle, R., and Ritman, E. (2007). Quantitative X-ray imaging of intraplaque hemorrhage in aortas of ApoE-/-/LDL-/-double knockout mice. *Investigative Radiology*, 42(5):263.

[Leber et al., 2004] Leber, A., Knez, A., Becker, A., Becker, C., von Ziegler, F., Nikolaou, K., Rist, C., Reiser, M., White, C., Steinbeck, G., et al. (2004). Accuracy of multidetector spiral computed tomography in identifying and differentiating the composition of coronary atherosclerotic plaques:: A comparative study with intracoronary ultrasound. *Journal of the American College of Cardiology*, 43(7):1241–1247.

[Ledley et al., 1974] Ledley, R., Wilson, J., Golab, T., and Rotolo, L. (1974). The ACTA-scanner: the whole body computerized transaxial tomograph. *Computers in Biology and Medicine*, 4(2):145–152.

[Lehmann et al., 1981] Lehmann, L., Alvarez, R., Macovski, A., Brody, W., Pelc, N., Riederer, S., and Hall, A. (1981). Generalized image combinations in dual kVP digital radiography. *Medical Physics*, 8:659.

[Lemacks et al., 2002] Lemacks, M., Kappadath, S., Shaw, C., Liu, X., and Whitman, G. (2002). A dual-energy subtraction technique for microcalcification imaging in digital mammography—A signal-to-noise analysis. *Medical Physics*, 29:1739.

[Lin et al., 1993] Lin, P., Beck, T., Borras, C., Cohen, G., Jucius, R., Kriz, R., Nickoloff, E., Rothenberg, L., Strauss, K., Villafana, T., et al. (1993). Specification and acceptance testing of computed tomography scanners. *AAPM: Report*.

[Liu et al., 2009] Liu, X., Yu, L., Primak, A., and McCollough, C. (2009). Quantitative imaging of element composition and mass fraction using dual-energy CT: Three-material decomposition. *Medical Physics*, 36:1602.

[Llopart et al., 2002] Llopart, X., Campbell, M., Dinapoli, R., San Segundo, D., and Pernigotti, E. (2002). Medipix2: A 64-k pixel readout chip with 55-micron square elements working in single photon counting mode. *IEEE Transactions on Nuclear Science*, 49(5):2279.

[Longo et al., 2005] Longo, R., Pollesello, P., Ricci, C., Masutti, F., Kvam, B., Bercich, L., Croce, L., Grigolato, P., Paoletti, S., De Bernard, B., et al. (2005). Proton MR spectroscopy in quantitative in vivo determination of fat content in human liver steatosis. *Journal of Magnetic Resonance Imaging*, 5(3):281–285.

[Ludbrook, 2010] Ludbrook, J. (2010). Linear regression analysis for comparing two measurers or methods of measurement: But which regression? *Clinical and Experimental Pharmacology and Physiology*, 37(7):692–699.

[Manuilskiy et al., 2004] Manuilskiy, A., Norlin, B., Nilsson, H., and Froejdh, N. (2004). Spectroscopy applications for the Medipix photon counting X-ray system. *Nuclear Instruments and Methods in Physics Research Section A: Accelerators, Spectrometers, Detectors and Associated Equipment*, 531(1):251.

[Mathieson et al., 2002] Mathieson, K., Passmore, M., Seller, P., Prydderch, M., O'Shea, V., Bates, R., Smith, K., and Rahman, M. (2002). Charge sharing in silicon pixel detectors. *Nuclear Instruments and Methods in Physics Research Section A: Accelerators, Spectrometers, Detectors and Associated Equipment*, 487(1–2):113 – 122.

[McCollough et al., 2012] McCollough, C., Chen, G., Kalender, W., Leng, S., Samei, E., Taguchi, K., Wang, G., Yu, L., and Pettigrew, R. (2012). Achieving routine submillisievert CT scanning: Report from the summit on management of radiation dose in CT. *Radiology*. Published online before print June 12, 2012. doi:10.1148/radiol.12112265.

[McNitt-Gray, 2006] McNitt-Gray, M. (2006). Tradeoffs in Image Quality and Radiation Dose for CT. *Medical Physics*, 33:2154.

[Münch et al., 2009] Münch, B., Trtik, P., Marone, F., and Stampanoni, M. (2009). Stripe and ring artifact removal with combined wavelet–fourier filtering. *Optics Express*, 17(10):8567–8591.

[Naghavi and Falk, 2010] Naghavi, M. and Falk, E. (2010). From vulnerable plaque to vulnerable patient. *Asymptomatic Atherosclerosis*, pages 13–38.

[Ndumele et al., 2011] Ndumele, C., Nasir, K., Conceiçao, R., Carvalho, J., Blumenthal, R., and Santos, R. (2011). Hepatic steatosis, obesity, and the metabolic syndrome are independently and additively associated with increased systemic inflammation. *Arteriosclerosis, Thrombosis, and Vascular Biology*, 31(8):1927–1932.

[Ohnesorge et al., 1999] Ohnesorge, B., Flohr, T., and Klingenbeck-Regn, K. (1999). Efficient object scatter correction algorithm for third and fourth generation CT scanners. *European Radiology*, 9:563–569.

[Pan et al., 2010] Pan, D., Roessl, E., Schlomka, J., Caruthers, S., Senpan, A., Scott, M., Allen, J., Zhang, H., Hu, G., Gaffney, P., et al. (2010). Computed Tomography in Color: NanoK-Enhanced Spectral CT Molecular Imaging. *Angewandte Chemie*, 122(50):9829–9833.

[Paulus et al., 2000] Paulus, M., Gleason, S., Kennel, S., Hunsicker, P., and Johnson, D. (2000). High resolution X-ray computed tomography: an emerging tool for small animal cancer research. *Neoplasia (New York, NY)*, 2(1–2):62.

[Petersilka et al., 2008] Petersilka, M., Bruder, H., Krauss, B., Stierstorfer, K., and Flohr, T. (2008). Technical principles of dual source CT. *European Journal of Radiology*, 68(3):362–368.

[Pfeiffer, 2004] Pfeiffer, K. (2004). *Evaluation of the Medipix detectors for medical X-ray imaging, with special consideration of mammography.* PhD thesis, Universitat Erlangen-Nurnberg.

[Poludniowski, 2007] Poludniowski, G. (2007). Calculation of x-ray spectra emerging from an x-ray tube. Part II. X-ray production and filtration in x-ray targets. *Medical Physics*, 34:2175.

[Poludniowski and Evans, 2007] Poludniowski, G. and Evans, P. (2007). Calculation of x-ray spectra emerging from an x-ray tube. Part I. Electron penetration characteristics in x-ray targets. *Medical Physics*, 34:2164.

[Popovtzer et al., 2008] Popovtzer, R., Agrawal, A., Kotov, N., Popovtzer, A., Balter, J., Carey, T., and Kopelman, R. (2008). Targeted gold nanoparticles enable molecular CT imaging of cancer. *Nano letters*, 8(12):4593.

[Qayyum et al., 2009] Qayyum, A., Chen, D. M., Breiman, R. S., Westphalen, A. C., Yeh, B. M., Jones, K. D., Lu, Y., Coakley, F. V., and Callen, P. W. (2009). Evaluation of diffuse liver steatosis by ultrasound, computed tomography, and magnetic resonance imaging: which modality is best? *Clinical Imaging*, 33(2):110 – 115.

[Radon, 1986] Radon, J. (1986). Integral values along certain manifolds. *IEEE Transactions on Medical Imaging*, 5(4):170–176. Translated from the original German text.

[Rahdert et al., 1999] Rahdert, D. A., Sweet, W. L., Tio, F. O., Janicki, C., and Duggan, D. M. (1999). Measurement of density and calcium in human atherosclerotic plaque and implications for arterial brachytherapy. *Cardiovascular Radiation Medicine*, 1(4):358 – 367.

[Ramachandran and Lakshminarayanan, 1971] Ramachandran, G. and Lakshminarayanan, A. (1971). Three-dimensional reconstruction from radiographs and electron micrographs: application of convolutions instead of Fourier transforms. *PNAS*, 68(9):2236–2240.

[Reed, 1975] Reed, S. (1975). The shape of the continuous X-ray spectrum and background corrections for energy-dispersive electron microprobe analysis. *X-ray Spectrometry*, 4(1):14–17.

[Reilly and Rader, 2003] Reilly, M. and Rader, D. (2003). The metabolic syndrome. *Circulation*, 108(13):1546–1551.

[Ritman, 2007] Ritman, E. (2007). Small-animal CT: its difference from, and impact on, clinical CT. *Nuclear Instruments and Methods in Physics Research Section A: Accelerators, Spectrometers, Detectors and Associated Equipment*, 580(2):968–970.

[Rodgers, 1996] Rodgers, C. (1996). Information content and optimisation of high spectral resolution measurements. In *Proc. SPIE*, volume 2830, pages 136–147.

[Roessl and Proksa, 2007] Roessl, E. and Proksa, R. (2007). K-edge imaging in x-ray computed tomography using multi-bin photon counting detectors. *Physics in Medicine and Biology*, 52(15):4679.

[Roessl et al., 2008] Roessl, E., Schlomka, J., and Proksa, R. (2008). Edge-on semiconductor x-ray detectors-towards high-rate counting computed tomography. In *Nuclear Science Symposium Conference Record, 2008. NSS'08. IEEE*, pages 1748–1751. IEEE.

[Ronaldson et al., 2011a] Ronaldson, J. P., Walsh, M., Nik, S. J., Donaldson, J., Doesburg, R. M. N., van Leeuwen, D., Ballabriga, R., Clyne, M. N., Butler, A. P. H., and Butler, P. H. (2011a). Characterization of Medipix3 with the MARS readout and software. *Journal of Instrumentation*, 6(01):C01056.

[Ronaldson et al., 2011b] Ronaldson, J. P., Zainon, R., Anderson, N., Butler, A., and Butler, P. (2011b). Performance of MARS-CT using Medipix3 for spectral imaging of soft-tissue. In *Proceedings of Nuclear Science and Medical Imaging Conference, 2011*. IEEE.

[Ronaldson et al., 2012] Ronaldson, J. P., Zainon, R., Scott, N. J., Gieseg, S. P., Butler, A., and Butler, P. (2012). Towards quantifying the composition of soft-tissues by spectral CT imaging with Medipix3. Unpublished manuscript.

[Ronaldson et al., 2011c] Ronaldson, J. P., Zainon, R., Sedayo, A., Scott, N., Butler, A., Butler, P., and Anderson, N. (2011c). Towards quantifying the composition of soft-tissues by spectral CT imaging with Medipix3. In *Proceedings of RSNA 2011 Scientific Assembly and Annual Meeting*.

[Ross et al., 2006] Ross, W., Cody, D., and Hazle, J. (2006). Design and performance characteristics of a digital flat-panel computed tomography system. *Medical Physics*, 33:1888.

[Rossmann, 1962] Rossmann, K. (1962). Recording of x-ray quantum fluctuations in radiographs. *JOSA*, 52(10):1162–1163.

[Rutherford et al., 1976] Rutherford, R. A., Pullan, B. R., and Isherwood, I. (1976). Measurement of effective atomic number and electron density using an EMI scanner. *Neuroradiology*, 11:15–21. 10.1007/BF00327253.

[Sato et al., 1981] Sato, F., Sasaki, S., Kawashima, N., Chino, F., et al. (1981). Late effects of whole or partial body x-irradiation on mice: life shortening.

International Journal of Radiation Biology and Related Studies in Physics, Chemistry, and Medicine, 39(6):607.

[Schlomka et al., 2008] Schlomka, J. P., Roessl, E., Dorscheid, R., Dill, S., Martens, G., Istel, T., Baumer, C., Herrmann, C., Steadman, R., Zeitler, G., Livne, A., and Proksa, R. (2008). Experimental feasibility of multi-energy photon-counting K-edge imaging in pre-clinical computed tomography. *Physics in Medicine and Biology*, 53(15):4031–4047.

[Scofield, 1973] Scofield, J. (1973). Theoretical photoionization cross sections from 1 to 1500 keV. Technical report, California University, Livermore. Lawrence Livermore Lab.

[Scott et al., 2012] Scott, N., Cameron, V., Raudsepp, S., Lewis, L., Simpson, E., Richards, A., and Ellmers, L. (2012). Generation and characterization of a mouse model of the metabolic syndrome: apolipoprotein E and aromatase double knockout mice. *American Journal of Physiology-Endocrinology And Metabolism*, 302(5):E576–E584.

[Shikhaliev, 2005] Shikhaliev, P. M. (2005). Beam hardening artefacts in computed tomography with photon counting, charge integrating and energy weighting detectors: a simulation study. *Physics in Medicine and Biology*, 50(24):5813.

[Shikhaliev and Fritz, 2011] Shikhaliev, P. M. and Fritz, S. G. (2011). Photon counting spectral CT versus conventional CT: comparative evaluation for breast imaging application. *Physics in Medicine and Biology*, 56(7):1905.

[Sorenson and Floch, 1985] Sorenson, J. and Floch, J. (1985). Scatter rejection by air gaps: an empirical model. *Medical Physics*, 12:308–316.

[Stadler et al., 2004] Stadler, N., Lindner, R., and Davies, M. (2004). Direct detection and quantification of transition metal ions in human atherosclerotic plaques: evidence for the presence of elevated levels of iron and copper. *Arteriosclerosis, Thrombosis, and Vascular Biology*, 24(5):949–954.

[Stephens et al., 1977] Stephens, D., Sheedy, P., Hattery, R., and MacCarty, R. (1977). Computed tomography of the liver. *American Journal of Roentgenology*, 128(4):579.

[Stine, 1989] Stine, R. (1989). An introduction to bootstrap methods. *Sociological Methods & Research*, 18(2-3):243–291.

[Stonestrom and Macovski, 1976] Stonestrom, J. and Macovski, A. (1976). Scatter considerations in fan beam computerized tomographic systems. *Nuclear Science, IEEE Transactions on*, 23(5):1453–1458.

[Taguchi et al., 2009] Taguchi, K., Srivastava, S., Kudo, H., and Barber, W. (2009). Enabling photon counting clinical x-ray CT. In *Nuclear Science Symposium Conference Record (NSS/MIC), 2009 IEEE*, pages 3581–3585. IEEE.

[Talla, 2011] Talla, P. (2011). *Investigation of photon counting pixel detectors for X-ray spectroscopy and imaging.* PhD thesis, University of Erlangen-Nuremberg.

[Tarantola, 2005] Tarantola, A. (2005). *Inverse problem theory and methods for model parameter estimation.* Society for Industrial Mathematics.

[Thiam et al., 2004] Thiam, S., Tracy, R., Robinson, P. J. W., and Warner, I. (2004). Determination of elements in native and bypass human coronary artery plaque deposits from the same heart using inductively coupled plasma-mass spectrometry. *Journal of Environmental Science and Health, Part A*, 39(6):1497–1503.

[Thompson et al., 2001] Thompson, A., Vaughan, D., for X-ray optics, C., and advanced light source (2001). *X-ray data booklet.* Lawrence Berkeley National Laboratory, University of California Berkeley, CA.

[Tlustos, 2010] Tlustos, L. (2010). Spectroscopic x-ray imaging with photon counting pixel detectors. *Nuclear Instruments and Methods in Physics Research Section A: Accelerators, Spectrometers, Detectors and Associated Equipment*, 623(2):823–828.

[Tucker et al., 1991] Tucker, D., Barnes, G., and Chakraborty, D. (1991). Semiempirical model for generating tungsten target x-ray spectra. *Medical Physics*, 18(2):211–218.

[Turbell, 2001] Turbell, H. (2001). *Cone-beam reconstruction using filtered backprojection.* PhD thesis, Linköping University.

[van Eijk, 2003] van Eijk, C. W. E. (2003). Inorganic scintillators in medical imaging detectors. *Nuclear Instruments and Methods in Physics Research Section A: Accelerators, Spectrometers, Detectors and Associated Equipment*, 509(1-3):17 – 25. Proceedings of the 4th Internatonal Workshop on Radiation Imaging Detectors.

[Walsh et al., 2011] Walsh, M. F., Opie, A. M. T., Ronaldson, J. P., Doesburg, R. M. N., Nik, S. J., Mohr, J. L., Ballabriga, R., Butler, A. P. H., and Butler, P. H. (2011). First CT using Medipix3 and the MARS-CT-3 spectral scanner. *Journal of Instrumentation*, 6(01):C01095.

[Wang et al., 2003] Wang, B., Gao, Z., Zou, Q., and Li, L. (2003). An experimental study in rabbits. *Acta Radiologica*, 44(1):92–97.

[Wang et al., 2008] Wang, G., Yu, H., and De Man, B. (2008). An outlook on x-ray CT research and development. *Medical Physics*, 35:1051–1064.

[Wang et al., 2011a] Wang, J., Garg, N., Duan, X., Liu, Y., Leng, S., Yu, L., Ritman, E. L., Kantor, B., and McCollough, C. H. (2011a). Quantification of iron in the presence of calcium with dual-energy computed tomography (DECT) in an ex vivo porcine plaque model. *Physics in Medicine and Biology*, 56(22):7305–7316.

[Wang et al., 2011b] Wang, X., Meier, D., Mikkelsen, S., Maehlum, G. E., Wagenaar, D. J., Tsui, B. M. W., Patt, B. E., and Frey, E. C. (2011b). MicroCT with energy-resolved photon-counting detectors. *Physics in Medicine and Biology*, 56(9):2791–2816.

[Whiddington, 1912] Whiddington, R. (1912). The transmission of cathode rays through matter. *Proceedings of the Royal Society of London. Series A*, 86(588):360.

[Williams et al., 1999] Williams, M., Mangiafico, P., and Simoni, P. (1999). Noise power spectra of images from digital mammography detectors. *Medical Physics*, 26:1279–1293.

[Yaffe, 2001] Yaffe, M. (2001). Digital mammography–detector considerations and new applications. *Nuclear Instruments and Methods in Physics Research Section A: Accelerators, Spectrometers, Detectors and Associated Equipment*, 471(1-2):6–11.

[Yaffe and Rowlands, 1997] Yaffe, M. J. and Rowlands, J. A. (1997). X-ray detectors for digital radiography. *Physics in Medicine and Biology*, 42(1):1.

[Yaroslavsky, 2003] Yaroslavsky, L. (2003). *Digital Holography and Digital Image Processing:: Principles, Methods, Algorithms.* Springer.

[Ye, 1998] Ye, J. (1998). On measuring and correcting the effects of data mining and model selection. *Journal of the American Statistical Association*, 93(441):120–131.

[Zainon, 2012] Zainon, R. (2012). *Spectral micro-CT imaging of ex vivo atherosclerotic plaque.* PhD thesis, Univerisity of Canterbury, Christchurch, New Zealand.

[Zainon et al., 2011] Zainon, R., Ronaldson, J. P., Butler, A., and Butler, P. (2011). Establishing a linear basis for quantifying material composition using spectral computed tomography. In *Proceedings of 2011 International Conference on Biomedical Engineering and Biotechnology (BEB2011).* IEEE.

[Zainon et al., 2012] Zainon, R., Ronaldson, J. P., Janmale, T., Scott, N. J., Buckenham, T., Butler, A., Butler, P., Doesburg, R., Gieseg, S. P., Roake, J., and Anderson, N. (2012). Spectral CT of carotid atherosclerotic plaque: comparison with histology. *European Radiology*. Published online before print July 4, 2012. PubMed PMID:22760344. doi:10.1007/s00330-012-2538-7.

[Zarb et al., 2011] Zarb, F., Rainford, L., and McEntee, M. F. (2011). Developing optimized CT scan protocols: Phantom measurements of image quality. *Radiography*, 17(2):109 – 114.

[Zeller, 2009] Zeller, H. (2009). Simulation of photon interactions in spectral CT. Technical report, University of Canterbury.

[Zhu et al., 2009] Zhu, S., Tian, J., Yan, G., Qin, C., and Feng, J. (2009). Cone beam micro-CT system for small animal imaging and performance evaluation. *Journal of Biomedical Imaging*, 2009:1–9.